Objective Molecular Dynamics: An atomistic analogue of exact solutions of continuum mechanics

A THESIS
SUBMITTED TO THE FACULTY OF THE GRADUATE SCHOOL
OF THE UNIVERSITY OF MINNESOTA
BY

Gunjan Pahlani

IN PARTIAL FULFILLMENT OF THE REQUIREMENTS
FOR THE DEGREE OF
DOCTOR OF PHILOSOPHY

Richard D. James, Adviser
Thomas E. Schwartzentruber, Co-Adviser

September, 2022

Acknowledgements

There are many people I want to express my gratitude for their contribution to my time in graduate school. First and foremost, I would like to thank my adviser, Prof. Richard James, for his continuous support throughout my Ph.D. journey. I am really grateful to him for always being so approachable and devoting a lot of his time discussing my research. I don't remember a single day where I had come less motivated after meeting him. His enthusiasm for research and expertise in the field has always inspired me to learn and perform better. I truly resonate with a famous quote made by Sir Issac Newton: "If I have seen further than others, it is by standing upon the shoulders of giants." I believe that if I have gained any research vision then it has been imparted to me by my adviser and I feel fortunate for having received an opportunity to work with Prof. James.

I feel extremely lucky to have Prof. Tom Schwartzentruber as my co-adviser. I would like to sincerely thank him for his constant support. I really appreciate our discussions on gas dynamics and learning from him. He has played an integral role in my PhD journey. I collectively thank Prof. James and Prof. Schwartzentruber for their interest in my research, and I am confident that my thesis wouldn't have taken the shape it has without their amazing mentorship.

I would like to wholeheartedly express my gratitude to other thesis committee members Prof. Ellad Tadmor, Prof. Graham Candler and Prof. Traian Dumitrica for their helpful and constructive expert feedback. Besides their research advises, I have thoroughly enjoyed their courses over the years.

I would also like to thank Prof. Ryan Elliott whose courses on continuum mechanics

in my very first semester at the university planted a seed of interest in the subject. Also, thanks to Prof. Shakti Gupta and Prof. Viswanath Chinthapenta for providing the first exposure to research during my undergraduate studies at IIT Hyderabad, India.

I am greatly thankful to my colleague Dr. Erik Torres for his contributions in our discussions on my research. Also, thanks to Dr. Ananya R. Balakrishna for her suggestions on my PhD research and my overall professional growth. She has always given me very helpful advices to do well in my career. There are many peers at the university who really need special mention for their advices and friendship. I am thankful to Dr. Narendra Singh for always being so reachable for valuable research discussions at any time of the day. I also want to thank Dr. Vivek Dabade and Dr. Deepti Verma for mentoring me from time to time and always wanting the best for me.

My other graduate peers in AEM, Moon-Ki, Michael, Ioannis, Mingjian, Eric, Hanlin, Ariel, Giorgos, Fan, Eduardo who have helped me a lot throughout my PhD journey in various aspects. I have learnt a lot from them and enjoyed the time spent together. I also want to thank all the solid lab members (former and present), with whom I have spent a lot of time, and have had many productive discussions. I also appreciate the help from AEM administrative staff, Molly, Hanna, and Ray Muno.

I would also like to thank my friends Merin, Sahadeo, Jyot, Yorkinoy, Sagnik, Manash, Alex, Chiara, Eric, Navaneeth, JV, Sushmita, Sarthak, Oshin, Hashma, Jazeem, Mishfad, Arjun for creating such a homely environment. My undergrad friends Akshay, Apoorva, Kalyani, and Baggan for always being there and cheering me in tough times. The journey became much easier with all of them being around.

I want to especially thank my best friend Dr. Sajal Singh for always being there through thick and thin. He has always encouraged me to do better and truly has strong contribution in making this journey possible. I truly derive lot of inspiration from him.

I want to thank my family, my parents Rashmi and Mohan Pahlani, and my sisters Drishti and Dr. Manisha for their constant support and encouragement throughout

this academic journey. They have made a lot of sacrifices so that I could do what I wanted to do in my career and life. They are my pillars of strength. I want to thank my grandparents Atur and Nichal Pahlani for their countless blessings. Though they are not with us to see me graduate with a PhD, but I am sure both of them are very proud to see their little granddaughter complete this milestone.

Finally, I would like to thank the almighty for keeping my family safe during uncertain times specially during the COVID-19 pandemic when I was thousands of miles away from them.

Dedication

To my parents Rashmi and Mohan Pahlani and grandparents Atur and Nichal Das Pahlani

Abstract

This thesis is aimed at the computational development and application of the method of Objective Molecular Dynamics (OMD). At first, the thesis develops OMD as an efficient computational tool by focusing on the development of the effective implementation of the method for the time-dependent translation group. Later, it focuses on its usage in studying gas and dislocation dynamics under strong non-equilibrium conditions.

OMD is a generalization of periodic MD to non-equilibrium cases that exploits the invariance of the equations of MD and the underlying potential energy hypersurface. The method is used to inform higher-scale theories. This is motivated by the fact that OMD enables forging of rigorous links between fundamental quantum mechanics and nonstandard macroscopic continuum mechanics. It provides an atomistic analogue of motions that are exact solutions of the macroscopic equations for general solids or fluids. The other advantage is that in OMD only a few atoms are actually simulated, but the full infinite set of atoms satisfy exactly the MD equations. This considerably reduces the computational cost of the problem.

The thesis makes comparison of the predictions from the particle-level method of OMD with solutions of the Navier-Stokes (NS) equations combined with Newtonian and Fourier models for a compressible, heat- conducting monoatomic gas. By studying in detail the macroscopic motions corresponding to diverse OMD simulations, the breakdown of NS equations is investigated and a generalization of the Navier-Stokes equations based on Rivlin-Ericksen (RE) theory is postulated. RE theory agrees accurately with NS for slow flows but makes significant improvements over NS relation in capturing far-from-equilibrium momentum transport. This work finds application in facilitating the use of continuum CFD modeling even in the regime of far-from-equilibrium flows which will be highly useful for the modeling of vehicle scale hypersonic and micro-nano scale flows.

Next, the method is applied to study high-temperature chemically reacting flows in various regimes relevant to hypersonic flows to provide in-depth molecular level analysis. The study explores dissociation, recombination, and energy exchange in nitrogen flows and reports the existence of non-equilibrium population distributions and significant microscopic selectivity of reactive processes. This is known to have a direct impact on continuum thermo-chemistry models. The comparison of OMD with CFD shows the inadequacy of the widely used standard Park's model in capturing the correct physics of strong thermo-chemical non-equilibrium gas.

Finally, the same method is applied to investigate a very different system than the previous cases. It is demonstrated that OMD is a powerful method of simulation for dislocation motion, including cross-slip and the transition to twinning, as well as frictional sliding by careful choice of initial conditions. The study investigates the phenomenon of cross-slipping where screw dislocation leaves its habit plane and glides in a conjugate cross-slip plane. It is answered how large a stress can FCC nickel sustain before it cross-slips in non-equilibrium regime under the effect of a large strain rate at finite temperature by taking a kinetic viewpoint. Surprisingly, transition state theory captures some aspects of the behavior of cross-slip under high-rate deformation even in these far-from-equilibrium situations. This finding can assist the modeling of cross-slip at the mesoscopic scale within the framework of dislocation dynamics simulation under high-rate conditions. The thesis also reports some important pathways that material chooses to relax the stress under different macroscopic motions.

Another contribution is to show how OMD techniques can be used to study homoenergetic dilatational flow exhibiting spontaneous condensation. Moreover, to illustrate that both solid boundaries and fluid can be treated in the same exact OMD simulation, the transitional flow of argon gas exhibiting slip in a nanochannel is also studied. The thesis also reports the modeling of sliding surfaces using the framework of OMD.

Contents

List of Tables

List of Figures

Chapter 1

Introduction

1.1 Molecular Dynamics and Continuum Mechanics

Increase in computing power has advanced the development and usage of computational tools providing another avenue for exploration. Atomistic modeling plays an indispensable role, especially when dealing with extreme environments which push experimental and theoretical methods beyond their current limits necessitating a first-principle-based approach.

Molecular Dynamics (MD) is a powerful computer simulation technique that elucidates the macroscopic response of a system by exploring the dynamics of atoms deterministically at the microscopic scale. The first MD simulation was reported for hard-sphere system[1, 2], almost six decades ago. Since then, its application has been extended to multitude of real systems. MD allows to experiment in silico: by employing computers to solve Newton's equation of motion for every particle. The computed trajectory through phase space (positions and velocities of atoms) is then analyzed to estimate the statistical properties of the system [3]. The method relies on the sole input of potential energy hypersurface whose existence stems from time-dependent Schrödinger equation in conjunction with adiabatic approximation of quantum mechanics. This results in instantaneous relaxation of electrons to the appropriate ground state configuration which enables the decoupling of the motion of electrons from the motion of nuclei whose dynamics can be treated classically [4, 5]. Though better than the full quantum treatment of the system in terms of complexity, it still suffers from two well-known limitations:

its accessibility to only short time and length scales. The time scale limitation arises because atomistic simulation uses time steps on the order of femto second to capture the highest frequency of atomic vibrations and to preserve the accuracy of numerical integration schemes. Advent of high-speed computers has improved the situation but due to the sequential nature of time stepping, the limitation still persists. Consequently, the total simulation time is typically limited to less than one microsecond and hence the method is prohibitively expensive for its usage in direct engineering applications.

The other computational modeling approach which overcomes the above-mentioned limitations is the theory of continuum mechanics that approximates the system as a continuous medium. Continuum (macroscopic) variables represent averages over huge numbers of atoms, such that random fluctuation of atoms have no notable effect on instantaneous local quantities. The evolution of these macroscopic variables is based on the numerical solution of the partial differential equations of macroscopic conservation equations. The theory of continuum mechanics is incredibly successful theory but is not complete. It requires constitutive relations as closure for the treatment of smaller scales and which are usually fitted to limited experimental measurements and are not accurate under strong non-equilibrium conditions. A first-principles approach, such as MD, does not suffer from this limitation hence the use of atomistic simulations to guide the development of higher-scale theories such as continuum mechanics can result in the development of better physical models and can expand its validity regime.

1.2 Non-Equilibrium Molecular Dynamics

Equilibrium MD (EMD) is linked to equilibrium statistical mechanics [6, 7], where the time evolution of a single atomic system is believed to be in statistical agreement with the evolution of very large number of identical systems (ensemble) in phase space at same moment. This connection led to the idea of defining macroscopic observables which are identified by ensemble averages by the long time average of the phase function. This comes from Boltzmann's idea of ergodicity where it is understood that under imposed macroscopic constraints, if given sufficient time then a system will visit all points and will sample consistent time-invariant probability density in phase space. An alternative

probabilistic interpretation for predicting macroscopic observables using phase averages was provided by Gibbs[8]. The fundamental problem of statistical mechanics is the determination of correct ensemble to represent a dynamical system under given conditions [9]. The case of statistical equilibrium which is characterized by the fact that long time behavior of system is definite and independent of time has such ensembles worked out in full detail. For example, a microcanonical ensemble corresponds to the system which is isolated with fixed total energy E, a canonical ensemble corresponds to a system at constant temperature T, and a (generalized) stress ensemble corresponds to system subjected to constant external stress[10]. Thus, different kinds of ensembles correspond to various macroscopic boundary conditions imposed on the system. The simplest equilibrium molecular dynamics algorithm uses Hamilton's equations of motion alone, which would be appropriate for a microcanonical or adiabatic system. The other macroscopic constraints are achieved by imposing a thermostat and barostat on the system for a constant temperature/constant stress ensemble.

On the other hand, Non-Equilibrium Molecular Dynamics (NEMD) does not have a well-developed theoretical connection with a statistical mechanics framework, because of the absence of a general nonequilibrium statistical mechanics. Thus, the use of equilibrium concepts of thermostat and barostat which are designed to sample the equilibrium probability density for tuning a system under far-from-equilibrium conditions is questionable since it can pollute the natural dynamics of atoms.

The need to better simulate the non-equilibrium real world has resulted in the emergence of various ways of performing nonequilibrium simulations[11]. These are divided into two broad categories [12]. The first method tries to model real systems closely by explicitly modeling atomistic boundaries/reservoirs to apply the external perturbation[13]. This type of simulation is often called a 'boundary driven' non-equilibrium simulation because the thermodynamic force arises due to the conditions of the momentum, heat, or chemical species reservoirs attached to the system of interest. Modeling in this manner can induce spatial inhomogeneities near the walls which call for a bigger system for simulation unless one is specifically interested in nanoscopic behavior. Periodic boundary conditions (PBCs) help mitigating this effect and is useful to analyze bulk phenomena

where one surrounds the fundamental simulation domain by periodic images of itself. This helps to remove finite-size/surface effects of the simulation. The famous Lees and Edwards method [14] which was developed to simulate simple shear motion though employs a variant of PBCs but is considered to belong to this class of simulation because it is the motion of the periodic images above and below the main simulation box that drives the shear flow. The bigger generalization of the nonequilibrium simulations of shear flow by Lees and Edwards (LE) is provided by the special subset of the method termed **Objective Molecular Dynamics (OMD)**[15, 16].

The novel method of OMD provides a framework for simulating non-equilibrium conditions that has a rigorous foundation based on the fundamental invariance (invariance under orthogonal transformations, translations, and permutations) of the underlying Born-Oppenheimer potential energy surface and the equations of molecular dynamics. Many molecular structures present in nature are connected to this invariance and are amenable to OMD methods. Those structures are called 'Objective Structures'[17]. By making the special choice of a time-dependent translation group, one can obtain OMD solutions representing a family of unsteady flows which are associated with this invariance as well. These macroscopic flows have Eulerian velocity fields of the form [18]

$$\mathbf{v}(\mathbf{x}, t) = \mathbf{A}(\mathbf{I} + t\mathbf{A})^{-1}\mathbf{x}. \tag{1.1}$$

Here, $\mathbf{A}$ is an assignable 3×3 matrix that can be interpreted as Lagrangian velocity gradient and t is the time. From a first principles perspective, OMD serves as an ideal tool to simulate these flows. By choosing $\mathbf{A}$ in different ways, the velocity field includes many examples of steady and unsteady compressible and incompressible flows, including cases with time-dependent vorticity and cases with strong singularities. The latter occurs when $\mathbf{A}$ is chosen such that $\det(\mathbf{I} + t\mathbf{A}) \to 0$ in finite time.

From a computational point of view, the method can be viewed as a generalization of periodic boundary conditions ($\mathbf{A} = \mathbf{0}$) and of Lees-Edwards boundary conditions ($\mathbf{A} = \mathbf{a} \otimes \mathbf{n},\ \mathbf{a} \cdot \mathbf{n} = 0$). However, it is formulated in a different way that enables the use of time-dependent isometry groups. A modest number of atoms are chosen as *simulated*

atoms. The MD equations are solved for only these atoms, and the motions of the other, typically infinite, set of atoms (the non-simulated atoms) are given by the group action on the simulated atoms at each time step. The basic theorem of OMD says that all the atoms, simulated and nonsimulated, satisfy pure MD equations for their forces exactly. In practice, the simulated atoms quickly diffuse into the non-simulated atoms, but, nevertheless, the statements made here remain true. Note that though the LE boundary conditions can be viewed as a special case of OMD, the typical implementation of the LE method using moving boxes does not generalize to OMD.

Another widely used method to conduct NEMD simulations imposes explicit external forces in the equation of motion in conjunction with compatible periodic boundaries to achieve any desired homogeneous motion. Because of the introduction of artificial non-Hamiltonian terms, it is doubtful that it would sample the correct non-equilibrium distribution. The method is not exact but can be useful to generate approximations in the situations of interest. This has the advantage of being able to treat some flows, not of the macroscopic form (1.1). The method was pioneered by Hoover, Evans, and others and is considered suitable for fluid flows[19, 20]. Note that since the perturbation is explicit in the equations of motion, it is possible to apply response theory to the system investigated using this method. Because of the fictitious forces, the method can give different results to those of OMD even in cases where the homogeneous motion matches the average motion of OMD. This is due to the significant dependence of the behavior of MD system on the specifics of atomic forces. In OMD, the MD equations are not modified: the force on each atom is only produced by the other (simulated and non-simulated) atoms. One can say that the forces that "drive the motion" are applied at infinity, but these forces are not explicitly introduced but are inherent in the method.

1.3 Connection of OMD with Continuum Mechanics

OMD simulates very special macroscopic motion given by (1.1) which comes from the invariance of the interaction between atoms. These are termed "universal motions" which are exact solutions of the momentum conservation equation of continuum mechanics under zero body force, and for every choice of the 3×3 matrix $\mathbf{A}$[18]. This is

given by:

$$\rho(\mathbf{v}_t + \nabla\mathbf{v}\mathbf{v}) = \rho(-\mathbf{A}(\mathbf{I}+t\mathbf{A})^{-1}\mathbf{A}(\mathbf{I}+t\mathbf{A})^{-1}\mathbf{x} + \mathbf{A}(\mathbf{I}+t\mathbf{A})^{-1}\mathbf{A}(\mathbf{I}+t\mathbf{A})^{-1}\mathbf{x}) = 0 = \boldsymbol{\nabla}\cdot\boldsymbol{\sigma} = 0. \tag{1.2}$$

where divergence of stress is identically zero since all accepted models in continuum mechanics (elastic/plastic, nonlinear elastic, Navier-Stokes, non-Newtonian, etc.) have the property that a motion with deformation gradient depending only on time ($\mathbf{F}$=($\mathbf{I}$+t$\mathbf{A}$)) has stress that depends only on time. Hence, these motions are promising candidate as an approach for making a direct connection with continuum mechanics for which there exist an exact atomistic analogue where every atom out to infinity, simulated or nonsimulated, satisfies the equations of molecular dynamics to high accuracy.

The overall objective of the dissertation is to investigate the non-equilibrium systems at an atomic scale with the aim to guide better model development for higher-scale theories using OMD. However, the efficient numerical implementation of OMD presents difficulties usually not present in other time-dependent numerical methods, and there does not currently exist an efficient numerical strategy for implementing OMD. As explained above, the main issue one has to confront in implementation is that the simulated atoms quickly diffuse chaotically into the sea of non-simulated atoms, and this requires that one develops an efficient method of finding neighbors.

The first goal of this dissertation is to provide a useful implementation of OMD for the time-dependent translation group. Next, the method of OMD is used for modeling gases with the aim to understand dilute gas dynamics under strong non-equilibrium conditions and later focuses on problems in materials science, particularly for the investigation of the dynamics of dislocations under high rate deformation.

1.4 Gas Dynamics

Hypersonic vehicles during reentry encounter varying flow regimes during their descent, varying from free-molecular to transition to continuum. The ability to make better predictions of the flows in the entire range determines the feasibility of space missions and

the development of future hypersonic vehicles. Experiments are difficult and expensive to conduct under the extreme environment encountered in such missions in ground-based experiment facilities and possess significant uncertainties. Therefore, numerical simulations play an instrumental and complementary role to understand hypersonic flows and guide better designs. Computational Fluid Dynamics (CFD) modeling, works well in the continuum regime where the collision rate is high enough such that near-equilibrium molecular distribution functions are maintained. CFD methods are less successful in the continuum-transition regime due to the breakdown of the underlying Navier-Stokes-Fourier (NSF) constitutive model. The approximations made there for the stress and heat flux, though applicable in the near-equilibrium regime, fall short in the transition regime.

The complexity of the failure of CFD is further increased when modeling diatomic flows due to the presence of additional internal degrees of freedom of rotation and vibration of the molecules in addition to translational which give rise to many more energy storage modes. Hypersonic flows characterized by high Mach number (internal thermodynamic energy of fluid particles is small compared to kinetic energy) are energetic and can create very high temperatures which can give rise to many processes, such as vibrational and electronic energy excitation, chemical reactions, ionization and gas-surface interactions [21]. In addition to transport non-equilibrium, strong thermo-chemical non-equilibrium can also be observed. This is due to rarefied conditions which leads to the comparable flow convective time scales with that of underlying gradients, chemistry and internal energy transfer. Thus, the concern about non-continuum flows is complicated by non-equilibrium chemistry [22].

1.4.1 Monoatomic gas

To simplify the complexity associated with the breakdown of continuum physics, let's first focus on the dynamics of mono-atomic gas (simplest of all thermodynamic materials) in continuum-transition regime. A viable technique to be used in this regime is the Bird's stochastic particle-based method of Direct Simulation Monte Carlo (DSMC)[23, 24]. DSMC statistically solves the Boltzmann Transport Equation (BTE) which defines

the evolution of the phase density $f(\mathbf{x}, t, \mathbf{v})$. In kinetic theory, phase density is defined such that $dN = f(\mathbf{x}, t, \mathbf{v})d\mathbf{x}d\mathbf{v}$ provides the number of molecules that occupy a cell of phase space $d\mathbf{x}d\mathbf{v}$ at time t. This definition introduces certain level of inaccuracy, since now the state of each particle is known within an error of $d\mathbf{x}d\mathbf{v}$. However, phase density provides the detailed characterization of the state of the gas where macroscopic quantities are defined by weighted averages of phase density, obtained by integration over microscopic velocity [25].

The DSMC method has had success describing dilute flows in wide regimes and is one of the most successful particle simulation methods for rarefied gaseous flows. However, in the continuum-transition regime where the density is not low enough, DSMC is highly expensive as a large number of computational cells and molecules and small time-steps are required to model near-continuum behavior. Hence there is a need to develop a better set of constitutive relations to be incorporated into CFD modeling.

Recently, investigations to develop new constitutive models have begun to emerge, and numerous approaches appear in the literature. One can take the kinetic viewpoint and work with the Boltzmann transport equation. However, its closed form analytical solutions are difficult to obtain except for some simple flows. It can be solved approximately via Chapman-Enskog (CE) perturbative method (developed independently by Enskog and Chapman [26, 27]) where the velocity distribution function is assumed to be a perturbation expansion of equilibrium Maxwell-Boltzmann distribution in Knudsen number (Kn). Retaining terms up to second and third order yields the Burnett and super-Burnett equations, respectively[28, 29]. The Burnett equations were studied extensively but are known to violate frame-indifference and the second law of thermodynamics at high Kn[30, 31]. In recent years, several works have focused on presenting augmented forms of the Burnett equation which contains additional terms from super-Burnett order to stabilize the Burnett equations or BGK-Burnett equations[32, 33]. However, although the CE expansion is believed to be asymptotic, there is no reasoning that it is convergent[34]. This raises questions over improvements made over Navier-Stokes constitutive law by including higher order terms in the CE expansion. Another approximate approach is the moment method. In this method, moments of the BTE

are taken and evolution equations of the higher order moments are derived. Number of moments needed to describe a particular process is unsettled but is known to increase with the increase in Knudsen number. For some strongly non-equilibrium system, one may need hundreds of moments equations which soon become intractable[35, 36]. Furthermore, each moment depends on the divergence of the next higher velocity moment, so closure conditions are needed. This difficulty is addressed by using physically motivated closure conditions[37, 38, 39], Grad's 13 moment method, Grad's 26 moment method[37, 40]. Some works that develop this approach include Eu's evolution equations [41] leading to a nonlinear constitutive coupled relation (NCCR), further developed by Myong [42] and Singh's moment equations based on a distribution function consistent with Onsager's principle [43] leading to Burnett-type stable constitutive relations [44]. Interestingly, there exists a close connection between Burnett, super-Burnett equations and Grad's moment method as derived in [45].

In spite of extensive work in this direction, there does not exist a simple non-classical, well accepted constitutive law like the Navier-Stokes relation for high gradient/rarefied flows. This part of the thesis investigates the existence of non-classical higher order constitutive relation which can potentially improve modeling of momentum transport for highly non-equilibrium flows of gases using OMD. The main questions investigated are:

(a) When does the Navier-Stokes equation break down? Which effects play an important role in guiding this breakdown for OMD universal flows?

(b) Does there exist a constitutive relation that can generalize the Navier-Stokes theory to non-equilibrium regimes?

1.4.2 Diatomic gas

The system of vibrationally excited and chemically reacting molecular gas in non-equilibrium is characterized by introducing different definitions of temperatures corresponding to different modes of energy. This is to take into account non-equilibrium in the energy transfer where different modes of energy are not in equilibrium with each other. In the framework of CFD, separate conservation equations for the total energy of mixture, vibrational energy for each diatomic species and electron energy are defined.

Additionally, mass conservation equations for every species with source terms containing reaction rates that govern the creation and removal of species are defined[46, 47]. To close the system of these conservation equations, transport, energy exchange, and chemistry models are incorporated which are although mature and sophisticated for the near-equilibrium regimes are known to be inadequate under strong non-equilibrium conditions[48, 49, 50, 51, 52, 53].

To design better higher scale models and investigate molecular physics, particle level modeling approach is used. This can either be based on deterministic dynamics (MD) [54, 3] or stochastic dynamics (DSMC)[23]. The determination of transport coefficients in DSMC is based on particle collision models. In the continuum limit, these collision models correspond to Navier-Stokes order viscosity and conductivity coefficients, consistent with 1st order Chapman-Enskog expansion. When extended to a non-equilibrium regime, particle transport mechanism in DSMC adjusts the relation between the collision model and viscosity coefficient to correspond to the non-equilibrium physical processes occurring in the flow field[55]. Therefore, the DSMC method is truthfully capable of capturing non-equilibrium transport-based features of rarefied monoatomic flows in transition and molecular regime but is limited by the stochastic collision cross-section models required as an input for reacting collisions when modeling diatomic flows. The traditional collision models used as input to DSMC are aimed to reproduce reaction and relaxation rates used in CFD, but these are known to be inaccurate [24]. An alternative is to use a combination of Quasi-Classical Trajectory (QCT) and master equation analysis where transition rates of all possible rovibrational levels are precomputed and are then incorporated into a Master equation simulation[56]. This becomes intractable since even for $N_2 - N_2$ collisions, where there are more than 10^{14} rates which need to be precomputed. The other approach of Direct Molecular Simulation (DMS) known as classical trajectory calculation DSMC (CTC-DSMC) developed by Norman, Valentini, and Schwartzentruber [57, 58, 59] in full form simplifies this problem by simulating collisions 'on the fly', during a reacting gas simulation. The post-collision states become initial conditions for next collision which makes it computationally tractable. DMS integrates exact trajectory calculation with DSMC and thus apart from dilute gas assumption (which allows decoupling of free molecular motion from collisions over

small enough time scales), is based on sole input of potential energy surface (PES) that governs the interactions between atoms. Therefore, it removes the uncertainties and avoid empiricism associated with DSMC. Hence, the method can be understood as an exact "Accelerated MD" for modeling dilute gases. Recent advances in computational resources have led to the use of quantum mechanical electronic structure calculations for the development of high-fidelity potential energy surface for studying hypersonic chemistry[60, 61]. These advancements have made the PES-based atomistic modeling of non-equilibrium simulations more precise.

The current implementation of DMS cannot completely describe reacting flows as three-body interactions are not simulated. In classical dynamics the third body is required to remove the chemical energy which is released when atoms recombine and therefore its modeling needs three-body collision rate whose estimation is still a subject of active research. Thus, the recombination reaction has not been investigated in the same level of detail using ab-initio particle methods under non-equilibrium conditions, unlike processes of dissociation and exchange. Consideration of all these processes is equally important to predict the correct thermochemical state around the hypersonic vehicle which directly influences heat flux to the surface and gas-surface reactions. Atomic flux to the surface can result in significant extra heating through the mechanism of surface-catalyzed recombination directly affecting the thermal protection system of the aircraft.

This part of the dissertation focuses on studying all the relevant processes corresponding to the ground electronic state in Nitrogen – ro-vibrational relaxation, dissociation, exchange as well as recombination using the pure deterministic method of molecular dynamics. Unlike DMS, it naturally captures three and higher body collisions and hence incorporates recombinations as well. There is great interest in the modeling of shock wave and nozzle expansion due to its interconnection with reentry problems. It is also shown in this work how OMD flows can be used to model gas kinetics in a reactor which resembles nonequilibrium processes occurring under these conditions more closely than the adiabatic and isothermal counterparts widely used in the literature.

The main goal of this part is to present the exhaustive treatment of nitrogen gas under strong non-equilibrium conditions using molecular dynamics. The insight can guide the development of better models for other analysis tools like CFD, DSMC, and DMS. The major physics investigated are

1) To assess the validity of continuum theory with widely used standard Park's model in modeling high temperature reacting nitrogen gas in strong nonequilibrium.

2) To make comparisons with different modeling approaches of Direct Molecular Simulation (DMS) and Direct Simulation Monte Carlo (DSMC) in dissociation and recombination dominated regimes respectively.

3) To investigate the microscopic dynamics and selectivity of dissociation, recombination, and exchange processes and departure of the instantaneous population distribution of ro-vibrational energy states from equilibrium Boltzmann distribution on which current CFD reaction and exchange models are based.

4) To study the compression and expansion kinetics of dissociation-recombination nitrogen mixture relevant to normal shock wave and nozzle expansion.

1.5 Plasticity of Crystalline Materials

Investigation of material behavior and its failure is complicated due to its multiscale nature where various coupled phenomena are occurring across several orders of magnitude in length and time scales [8, 62, 63]. This makes it difficult to segregate the role played by different phenomena in guiding the particular macroscopic behavior. A huge range of computational tools exists to analyze material behavior across many scales. Ab-initio and Density Functional Theory (DFT) operates on the lower end of the length and time scale and uses quantum mechanics to simulate the atoms and their associated electronic structure. MD analyzes the dynamics classically at an atomic scale where the information about the electronic structure is incorporated in the PES as an input. Next up in the ladder, dislocation dynamics (DD) and crystal plasticity (CP) analyzes the system at a mesoscopic scale. At larger scales, finite element (FE) techniques utilize continuum approaches to study materials with dimensions on the order of meters and time scales

on the order of seconds. Certainly as one goes higher on the ladder, the theory becomes incomplete and requires various input models which are either based on experiments or theories operating on lower scales.

In this dissertation, the focus is on investigating the dynamics of dislocations, specifically the phenomenon of cross-slip in Nickel[64]. Cross-slip in close-packed lattices will influence the behavior and arrangement of dislocations on a mesoscopic scale which can affect its macroscopic behavior. The aim is to investigate the homogeneous cross-slip behavior at an atomistic scale and provide insights that can be of assistance for the mesoscopic modeling like dislocation dynamics (DD) simulation [65] under high rate loading conditions. Correct implementation of DD simulations can further ensure that the CP model gets the correct input to model smaller-scale physics and no information is lost while doing the upscaling.

Dislocations are important defects of crystals that are the primary microscopic mechanism of plasticity. Thus the study of their dynamic behavior is important for a complete understanding of plastic deformation in crystalline materials. Cross-slip is a fundamental aspect of the motion of screw dislocations which provides an extra degree of freedom for their motion[66]. During cross-slip, a screw dislocation leaves its habit plane and glides in a conjugate "cross-slip" plane. It plays a crucial role in phenomena like work hardening, recovery, fatigue, creep, and pattern formation[67, 68]. Microscopically, cross-slip can activate secondary slip systems and enables the annihilation of dislocations of opposite Burgers vector and also allows passing of dislocations around obstacles such as precipitates or inclusions present in the dislocation path. Cross-slip is typically associated with Stage III hardening in FCC metals; however occasional cross-slip can also happen in other stages. Hence, its role as a softening or hardening mechanism depends on the details of its occurrence.

As in most microscopic phenomena associated with plasticity, cross-slip is a thermally activated process. Small groups of atoms hop from one metastable state to another with a rate that depends on the mechanism as well as the temperature and stress. Studies in the literature have often focused on a system under constant stress to study

kinetics and kinematics of a cross-slip event[69, 70]. At an atomic scale, this is achieved by using Parrinello-Rahman molecular dynamics and its variants which simulates NσT ensemble whose aim is to sample time-invariant equilibrium probability distribution at constant stress and temperature[71, 72]. This is analogous to quasi-static loading where the system follows near-equilibrium behavior. But in experiments, approximately constant strain rate and evolving temperature is quite common. In addition, study of cross-slip dynamics under extreme loading conditions is equally important and is less well understood. DD models dislocations as discrete objects and employ physics-based constitutive rules for dislocation core mechanisms. An activated theory-based probability model is used to incorporate cross-slip in DD simulations[73, 74, 75, 66], but its validity under strong non-equilibrium conditions is not certain. The main questions investigated in this part are:

(a) How does choice of macroscopic motion (guided by tensor A) affect the evolution pathway of cross-slipping under highly non-equilibrium conditions.
(b) Do strain-rate and dislocation line length govern the mechanism under given macroscopic motion?
(c) Is transition state theory applicable in this far-from-equilibrium regime?

1.6 Outline

The thesis is structured as follows:

Chapter 2 provides a brief overview of the method of Objective Molecular Dynamics. It gives the details of its computational design and also proves the satisfaction of the basic theorem of OMD at discrete level by the velocity Verlet algorithm. The design is further validated by making its comparison with the Navier-Stokes (NS) equations in the near-equilibrium regime. To show the reach of the method, the homogeneous phase transition in a super-critical Lennard-Jones argon driven by high rate expansion is also reported.
OMD for fluids is compatible with the introduction of certain types of solid boundaries, either modelled as atomistic solids or with certain confining potentials. To illustrate

this compatibility, flow in a nanochannel having realistic atomistic solid boundaries is modeled. It is shown that Maxwell's theory of slip breaksdown in the transition regime. Slip velocity and slip length is shown to be better captured by logarithm variation in the Knudsen number.

Chapter 3 proposes a constitutive equation for flows of mono-atomic gases in high-rate regimes where the Navier-Stokes theory breaks down using OMD as a computational viscometer. The model generalizes the Navier-Stokes relation and agrees well with that in all lower rate flows examined.
The proposed constitutive relation is calibrated with the method of OMD using families of compressible and incompressible flows of Lennard-Jones argon. The constitutive relation makes use of the higher-order objective strain rates due to Rivlin and Ericksen. The model is shown to agree with atomistic results much better than the Navier-Stokes equations in the transition regime.

Chapter 4 investigates non-equilibrium dissociation and recombination in dissociation-dominated and recombination-dominated regimes in an adiabatic MD reactor of nitrogen gas. Adiabtic reactor is achieved by setting $\mathbf{A}$ to $\mathbf{0}$ in the framework of OMD. These regimes are characterized by conditions where mole fraction of molecular nitrogen at $t = 0$ are higher and lower than predicted by equilibrium. Later, OMD method is used to perform uniform expansion and compression by choosing very special value of tensor $\mathbf{A}$ to study behavior of gas under conditions which are relevant to kinetics of gas in shock waves and nozzle expansion. These regimes are characterized by conditions where energy in the translational mode (characterized by translational temperature Tt) becomes greater and smaller than the average energy stored in the rotational and vibrational mode of the molecules (characterized by temperatures Tr, Tv) respectively as the gas evolves. This chapter also makes comparison of OMD with other approaches of DMS, DSMC and CFD for modeling high-speed gas flows under strong thermal and chemical nonequilibrium conditions.

Chapter 5 investigates dynamics of screw dislocations in FCC nickel. It is computed that how dislocations filling all of the space in a crystalline material undergo

time-dependent, three-dimensional motions during deformation. Effect of macroscopic motion (i.e., loading conditions) and initial conditions on the atomic scale deformation mechanisms is investigated. The effect of external strain rate and temperature on the critical stress for homogeneous cross-slip is also analyzed and compared with the transition state theory. Beyond dislocation motions, modeling of sliding surfaces using the OMD framework is also demonstrated. These examples highlight potential applications of the OMD framework to material systems.

Finally, Chapter 6 provides brief summary of the dissertation and future work.

Chapter 2

Computational Design of Objective Molecular Dynamics

2.1 Introduction

Objective Molecular Dynamics (OMD) is a method of simulation for objective structures (OS) which consist of a set of N identical molecules (N can either be finite or infinite), each having M atoms. They are assembled so that corresponding atoms in each molecule exists in the same environment as described in [17]. Note that the molecules in an objective molecular structure need not correspond to standard physical molecules as usually understood. OS generalizes the notion of a crystal or periodicity by using ideas from frame-indifference. Every discrete OS can be written as a discrete isometry group (i.e., groups of orthogonal transformations and translations of the form $\mathbf{Qx}+\mathbf{c},\ \mathbf{Q}\in \mathrm{O}(3),\ \mathbf{c}\in \mathrm{R}^3$) applied to the positions of a single molecule. For the OMD method the explicit isometries, and particularly the allowed parameter dependence of these isometries, is needed. This would also facilitate the application of non-classical loads using the OS framework. Motivated by this, the explicit forms of all subperiodic, discrete groups of isometries are calculated in [76].

Many nano-structures can be constructed using these isometries, and are compliant with OMD methods. By making the special choice of a time-dependent translation group, one can obtain OMD solutions representing a family of unsteady flows of the

form

$$\mathbf{v}(\mathbf{x}, t) = \mathbf{A}(\mathbf{I} + t\mathbf{A})^{-1}\mathbf{x} \tag{2.1}$$

where $\mathbf{A}$ is an assignable 3×3 matrix that can be interpreted as Lagrangian velocity gradient and t is the time [16, 18].

This chapter aims at providing efficient numerical strategy for implementing OMD for the time-dependent translation isometry group, and to explore some of the flow phenomena that are possible with the method. To achieve efficiency in OMD simulation, ideas from the theory of lattice invariant deformations of crystallography is used and concepts from neighbor list generation, such as minimum image convention and the cell list method used in traditional molecular dynamics codes is adapted [3]. The validity of computation is examined by carrying out the simulations on Lennard-Jones (LJ) systems for incompressible flows of a monoatomic gas, and comparing the atomistic simulations with the continuum Navier-Stokes-Fourier (NSF) model. OMD can also work well for many other complex phenomena in fluids such as phase transition, chemical dissociation, electronic transition, etc. as shown in this and the following chapters.

The method of OMD can be rephrased as a (time-dependent) invariant manifold of the MD equations. This has the usual meaning: the manifold is a surface in the space of positions, momenta and time for all the atoms. If you give initial conditions on this manifold at $t = 0$, you remain on this manifold for $t > 0$. The manifold is given by an explicit analytical formula and is also consistent with Velocity-Verlet (VV) algorithm which is used to solve equations of OMD numerically [77, 78]. In addition to the well-known desirable properties of VV algorithm such as being symplectic and time-reversible, it is proved in this work that the theorem of OMD holds true exactly at the discrete level with the VV algorithm.

This chapter is organized as follows: Section 2.2 describes the basics of Objective Molecular Dynamics. Section 2.3 gives the details of the numerical method. Section 2.4 shows the compatibility of OMD with velocity Verlet algorithm. Sections 2.5, 2.6 and 2.7 show validation and some applications of OMD.

2.2 Objective Molecular Dynamics

Objective molecular dynamics makes use of discrete groups of isometries as explained above. These are groups $\mathbf{G} = \{g_1, g_2, \dots\}$ of orthogonal transformations and translations with elements typically written in the notation

$$g_j = (\mathbf{Q}_j|\mathbf{c}_j) \in \mathbf{G}, \quad j = 1, ..., N, k = 1, ..., M, \tag{2.2}$$

where $\mathbf{Q}_j \in \mathrm{O}(3)$ and $\mathbf{c}_j \in \mathbb{R}^3$. The multiplication rule for isometries is

$$(\mathbf{Q}_j|\mathbf{c}_j)(\mathbf{Q}_k|\mathbf{c}_k) = (\mathbf{Q}_j\mathbf{Q}_k|\mathbf{c}_j + \mathbf{Q}_j\mathbf{c}_k), \tag{2.3}$$

the inverse of $(\mathbf{Q}|\mathbf{c})$ is $(\mathbf{Q}^T|-\mathbf{Q}^T\mathbf{c})$ and the identity is $(\mathbf{I}|0)$. For OMD, the translational part $\mathbf{c}_k$ is allowed to depend on time but this dependence must be affine [16]: $\mathbf{c}_k = \mathbf{a}_k t + \mathbf{b}_k$.

Consider any number of atoms labeled $1, ..., M$ with positive masses $m_1, ..., m_M$. These are called *simulated atoms*. Let $\mathbf{y}_k(t), t > 0, k = 1, \dots, M$, be the motions of these *simulated atoms*. Then there exist nonsimulated atoms whose motions are given in terms of the simulated atoms by

$$\mathbf{y}_{j,k}(t) = g_j(\mathbf{y}_k(t)) \tag{2.4}$$

where the elements $g_j(t) \in \mathbf{G}$ is a discrete group of isometries. The allowed time dependence of the g_j implies that

$$\frac{d^2\mathbf{y}_{j,k}(t)}{dt^2} = \frac{d^2}{dt^2} g_j(\mathbf{y}_k(t)) = \mathbf{Q}_j \frac{d^2\mathbf{y}_k(t)}{dt^2}, \quad g_j = (\mathbf{Q}_j|\mathbf{c}_j) \in \mathbf{G}, j = 1, ..., N, k = 1, ..., M \tag{2.5}$$

The fact that the non-simulated atoms of OMD satisfy the equations of MD rests on the the standard conditions of invariance satisfied by the atomic forces. That is, with the force on atom i, k denoted by the suggestive notation $-\partial\varphi/\partial\mathbf{y}_{i,k} : \mathbb{R}^{3MN} \to \mathbb{R}^3$, the function is assumed to be smooth and frame-indifferent, i.e., for all $\mathbf{Q} \in \mathrm{O}(3)$ and

$\mathbf{c} \in \mathbb{R}^3$,

$$\begin{aligned}\mathbf{Q}\frac{\partial\varphi}{\partial\mathbf{y}_{i,k}}(\dots,\mathbf{y}_{i_1,1},\dots\mathbf{y}_{i_1,M},\dots,\mathbf{y}_{i_2,1},\dots\mathbf{y}_{i_2,M},\dots)\\ = \frac{\partial\varphi}{\partial\mathbf{y}_{i,k}}(\dots,\mathbf{Q}\mathbf{y}_{i_1,1}+\mathbf{c},\dots\mathbf{Q}\mathbf{y}_{i_1,M}+\mathbf{c},\dots,\mathbf{Q}\mathbf{y}_{i_2,1}+\mathbf{c},\dots\mathbf{Q}\mathbf{y}_{i_2,M}+\mathbf{c},\dots),\end{aligned} \tag{2.6}$$

and also that it is permutation invariant,

$$\begin{aligned}\frac{\partial\varphi}{\partial\mathbf{y}_{\Pi(i,k)}}(\dots,\mathbf{y}_{i_1,1},\dots\mathbf{y}_{i_1,M},\dots,\mathbf{y}_{i_2,1},\dots\mathbf{y}_{i_2,M},\dots)\\ = \frac{\partial\varphi}{\partial\mathbf{y}_{i,k}}(\dots,\mathbf{y}_{\Pi(i_1,1)},\dots\mathbf{y}_{\Pi(i_1,M)},\dots,\mathbf{y}_{\Pi(i_2,1)},\dots\mathbf{y}_{\Pi(i_2,M)},\dots),\end{aligned} \tag{2.7}$$

where Π is any permutation that preserves species. Here, preservation of species means that if $(i,k) = \Pi(j,\ell)$ then the species (i.e., atomic mass and number) of atom i,k is the same as the species of atom j,ℓ.

The basic theorem of OMD then says that if $\mathbf{y}_k(t)$ are subjected to the equations of molecular dynamics, i.e.,

$$\begin{aligned}m_k\ddot{\mathbf{y}}_k(t) &= -\frac{\partial\varphi}{\partial\mathbf{y}_{1,k}}(\dots,\mathbf{y}_{i,1}(t),\dots,\mathbf{y}_{i,M}(t),\mathbf{y}_{i+1,1}(t),\dots,\mathbf{y}_{i+1,M}(t),\dots)\\ &= -\frac{\partial\varphi}{\partial\mathbf{y}_{1,k}}(\dots,g_i(\mathbf{y}_{1,1}(t),t),\dots,g_i(\mathbf{y}_{1,M}(t),t),g_{i+1}(\mathbf{y}_{1,1}(t),t),\dots,g_{i+1}(\mathbf{y}_{1,M}(t),t),\dots),\\ &\quad \mathbf{y}_k(0)=\mathbf{y}_k^0,\quad \dot{\mathbf{y}}_k(0)=\mathbf{v}_k^0,\quad k=1,\dots,M,\end{aligned} \tag{2.8}$$

then the equations of molecular dynamics are exactly satisfied by non simulated atoms $\mathbf{y}_{j,k}(t)$ in spite of the fact that their motion is coming from an explicit formula (2.4) :

$$m_k\ddot{\mathbf{y}}_{j,k}(t) = -\frac{\partial\varphi}{\partial\mathbf{y}_{j,k}}(\dots,\mathbf{y}_{i,1}(t),\dots,\mathbf{y}_{i,M}(t),\mathbf{y}_{i+1,1}(t),\dots,\mathbf{y}_{i+1,M}(t),\dots)$$

Notice that because of the substitution of the group elements acting on simulated atoms on the right hand side, (2.8) is a system of ordinary differential equations in standard form for the simulated atoms.

In the case of the translation group given by $G_T = \{(\mathbf{I}|\nu^1\hat{\mathbf{e}}_1 + \nu^2\hat{\mathbf{e}}_2 + \nu^3\hat{\mathbf{e}}_3) : \nu =$

$(\nu^1, \nu^2, \nu^3) \in \mathbb{Z}^3\}$, the basic method is the following. Give a 3×3 matrix $\mathbf{A}$ and three linearly independent vectors $\mathbf{e}_1, \mathbf{e}_2, \mathbf{e}_3$, $(\mathbf{e}_1 \times \mathbf{e}_2) \cdot \mathbf{e}_3 > 0$, choose $\hat{\mathbf{e}}_i = (\mathbf{I} + t\mathbf{A})\mathbf{e}_i$, $i = 1, 2, 3$. This choice preserves the group properties and the affine time-dependence. The motions of the nonsimulated atoms are given in terms of the simulated atoms by

$$\mathbf{y}_{\nu,k}(t) = g_\nu(\mathbf{y}_k(t)), \quad \mathbf{y}_{\nu,k}(t) = \mathbf{y}_k(t) + \sum_{i=1}^{3} \nu^i (\mathbf{I} + t\mathbf{A})\mathbf{e}_i, \quad g_\nu \in G_T \tag{2.9}$$

where, $\mathbf{y}_k(t) = \mathbf{y}_{(0,0,0),k}(t), t > 0, k = 1, \ldots, M$, are the motions of the M *simulated atoms*. This simulation fills all of space but in certain cases it can be confined by rigid boundaries [18]. The matrix $\mathbf{A}$ is the same as that appearing in the formula (2.1) for the macroscopic motion.

2.3 Numerical Method

Depending on the choice of $\mathbf{A}$, it can happen that at some $t = T > 0$, $(\mathbf{I} + t\mathbf{A})$ ceases to be invertible. Then the simulation is stopped before time T. So, below it is assume that $0 \leq t < T$ so that $(\mathbf{I} + t\mathbf{A})$ is invertible.

During a typical simulation, the simulated atoms quickly diffuse into the nonsimulated atoms. Thus, the simulated atoms can become highly strung-out. When it is said that the motion $\mathbf{y}_k(t)$ of simulated atom k satisfies the equations of molecular dynamics, then note that the force on this atom generally arises from both simulated and nonsimulated atoms. Here, it is assumed that, in addition to the usual invariances, the force on any atom is only produced by other (simulated or nonsimulated) atoms within a cut-off d_{cut}. Thus, the critical issue for making an efficient simulation is to find all atoms within d_{cut} of each simulated atom at each time step. Below, an efficient method for doing this is developed based on 1) occasionally redefining which atoms are the simulated atoms, 2) using basic (time-dependent) periodicity of the motion, 3) using an integer Gram-Schmidt process to redefine the unit cell to be "fat" and then redefining the simulated atoms in a consistent way. The method outlined below keeps the simulated atoms in a deforming unit cell by occasional redefinition of simulated atoms, until that cell becomes elongated.

2.3.1 Starting the simulation

At $t = 0$ assign initial positions and initial velocities of simulated atoms in a parallelepiped defined by $\mathbf{e}_1, \mathbf{e}_2, \mathbf{e}_3$, and extend them periodically using $\mathbf{e}_1, \mathbf{e}_2, \mathbf{e}_3$ to get the nonsimulated atoms as given by (2.9). Start the simulation.

2.3.2 Nonsimulated atoms

A basic property of OMD is that one can redefine the simulated atoms at any particular time step, by choosing a new set of simulated atoms that are images of the the given set of simulated atoms under the group. The group element chosen can be different for different simulated atoms. When restarting the simulation, the new simulated atoms are given velocities that are obtained by time differentiating (2.9). The methods described here to speed up OMD rely on occasionally choosing new simulated atoms that are in some sense close together.

At every time step use (2.9) to get the positions of the nonsimulated atoms which can also be understood as images of simulated atoms.

2.3.3 Criterion that a simulated atom lies in a unit cell

If a simulated atom j passes out of the unit cell $\mathcal{U}(t_1) = \{\lambda_1(\mathbf{I} + t_1\mathbf{A})\mathbf{e}_1 + \lambda_2(\mathbf{I} + t_1\mathbf{A})\mathbf{e}_2 + \lambda_3(\mathbf{I} + t_1\mathbf{A})\mathbf{e}_3 : 0 \leq \lambda_1, \lambda_2, \lambda_3 < 1\}$ at time t_1, then it is declared no longer to be a simulated atom and is replaced by the $\mathbf{y}_{\nu,j}$ (note: same j), which has just entered $\mathcal{U}(t_1)$. The passing in and out of $\mathcal{U}(t_1)$ and the value of ν can be detected in the following way. Let $\mathbf{e}^1, \mathbf{e}^2, \mathbf{e}^3$ be the reciprocal vectors, i.e., the unique vectors that satisfy $\mathbf{e}^i \cdot \mathbf{e}_j = \delta^i_j$. Outward normals of the faces of $\mathcal{U}(t_1)$ are

$$\pm(\mathbf{I} + t_1\mathbf{A})^{-T}\mathbf{e}^1, \quad \pm(\mathbf{I} + t_1\mathbf{A})^{-T}\mathbf{e}^2, \quad \pm(\mathbf{I} + t_1\mathbf{A})^{-T}\mathbf{e}^3. \tag{2.10}$$

Thus, because $\mathbf{e}_1, \mathbf{e}_2, \mathbf{e}_3$ has been chosen as linearly independent and right handed, a point $\mathbf{x} \in \mathcal{U}$ if and only if

$$0 \leq \mathbf{x} \cdot (\mathbf{I} + t_1\mathbf{A})^{-T}\mathbf{e}^i < 1, \tag{2.11}$$

So, if any of the inequalities in (2.11) are violated by $\mathbf{x} = \mathbf{y}_j(t_1)$, then atom j has passed out of $\mathcal{U}(t_1)$, and it should be replaced by (ν, j) that has just entered $\mathcal{U}(t_1)$. If, say, (2.11) is violated at $i = 2$ and at 1, then the new simulated atom is $((0, -1, 0), j)$. Fig. 2.1 illustrates this procedure. The green atom goes outside the domain and at the same time its image (blue atom) enters the domain from the neighboring cell of non simulated atoms. In this case the inequalities in (2.11) are violated at i=3 and at 0. Therefore, the ν of the redefined new simulated atom is $(0, 0, 1)$. As noted above the new simulated atom has a different velocity than the old one depicted by the red vector in the Fig. 2.1 – their velocities are related by the time derivative of (2.9):

$$\dot{\mathbf{y}}_{\nu,k}(t) = \dot{\mathbf{y}}_k(t) + \nu^i \mathbf{A}\mathbf{e}_i. \tag{2.12}$$

So, when using the velocity Verlet algorithm (see below) for the new simulated atom, the new position and the new velocity have to be used.

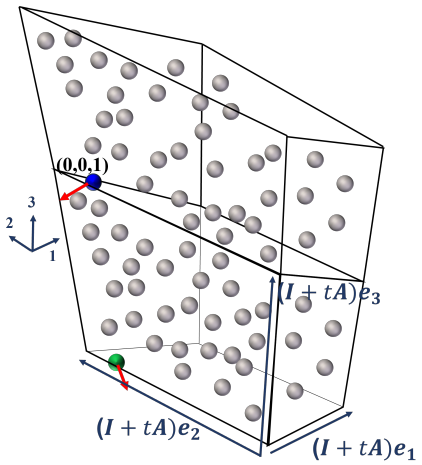

Figure 2.1: Criteria for redefinition: Simulated atom (green) goes outside the domain and is replaced by the non-simulated atom (blue) which enters at the same time

2.3.4 Computation of forces

The force on a simulated atom is calculated using either minimum image convention or cell linked-list method which are commonly used techniques in molecular dynamics to accelerate the computation of potential and force evaluation [3, 79]. The choice of the method depends on the number of simulated atoms in the system. Both the above methods are modified here to take into account the time-dependence of the parallelepiped associated to the three vectors $((\mathbf{I}+t\mathbf{A})\mathbf{e}_1, (\mathbf{I}+t\mathbf{A})\mathbf{e}_2, (\mathbf{I}+t\mathbf{A})\mathbf{e}_3)$. These vectors constitute the fundamental domain comprising of simulated atoms.

In the minimum image convention, every simulated atom is at most interacting with one image of other simulated atoms in the fundamental domain as long as the minimum distance between points on opposite faces of domain is less than twice the cut-off radius d_{cut} of the interatomic potential. The main idea then is to minimize the distances between each pair of simulated atoms in the domain to find the nearest image.

The distance between simulated atom k and m at time t can be written as:

$$\mathbf{r}_{k,m} = \mathbf{y}_k - \mathbf{y}_m = \{\lambda_1(\mathbf{I}+t\mathbf{A})\mathbf{e}_1 + \lambda_2(\mathbf{I}+t\mathbf{A})\mathbf{e}_2 + \lambda_3(\mathbf{I}+t\mathbf{A})\mathbf{e}_3\}$$

$$\mathbf{\Lambda} = [\lambda_1, \lambda_2, \lambda_3]^{\mathrm{T}} = [\mathbf{r}_{k,m}\cdot(\mathbf{I}+t\mathbf{A})^{-\mathrm{T}}\mathbf{e}^1,\ \mathbf{r}_{k,m}\cdot(\mathbf{I}+t\mathbf{A})^{-\mathrm{T}}\mathbf{e}^2,\ \mathbf{r}_{k,m}\cdot(\mathbf{I}+t\mathbf{A})^{-\mathrm{T}}\mathbf{e}^3]^{\mathrm{T}} \tag{2.13}$$

$\mathbf{r}_{k,m}$ is the shortest distance if and only if $|\lambda_i| \leq 0.5$. If $|\lambda_i| > 0.5$ then simulated atom k interacts with an image of simulated atom m and the distance between them is given by $\mathbf{r}_{k,m} - \lfloor(\lambda_i)\rfloor(\mathbf{I}+t\mathbf{A})\mathbf{e}_i$ where $\mathbf{r}_{k,m}$ and λ_i is known from the calculation above and $\lfloor x\rfloor$ is the closest integer to x. This is illustrated in the Fig. 2.2(a). In other words, it is similar to representing an alike fundamental domain centered around each atom (blue atom in the Fig. 2.2(a)) and computing the forces using atoms within cutoff d_{cut}.

The cell list algorithm is another effective method which is used here when the number of simulated atoms in the domain is large. Here, the fundamental domain is subdivided into cells. All atoms are assigned to the cells according to their positions, and the interactions are computed between particles in the same or neighbouring cells. So rather than looping over each particle pair in the simulation domain, one only loops over the particle pairs in these 27 cells (or 9 cells in 2d). This is true only when minimum distance between opposite faces of each cell is greater than the cut-off radius d_{cut}. This is 'minimum distance requirement'. The number of cells in each direction $(\mathbf{I}+t\mathbf{A})\mathbf{e}_i$ can be changed on the fly depending on the dimensions of the domain and particle density, which can vary during a simulation. This number is computed using $n_i = \{\lfloor d_{i,min}/d_{cut}\rfloor - 1\}$, where $d_{i,min}$ is the minimum distance between two neighboring parallel faces of the fundamental domain. The formula for its computation is given in Section 2.3.5. Since $d_{i,min}$ decreases as the flow evolves, the total number of cells changes in order to satisfy the minimum distance requirement. For dilute systems with a fairly big fundamental domain, n_i given by the above expression doesn't give optimized load balancing when parallelized. This happens because of the presence of very few atoms in each cell. In that case, the cell size is increased to achieve a good speedup.

The method is depicted in the Fig. 2.2(b). Here, different colors of the atoms correspond to different cells. Only a few subdivisions are shown here for clarity. The

motion of the fundamental domain depends on the choice of $\mathbf{A}$.

Algorithm 1 Cell list: Assign atoms to cells

for i=1 to 3 **do** ▷ Number of cells in direction i
  $n_i \leftarrow \{\lfloor d_{i,min}/d_{cut} \rfloor - 1\}$
end for
for k=1 to N **do** ▷ Assign simulated atoms to different cells
  $\lambda_1 \leftarrow \mathbf{y}_k \cdot (\mathbf{I} + t\mathbf{A})^{-\mathrm{T}} \mathbf{e}^1$
  $\lambda_2 \leftarrow \mathbf{y}_k \cdot (\mathbf{I} + t\mathbf{A})^{-\mathrm{T}} \mathbf{e}^2$
  $\lambda_3 \leftarrow \mathbf{y}_k \cdot (\mathbf{I} + t\mathbf{A})^{-\mathrm{T}} \mathbf{e}^3$
  $(c_1[k], c_2[k], c_3[k]) \leftarrow (\lfloor n_1[\lambda_1 - \frac{1}{2n_1}] \rfloor, \lfloor n_2[\lambda_2 - \frac{1}{2n_2}] \rfloor, \lfloor n_3[\lambda_3 - \frac{1}{2n_3}] \rfloor)$
  if $c_i[k]$ is less than 0 **then** ▷ $c_i[k] \in \{0, , , n_i - 1\}, c_i[k] \in \mathbb{Z}^+$, $i \in \{1, 2, 3\}$
    $c_i[k] \leftarrow n_i - 1$
    $\mathbf{y}_k \leftarrow \mathbf{y}_k + (\mathbf{I} + t\mathbf{A})\mathbf{e}_i$ ▷ Redefine non-simulated atom as simulated atom
  end if
  if $c_i[k]$ is greater than or equal to n_i **then**
    $c_i[k] \leftarrow 0$
    $\mathbf{y}_k \leftarrow \mathbf{y}_k - (\mathbf{I} + t\mathbf{A})\mathbf{e}_i$
  end if
  $c \leftarrow (n_1 n_2 c_3[k]) + (n_1 c_2[k]) + (c_1[k]) + 1$ ▷ Cell identifier, $c \in \{0, 1, ...(n_1 n_2 n_3 - 1)\}$
  $natoms[c] \leftarrow natoms[c] + 1$ ▷ Counter for the number of simulated atoms in c^{th} cell
  $list(c, natoms[c]) \leftarrow k$ ▷ List of the simulated atoms in c^{th} cell
end for

When the number of atoms in the system is comparatively fewer, an image convention is used. This is because the relative overhead of the generation of cells and sorting increases with a decrease in the number of atoms. Both the methods are general and work with any $\mathbf{A}$.

2.3.5 Criterion for excessive distortion of the unit cell

As mentioned above, for the minimum image convention and the cell-linked list, it is necessary that the distance between two neighboring parallel faces should maintain a particular minimum length. Since the unit cell follows the macroscopic motion of the flow, it distorts with time and hence the minimum distance decreases. One needs a criteria to decide that when the unit cell has distorted enough and the new unit cell is needed. To formulate this criterion, let $\mathcal{N}$ be the neighbors of $\mathcal{U}$. Suppose the minimum

Algorithm 2 Cell list: Compute forces

for k=1 to N **do** ▷ Looping over total number of simulated atoms in the fundamental domain
  for $l_i = c_i[k] - 1$ to $c_i[k] + 1$ **do** ▷ Looping over neighboring cells in i^{th} direction, $i \in \{1, 2, 3\}$
    if l_i is less than 0 **then** ▷ Accounting for atoms near the domain boundary
      $rshift[i] \leftarrow -1$
    else if l_i is greater than or equal to n_i **then**
      $rshift[i] \leftarrow +1$
    else
      $rshift[i] \leftarrow 0$
    end if
    $c_1 \leftarrow ((l_1 + n_1) \bmod \mathrm{n}_1) + ((\mathrm{l}_2 + \mathrm{n}_2) \bmod \mathrm{n}_2)\mathrm{n}_1 + ((\mathrm{l}_3 + \mathrm{n}_3) \bmod \mathrm{n}_3)\mathrm{n}_1\mathrm{n}_2 + 1$
    for $p = 1$ to $natom[c_1]$ **do** ▷ Looping over number of atoms in c_1^{th} cell
      $\tilde{k} \leftarrow list(c_1, p)$
      $\mathbf{r} \leftarrow (\mathbf{y}_{\tilde{k}} + rshift[i](\mathbf{I} + t\mathbf{A})\mathbf{e}_i) - \mathbf{y}_k$ ▷ Minimum interatomic distance
      if $|\mathbf{r}|$ is less than cutoff **then**
        Compute forces
      end if
    end for
  end for
end for

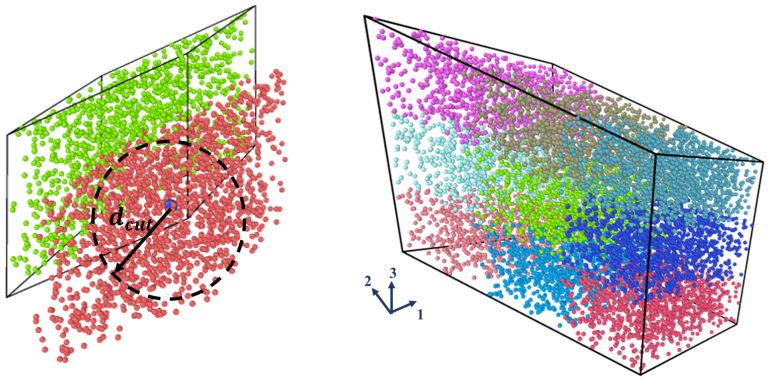

(a) (b)

Figure 2.2: Different techniques for computation of forces (a) Minimum Image Convention adapted to consider deformation of domain (b) Cell List: Simulation domain is divided into cells. Both domain and cells are identically deformed.

distance between $\mathcal{U}$ and $\partial(\mathcal{U}\cup\mathcal{N})$ is achieved at the two points $\mathbf{x}\in\partial\mathcal{U}$ and $\mathbf{y}\in\partial(\mathcal{U}\cup\mathcal{N})$ (Clearly it can be assumed both points are on their respective boundaries). $\mathbf{y}-\mathbf{x}$ must be a generalized outward normal to $\mathcal{U}$, i.e., $(\mathbf{y}-\mathbf{x})\cdot(\mathbf{x}'-\mathbf{x})\leq 0$ for all $\mathbf{x}'\in\partial(\mathcal{U}\cup\mathcal{N})$ because otherwise one could reduce the distance $|\mathbf{y}-\mathbf{x}|$ by perturbing $\mathbf{x}$. Also, $\mathbf{y}$ cannot be on an edge of $\partial(\mathcal{U}\cup\mathcal{N})$ because all edges of $\mathcal{U}\cup\mathcal{N}$ have interior acute angles and so the distance $|\mathbf{y}-\mathbf{x}|$ could be reduced by perturbing $\mathbf{y}$. Thus, $\mathbf{y}$ must be on a face and $\mathbf{x}-\mathbf{y}$ must be perpendicular to that face. Hence, $|\mathbf{y}-\mathbf{x}|$ must be the minimum distance between two neighboring parallel faces, which is

$$\min_{i=1,2,3}\frac{1}{|(\mathbf{I}+t\mathbf{A})^{-T}\mathbf{e}^i|} \tag{2.14}$$

So the criterion for restarting the simulation with a new unit cell is when the following inequality is first violated

$$\min_{i=1,2,3}\frac{1}{|(\mathbf{I}+t\mathbf{A})^{-T}\mathbf{e}^i|}\leq md_{cut}. \tag{2.15}$$

Here, $m=2$ for the whole fundamental domain when using minimum image convention and m depends on the maximum number of cells $\max_{i=1,2,3} n_i$ when cell list method is

used to maintain 'minimum distance requirement'. Fig. 2.3 shows a fat cubical domain ($t = 0$) which later gets deformed to a highly distorted cell (different projections shown) at time t_1. Here the criterion (2.15) is violated and some part of the cutoff region is located out of the box.

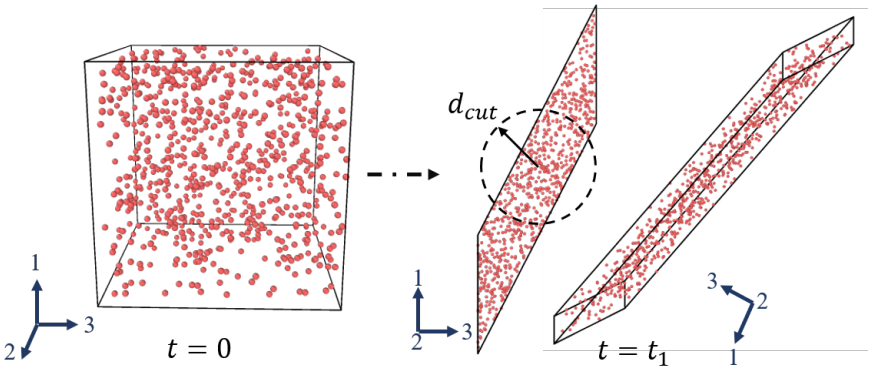

Figure 2.3: Criteria for distortion: A sufficiently fat box at $t = 0$ gets highly deformed at $t = t_1$.

2.3.6 Approximate orthogonalization by an integer Gram-Schmidt method

In principle, the simulation may be done in a previously defined suitably distorted box, but for a number of practical reasons this may be unattractive. For example, the cut-off sphere may then be located in many boxes at the same time. Also, one cannot use the idea of the minimum image convention and the cell list because then simulated atoms would be interacting with more than one image of non simulated atoms. To improve this situation, a given lattice basis that has become highly distorted is transformed into a "fat" lattice basis which is closer to orthogonal. One needs a suitable mathematical definition of "fat basis" to achieve this. Orthogonal basis can be determined by considering the lengths of the Gram-Schmidt vectors. Orthogonality of a lattice basis is closely tied to the lengths of the Gram-Schmidt vectors [80].

Gram-Schmidt orthogonalization: Given a basis $\{\mathbf{b}_1, \mathbf{b}_2, \ldots, \mathbf{b}_m\}$ of a subspace $\mathbb{H}_m$ of $\mathbb{R}^n$, this method gives back an orthogonal basis $\{\mathbf{b}_1^*, \mathbf{b}_2^*, \ldots, \mathbf{b}_m^*\}$ of $\mathbb{H}_m$.

$$\begin{aligned}
\mathbf{b}_1^* &= \mathbf{b}_1, \\
\mathbf{b}_2^* &= \mathbf{b}_2 \ - \mu_{1,2}\mathbf{b}_1, \quad \text{where}, \mu_{1,2} = \frac{\mathbf{b}_2 \cdot \mathbf{b}_1^*}{\mathbf{b}_1^* \cdot \mathbf{b}_1^*} \\
\mathbf{b}_m^* &= \mathbf{b}_m - \sum_{i<m} \mu_{i,m}\mathbf{b}_i, \quad \text{where}, \mu_{i,m} = \frac{\mathbf{b}_m \cdot \mathbf{b}_i^*}{\mathbf{b}_i^* \cdot \mathbf{b}_i^*}
\end{aligned} \tag{2.16}$$

In matrix form, $\mathbf{B} = \mathbf{B}^*\mathbf{U}$, where basis vectors are columns in $\mathbf{B}$ and $\mathbf{B}^*$ and $\mathbf{U}$ is an upper triangular matrix with diagonal elements 1.

$$\begin{bmatrix} \mathbf{b}_1 & \mathbf{b}_2 & \dots & \mathbf{b}_m \end{bmatrix} = \begin{bmatrix} \mathbf{b}_1^* & \mathbf{b}_2^* & \dots & \mathbf{b}_m^* \end{bmatrix} \begin{bmatrix} \mu_{1,1} & \mu_{1,2} & \cdots & \mu_{1,m} \\ 0 & \mu_{2,2} & \cdots & \mu_{2,m} \\ \vdots & \vdots & \ddots & \vdots \\ 0 & 0 & \cdots & \mu_{m,m} \end{bmatrix}$$

Since the coefficients $\mu_{i,j}$ do not usually lie in $\mathbb{Z}$, the resulting vectors are not usually elements of the lattice and hence Gram-Schmidt process is not useful, in general, for lattices. Lenstra, H. Lenstra, and L. Lovasz proposed the celebrated LLL algorithm [81], an approximation of basis reduction which exploits a Gram-Schmidt orthogonalization GSO. This is called an integer Gram-Schmidt process.

The LLL Algorithm contains two steps [82]:

1. **Normalization:** Lattice invariant operations are applied to transform the upper triangular matrix $\mathbf{U}$ to as close as possible to the identity matrix. If $\mathbf{U}$ were the identity, then $\mathbf{B}$ itself would be orthogonal. Let $\mu_{i,j}$ be the $j-th$ entry of the $i-th$ row of $\mathbf{U}$. By subtracting $\lfloor \mu_{i,j} \rfloor$ times the ith column of $\mathbf{U}$ from the j-th column, the new entry $\mu_{i,j}^{'}$ at position i, j will satisfy $-(1/2) < \mu_{i,j}^{'} \leq (1/2)$. The entries in a row below the i-th row of $\mathbf{U}$ remain unchanged. By following these steps from the last to the first row, one obtains a basis $\mathbf{B}^{'} = \mathbf{B}^*\mathbf{U}^{'}$ with $|\mu_{i,j}^{'}| \leq 1/2$ for every $1 \leq i < j \leq m$ in GSO. This step is also called size reduction.

2. **Swapping:** If there exists a j such that

$$||\mathbf{b}_{j+1}^* + \mu_{j+1,j}\mathbf{b}_j^*||^2 < \frac{3}{4}\,||\mathbf{b}_j^*||^2, \tag{2.17}$$

swap $\mathbf{b}_j$ and $\mathbf{b}_{j+1}$. Then return to Normalization.

The constant $\delta = 3/4$ in (2.17) is chosen for the simplicity. Any constant between 1/4 and 1 can guarantee that the algorithm terminates in polynomial time. If the basis vectors $\mathbf{b}_j^*$ violate (2.17) then the algorithm terminates. The LLL-algorithm alternates the normalization and swapping steps: it normalizes the basis and then searches for two consecutive basis elements which should be swapped. This is continued until (2.17) does not hold. The final $\mathbf{B}^{'}$ matrix is called the δ-LLL reduced matrix.

2.3.7 Remapping the simulated atoms

Once the new nice lattice basis is obtained from the LLL Algorithm, then atoms are mapped into the parallelepiped formed by this new set of basis vectors. Every simulated atom in the distorted unit cell has a corresponding non simulated atom in the new unit cell. These images are then redefined as the new simulated atoms and simulation is continued. One has to be careful to restart with the correct positions and velocities, noting that some of the new simulated atoms were previously nonsimulated atoms. Some methods available in the literature rely on the possibility of finding a reproducible lattice where the lattice points occupy the same points as that of initial lattice [83, 84, 85]. That condition is not imposed on the simulation cell here. Rather, the idea is to get a basis which is close to being orthogonal and hence can construct sufficient fat unit cell which obeys the minimum distance criteria. It is seen in Section 2.5 that there is no discontinuity in the macroscopic properties of the system during remapping, as must be true. The resulting simulation is exactly the same as if the original set of simulated atoms had been used for all time.

Let $\tilde{\mathbf{e}}_\mathbf{i}$ be the new basis vectors. If the remapping is done at time t_1 then $\mathbf{e}_i$ changes to,

$$(\mathbf{I} + t_1\mathbf{A})\mathbf{e}_i = \tilde{\mathbf{e}}_i \Rightarrow \mathbf{e}_i = (\mathbf{I} + t_1\mathbf{A})^{-1}\tilde{\mathbf{e}}_i \tag{2.18}$$

This changes the corresponding reciprocal vectors $\mathbf{e}^i$. (It is important to change the values of $\mathbf{e}_i$ and $\mathbf{e}^i$ whenever remapping happens in the code.) The positions and velocities of the non-simulated atoms which are redefined as simulated atoms at time t_1

are then given by

$$\mathbf{y}_{\nu,k}(t_1) = \mathbf{y}_k(t_1) + \sum_{i=1}^{3} \nu^i \tilde{\mathbf{e}}_i \tag{2.19}$$

$$\dot{\mathbf{y}}_{\nu,k}(t_1) = \dot{\mathbf{y}}_k(t_1) + \sum_{i=1}^{3} \nu^i \mathbf{A}\mathbf{e}_i \tag{2.20}$$

where value of triplet of integers $\nu^{\mathbf{i}}$ for the non simulated atoms lying in the fat cell are

$$\nu^i = -\lfloor (\mathbf{y}_k(t_1) \cdot (\mathbf{I} + t_1\mathbf{A})^{-T}\mathbf{e}^i - 0.5) \rfloor \tag{2.21}$$

Fig. 2.4 shows an example of remapping for a general incompressible flow. A new basis is defined at this instant using the LLL Algorithm. Orange atoms are remapped to blue atoms which are redefined as simulated atoms. Depending on the value of the matrix $\mathbf{A}$, and especially for certain highly distorting compressible flows, it can happen that, at some point in time, there might not exist a unit cell which is sufficiently fat and which obeys the minimum distance criteria. At this point the cutoff necessarily forces atoms to lie in several – or in particularly unfavorable cases many – copies of any fundamental domain. Depending on the size of this domain, other neighboring domains of non-simulated atoms are constructed and forces are computed from the atoms lying in these neighboring and center domains.

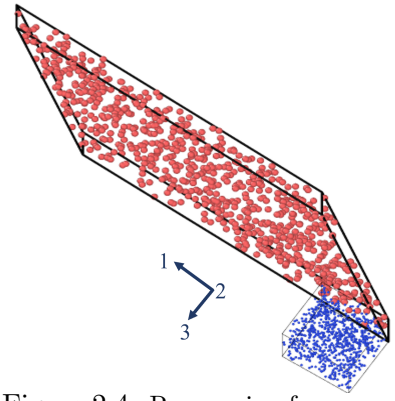

Figure 2.4: Remapping for general incompressible flows: orange atoms are remapped to blue atoms.

Fig. 2.5 shows a final flowchart for single time stepping in the OMD simulation. Ovito software has been used for all the visualization purpose in this work [86].

2.4 Velocity Verlet Algorithm and Objective MD

The propagation scheme of the Velocity Verlet algorithm is widely used in traditional MD codes. It is shown here that the algorithm is nicely consistent with Objective MD.

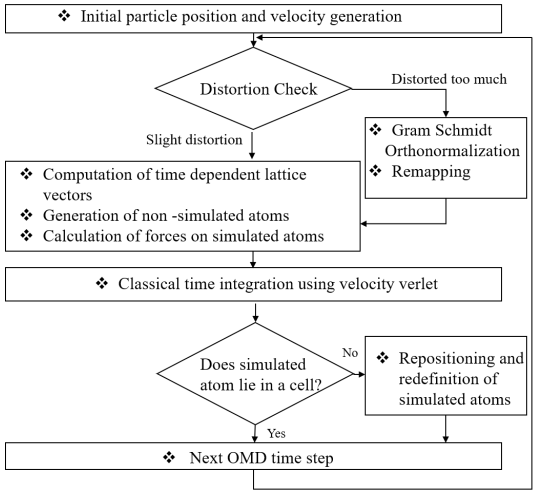

Figure 2.5: Flow chart of single time stepping in OMD.

It exactly inherits the invariant manifold of (continuous) molecular dynamics: if you start on the manifold, you stay on the manifold exactly, even with discrete time steps. Or, equivalently, if you use the velocity Verlet algorithm only for the simulated atoms then it is automatically being used for all the atoms.

This is explained here in the general case of time dependent isometry groups. The time dependent translation group is a special case.

2.4.1 Velocity Verlet algorithm

Let $\mathcal{G} = \{g_1, g_2, \ldots, g_N\}$, $g_1 = id$, be a time-dependent discrete group of isometries with affine time dependence:

$$g_i = (\mathbf{Q}_i | \mathbf{a}_i t + \mathbf{b}_i), \quad \mathbf{Q}_i \in \mathrm{O}(3), \quad \mathbf{a}_i, \mathbf{b}_i \in \mathbb{Z}^3, \quad i = 1, \ldots, N. \tag{2.22}$$

Suppose the atomic forces satisfy frame-indifference and permutation invariance. Consider a continuous OMD simulation defined by

$$\begin{aligned} m_k\ddot{\mathbf{y}}_{1,k}(t) &= -\frac{\partial\varphi}{\partial\mathbf{y}_{1,k}}(\dots,\mathbf{y}_{i,1}(t),\dots,\mathbf{y}_{i,M}(t),\mathbf{y}_{i+1,1}(t),\dots,\mathbf{y}_{i+1,M}(t),\dots) \\ &= -\frac{\partial\varphi}{\partial\mathbf{y}_{1,k}}(\dots,g_i(\mathbf{y}_{1,1}(t),t),\dots,g_i(\mathbf{y}_{1,M}(t),t),g_{i+1}(\mathbf{y}_{1,1}(t),t),\dots,g_{i+1}(\mathbf{y}_{1,M}(t),t),\dots), \\ &\quad \mathbf{y}_{1,k}(0)=\mathbf{y}_k^0,\quad \dot{\mathbf{y}}_{1,k}(0)=\mathbf{v}_k^0,\quad k=1,\dots,M, \end{aligned} \tag{2.23}$$

Here the notation $g_i(\mathbf{y},t)$ stands for $\mathbf{Q}_i\mathbf{y}(t)+\mathbf{a}_it+\mathbf{b}_i$. From now on, the notation is simplified and $\mathbf{y}_i(t)$ is written as $\mathbf{y}_{1,i}(t)$. The $\mathbf{y}_i(t)$, $i=1,\dots,M$, are called the simulated atoms.

Consider a sequence of equal time steps, $0,t_1,t_2,\dots$, with $t_{i+1}-t_i=\Delta t$, The velocity Verlet algorithm applied to this "small" system, i.e., the equations for the simulated atoms, is

$$\begin{aligned} \mathbf{y}_k(t_{i+1}) &= \mathbf{y}_k(t_i)+\mathbf{v}_k(t_i)\Delta t-\frac{(\Delta t)^2}{2m_k}\frac{\partial\varphi}{\partial\mathbf{y}_{1,k}}(\dots,g_i(\mathbf{y}_1(t_i),t_i),\dots,g_i(\mathbf{y}_M(t_i),t_i),\dots), \\ \mathbf{v}_k(t_{i+1}) &= \mathbf{v}_k(t_i)-\frac{\Delta t}{2m_k}\left(\frac{\partial\varphi}{\partial\mathbf{y}_{1,k}}(\dots,g_i(\mathbf{y}_1(t_i),t_i),\dots,g_i(\mathbf{y}_M(t_i),t_i),\dots)\right. \\ &\quad \left.+\frac{\partial\varphi}{\partial\mathbf{y}_{1,k}}(\dots,g_i(\mathbf{y}_1(t_{i+1}),t_{i+1}),\dots,g_i(\mathbf{y}_M(t_{i+1}),t_{i+1}),\dots)\right) \end{aligned} \tag{2.24}$$

Here, the usual velocity Verlet algorithm is consolidated into two equations.

2.4.2 Proof that the velocity Verlet algorithm for the simulated atoms implies its satisfaction for the full system

Denote the full set of atom motions by $\mathbf{y}_{n,k}(t)=g_n(\mathbf{y}_k(t),t)$. In the continuous case these satisfy the full system of MD, according to the basic theorem of OMD.

Fix $m\in\{1,\dots,N\}$ throughout this section. Define the permutation Π (which depends on m but not on t) by

$$\mathbf{y}_{\Pi(\ell,k)}(t)=g_m^{-1}(\mathbf{y}_{\ell,k}(t),t)=g_m^{-1}g_\ell(\mathbf{y}_k(t)). \tag{2.25}$$

Recalling that $g_1 = id$ note that $\Pi(m,k) = (1,k)$. Apply the group element $g_m(\,\cdot\,, t_{i+1})$ to the first of (2.24). This gives

$$\begin{aligned}
\mathbf{y}_{m,k}(t_{i+1}) &= g_m(\mathbf{y}_k(t_{i+1}), t_{i+1}) \\
&= g_m\bigg(\mathbf{y}_k(t_i) + \mathbf{v}_k(t_i)\Delta t - \frac{(\Delta t)^2}{2m_k}\frac{\partial \varphi}{\partial \mathbf{y}_{1,k}}(\dots, \mathbf{y}_{\ell,1}(t_i), \dots, \mathbf{y}_{\ell,M}(t_i), \dots),\ t_{i+1}\bigg) \\
= \mathbf{Q}_m\mathbf{y}_k(t_i) + \mathbf{Q}_m\mathbf{v}_k(t_i)\Delta t - \frac{(\Delta t)^2}{2m_k}\mathbf{Q}_m\frac{\partial \varphi}{\partial \mathbf{y}_{\Pi(m,k)}}(\dots, \mathbf{y}_{\ell,1}(t_i), \dots, \mathbf{y}_{\ell,M}(t_i), \dots) + \mathbf{a}_m t_{i+1} + \mathbf{b}_m, \\
&= \mathbf{Q}_m\mathbf{y}_k(t_i) + \mathbf{a}_m t_i + \mathbf{b}_m + \mathbf{Q}_m\mathbf{v}_k(t_i)\Delta t + \mathbf{a}_m\Delta t \\
&\quad - \frac{(\Delta t)^2}{2m_k}\mathbf{Q}_m\frac{\partial \varphi}{\partial \mathbf{y}_{m,k}}(\dots, \mathbf{y}_{\Pi(\ell,1)}(t_i), \dots, \mathbf{y}_{\Pi(\ell,M)}(t_i), \dots) \\
&= \mathbf{y}_{m,k}(t_i) + \mathbf{v}_{m,k}(t_i)\Delta t - \frac{(\Delta t)^2}{2m_k}\mathbf{Q}_m\frac{\partial \varphi}{\partial \mathbf{y}_{m,k}}(\dots, g_m^{-1}(\mathbf{y}_{\ell,1}(t_i), t_i), \dots, g_m^{-1}(\mathbf{y}_{\ell,M}(t_i), t_i), \dots) \\
&= \mathbf{y}_{m,k}(t_i) + \mathbf{v}_{m,k}(t_i)\Delta t \\
&\quad - \frac{(\Delta t)^2}{2m_k}\mathbf{Q}_m\frac{\partial \varphi}{\partial \mathbf{y}_{m,k}}(\dots, \mathbf{Q}_m^T\mathbf{y}_{\ell,1}(t_i) - \mathbf{Q}_m^T(\mathbf{a}_m t_i + \mathbf{b}_m), \dots, \mathbf{Q}_m^T\mathbf{y}_{\ell,M}(t_i) - \mathbf{Q}_m^T(\mathbf{a}_m t_i + \mathbf{b}_m), \dots) \\
&= \mathbf{y}_{m,k}(t_i) + \mathbf{v}_{m,k}(t_i)\Delta t - \frac{(\Delta t)^2}{2m_k}\frac{\partial \varphi}{\partial \mathbf{y}_{m,k}}(\dots, \mathbf{y}_{\ell,1}(t_i), \dots, \mathbf{y}_{\ell,M}(t_i), \dots).
\end{aligned} \tag{2.26}$$

This is the first step in the velocity Verlet algorithm for the full system. The last few lines above use permutation invariance and frame-indifference and follow the lines of the continuous proof.

In the above argument the quantity $\mathbf{v}_{m,k}(t)$ is simply defined (for obvious reasons) by the formula $\mathbf{v}_{m,k}(t) = \mathbf{Q}_m\mathbf{v}_k(t) + \mathbf{a}_m$.

Now apply the transformation $\mathbf{v} \to \mathbf{Q}_m\mathbf{v} + \mathbf{a}_m$ (no t dependence) to both sides of

the second step of the algorithm (2.24) to get

$$\begin{aligned}\mathbf{v}_{m,k}(t_{i+1}) &= \mathbf{v}_{m,k}(t_i) - \frac{\Delta t}{2m_k}\mathbf{Q}_m\Bigg(\frac{\partial\varphi}{\partial\mathbf{y}_{1,k}}(\dots,\mathbf{y}_{\ell,1}(t_i),\dots,\mathbf{y}_{\ell,M}(t_i),\dots)\\ &\quad+\frac{\partial\varphi}{\partial\mathbf{y}_{1,k}}(\dots,\mathbf{y}_{\ell,1}(t_{i+1}),\dots,\mathbf{y}_{\ell,M}(t_{i+1}),\dots)\Bigg)\\ &= \mathbf{v}_{m,k}(t_i) - \frac{\Delta t}{2m_k}\Bigg(\frac{\partial\varphi}{\partial\mathbf{y}_{m,k}}(\dots,\mathbf{y}_{\ell,1}(t_i),\dots,\mathbf{y}_{\ell,M}(t_i),\dots)\\ &\quad+\frac{\partial\varphi}{\partial\mathbf{y}_{m,k}}(\dots,\mathbf{y}_{\ell,1}(t_{i+1}),\dots,\mathbf{y}_{\ell,M}(t_{i+1}),\dots)\Bigg).\end{aligned}\tag{2.27}$$

This completes the argument.

2.5 Compressible Heat Conducting Viscous Monoatomic Gas

The macroscopic motion simulated by OMD in Lagrangian and Eulerian description is given by $\mathbf{y}(x,t) = (\mathbf{I}+t\mathbf{A})\mathbf{x}$ and $\mathbf{v}(\mathbf{y},t) = \mathbf{A}(\mathbf{I}+t\mathbf{A})^{-1}\mathbf{y}$, respectively. These are termed affine motions. It is showed in section 1.3 that OMD family of flows satisfies equation of balance of linear momentum motion identically for all accepted constitutive laws of continuum mechanics of solids and fluids, e.g., Navier-Stokes fluids, general non-Newtonian fluids, nonlinear elastic solids, plastic solids, etc.. The other two mass and energy balance laws are

$$\begin{aligned}\rho_t + \nabla\cdot(\rho\mathbf{v}) &= 0,\\ \rho(e_t + \nabla e\cdot\mathbf{v}) &= \boldsymbol{\sigma}\cdot\nabla\mathbf{v} - \nabla\cdot\mathbf{q}.\end{aligned}\tag{2.28}$$

The first of these determines the density $\rho(t) = \rho_0\exp\Big(-\int_0^t \mathrm{tr}\big(\mathbf{A}(\mathbf{I}+s\mathbf{A})^{-1}\big)\mathrm{ds}\Big)$. With the motion $\mathbf{v}(\mathbf{y},t) = \mathbf{A}(\mathbf{I}+t\mathbf{A})^{-1}\mathbf{y}$ the temperature field T becomes uniform and time dependent $T(t)$. All accepted constitutive relations then make stress and energy also independent of position, $\boldsymbol{\sigma} = \boldsymbol{\sigma}(t)$, $e = e(t)$. This pure time dependence gives the following parameter $\mathbf{A}$-dependent ordinary differential equation for the temperature

after incorporating the Navier-Stokes-Fourier constitutive model and equation of state:

$$e = c_v T,$$

$$\boldsymbol{\sigma} = p\mathbf{I} - \mu(\nabla\mathbf{v} + \nabla\mathbf{v}^T - \frac{2}{3}(\nabla\cdot\mathbf{v})\mathbf{I}),$$

$$\frac{dT}{dt} = \frac{-R}{c_v}\operatorname{tr}\big(\mathbf{A}(\mathbf{I}+t\mathbf{A})^{-1}\big)T(t) + \frac{\mu(T(t))}{\rho_0 c_v}(|\mathbf{A}(\mathbf{I}+t\mathbf{A})^{-1}|^2 + \operatorname{tr}\big((\mathbf{A}(\mathbf{I}+t\mathbf{A})^{-1})^2\big) - \frac{2}{3}(\operatorname{tr}(\mathbf{A}(\mathbf{I}+t\mathbf{A})^{-1}))^2)$$
$$\exp\bigg((-\int_0^t \operatorname{tr}\mathbf{A}(\mathbf{I}+s\mathbf{A})^{-1}\mathrm{d}s)\bigg), \quad (2.29)$$

$$T(0) = T_0.$$

2.5.1 General incompressible flow

A general incompressible flow (shear in three directions) gives a family of choices of $\mathbf{A}$ out of many flows possible. Incompressibility imposes the condition, $\det(\mathbf{I}+t\mathbf{A}) = 1,\ t > 0$. The characteristic equation in t then yields the condition,

$$\det\mathbf{A} = \operatorname{tr}\mathbf{A} = \operatorname{tr}\mathbf{A}^2. \quad (2.30)$$

A necessary and sufficient condition for (2.30) is that there exists an orthonormal basis such that, in this basis,

$$\mathbf{A} = \begin{bmatrix} 0 & 0 & \kappa \\ \gamma_1 & 0 & \gamma_3 \\ 0 & 0 & 0 \end{bmatrix}.$$

In general, this is matrix of rank 2. Note that there are many of these isochoric affine flows which are not viscometric flows [87]. In abstract form, $\mathbf{A} = \kappa\mathbf{e_1}\otimes\mathbf{e_3} + \mathbf{e_2}\otimes\mathbf{g}$ and $\mathbf{v}(\mathbf{x},t) = \mathbf{A}\mathbf{x} - \kappa t\gamma_1\gamma_3\mathbf{e_2}$ where $\mathbf{e_1},\mathbf{e_2},\mathbf{e_3}$ are orthonormal and $\mathbf{g} = \gamma_1\mathbf{e_1} + \gamma_3\mathbf{e_3}$.

These flows have an extra feature which is not present in other viscometric flows. Here, vorticity (independent of position) grows linearly in time given by

$$\boldsymbol{\nabla}\times\mathbf{v} = (\gamma_3 - \kappa\gamma_1 t)\mathbf{e_1} - \kappa\mathbf{e_2} - \gamma_1\mathbf{e_3}. \quad (2.31)$$

Conservation of mass determines the density:

$$\rho = \rho(0)\exp\Big(-\int_0^t E\mathrm{d}s\Big) = \rho(0)\exp\Big(-\int_0^t \mathrm{tr}\mathbf{A}(\mathbf{I}+s\mathbf{A})^{-1}\mathrm{d}s\Big) = \rho(0)\exp(0) = \rho(0) = \rho_0 \tag{2.32}$$

Conservation of energy determines the temperature. The resulting ordinary differential equation is solved using a Runge-Kutta solver for the given viscosity model,

$$\dot{T} = \frac{\mu(T)}{c_v\rho_0}(\gamma_1^2 + \kappa^2 + (\gamma_3 - \gamma_1\kappa t)^2) \tag{2.33}$$

2.5.2 Numerical validation

Here, a general incompressible flow for a model of Argon gas is simulated and the temperature evolution from continuum and atomistic calculations is compared. Initially, the simulated atoms are defined on a domain constructed by linearly independent vectors $\mathbf{e}_1, \mathbf{e}_2$ and $\mathbf{e}_3$. The initial coordinates and momenta correspond to a specified equilibrium state of a gas. (Here, ρ=1.78 kg/m^3, $T(0) = 350$ K). The initial velocity of each simulated atom is drawn from a Maxwell–Boltzmann distribution whose variance is determined by the temperature. A pairwise additive short-range Lennard-Jones potential is used to define the interaction between atoms, given by

$$\phi(r_{ij}) = 4\epsilon\left[\left(\frac{\sigma}{r_{ij}}\right)^{12} - \left(\frac{\sigma}{r_{ij}}\right)^{6}\right], \tag{2.34}$$

where r_{ij} is the distance between atoms, $\epsilon = 1.65\times10^{-21}$J, and $\sigma = 3.4\times10^{-10}$m. It is important for comparison that the input parameters of the continuum model are consistent with the force field used in MD. The Lennard-Jones (12-6) temperature dependent viscosity model which was computed directly from the kinetic theory [88] is used here. It is in agreement with the Newtonian constitutive model used here to compute the continuum temperature profile. Reduced units are used for the OMD simulations by making distance and energy dimensionless by use of the molecular diameter σ, and characteristic interaction energy ϵ, respectively. The time step varies from 0.05 to 1 femtosecond depending on the temperature of the system.

The mean fluid velocity is obtained using the mass averaged position: $\langle\mathbf{v}\rangle = \frac{\sum_{i=1}^{N} m_i\mathbf{v}_i}{\sum_{i=1}^{N} m_i}$

where N is the total number of simulated atoms; this follows the well-studied multi-scale idea that one should average the momentum, not the velocity. The macroscopic temperature is computed as:

$$T = \frac{m}{3k_b}[\langle v_1^2 + v_2^2 + v_3^2\rangle - (\langle v_1\rangle^2 + \langle v_2\rangle^2 + \langle v_3\rangle^2)], \tag{2.35}$$

where m is a mass of an atom and k is Boltzmann's constant.

1600 simulated atoms for the simulation is used. The evolution of temperature coming from OMD and NSF computations is compared. OMD and NSF agree very well as shown in the Fig. 2.6(a). The remapping of the fundamental domain is performed several times during the simulation due to significant deformation. It is noticed that there is no discontinuity in the temperature field due to remapping, as must be true. For the strain rate considered in this case, $\gamma_1 = \kappa = \gamma_3 = 0.0001$ (in reduced units), the fundamental assumptions behind the conventional linear constitutive law (Fourier's law, Navier-Stokes) works very well. This is evident from the comparison between velocity distribution function (VDF) determined from OMD and from the Chapman-Enskog method [24, 29], computed using the local moments $(\rho, T, \boldsymbol{\sigma})$ obtained from simulations as shown in Fig. 2.7. The computed VDF follows the near equilibrium conditions and deviates little from the equilibrium Maxwell-Boltzmann distribution. For higher rates, one can expect that the linear constitutive law will no longer remain valid and a non linear constitutive laws will be needed. This is very well shown in the comparison (Fig. 2.6(b)) made for a much higher value of velocity gradient ($\gamma_1 = \kappa = \gamma_3 = 0.05$ (in reduced units)). Here, the discrepancy is quite apparent.

The velocity gradient considered in this comparison study is not constant in time. It takes some time for the simulation to attain the gradient imposed on it. One needs to wait for the transient stage to settle before extracting any data. It is noticed that one can take the advantage of basic theorem of OMD by starting with a much lower number of simulated atoms and once the system comes out of the transient regime, the number of simulated atoms can be increased to improve the statistics. This can be done by simply designating some non-simulated atoms as simulated atoms and restarting the

simulation with the initial conditions given by the last time-step. The extreme sensitivity of nonlinear dynamical systems to perturbations of initial conditions in practice assures better statistics, i.e., better approximation of the invariant manifold.

In Fig. 2.8 the gradient imposed and the one attained in the simulations is compared. Fluctuations increase with time due to increase in temperature of the system. Comparison with NSF is made once the system is out of this transient regime 2.6(b). Note that for a comparatively bigger system, it takes more time to attain fully developed gradient field.

OMD works well in highly non-equilibrium settings where there is no well developed constitutive equation. It can provide interesting insight on the response of the gas in that regime. An alternative is to use DSMC [23] method, which represents a valuable and efficient tool to investigate the nonequilibrium structure of the gas, but limited to the dilute regime and relies on a variety of collision models. DMS [59, 57, 89] eliminates the need for collision models by relying on a set of PES, but is still limited to the dilute gas regime.

Next, the effect of remapping on temperature evolution is explored. Fig. 2.9(a) shows two independent OMD simulations, one where remapping is done (20 instances of remapping) and another where it is not performed. The simulation is done for comparatively higher density state ($\rho = 674.3$ kg/m^3) than the previous one to get many occurrences of the criterion for remapping. The temperature fields agree well with each other. Hence, remapping is only performed from the computational perspective since it makes the computation less intensive. The effect of another important parameter, number of simulated atoms, on the predictions is also investigated. The method works for any number of simulated atoms, but the question is to find an appropriate lower bound so that it represents the correct physics of the system. Fig. 2.9(b) shows the comparison between different simulations which use various numbers of simulated atoms. Surprisingly, even 200 atoms represents the macroscopic system remarkably well in these cases and gives correct trends. The inherent length scale of the phenomenon needs to be considered when fixing the number of atoms to be simulated. For the system considered,

the size of fundamental domain needs to be bigger than mean free path of the gas to eliminate nonphysical effects. 1600 atoms is chosen to be an optimum number for the simulation considered. Note that to capture much lower gradients one needs to increase the number of simulated atoms further to reduce the surrounding statistical noise of the system. Ensemble averaging by running many instances of OMD also improves statistics for applications involving macroscopically homogeneous simulations.

One can place the simulated atoms at any positions, map these to other locations using the group, simulate the equations of molecular dynamics using just this original set of atoms while calculating the forces on these from all other atoms within the cut-off. It is found that, as expected, reproducible macroscopic behavior is achieved more quickly if the simulated atoms are given initial velocities, consistent on average with the macroscopic Eulerian velocity $\mathbf{v}(\mathbf{x}, t) = \mathbf{A}(\mathbf{I} + t\mathbf{A})^{-1}\mathbf{x}$.

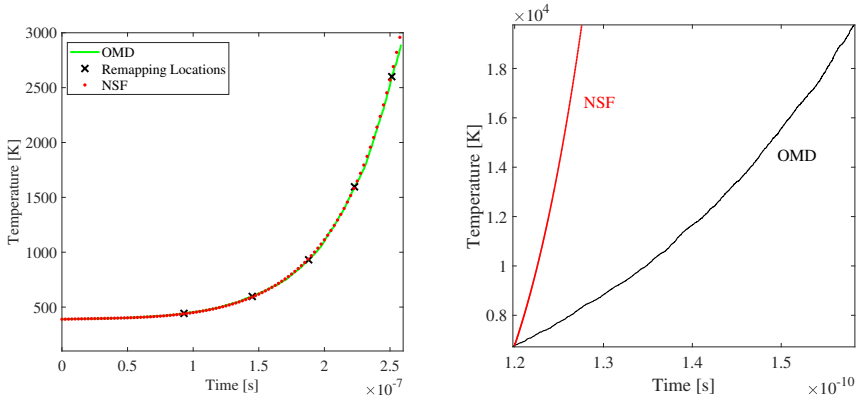

(a) (b)

Figure 2.6: Evolution of temperature for general incompressible flow of Argon gas (a) $\gamma_1 = \kappa = \gamma_3 = 0.0001$ (b) $\gamma_1 = \kappa = \gamma_3 = 0.05$.

2.6 Phase Change

There are no fundamental restrictions on the density of the fluid in the simulations, and phase change can occur spontaneously during a simulation. To illustrate the phenomenon of phase change, the dilatation of the infinite system of supercritical Argon

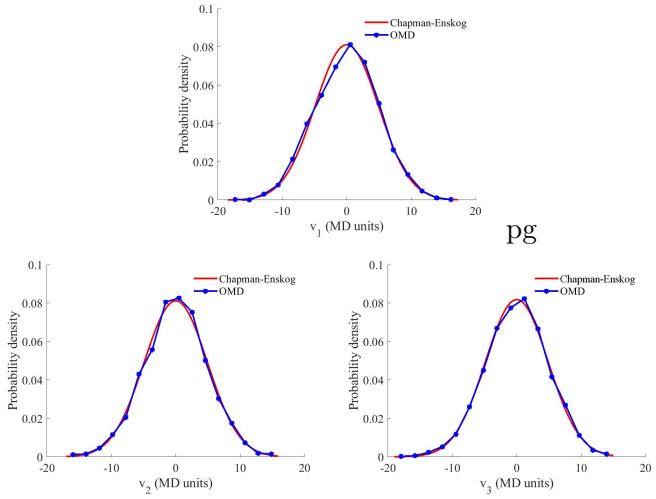

Figure 2.7: Comparison of velocity distribution function for different velocity components.

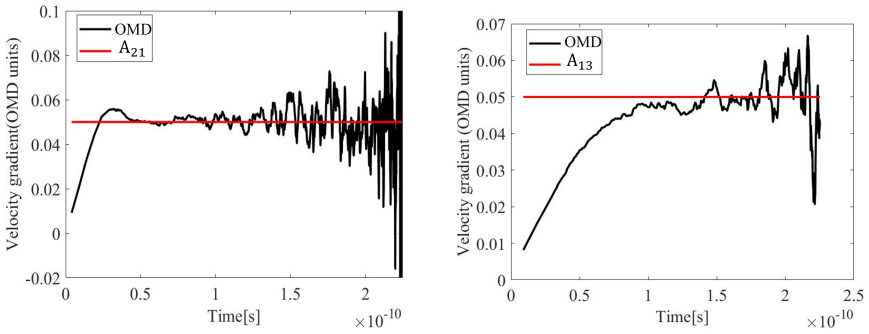

Figure 2.8: Time taken by the system to adapt to the boundary conditions.

using the Lennard-Jones potential is performed. Here, $\mathbf{A} = \kappa \mathbf{e}_1 \otimes \mathbf{e}_1 + \kappa \mathbf{e}_2 \otimes \mathbf{e}_2 + \kappa \mathbf{e}_3 \otimes \mathbf{e}_3$, $\kappa > 0$. This flow field comes under the general nine parameter family of compressible flows where density is given by

$$\rho(t) = \frac{\rho(0)}{(\kappa t + 1)^3} \tag{2.36}$$

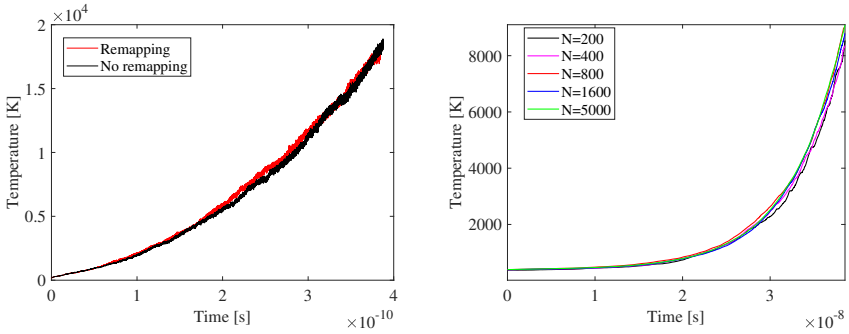

(a) (b)

Figure 2.9: Effect of (a) remapping and (b) number of simulated atoms on the temperature evolution.

The values of initial density and dilatation rate in OMD units are chosen to be $\rho = 674.3$ kg/m^3 and $\kappa = 0.01$ (OMD units) respectively. Fig. 2.11(a) illustrates phase transition driven by high rate expansion where clusters of varying sizes appear spontaneously during the simulation. Fig. 2.11(b) shows a zoomed view of a cluster. Note that the clusters are composed of both simulated and non-simulated (redefined as simulated atoms at this time instant) atoms. The $\rho - T$ diagram is shown in the Fig. 2.10. As the simulation proceeds, the temperature of the system decreases due to rapid adiabatic expansion.

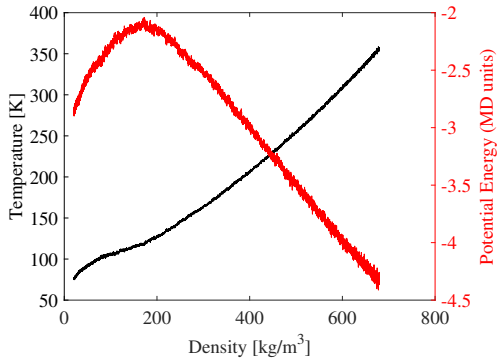

Figure 2.10: $\rho - T$ diagram with evolution of the potential energy and temperature.

A slight rise in the temperature due to the release of latent heat shows the onset of condensation. At this instant, the potential energy starts decreasing due to clustering of atoms. Note that, macroscopic variables (density, temperature, stress, etc.) cease to be macroscopically uniform once the two phase system is fully developed. Also, in order to examine the properties of a heterogeneous system like this, it is necessary to use many more simulated atoms than in the case of a single phase system.

These studies can be highly useful in studying the actual dynamics of the birth of the new phase, exploring the actual morphology of clusters produced in the expansions and to produce benchmark results for testing various explicit nucleation models. This will appear in forthcoming work, but here it is simply shown that this is a feasible possibility with the OMD method as described here.

Several studies report molecular dynamics simulation of phase change in Argon using various cooling protocols. Kraska studied homogeneous nucleation of argon from a supersaturated vapor phase using a NVE ensemble [90]. Diemand et al. studied large-scale MD simulations of homogeneous vapor-to-liquid nucleation under NVT ensemble [91]. These techniques are associated with reproducing equilibrium probability density at a given external environment whereas OMD operates in highly non-equilibrium environment. Ashurst and Holian studied the expansion and fragmentation of a 3D system without free boundaries [92]. The present system where the fundamental domain edge length grows like $L(t) = (\mathbf{I} + t\mathbf{A})L_0$ is similar to the one considered in [92] with $\mathbf{A}$ being a diagonal matrix with diagonal entries given by κ.

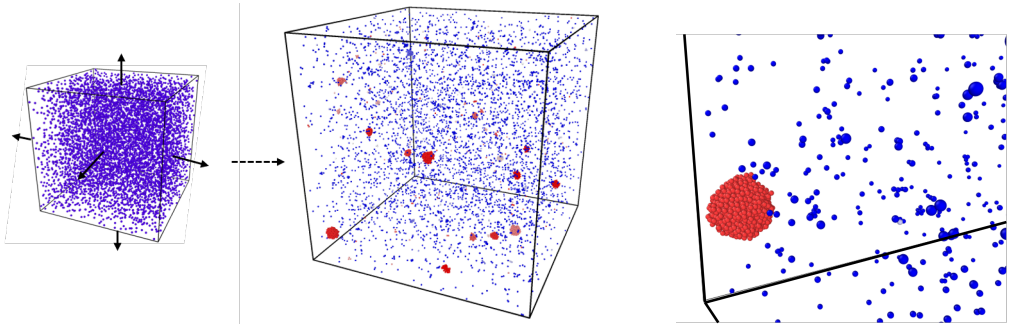

(a) (b)

Figure 2.11: Phenomenon of phase change showing (a) sudden dilatation of box leading to cluster (red) formation and (b) Zoomed view of a cluster.

2.7 Shear-driven Gas Flow in Nano Channel

In this section OMD is used to study confined flows where walls are modeled explicitly using Lennard-Jones force field. The flow of Lennard-Jones argon subjected to boundary driven shear where the gas is confined between two thin face-centered cubic infinite walls a distance H apart is studied. Fig. 2.12 illustrates the fundamental domain composed of simulated atoms which only include three layer atomically thin lower wall (red atoms). The other wall is composed of non-simulated atoms and moves with a net velocity in $\mathbf{e}_1$ direction is not shown. Wall atoms have lattice parameter, mass and diameter equivalent to platinum ($a_p = 0.392$ nm, $m_w = 3.2398$ x 10^{-22} kg, $\sigma_w = 2.4626$ x 10^{-10} m) and depth of potential well is $\epsilon_w = 31.36$ kJ/mol. For the cross interactions

between walls and gas, the length parameter is determined from the Lorentz-Berthelot mixing rule [93] $\sigma_c = (\sigma_w + \sigma_{Ar})/2$ and energy parameter $\epsilon_c = 0.6580$ kJ/mol is taken from the literature [94]. It is emphasized that both the wall and gas are treated in one simulation with the given $\mathbf{A}$, all atoms satisfying the MD equations; the platinum atoms happen to move macroscopically as a block because they are strongly bonded. The initial system is equilibrated to a temperature of 300K and then shear motion is induced by choosing $\mathbf{A} = \kappa \mathbf{e}_1 \otimes \mathbf{e}_2$ where κ is of the order $10^9 s^{-1}$. To reduce time in achieving the fully developed flow, a macroscopic constant velocity gradient κ is imposed on the initial velocity field.

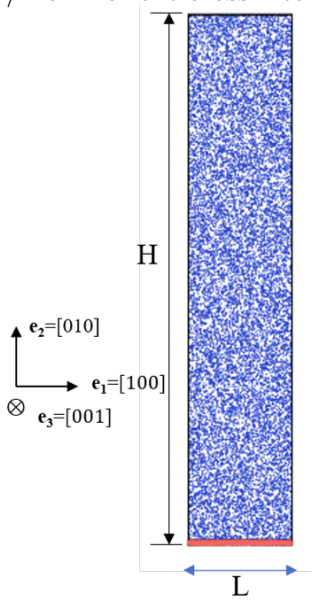

Figure 2.12: Fundamental domain of simulated atoms (Wall: Orange atoms, Gas: Blue atoms)

The velocity profile of the gas in the channel as a function of non-dimensional channel height is plotted in Fig. 2.13(a). Near the walls, the formation of a Knudsen layer of thickness of the order of few mean free paths ($\lambda = 16$ nm) is seen. In the middle of the channel the velocity varies linearly, whereas in Knudsen layer the velocity gradient differs significantly from that of the mainstream. In this region, the paths of gas molecules

Table 2.1: Summary of different sizes of nano channel considered

H (nm)	ρ (kg/m^3)	κ (ps^{-1})
150	8.32	0.0046
150	8.07	0.0046
150	8.0	0.0046
150	5.0	0.0046
100	5.0	0.0069
100	2.0	0.0069

are severely affected by the presence of solid walls resulting in significant amount of velocity slip v_s. The existence of velocity slip was first predicted by Maxwell [9].

The quantity v_s is computed by averaging the velocity along $\mathbf{e}_1$ of atoms lying in a bin adjacent to the wall, minus the velocity of wall itself; for the lower wall this velocity is zero. Different sizes of computational domain LxWxH and density of the gas are chosen to simulate the flow at varying Knudsen number Kn = λ/H, where λ is defined in terms of viscosity using Cercignani's definition [95], and $\lambda = \frac{\mu}{p}\frac{\pi m}{2k_bT}$. For the viscosity model, the Newtonian viscosity which was computed for the Lennard-Jones force field using the Chapman-Enskog expansion of the velocity distribution function [88] is used. The simulation details is listed in Table 2.1. κ is varied for different simulations to maintain a constant Mach number Ma = $\frac{v_w}{\sqrt{\gamma k_b T/m}}$ of ≈ 1.5 with varying Knudsen number. Here v_w is the wall velocity given by $v_w = \kappa$H.

The Knudsen number characterizing these flows is in the transition regime. For sufficiently small Knudsen numbers Maxwell's theory of slip accurately predicts a non-dimensional slip length for isothermal flow given by [96]

$$l_s^* = \frac{v_s}{\mathrm{H}(\mathrm{dv_2/d_{y_2}})|_\mathrm{w}} = \frac{2-\sigma}{\sigma}\mathrm{Kn}$$

where σ is the tangential momentum accommodation coefficient (TMAC).

The interesting question is how the slip velocity behaves in the transition regime. Fig. 2.13(b) shows the OMD prediction of slip velocity normalized by wall velocity $v_s^* = v_s/v_w$ and normalized slip length l_s^* as a function of Knudsen number. It can be

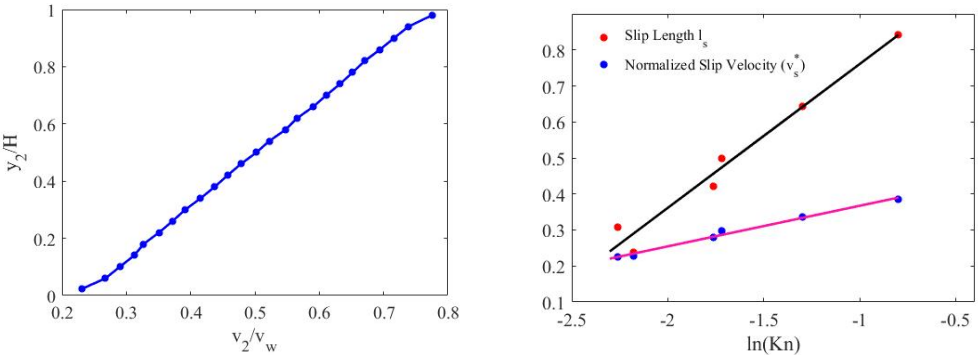

(a) (b)

Figure 2.13: Slip flow over smooth platinum surface (a) Normalized velocity profile (b) Variation of slip length and normalized slip velocity with the Knudsen number.

seen from the plot that the normalized slip velocity and slip length vary as the log of the Knudsen number, when the Newtonian viscosity and Cercignani's mean free path definition is used. It therefore deviates from the Maxwell first order slip model which predicts a linear dependence. A similar finding for the hard sphere definition of mean free path $\lambda = \frac{m}{\sqrt{2}\pi\rho d^2}$ was predicted by Bhattacharya et al [97]. This logarithmic dependence can prove to be important in proposing new simple slip models which only depend on average temperature, density and Newtonian viscosity and which could work well also in the transition regime. This result provides motivation to validate this simple slip model for a wide range of flow system geometries and regime of (Kn, Ma). Another approach is to improve the prediction of mean free path [98] and viscosity which goes into the slip model. It was shown in prior work that when an effective viscosity is obtained from the shear stress at a thermal wall, then the Maxwell model works reasonably well, even in the transient regime [99]. On the other hand there exist higher order velocity slip boundary conditions which are shown to improve the flow field predictions in some situations of interest. A review can be found in Reese and Zhang [100].

2.8 Summary and Conclusions

In summary, this chapter details computational aspects of a novel objective molecular dynamics (OMD) method. The method can simulate three parameter family of general incompressible and nine parameter family of compressible flows at the atomistic scale. The framework developed is quite easy to implement. One only needs to provide a 3×3 matrix $\mathbf{A}$ to consider different flows, and every atom in the infinite system satisfies the equations of molecular dynamics exactly for its forces. This is also proven in a discrete sense by showing the consistency of OMD with the velocity Verlet algorithm widely used in MD simulations. The trend of the temperature field for general incompressible flows is in good agreement with linear continuum theory in the regime of small velocity gradients where conventional hydrodynamic closure for the transport fluxes (Fourier's law, Newton's law, etc.) remains valid. In the regime of higher rates, the Navier-Stokes-Fourier theory is no longer accurate and there is a need to develop new constitutive equations which is the focus of the next chapter. OMD solutions are possible in any material and fluid with an arbitrary number of simulated atoms. It is also reported in this work how OMD also provides a structure for simulating non-homogeneous phenomena of phase transition and boundary driven shear flow.

In the next chapter, the focus is on developing generalization of Navier-Stokes theory in the regime of high velocity gradients for dilute gas using the computational OMD method developed in this chapter.

Chapter 3

Constitutive Relation Generalizing the Navier-Stokes Theory

3.1 Introduction

The behavior of gases under the extreme conditions of hypersonic flows is not well understood. Extreme conditions encountered in these flows can lead to failure of classical constitutive laws: Newton's law of viscosity and Fourier's law of heat conduction. In general, this breakdown is closely associated with large Knudsen number (Kn) where mean free path becomes comparable to characteristic length scale of the problem of interest [24]. Traditionally, Kn is used to classify gas flow regimes into continuum, transitional and free molecular flow. The similar flow regimes are also observed in channels of micro/nano systems. In the transitional and free-molecular regime, a conventional description of gas in terms of Navier-Stokes-Fourier equations of hydrodynamics is no longer valid. In this work, breakdown of these classical field equations is noticed due to the comparable effects of the gradient of flow velocity and mean collision frequency of the gas. This leads to disruption of local equilibrium which is better assessed by the dimensionless invariants of symmetric part of the velocity gradient tensor $\mathbf{E} = \frac{1}{2}(\nabla\mathbf{v} + \nabla\mathbf{v}^{\mathrm{T}})$.

This chapter aims at generalizing the Navier-Stokes theory to high-rate regimes. To develop that, a route which is different than the traditional approaches usually adopted in the field of gas dynamics is taken. The problem is approached using patterns of thought of classical constitutive theory. Theories proposed by Reiner, Rivlin and Ericksen [101, 102, 103, 104] are examined using the deterministic method of OMD. In contrast to kinetic theory approach, transport coefficients do not emerge naturally from the theory itself. A frame-indifferent constitutive relation is proposed and calibrated using various flows of Lennard-Jones (model for the potential energy which takes into account both the softness of particles and their mutual attraction at large distances) argon gas as described by 2.34. The model is termed the RE constitutive relation (or RE model for short).

This chapter is organized as follows: Section 3.2 compares OMD simulations with Navier-Stokes fluid dynamics. Section 3.3 discusses the Reiner-Rivlin constitutive model and shows the inability of the model to predict correct trends. Section 3.4 defines Rivlin-Ericksen constitutive model, calibrates it using OMD modeling of simple shear flow, makes connection with exact moment method for Maxwellian gas (molecules interacting by an inverse-fifth power law of force) and shows that it improves the Navier-Stokes-Fourier (NSF) constitutive relation. Later, it extends the calibration to various incompressible, compressible and unsteady flows and shows the agreement of proposed model with OMD simulations. Section 3.5 discusses the thermodynamics and stability of the proposed RE model. Section 3.6 explains a connection between the RE and Burnett equations. Finally the conclusions are contained in Section 3.7.

3.2 Comparison of OMD and NSF Theory

3.2.1 Simple shear flow

The main difference between the planar Couette and uniform simple shear (USF) flow considered in this work is the absence of energy transport in the OMD flow. The temperature field is uniform and the heat flux $\mathbf{q}$ is identically zero in these flows. USF despite being the simplest flow provides wealth of interesting insights about the behaviour of gas in non-equilibrium regime [49].

From the value of $\mathbf{A} = \kappa \mathbf{e_1} \otimes \mathbf{e_2}$, the Eulerian velocity field and viscous stress tensor predicted by NS are given by

$$\mathbf{v}(\mathbf{x}, t) = \mathbf{A}(\mathbf{I} + t\mathbf{A})^{-1}\mathbf{x} = (\kappa \mathbf{e}_1 \otimes \mathbf{e}_2)(\mathbf{I} - \kappa \mathbf{e}_1 \otimes \mathbf{e}_2)\mathbf{x} = \kappa x_2 \mathbf{e_1} = \begin{bmatrix} \kappa x_2 \\ 0 \\ 0 \end{bmatrix}, \tag{3.1}$$

$$\boldsymbol{\tau} = -(-p\mathbf{I} + \boldsymbol{\sigma}) = \mu(\nabla \mathbf{v} + \nabla \mathbf{v}^T - \frac{2}{3}(\boldsymbol{\nabla} \cdot \mathbf{v})\mathbf{I}) = \mu \begin{bmatrix} 0 & \kappa & 0 \\ \kappa & 0 & 0 \\ 0 & 0 & 0 \end{bmatrix} \tag{3.2}$$

Conservation of mass and energy determines the density and temperature respectively

$$\rho(t) = \rho(0) \exp\left(- \int_0^t \boldsymbol{\nabla} \cdot \mathbf{v} ds \right) = \rho(0), \quad \dot{T}(t) = \frac{\mu(T(t))\kappa^2}{c_v \rho(0)} \tag{3.3}$$

For the OMD computations, temperature is defined by the variance of the kinetic energy and the Boltzmann definition is used for the stress, where there is no contribution to momentum flux from collisions due to the operational regime of a dilute gas[24]. These are given by

$$T = \langle \frac{m}{3k_b N} \left[\sum_i^N (|\mathbf{v}_i'|^2) \right] \rangle$$

$$\boldsymbol{\sigma} = \langle \frac{\rho}{N} \sum_i^N \left[\mathbf{v}_i' \otimes \mathbf{v}_i' \right] \rangle \tag{3.4}$$

In these expression, $\mathbf{v}_i'$ denotes thermal velocity (i.e., the difference between the particle velocity and the mean velocity of flow) of particle i, N denotes number of simulated atoms and an angular bracket denotes an ensemble average over multiple simulations initialized at same macroscopic equilibrium conditions with varying random seeds for initial positions and velocities.

To make sure that OMD system is out of its transient regime, it is run for sufficient

time so that the externally imposed velocity gradient is properly set up in the simulations. This is evident from Fig. 3.2(a) which shows the OMD and analytical velocity field in $x_1 - x_2$ plane. To extract this field from simulations, the fundamental domain is discretized into spatial bins in $\mathbf{e}_2$ direction and velocities of all the atoms in a bin are averaged to obtain local velocity vector. Close agreement between two shows that the flow is fully developed in the simulations.

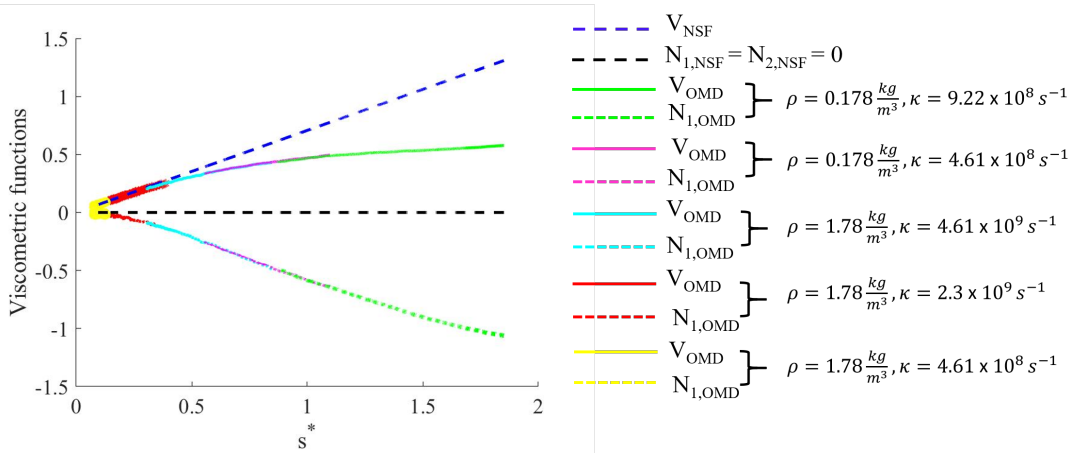

(a)

Figure 3.1: Comparison of viscometric functions for various combination of (ρ, κ)

When a general fluid undergoes motion of simple shear, it can be shown that the constitutive response of the stress is completely characterized by three dimensionless viscometric functions given by

$$\begin{aligned} N_1 &= N_1(s^*(t)) = -(\sigma_{11} - \sigma_{22})/p \\ N_2 &= N_2(s^*(t)) = -(\sigma_{22} - \sigma_{33})/p \\ V &= V(s^*(t)) = -\sigma_{12}/p \end{aligned} \tag{3.5}$$

where first two viscometric functions are associated with the normal stresses present in the system and the third viscometric function corresponds to nonlinear transport in shearing. A comparison of NSF and OMD evolutions of the viscometric functions are plotted in Fig. 3.1 against the breakdown parameter s^* given by the ratio of shear rate

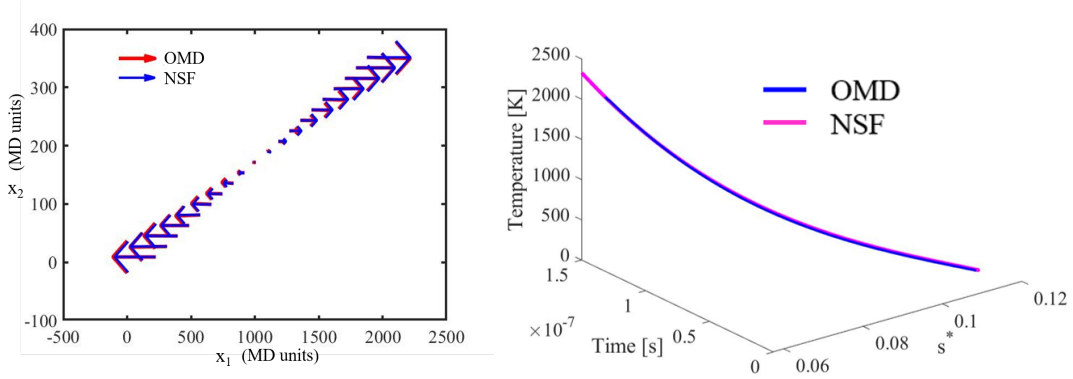

(a) (b)

Figure 3.2: Comparison between atomistic and continuum theory. (a) Velocity field map on x_3 plane ($\kappa = 1.84\text{x}10^{10}\text{s}^{-1},\ \rho = 0.178\text{kg/m}^3$) and (b) Evolution of temperature of gas in simple shear for $\kappa = 3.69\text{x}10^{8}\text{s}^{-1},\ \rho = 1.78\text{kg/m}^3$

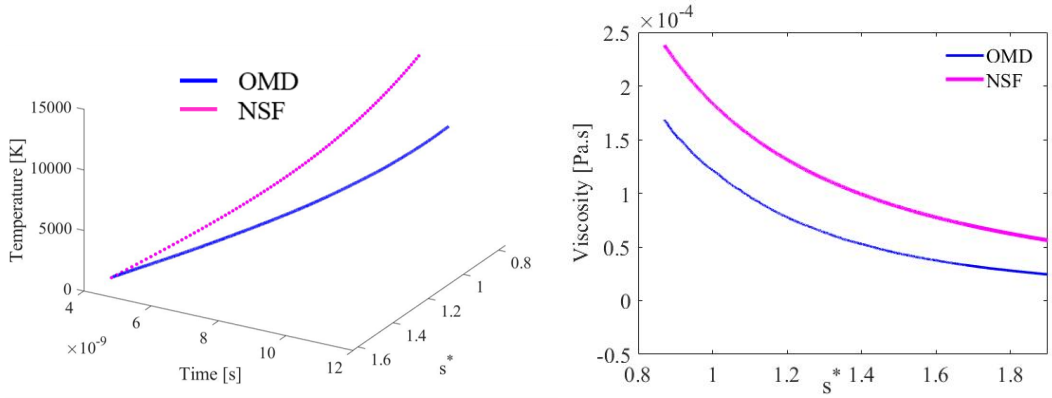

(a) (b)

Figure 3.3: Comparison between atomistic and continuum theory. (a) Evolution of temperature of gas in simple shear for $\kappa = 9.22\text{x}10^{8}\text{s}^{-1},\ \rho = 0.178\text{kg/m}^3$ (b) Comparison between effective μ and newtonian viscosity μ_{NSF} as a function of breakdown parameter for $\kappa = 9.22\text{x}10^{8}\text{s}^{-1}$.

and collision frequency of the gas.

$$s^*(t) = \frac{\sqrt{2}\kappa}{\nu(T(t))} = \frac{\sqrt{2}\kappa\mu_{\text{NSF}}(t)}{p(t)}$$

$$s^*(t) = \frac{|v_1|}{\sqrt{\gamma RT}} \frac{\mu_{\mathrm{NSF}}}{p} \sqrt{\frac{\pi RT}{2}} \frac{1}{|v_1|} \left| \frac{dv_1}{dx_2} \right| 2\sqrt{\frac{\gamma}{\pi}} = \mathrm{Ma_L} \frac{\lambda}{|v_1|} \left| \frac{dv_1}{dx_2} \right| 2\sqrt{\frac{\gamma}{\pi}} = \mathrm{Ma}_L \mathrm{Kn_{GLL}} 2\sqrt{\frac{\gamma}{\pi}} = \sqrt{2}\gamma \frac{\mathrm{Ma}_L^2}{\mathrm{Re}_L} \tag{3.6}$$

where ν is collision frequency of the gas, μ_{NSF} is LJ viscosity, consistent with NSF equations and λ is mean free path. It can be seen from Eq (3.6) that s^* can also be interpreted in terms which are more familiar in the literature of rarefied gas. s^* is equivalent to product of GLL Knudsen number [105, 106] where length scale is associated with the gradient of velocity and local Mach number. It shows that both the dimensionless numbers are required to classify the breakdown regime. Large values of $\mathrm{Ma_L Kn_{GLL}}$ or $\mathrm{Ma_L^2/Re_L}$ corresponds to a regime of transition and molecular flow where the NS relations are not valid. Note that $(|v_1|/\kappa)$ is used as an intrinsic length to define a local Reynolds number of the flow [107]. s^* is also referred to as local shear-stress Knudsen number in the literature. Ou et al. [108] conducted DSMC analysis of wall-bounded rarefied shear flows and also showed that shear stress Knudsen number is the only parameter which is needed to characterize the macroscopic flow profile and non-linear momentum transport in the bulk. This is in accordance with the finding presented here.

The collision frequency of the system increases with time due to an increase in temperature because of viscous dissipation, evident from energy balance equation (3.3). This results in decrease in s^*. In other words, as the simulation evolves, system comes closer to attaining a local equilibrium state. Fig. 3.1 shows evolution of viscometric functions for different combination of κ and ρ. The fact that all data points collapse onto a profile implies that the parameter s^* is capable of estimating in a unified way the degree of non-equilibrium in the gas for simple shear across various state points and rates. It is clearly observed that contrary to NSF, the first viscometric function predicted by OMD does not vanish whereas the second viscometric function is identically zero in both the theories. This finding clearly contradicts the assumption of coaxiality between principal direction of stress and the strain rate tensor assumed in NS model.

This behavior is also predicted by the solution of the Boltzmann equation for Maxwell molecules [49]. Also the NS theory predicts a higher value of shear stress as compared to OMD, as shown by the evolution of the third viscometric function V.

According to linear Newton's law, $V = s^*/\sqrt{2}$ (shown by dashed blue line in Fig. 3.1) which is in contrast to the behavior shown by gas. V is a highly non-linear function of s^* in this far-from-equilibrium regime considered. This provides an evidence of shear-thinning effect where effective viscosity defined by the ratio between shear stress and shear rate $\mu = \frac{\tau_{12}}{\kappa}$ is much smaller than the Newtonian viscosity $\mu_{\rm NSF}$ and is a function of shear rate κ as shown in Fig. 3.3(b).

Note that the variation of $\mu_{\rm NSF}$ and μ in Fig. 3.3(b) is due to evolution of temperature in the simulation. The shear rate κ remains constant in a simulation and is given by $\kappa = 4.6\text{x}10^9 s^{-1}$. As s^* decreases in the simulation, the OMD results (V, N_1, N_2, μ) converge to the NSF solution $(s^*/\sqrt{2}, 0, 0, \mu_{\rm NSF})$ for sufficiently long times as shown in Fig. 3.1. It also shows that for a constant shear rate κ, the discrepancy between the NS and OMD solutions increases as the gas becomes rarefied.

Figs. 3.2(b) and 3.3(a) show a comparison between NSF and OMD for a lower and higher value of the shear rate κ respectively. For relatively small κ where s^* is in the range $(0.05 - 0.12)$, the temperature evolution measured in the simulation agrees well with that predicted theoretically using NSF. On the other hand, for large shear rates there is significant discrepancy between the two. The NSF model predicts much higher temperature as compared to OMD. In such situations, NSF equations can be considered insufficient.

3.2.2 Pressure shear flow

In Figs. 3.4(a) and (b) OMD temperature profile evolution is compared with the NSF theory for an unsteady, compressible velocity field of the form.

$$\mathbf{v}(\mathbf{x}, t) = \frac{1}{1 + (\mathbf{a}\cdot\mathbf{n})t}(\mathbf{n}\cdot\mathbf{x})\mathbf{a} \tag{3.7}$$

This is achieved by choosing $\mathbf{A} = \mathbf{a}\otimes\mathbf{n}, \quad \mathbf{a}\cdot\mathbf{n} \neq 0$, where a particular case is selected: $\mathbf{a} = a\mathbf{e}_1, \quad \mathbf{n} = n_1 e_1 + n_2\mathbf{e}_2, \quad a n_{1,2} = \gamma_{1,2} > 0$. This flow reveals the competition between two effects: dilatation and shear. When dilatation dominates the thermal energy of the gas, the temperature decreases; and when the shear effect overpowers, the temperature of the system increases, as expected. (The "pressure-shear viscometer"[18]

is intended to produce such flows.) Different values of $\gamma_{1,2}$ are chosen for comparison with the NSF equation. For $\gamma_1 = \gamma_2 = 2.304 \times 10^8$ s^{-1}, temperature of the system drops and NSF and OMD agree very well. For $\gamma_1 = \gamma_2 = 2.30 \times 10^9$ s^{-1}, the NSF temperature rises. On the other hand, OMD predicts a continual decrease in temperature as shown in Fig. 3.4(b). Under high macroscopic flow gradient and rate, the gas exhibits such strong non-equilibrium behavior that its correct prediction is beyond the range of applicability of NSF. This qualitative failure of NSF motivates the development of higher order theory for highly non-equilibrium flows.

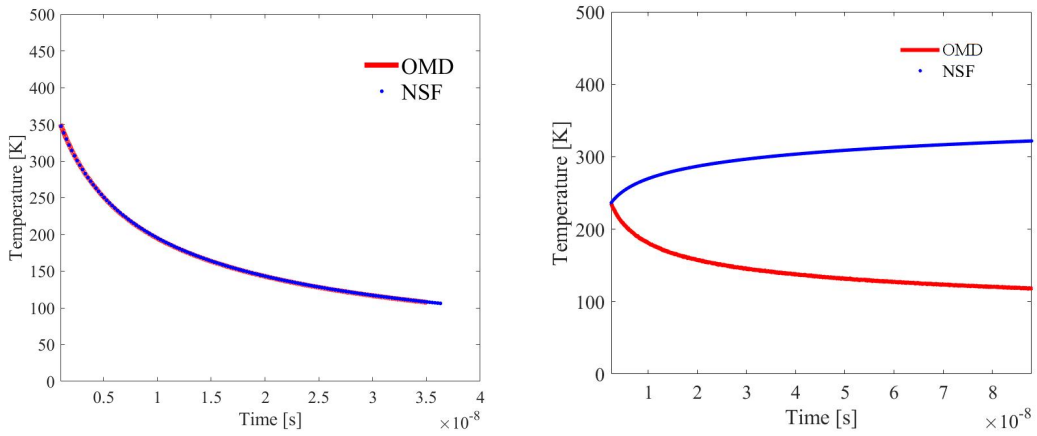

Figure 3.4: Comparison of temperature evolution of Lennard Jones argon gas for planar shear. (a)$\gamma_1 = \gamma_2 = 2.304 \times 10^8$ s^{-1}, (b) $\gamma_1 = \gamma_2 = 2.30 \times 10^9$ s^{-1}. Red line: OMD, Blue line: Navier–Stokes.

3.3 Failure of Reiner-Rivlin Model

A possible approach to an improved constitutive relation is the Reiner-Rivlin theory [102, 101]. That theory assumes the stress to be a function of deformation gradient and the velocity gradient. $\boldsymbol{\sigma} = f(\mathbf{F}, \nabla\mathbf{v})$. When the principle of material frame indifference in addition to the underlying symmetry of the proper unimodular group ($f(\mathbf{FU}, \nabla\mathbf{v}) =$

$f(\mathbf{F}, \nabla\mathbf{v})\ \forall\mathbf{U},\ \det\mathbf{U} = 1)$ is used, this dependence reduces to

$$\boldsymbol{\sigma} = \hat{\phi}_0(\rho, I_i(\mathbf{d}))\mathbf{I} + \hat{\phi}_1(\rho, I_i(\mathbf{d}))\mathbf{d} + \hat{\phi}_2(\rho, I_i(\mathbf{d}))\mathbf{d}^2 \tag{3.8}$$

where $\mathbf{d} = (\nabla\mathbf{v} + \nabla\mathbf{v}^T)/2$ and $\hat{\phi}_i$ are coefficients of invariants of tensor $\mathbf{d}$ and density of fluid. In contrast to NSF, this model incorporates the non-linearity by taking higher order term of the form $\mathbf{d}^2$ but the principle of material frame-indifference implies the collinearity of the stress tensor $\boldsymbol{\sigma}$ and $\mathbf{d}$. The Reiner-Rivlin form is investigated by simulating isochoric uniform simple shear flow where $\mathbf{A}$ is trace free, rank one tensor of the form $\mathbf{A} = \kappa\mathbf{e}_1 \otimes \mathbf{e}_2$, where flow is in $\mathbf{e}_1$ direction, velocity gradient along $\mathbf{e}_2$ direction and κ is shear rate. Eigenvectors of $\mathbf{d}$ for such flow are uniform in space. Fig. 3.6 compares the evolution of angle $(\theta_{\sigma 1}, \theta_{\sigma 2}, \theta_{\sigma 3}),\ (\theta_{d1} = 45°, \theta_{d2} = 135°, \theta_{d3} = 90°)$ enclosed by $\mathbf{e}_1$ direction with the eigenvectors of $\boldsymbol{\sigma}(\sigma 1, \sigma_2, \sigma_3)$, computed from OMD simulations and eigenvectors of $\mathbf{d}$ (d_1, d_2, d_3) for simple shear flow. The comparison clearly shows the space independent lagging $(\theta_{\sigma_{1,2}} - \theta_{\mathbf{d}_{1,2}} \approx 30°)$ between two tensors $\boldsymbol{\sigma}$ and $\mathbf{d}$ which is in contrast to the Reiner-Rivlin and Navier Stokes theories.

This inadequacy is also supported by the evolution of the molecular density function $f(t, \mathbf{y}, \mathbf{v})$ of the kinetic theory of gases. f represents the probability density of finding an atom with velocity $\mathbf{v}$ in a small neighborhood of $\mathbf{y}$ at time t, in Eulerian form. The Boltzmann Equation is a nonlinear integral-differential equation that represents the time evolution of distribution function f in one particle phase space which can also be derived with the more general Liouville Equation. The OMD assumption in MD has a direct analog for the Boltzmann equation, corresponding precisely to homoenergetic solutions [18, 109, 110, 111]. To understand this connection, an OMD simulation with the time-dependent translation group is considered as above, and the statistics of the MD solutions is examined. Draw a ball B_0 of any diameter centered at the origin. Now choose integers ν_1, ν_2, ν_3 and draw a ball B_ν of the same diameter centered at $\mathbf{y} = (\mathbf{I} + t\mathbf{A})(\nu_1\mathbf{e}_1 + \nu_2\mathbf{e}_2 + \nu_3\mathbf{e}_3)$. Since the simulated atoms quickly diffuse into the nonsimulated atoms during a simulation, it is not unusual that B_0 and B_ν at any particular time contain some simulated atoms and some nonsimulated atoms. The velocities of atoms in B_0 and B_ν are different. Nevertheless, if one knows the velocities of atoms in B_0, then one can calculate by explicit formulas the velocities of atoms in B_ν.

But, based on its interpretation, this must imply an ansatz for the molecular density function f. It is

$$f(t, \mathbf{x}, \mathbf{v}) = g(t, \mathbf{v} - \mathbf{A}(\mathbf{I} + t\mathbf{A})^1\mathbf{x}) = g(t, \mathbf{w}) \tag{3.9}$$

On substituting this OMD ansatz into the general form of the Boltzmann equation, one obtains an exact reduction to an equation for $g(t, \mathbf{w})$. Here, $\mathbf{w}$ is nothing but thermal velocity where mean velocity $(\mathbf{A}(\mathbf{I} + t\mathbf{A})^{-1}\mathbf{x})$ is subtracted off from the velocity $\mathbf{v}$.

In the limit of near-equilibrium limit, Chapman-Enskog (CE) analyis leads to CE density function which reduces conservation equations to Navier Stokes equations. CE density function (DF) for OMD flows in terms of viscous stress tensor is written as [24]

$$g(\mathbf{w}) = g_0(\mathbf{w})(1 + \Phi(\mathbf{w}))$$

where

$$\Phi(\mathbf{w}) = \frac{-m}{pkT}[\tau_{12}w_1w_2 + \tau_{13}w_1w_3 + \tau_{23}w_2w_3 + \frac{1}{2}\tau_{11}(w_1^2 - w_3^2) + \frac{1}{2}\tau_{22}(w_2^2 - w_3^2)]$$

$$g_0(\mathbf{w}) = \frac{m}{(2\pi kT)^{3/2}} \exp\left(\frac{-m}{2kT}(w_1^2 + w_2^2 + w_3^2)\right)$$

In-plane DF is obtained by averaging over all the thermal velocities in $\mathbf{e}_3$ direction. This leads to

$$g(w_1, w_2) = \frac{0.0635m}{k^2pT^2} \exp\Big(-\frac{m}{2kT}(w_1^2 + w_2^2)\Big)\Big(2.506kpT +$$
$$(1.253(kT - mw_1^2)\tau_{11} - 2.506mw_1w_2\tau_{12} + 1.253(kT - mw_2^2)\tau_{22}\Big)$$

This CE density function further reduces for uniform simple-shear OMD flows to

$$g(w_1, w_2) = \frac{0.0635m}{k^2pT^2} \exp\Big(-\frac{m}{2kT}(w_1^2 + w_2^2)\Big)2.506\Big(kpT - mw_1w_2\tau_{12}\Big) \tag{3.10}$$

where $\tau_{ii} = 0$ and $\tau_{12} = \mu_{\text{NSF}}\kappa$

In Fig. 3.5(a) this reduced density function g is plotted in $w_1 - w_2$ plane at $t =$ 1.62x10^{9}s for $\kappa =$ 4.6x10^{9}s^{-1}. Large shear rate has been chosen to eliminate noise in the system and hence make the feature apparent. Dashed red and solid black lines

points along in-plane eigen vectors $(\Lambda_{\sigma_2}, \Lambda_{d_2})$ corresponding to eigen values (σ_2 and d_2) of OMD computed stress tensor $\boldsymbol{\sigma}$ and $\mathbf{d}$ respectively. The maximum of the density function is achieved along $x = |y|(\theta_{d_2} = 45°, \theta_{d_2} = 135°)$ line. This indicates presence of shear stress τ_{12} in accordance with the Boltzmann definition of the stress tensor based on thermal velocity. This also verifies the underlying assumption of collinearity of stress tensor $\boldsymbol{\sigma}$ and strain rate tensor $\mathbf{d}$ inherent in Navier-Stokes relation and hence is reflected in near-equilibrium CE analysis derived density.

Fig. 3.5(b) plots the distribution function computed from OMD simulation which shows the inability of CE type distribution to describe the correct statistics of atoms under highly non-equilibrium conditions. It is obtained by discretizing the $\mathrm{w}_1 - \mathrm{w}_2$ plane into small bins and analyzing the statistics of simulated atoms in the fundametal domain. The OMD computed distribution is qualitatively very different than CE and also shows the existence of ellipticity which is alligned along eigen vector of stress tensor $(\theta_{\sigma_2} \approx 165°)$ computed using (3.4) and hence indicates lagging in $\mathrm{w}_1 - \mathrm{w}_2$ plane confirming the failure of collinearity assumption. Thus the assumption underlying Reiner-Rivlin constitutive equation that the stress tensor is, apart from hydrostatic pressure, a function of velocity gradient only is not generally valid for dilute gas under large rates. A theory which could relax this assumption will be more suitable for deriving accurate constitutive relations.

3.4 Rivlin-Ericksen Constitutive Model

The Rivlin-Ericksen (RE) model [102], which is more general than the Reiner-Rivlin relation, assumes the stress to be dependent on the deformation gradient, velocity gradient, acceleration gradient, etc. Intuitively, it can capture the dependence of the state of the fluid on past collisions, not captured by the velocity gradient alone. In general, a fluid where stress depends on only finite number of these time derivatives is called "fluid of differential type". If the fluid is assumed to be isotropic, possesing material symmetry of unimodular group, $(G = SL(3))$ then the Principle of Frame Indifference leads to the conclusion that stress must depend on the density ρ and and time derivatives of the deformation gradient through the objective Rivlin-Ericksen tensors $\mathbf{A}_1, \mathbf{A}_2, ...$ defined

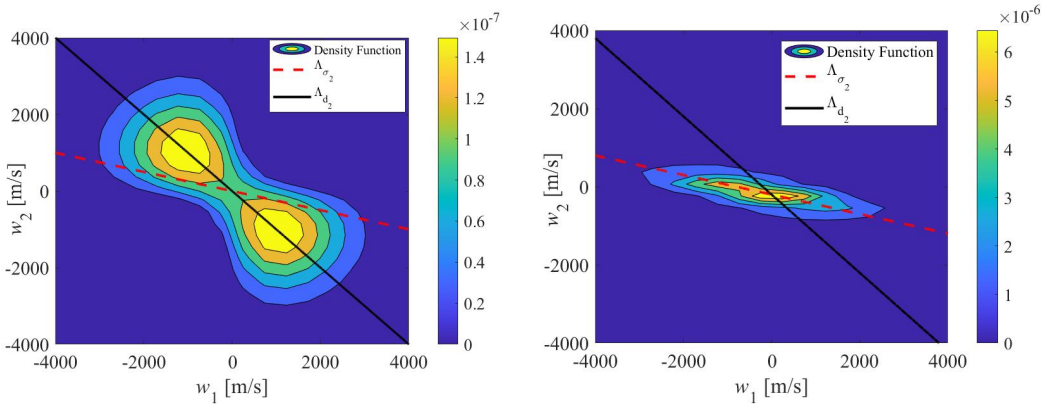

Figure 3.5: Snapshot of (a) Chapman-Enskog (b) OMD reduced velocity distribution function $g(\mathrm{w}_1, \mathrm{w}_2)$. Red and black solid lines points along in-plane eigen vectors corresponding to eigen values (σ_2 and d_2) of OMD computed stress tensor (σ) and strain rate tensor $\mathbf{d}$.

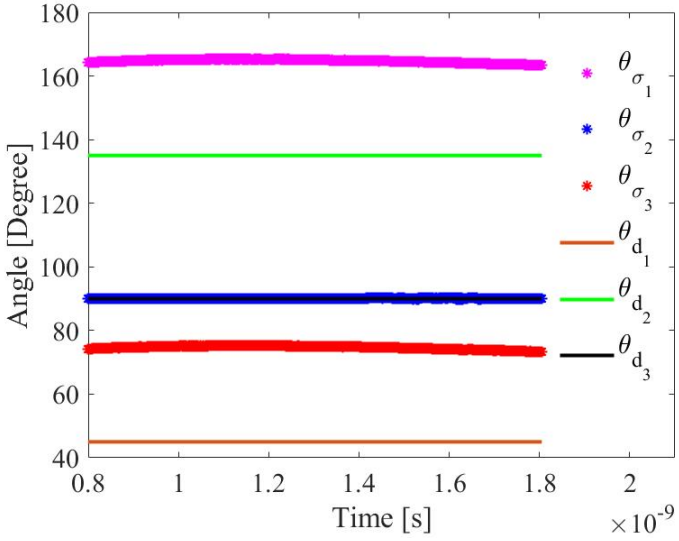

Figure 3.6: Time evolution of the angle enclosed by eigen vectors of stress tensor $\boldsymbol{\sigma}$ and $\mathbf{d}$ with $\mathbf{e}_1$.

by

$$\mathbf{A}_i = \partial^i(\mathbf{F}_t(\tau)^{\mathrm{T}}\mathbf{F}_t(\tau))/\partial\tau^i|_{\tau=t},$$

where $\mathbf{F}_t(\tau)$ is the relative deformation gradient. The Rivlin-Ericksen tensors satisfy the recursive relation

$$\mathbf{A}_1 = \nabla\mathbf{v} + \nabla\mathbf{v}^{\mathrm{T}}, \quad \mathbf{A}_n = \dot{\mathbf{A}}_{n-1} + (\nabla\mathbf{v})^{\mathrm{T}}\mathbf{A}_{n-1} + \mathbf{A}_{n-1}(\nabla\mathbf{v}), \tag{3.11}$$

where the dot denotes the material time derivative. The physical dimension of $\mathbf{A}_n$ are T^{-n}.

Thus, the stress tensor $\boldsymbol{\sigma}$ is expressible as an isotropic tensor function of Rivlin-Ericksen tensors $\mathbf{A}_1, \mathbf{A}_2, ..., \mathbf{A}_n$

$$\boldsymbol{\sigma} = f(\rho, \mathbf{A}_1, \mathbf{A}_2, \mathbf{A}_3, ...)$$

This reduces to Reiner-Rivlin theory by setting $n = 1$. There is also a relation between RE theory and constitutive models of materials with memory [112] which is given by

$$\boldsymbol{\sigma} = \mathbf{F}(t)\phi\{\mathbf{C}(s)\}\mathbf{F}^{\mathrm{T}}(s) \quad -\infty < s \leq t \tag{3.12}$$

where $\mathbf{C}(s) = \mathbf{F}_t^{\mathrm{T}}(s)\mathbf{F}_t(s)$ is the Cauchy strain at time s. The constitutive Eq. (3.12) accounts for the dependence on the full past history of deformation and temperature. Its connection with RE model comes from the hypothesis that for sufficiently smooth history of deformation, $\mathbf{C}(s)$ can be expanded as Taylor series about time t at which the stress is measured, and for the fluid with instantaneous memory which does not exhibit gradual stress relaxation (for e.g., a dilute gas considered in this work) (3.12) can be expressed in terms of the instantaneous values of deformation gradient matrix and its time derivatives and hence the Rivlin-Ericksen tensors. Thus, for a properly invariant constitutive relation that embodies the dependence of the past history of deformation on the present, the RE model is quite general.

An interesting feature of OMD flows is that these satisfy $\mathbf{A}_i = 0$ for order three and higher ($i \geq 3$), a feature shared by some viscometric flows as well [87]. (Generally, OMD flows and viscometric flows are different.) Rivlin noticed this reduction to find some exact solutions for simple shearing and torsional flow[113]. Viscometric flows are

widely used in experimental research to find viscometric functions which can characterize complex fluid behavior and determine its fundamental properties. Unlike OMD flows, not all viscometric flows are exact solutions of the equations of motion. Also there doesn't exist an exact atomistic analogue for viscometric flows except simple shearing, which is also an OMD flow. The reduction of differential type constitutive relations for affine velocity fields was noticed earlier by C. Bird et al. [114] but its connection with atomic level theory dealt in this work has remained unnoticed in the field. For rigorous definitions of viscometric flows, reader is referred to literature by Coleman and Noll et al. [87]. In view of these facts it is believed that the OMD flows have been underutilized both theoretically and experimentally.

In this work the stress tensor is assumed to have a representation of the form

$$\boldsymbol{\sigma} = p\mathbf{I} + \tilde{f}(\rho, \mathbf{A}_1, \mathbf{A}_2)$$

$$\begin{aligned}\boldsymbol{\sigma} = p\mathbf{I} + \mu\mathbf{A}_1 + \alpha_1\mathbf{A}_2 + \alpha_2\mathbf{A}_1^2 + \alpha_3\mathbf{A}_2^2 + \alpha_4(\mathbf{A}_1\mathbf{A}_2 + \mathbf{A}_2\mathbf{A}_1) \\ +\alpha_5(\mathbf{A}_1^2\mathbf{A}_2 + \mathbf{A}_2\mathbf{A}_1^2) + \alpha_6(\mathbf{A}_1\mathbf{A}_2^2 + \mathbf{A}_2^2\mathbf{A}_1) + \alpha_7(\mathbf{A}_1^2\mathbf{A}_2^2 + \mathbf{A}_2^2\mathbf{A}_1^2),\end{aligned} \tag{3.13}$$

where α_i is a scalar function of the invariants of $\mathbf{A}_1$ and $\mathbf{A}_2$. $\mathbf{A}_2$ for OMD flows simplifies to

$$\begin{aligned}\mathbf{A}_2 = \dot{\mathbf{A}}_1 + (\nabla\mathbf{v})^{\mathrm{T}}\mathbf{A}_1 + \mathbf{A}_1(\nabla\mathbf{v}) = -(\nabla\mathbf{v})(\nabla\mathbf{v}) - (\nabla\mathbf{v})^{\mathrm{T}}(\nabla\mathbf{v})^{\mathrm{T}} \\ +(\nabla\mathbf{v})^{\mathrm{T}}(\nabla\mathbf{v} + \nabla\mathbf{v}^{\mathrm{T}}) + (\nabla\mathbf{v} + \nabla\mathbf{v}^{\mathrm{T}})(\nabla\mathbf{v}) = 2(\nabla\mathbf{v})^{\mathrm{T}}(\nabla\mathbf{v})\end{aligned} \tag{3.14}$$

These simplifications reduce the viscous stress tensor to

$$\boldsymbol{\tau} = -(\boldsymbol{\sigma} - (\mathrm{tr}(\boldsymbol{\sigma})/3)\mathbf{I}) = -(\sigma - p\mathbf{I}),$$

$$\begin{aligned}\boldsymbol{\tau} = \mu[\mathbf{A}_1 - \frac{\mathrm{tr}(\mathbf{A}_1)}{3}\mathbf{I}] + \alpha_1[\mathbf{A}_2 - \frac{\mathrm{tr}(\mathbf{A}_2)}{3}\mathbf{I}] + \alpha_2[\mathbf{A}_1^2 - \frac{\mathrm{tr}(\mathbf{A}_1^2)}{3}\mathbf{I}] \\ +\alpha_3[\mathbf{A}_2^2 - \frac{\mathrm{tr}(\mathbf{A}_2^2)}{3}\mathbf{I}] + \alpha_4[(\mathbf{A}_1\mathbf{A}_2 + \mathbf{A}_2\mathbf{A}_1) - \frac{\mathrm{tr}(\mathbf{A}_1\mathbf{A}_2 + \mathbf{A}_2\mathbf{A}_1)}{3}\mathbf{I}] \\ +\alpha_5[(\mathbf{A}_1^2\mathbf{A}_2 + \mathbf{A}_2\mathbf{A}_1^2) - \frac{\mathrm{tr}(\mathbf{A}_1^2\mathbf{A}_2 + \mathbf{A}_2\mathbf{A}_1^2)}{3}\mathbf{I}] \\ +\alpha_6[(\mathbf{A}_1\mathbf{A}_2^2 + \mathbf{A}_2^2\mathbf{A}_1) - \frac{\mathrm{tr}(\mathbf{A}_1\mathbf{A}_2^2 + \mathbf{A}_2^2\mathbf{A}_1)}{3}\mathbf{I}] \\ +\alpha_7[(\mathbf{A}_1^2\mathbf{A}_2^2 + \mathbf{A}_2^2\mathbf{A}_1^2) - \frac{\mathrm{tr}(\mathbf{A}_1^2\mathbf{A}_2^2 + \mathbf{A}_2^2\mathbf{A}_1^2)}{3}\mathbf{I}] \end{aligned} \tag{3.15}$$

where p is the pressure given by the equation of state $p = \rho RT$, R is the gas constant and T is the temperature. The condition $\alpha_i = 0$ reduces this solution to Newton's viscosity law, where stress is linearly proportional to strain rate, given by

$$\boldsymbol{\tau} = 2\mu\mathbf{E}, \quad \mathbf{E} = \frac{1}{2}(\mathbf{A}_1 - \frac{\mathrm{tr}(\mathbf{A}_1)}{3}\mathbf{I}) = \frac{1}{2}(\nabla\mathbf{u} + \nabla\mathbf{u}^T) - \frac{1}{3}\nabla\cdot\mathbf{u}$$

Since τ is tracefree, it reduces to only six independent terms of the form

$$\boldsymbol{\tau} = \alpha_i\mathbf{S}_i$$

where the $\mathbf{S}_i$ form an orthogonal basis of the form: $\mathbf{S}_1 = \mathbf{e}_1 \otimes \mathbf{e}_2 + \mathbf{e}_2 \otimes \mathbf{e}_1$, $\mathbf{S}_2 = \mathbf{e}_1 \otimes \mathbf{e}_3 + \mathbf{e}_3 \otimes \mathbf{e}_1$, $\mathbf{S}_3 = \mathbf{e}_2 \otimes \mathbf{e}_3 + \mathbf{e}_3 \otimes \mathbf{e}_2$, $\mathbf{S}_4 = \mathbf{e}_1 \otimes \mathbf{e}_1$, $\mathbf{S}_5 = \mathbf{e}_2 \otimes \mathbf{e}_2$, $\mathbf{S}_6 = \mathbf{e}_3 \otimes \mathbf{e}_3$ and $\mathbf{S}_i\mathbf{S}_j = \delta_{ij}$.

3.4.1 Simple shear

For simple shear the Rivlin-Ericksen tensors are given by

$$\mathbf{A}_1 = \kappa\mathbf{e}_1 \otimes \mathbf{e}_2 + \kappa\mathbf{e}_2 \otimes \mathbf{e}_1, \quad \mathbf{A}_2 = 2\kappa^2\mathbf{e}_2 \otimes \mathbf{e}_2$$

Substitution of these tensors in (3.15) reduces viscous stress to

$$\boldsymbol{\tau} = (\kappa\mu + 2\kappa^3\alpha_4 + 4\kappa^5\alpha_6)\mathbf{S}_1 + (\frac{-2}{3}\kappa^2\alpha_1 + \frac{1}{3}\kappa^2\alpha_2 - \frac{2}{3}\kappa^4\alpha_3 - \frac{2}{3}\kappa^4\alpha_5 - \frac{8}{3}\kappa^6\alpha_7)\mathbf{S}_4$$
$$+(\frac{4}{3}\kappa^2\alpha_1+\frac{1}{3}\kappa^2\alpha_2+\frac{8}{3}\kappa^4\alpha_3+\frac{8}{3}\kappa^4\alpha_5+\frac{16}{3}\kappa^6\alpha_7)\mathbf{S}_5+(-\frac{2}{3}\kappa^2\alpha_1+-\frac{2}{3}\kappa^2\alpha_2-\frac{4}{3}\kappa^4\alpha_4-\frac{4}{3}\kappa^4\alpha_5-\frac{8}{3}\kappa^6\alpha_7)\mathbf{S}_6 \tag{3.16}$$

where the matrix forms are given by: $\mathbf{S}_1 = \mathbf{e}_1 \otimes \mathbf{e}_2 + \mathbf{e}_2 \otimes \mathbf{e}_1$, $\mathbf{S}_2 = \mathbf{e}_1 \otimes \mathbf{e}_3 + \mathbf{e}_3 \otimes \mathbf{e}_1$, $\mathbf{S}_3 = \mathbf{e}_2\otimes\mathbf{e}_3+\mathbf{e}_3\otimes\mathbf{e}_2$, $\mathbf{S}_4 = \mathbf{e}_1\otimes\mathbf{e}_1$, $\mathbf{S}_5 = \mathbf{e}_2\otimes\mathbf{e}_2$, $\mathbf{S}_6 = \mathbf{e}_3\otimes\mathbf{e}_3$, $\mathbf{S}_i \cdot \mathbf{S}_j = \delta_{ij}$. It is shown in the section 3.2.1 that the second viscometric function is identically zero in simple shear. This observation is used to find relations between different α_i which are given by

$$\tau_{22} = \tau_{33} \quad \Longrightarrow \ (\boldsymbol{\tau}\cdot\mathbf{S}_5 - \boldsymbol{\tau}\cdot\mathbf{S}_6) = \mathbf{0}$$

$$\kappa^2(2\alpha_1 + \alpha_2) + \kappa^4(4\alpha_3 + 4\alpha_5) + \kappa^6(8\alpha_7) = 0$$

$$\Longrightarrow \ \alpha_2 = -2\alpha_1, \quad \alpha_5 = -\alpha_3, \quad \alpha_7 = 0$$

Further assumptions is introduced by setting both coefficients α_4 and α_6 to zero. These constraints reduces eq (3.16) to the final form

$$\boldsymbol{\tau} = (\kappa\mu)\mathbf{S}_1 + (\frac{-4}{3}\kappa^2\alpha_1)\mathbf{S}_4 + (\frac{2}{3}\kappa^2\alpha_1)\mathbf{S}_5 + (\frac{2}{3}\kappa^2\alpha_1)\mathbf{S}_6 \tag{3.17}$$

In this flow, contributions of coefficients α_3 and α_5 are not present due to the identity

$$(\mathbf{A}_1^2\mathbf{A}_2 + \mathbf{A}_2\mathbf{A}_1^2) - \mathbf{A}_2^2 = 0.$$

Note that this behavior may not be general to other flows. Equation (3.17) is made dimensionless by introducing appropriate variables and parameters defined by

$$|\boldsymbol{\tau}|^* = \frac{|\boldsymbol{\tau}|}{p}, \quad \mu^* = \frac{\mu}{\mu_{\mathrm{NSF}}}, \quad \kappa^* = \frac{\kappa}{\nu} = \frac{\kappa\mu_{\mathrm{NSF}}}{p}, \quad \alpha_1^* = \frac{p\alpha_1}{\mu_{\mathrm{NSF}}^2}$$

where $p = \frac{1}{3}\,\mathrm{tr}(\boldsymbol{\sigma})$ is thermodynamic pressure given by equation of state $p = \rho RT$. The reduced viscous stress tensor then becomes

$$\boldsymbol{\tau}^* = (\kappa^*\mu^*)\mathbf{S}_1 + (\frac{-4}{3}\kappa^{*2}\alpha_1^*)\mathbf{S}_4 + (\frac{2}{3}\kappa^{*2}\alpha_1^*)\mathbf{S}_5 + (\frac{2}{3}\kappa^{*2}\alpha_1^*)\mathbf{S}_6 \tag{3.18}$$

Taking the inner-product of eq (3.18) with $\mathbf{S}_1$ and $\mathbf{S}_4$ provides value of μ^* and α_1^* respectively. These are given by

$$\mu^* = \frac{\tau_{12}^*}{\kappa^*}, \quad \alpha_1^* = \frac{-3}{4}\frac{\tau_{11}^*}{\kappa^{*2}} = \frac{3}{2}\frac{\tau_{22}^*}{\kappa^{*2}}$$

These coefficients are computed from OMD solutions of viscous stresses for various combinations of ρ, κ and are fitted against the breakdown parameter s^* to forms given by

$$\mu^* = \frac{1}{1 + c_1(s^*)^{c_2}} \quad \alpha_1^* = \frac{1}{2}(c_3 + c_4(s^*)^{c_5})^{c_6},$$

where $c_1 = 1/2, c_2 = 3/2, c_3 = 0.4766, c_4 = 0.4599, c_5 = 1.7714,$ and $c_6 = -0.8920$ for LJ potential model. The fitting parameters are assumed to be universal and independent of the state point of the gas. Fig. 3.7 shows the suitability of the functional form chosen by comparing the fitted data with the OMD evolution of μ^* and α_1^* as a function of s^*. These coefficients are used to provide final form of non-linear constitutive model given by:

$$\boldsymbol{\tau}^* = \frac{\kappa^*}{1 + c_1(s^*)^{c_2}}\mathbf{S}_1 - \frac{2}{3}\kappa^{*2}(c_3 + c_4(s^*)^{c_5})^{c_6}\mathbf{S}_4 + \frac{1}{3}\kappa^{*2}(c_3 + c_4(s^*)^{c_5})^{c_6}\mathbf{S}_5 + \frac{1}{3}\kappa^{*2}(c_3 + c_4(s^*)^{c_5})^{c_6}\mathbf{S}_6 \tag{3.19}$$

The motivation behind these specific choices of the functional forms comes from Maxwell's differential system for the evolution of second moments of velocity distribution function [107]. It is given by

$$\dot{\tau}_{ij} + \tau_{ij}\mathbf{v}_{k,k} - \frac{2}{3}\tau_{kl}\mathbf{E}_{kl}\delta_{ij} + \tau_{ki}\mathbf{v}_{j,k} + \tau_{kj}\mathbf{v}_{i,k} + (\mathbf{M}_{ijk} - \frac{2}{3}\mathbf{q}_k\delta_{ij})_{,k} + 2p\mathbf{E}_{ij} = -\nu\tau_{ij} \tag{3.20}$$

where $\nu = \frac{p}{\mu_{\mathrm{NSF}}}$ for Maxwellian molecules (the production terms of moment equation (3.20) can be evaluated without knowing the phase density and can be expressed explicitly in terms of moments). $\mathbf{M}_{ijk}$ is a moment of order three and $\mathbf{E} = \frac{1}{2}(\nabla\mathbf{v} + \nabla\mathbf{v}^T) -$

$\frac{1}{3}(\nabla \cdot \mathbf{v})\mathbf{I}$. For OMD flows, $\mathbf{q}$ vanishes identically and moments of order 2, 3 and higher are functions of time only. When substituted with this ansatz, (3.20) reduces to a closed system of six ordinary differential equations for τ_{ij} [107]:

$$\frac{1}{\nu}\dot{p} + \frac{\sqrt{2}}{3}s^*\tau_{12} = 0, \quad \frac{1}{\nu}\dot{\tau}_{12} + \tau_{12} + \frac{s^*}{\sqrt{2}}(p + \tau_{22}) = 0$$

$$\frac{1}{\nu}\dot{\tau}_{22} + \tau_{22} - \frac{\sqrt{2}}{3}s^*\tau_{12} = 0, \quad \frac{1}{\nu}\dot{\tau}_{11} + \tau_{11} + \frac{\sqrt{2}}{3}s^*(\tau_{12}) = 0$$

$$\frac{1}{\nu}\dot{\tau}_{13} + \tau_{13} + \frac{s^*}{\sqrt{2}}\tau_{23} = 0, \quad \frac{1}{\nu}\dot{\tau}_{23} + \tau_{23} = 0 \tag{3.21}$$

Further, it is assumed that nonconserved variables have already attained steady state .i.e., $\dot{\tau}_{ij} = 0$. The similar closure condition is also used to develop nonlinear coupled constitutive relation by Myong et al. [42]. This is based on the adiabatic approximation of Eu et al. [115, 41, 116] which comes from the observation of widely separated time scale evolution of conserved and nonconserved variables. In these studies it was seen that higher-order moments decay faster than the conserved variable. This is well characterized by sufficiently high Deborah number De which is proportional to s^*, defined by the ratio of time scale of fluid relaxation and time scale of external loading. With high deformation rate, one operates in the regime where gas follow this non-Newtonian behavior. Therefore, in the hydrodynamic time scale, following algebraic type equations for τ_{ij} is achieved:

$$\tau_{12}^* = \frac{\kappa^*}{1 + \frac{1}{3}s^{*2}}, \quad \tau_{22}^* = \frac{2}{3}\kappa^{*2}(1 + \frac{1}{3}s^{*2})^{-1}, \quad \tau_{11} = -2(\tau_{22} = \tau_{33}) \tag{3.22}$$

The similarity between equations (3.19) and (3.22) shows the connection between RE theory and moment method applied to the Boltzmann equation for a gas composed of molecules interacting by an inverse-fifth power law of force (Maxwellian molecules) in simple shear. This connection serves as an inspiration for the specific functional forms of coefficients μ and α_1 chosen in RE model. However, RE theory for LJ gas is more general since the coefficients μ and α_1 are not identical in contrast to kinetic theory of Maxwellian molecules. The final RE constitutive relation for viscous stress is given by

$$\boldsymbol{\tau} = (\mu_{\mathrm{NSF}})\mu^*[\mathbf{A}_1 - \frac{\mathrm{tr}(\mathbf{A}_1)}{3}\mathbf{I}] + \frac{(\mu_{\mathrm{NSF}})^2}{p}\alpha_1^*[\mathbf{A}_2 - 2\mathbf{A}_1^2 - (\frac{\mathrm{tr}(\mathbf{A}_2)}{3} - \frac{\mathrm{tr}(2\mathbf{A}_1^2)}{3})\mathbf{I}]$$
$$\mu^* = \frac{1}{1 + c_1(s^*)^{c_2}}, \quad \alpha_1^* = \frac{1}{2}(c_3 + c_4(s^*)^{c_5})^{c_6} \tag{3.23}$$

The first term in Eq (3.23) introduces the generalized viscosity μ which has a correction factor of the form $1/(1+c_1(s^*)^{c_2})$ to capture viscosity thinning effect. On the other hand, second term in the above equation accounts for the non-coaxiality of principal direction of stress and the strain rate tensor, observed in high GLL Knudsen and local Mach number regime. When s^* is sufficiently small such that near equilibrium description is valid, μ converges to μ_{NSF} and the contribution of second term vanishes retrieving Navier-Stokes constitutive model.

Fig. 3.8 shows the evolution of viscous stresses τ_{12}, τ_{11} and τ_{22} as a function of time for shear rate of $\kappa = 1.84\text{x}10^9$. It is clearly observed from the comparison that the Rivlin-Ericksen (RE) model agree with the predictions of OMD fairly well up to large deformation rates as compared to Navier-Stokes theory which predicts presence of considerably high viscous stress in the system. Fig. 3.9 also backs the suitability of RE model. It shows the temperature evolution of the gas under the conditions where NSF was shown to fail in Sec 3.2.1. It shows that RE model works remarkably well and yields true behavior of gas in contrast to NSF for simple shear.

Next, the calibration done in this section is extended to include a bigger family of multi-axial general in-compressible and compressible flows.

3.4.2 Incompressible flows

The definition of unified variable s^* proposed in the previous section is generalized to define the non-equilibrium physics of OMD family of incompressible flows. A breakdown parameter is introduced that takes into account the presence of multi-axial gradients in

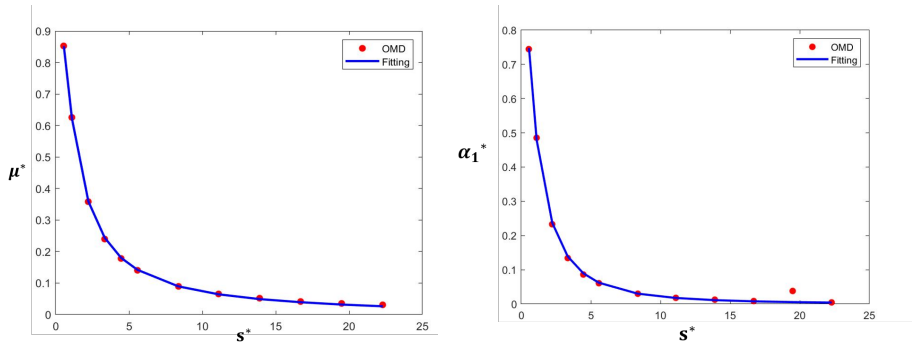

(a) (b)

Figure 3.7: Fitting of the coefficients of Rivlin-Ericksen model for LJ argon gas under simple shear. (a) μ^* (b) α_1^*.

the flow. It is defined in terms of the second invariant of $\mathbf{A}_1$ by

$$s^* = \frac{\sqrt{([\mathbf{A}_1 - \frac{\mathrm{tr}(\mathbf{A}_1)}{3}\mathbf{I}] : [\mathbf{A}_1 - \frac{\mathrm{tr}(\mathbf{A}_1)}{3}\mathbf{I}])}}{\nu} = \frac{2|\mathbf{E}|}{\nu}. \tag{3.24}$$

where $|\mathbf{E}|$ denotes Frobenius norm of strain rate tensor $\mathbf{E}$. This parameter s^* characterizes the failure of NSF and it is equivalent to Truncation number Tr defined by Truesdell et al.[107]:

$$\mathrm{Tr} = \sqrt{2}\frac{|\mathbf{E}|}{\nu} = \sqrt{2}\frac{\mu}{p}|\mathbf{E}| = \frac{s^*}{\sqrt{2}}.$$

s^* serves as a dimensionless measure of the rate of dissipation of energy through distortion according to classical fluid mechanics as given by the second term on the right hand side of entropy generation equation.

$$\begin{aligned} \rho T\dot{\eta} &= (\lambda + \frac{2}{3}\mu)(\nabla\cdot\mathbf{v})^2 - \sigma\cdot\mathbf{E} - \mathrm{div}\mathbf{q} \\ &= (\lambda + \frac{2}{3}\mu)(\nabla\cdot\mathbf{v})^2 + 2\mu|\mathbf{E}|^2 + \mathrm{div}(k\nabla T) \end{aligned} \tag{3.25}$$

where the Navier-Stokes and Fourier relations are used to obtain (3.25). The first term on the right hand side is associated with compressibility and bulk viscosity, which is assumed to be identically zero for monatomic gas flows. The third term vanishes for the homogeneous affine motions of OMD.

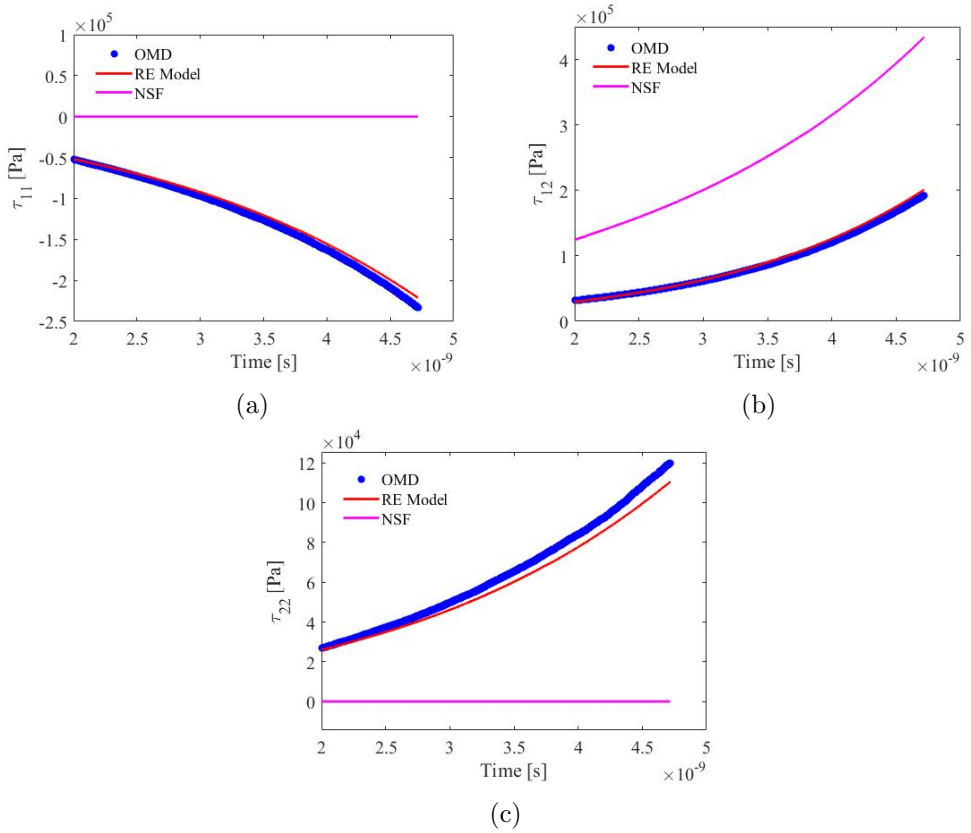

Figure 3.8: Evolution of OMD viscous stress tensor (a) τ_{11} (b) τ_{12} and (c) τ_{22} relative to Rivlin-Ericksen and Navier-Stokes theory ($\kappa = 1.84\text{x}10^9\text{s}^{-1}, \rho = 0.178\text{kg/m}^3$).

Equation (3.25) provides the guidance to choose the correct invariants of the flow which are associated with positive entropy generation and hence can drive the system far from equilibrium beyond the regime of applicability of NSF. In addition to s^*, flow compressibility also contributes towards entropy generation. Its effect will be taken into account in Sect 3.4.3 when dealing with compressible flows.

The usage of invariant, dimensionless description s^* helps in generalizing this constitutive framework across wide range of flows, flow gradients and state points of the dilute gas.

It can be seen from (3.17) that the contribution of the coefficients α_3 and α_5 are not

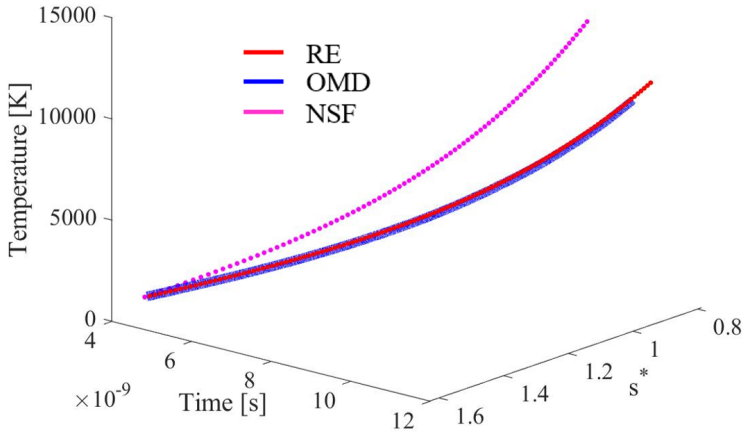

(a)

Figure 3.9: Evolution of OMD tempertaure field relative to Rivlin-Ericksen and Navier-Stokes theory for $\kappa = 9.22\text{x}10^8\text{s}^{-1},\ \rho = 0.178\text{kg/m}^3$.

present in simple shear due to identity

$$\alpha_5 = -\alpha_3, \quad \mathbf{A}_2^2 = \mathbf{A}_1^2\mathbf{A}_2 + \mathbf{A}_2\mathbf{A}_1^2 \tag{3.26}$$

The contributions of these terms in an OMD motion where (3.26) doesn't hold is investigated here using bi-axial shear flow based on $\mathbf{A} = \kappa\mathbf{e_2} \otimes \mathbf{e_1} + \kappa\mathbf{e_3} \otimes \mathbf{e_2}$. The velocity field and breakdown parameter s^* are then given by

$$\mathbf{v}(\mathbf{x}, t) = \mathbf{A}(\mathbf{I} + t\mathbf{A})^{-1} = \kappa\mathbf{e}_2 \otimes \mathbf{e}_1 + \kappa\mathbf{e}_3 \otimes \mathbf{e}_2 - \kappa^2 t\mathbf{e}_3 \otimes \mathbf{e}_1$$

$$s^* = \frac{\sqrt{(2\kappa^2 + (\kappa^2 t)^2)2}}{\nu}$$

The viscous stress tensor becomes

$$\begin{aligned}\boldsymbol{\tau} = (\kappa\mu + 2\kappa^5 t\alpha_3)\mathbf{S}_1 + (-\kappa^2 t\mu - 2\kappa^2\alpha_1 - 2\kappa^4\alpha_3 - 4\kappa^6 t^2\alpha_3)\mathbf{S}_2 + (\kappa\mu + 2\kappa^3 t\alpha_1 + 4\kappa^5 t\alpha_3)\mathbf{S}_3 \\ +(\frac{4}{3}\kappa^2\alpha_1 + \frac{2}{3}\kappa^4 t^2\alpha_1 + \frac{4}{3}\kappa^4\alpha_3)\mathbf{S}_4 + (-\frac{2}{3}\kappa^2\alpha_1 + \frac{2}{3}\kappa^4 t^2\alpha_1 - \frac{8}{3}\kappa^4\alpha_3)\mathbf{S}_5 \\ +(-\frac{2}{3}\kappa^2\alpha_1 - \frac{4}{3}\kappa^4 t^2\alpha_1 + \frac{4}{3}\kappa^4\alpha_3)\mathbf{S}_6\end{aligned} \tag{3.27}$$

where the dimensionless number $\alpha_3^* = \alpha_3 p/\mu_{NSF}^2$ can be computed by taking inner product of (3.27) with $\mathbf{S}_1$. This yields

$$\alpha_3^* = \frac{\tau_{12}^* - k^*\mu^*(s^*)}{2(\kappa t)(\kappa^{*4})}$$

where $|\boldsymbol{\tau}|^* = |\boldsymbol{\tau}|/p$, $\kappa^* = \kappa/\nu$ and μ^* is given by (3.23).

The OMD solution predicts that $\alpha_3 << \mu, \alpha_{1,2}$. Thus the effect of α_3 can be neglected and the final proposed constitutive model only depends on coefficients μ, α_1 and α_2 which are functions of s^* according to (3.23). To validate this proposed constitutive model, flow features of biaxial-shear ($\kappa = 4.6083\text{x}10^9 s^{-1}$) are compared with the predictions of OMD.

It is evident from this comparison shown in Figs. 3.10(a) and (b) that RE theory closely agrees with OMD and dramatically improves predictions based on the Navier-Stokes solutions. In particular, it shows that NSF predicts considerably higher shear stresses (τ_{12}, τ_{23}) than OMD and RE. This is consistent with the behavior observed for simple shear flow, investigated in Sec 3.2.1 where inability of the NSF to capture viscosity thinning and normal stress effects results in large discrepancies.

OMD flow considered here never attains stationary state. This is because external work of the form $(\sigma \cdot \nabla \mathbf{v})$ is continuously being done on the system and there is no balancing source of energy dissipation in 2.28. This results in a monotonic increase in temperature of the gas due to viscous heating since there is no introduction of any artificial thermostats that might raise other issues of validity. At given $|\mathbf{E}|$, the increase

in temperature increases the collision frequency of the gas which results in decrease in departure of the system from equilibrium, as measured by s^*. In other words, as the simulation evolves, the flow approaches near-equilibrium conditions. Note that the non-linear transport guided behavior of gas is realized when parameter s^* is comparatively higher. This is achieved either by increasing the numerator (introduction of sharp gradients) or decreasing the denominator (low collision frequency of the gas i.e., making the gas more dilute). In this work, similar non-equilibrium physics of rarefied monoatomic gas is captured by increasing the temporal gradients in the system. As the gas becomes more and more dilute, strain rate requires to capture the NSF breakdown decreases consistent with Fig. 3.1.

Next, a general isochoric case, that of general incompressible unsteady flows is considered. The necessary condition for this to hold true is $\nabla \cdot \mathbf{v} = 0$. This condition of incompressiblility is equivalent in Lagrangian form to $\det(\mathbf{I} + t\mathbf{A}) = 1$ for all $t > 0$.

Necessary and sufficient condition for $\det(\mathbf{I} + t\mathbf{A}) = 1$ for all $t > 0$ are that $\det\mathbf{A} = \mathrm{tr}\mathbf{A} = \mathrm{tr}(\mathbf{A}^2) = 0$. In a suitable orthonormal basis necessary and sufficient conditions are that

$$\mathbf{A} = \begin{bmatrix} 0 & \kappa & 0 \\ 0 & 0 & 0 \\ \gamma_1 & \gamma_2 & 0 \end{bmatrix}$$

in this basis. In abstract form, $\mathbf{A} = \kappa \mathbf{e_1} \otimes \mathbf{e_2} + \mathbf{e_3} \otimes \mathbf{g}$, where $\mathbf{e_1}, \mathbf{e_2}, \mathbf{e_3}$ are orthonormal and $\mathbf{g} = \gamma_1 \mathbf{e_1} + \gamma_2 \mathbf{e_2}$.

The corresponding Eulerian description of motion is given by

$$\mathbf{v}(\mathbf{x}, t) = \mathbf{A}\mathbf{x} - \kappa t \gamma_1 \mathbf{e_3}$$

This flow differs from traditional viscometric flows by the presence of time-dependent vorticity, $\mathrm{curl}\mathbf{v} = (\gamma_2 - \kappa\gamma_1 t)\mathbf{e}_1 - \gamma_1 \mathbf{e}_2 - \kappa \mathbf{e}_3$. Figs. 3.11 and 3.12 compare the OMD viscous stress evolution with that of RE model for $\gamma_1 = \kappa = \gamma_2 = 2.3041$ x $10^9 s^{-1}$. The

RE theory is shown to agree with OMD predictions reasonably well even under these extreme conditions.

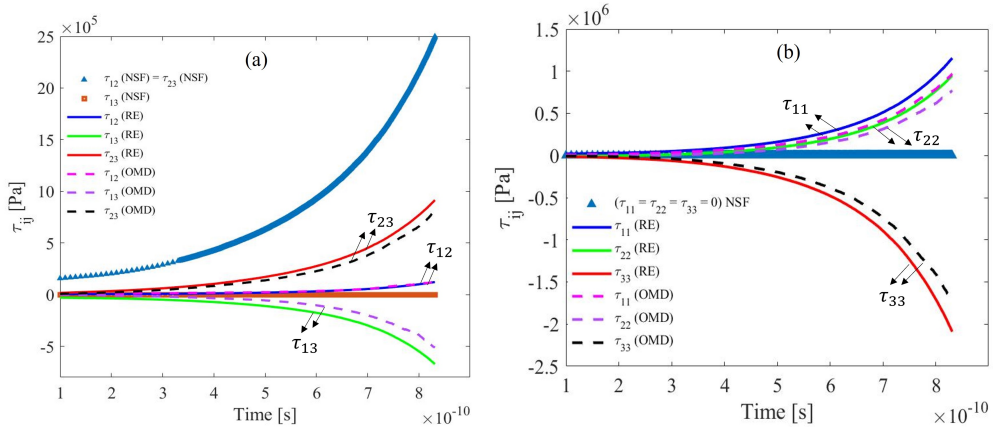

Figure 3.10: Comparison of the OMD evolution (dashed lines) of (a) deviatoric normal stresses (b) shear stresses with theoretical solutions of Navier-Stokes (symbols) and Rivlin-Ericksen model (solid lines) for biaxial shear.

3.4.3 Compressible flows

OMD also provides a method to simulate a nine parameter family ($\mathbf{A}$) of compressible flows where $\nabla \cdot \mathbf{v}$ is nonzero. In this case a finite value of the first invariant of $\mathbf{A}_1$ needs to be considered when defining the breakdown regime of gas flows. The evolution of density in these compressible flows is given by

$$\rho = \rho(0) exp(-\int_0^t E ds) = \rho(0) exp(-\int_0^t \mathrm{tr}\mathbf{A}(\mathbf{I} + s\mathbf{A})^{-1} ds) \tag{3.28}$$

where $\rho(0)$ is the initial density. Expansion of the gas can lead to a decrease in the molecular collision rate, which in turn can contribute to a failure of the NSF equations. For expanding flows Bird proposed the following parameter for continuum breakdown

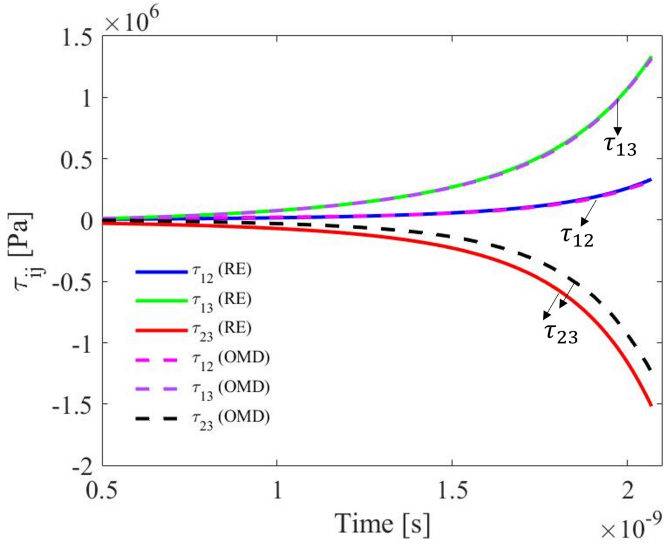

Figure 3.11: Shear stress evolution comparison between OMD and RE solution for general unsteady incompressible flows

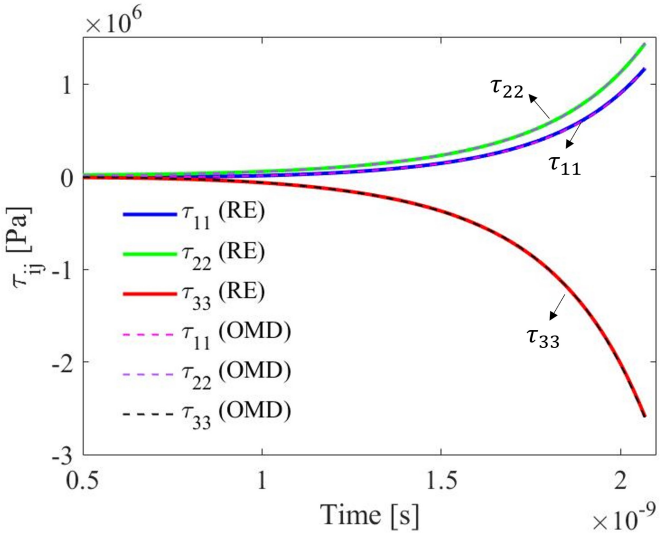

Figure 3.12: Normal stress evolution comparison between OMD and RE solution for general unsteady incompressible flows

[117, 106]

$$P = \frac{1}{\nu}(\frac{D(ln\rho)}{Dt}) = \frac{1}{\rho\nu}(\frac{D\rho}{Dt})$$
$$= \frac{1}{\rho\nu}(-\nabla\cdot(\rho\mathbf{v})) = \frac{-\mathrm{tr}(\mathbf{A}(\mathbf{I}+t\mathbf{A})^{-1})}{\nu} = \frac{-\mathrm{tr}(\mathbf{A}(\mathbf{I}+t\mathbf{A})^{-1})\mu_{\mathrm{NSF}}}{p}$$

where D is the total derivative. This criterion is used to incorporate terms of the form $P = \rho^*/\rho$ in the earlier computed coefficients μ^* and α_2^* to include the contribution of time-dependent density variations. The following coefficients of the RE model which work well for both compressible and incompressible flows is suggested.

$$\mu^* = \frac{1}{1 + c_1(s^*)^{c_2}(1 - c_7\frac{P}{s^*})^{c_8}}$$

$$\alpha_1^* = \frac{1}{2}(c_3 + c_4(s^*)^{c_5} + c_9(-P)^{c_{10}})^{c_6} \tag{3.29}$$

where $c_i, i = 1,..,6$ remains same as that derived from in-compressible flows. $c_i, i = 7,...10$ will now be calibrated using family of compressible flows.

To extend the callibration of RE equations, the pressure shear flow field ($\mathbf{A} = \kappa(\mathbf{e}_1 \otimes \mathbf{e}_1 + \mathbf{e}_1 \otimes \mathbf{e}_2)$) which was compared in Sect 3.2.2 with OMD is considered. The Rivlin-Ericksen model can be used to obtain the viscous stress given by

$$\boldsymbol{\tau} = (\frac{\kappa\mu}{(1+\kappa t)} - \frac{2\kappa^2\alpha_1}{(1+\kappa t)^2})\mathbf{S}_1 + (\frac{4}{3}\frac{\kappa\mu}{(1+\kappa t)} - \frac{16}{3}\frac{\kappa^2\alpha_1}{(1+\kappa t)^2})\mathbf{S}_4$$
$$(-\frac{2}{3}\frac{\kappa\mu}{(1+\kappa t)} + \frac{8}{3}\frac{\kappa^2\alpha_1}{(1+\kappa t)^2})\mathbf{S}_5 + (-\frac{2}{3}\frac{\kappa\mu}{(1+\kappa t)} + \frac{8}{3}\frac{\kappa^2\alpha_1}{(1+\kappa t)^2})\mathbf{S}_6 \tag{3.30}$$

μ^* and α_1^* can be obtained by using identities:

$$\mu^* = (\boldsymbol{\tau}^* : \mathbf{S}_1 - \frac{3}{8}\boldsymbol{\tau}^* : \mathbf{S}_4)\frac{2(1+\kappa t)}{\kappa^*}$$

$$\alpha_1^* = (\frac{4}{3}\boldsymbol{\tau}^* : \mathbf{S}_1 - \boldsymbol{\tau}^* : \mathbf{S}_4)\frac{(1+\kappa t)^2}{\kappa^{*2}}\frac{3}{8}$$

These coefficients are fitted to obtain the values listed in the Table 3.1. In Fig. 3.13

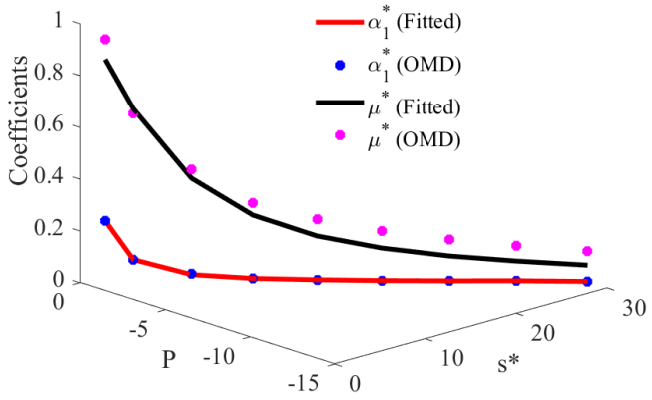

Figure 3.13: Fitting of the coefficients of Rivlin-Ericksen model for universal flows of LJ argon gas.

the fitted data is compared with the OMD evolution of μ^* and α_1^* as a function of s^* and P. These are obtained by simulating hundreds of flows with varying κ and state points (ρ, T). Note that both s^* and P are invariants of tensor $\mathbf{d}$ and hence are not independent variables. It can be seen from (Eq. 3.29) that the generalized transport coefficients reduce to those for Navier-Stokes in the limit of zero gradients.

1d expansion and compression

The final fitted model is next validated by simulating 1d extensional and compression flow where the gas grows steadily rarer and denser, respectively. The input matrix is chosen to be

$$\mathbf{A} = \begin{bmatrix} \kappa & 0 & 0 \\ 0 & 0 & 0 \\ 0 & 0 & 0 \end{bmatrix}$$

The velocity field is given by $\mathrm{v}_1 = \frac{\kappa}{\kappa \mathrm{t}+1}\mathrm{x}_1, \mathrm{v}_2 = 0, \mathrm{v}_3 = 0$. where $\kappa > 0$ results in expansion and $\kappa < 0$ results in compression. The RE viscous stress tensor for this flow

reduces to

$$\boldsymbol{\tau} = (\frac{4}{3}\frac{\kappa\mu}{(1+\kappa t)} - \frac{4\kappa^2\alpha_1}{(1+\kappa t)^2})\mathbf{S}_4 + (-\frac{2}{3}\frac{\kappa\mu}{(1+\kappa t)} + \frac{2\kappa^2\alpha_1}{(1+\kappa t)^2})\mathbf{S}_5 + (-\frac{2}{3}\frac{\kappa\mu}{(1+\kappa t)} + \frac{2\kappa^2\alpha_1}{(1+\kappa t)^2})\mathbf{S}_6, \tag{3.31}$$

where $\tau_{22} = \tau_{33} = -\tau_{11}/2$ and shear stresses are not present in the system. Fig. 3.14 compares the NSF and RE predictions of stresses with OMD results for $\kappa = 1.3825\text{x}10^9\text{s}^{-1}$. The RE model is shown to agree with OMD results reasonably well. On the other hand, NSF model over predicts stresses in the system by a significant amount. Fig. 3.15 compares the evolution of temperature. The initial equilibrium state of the system is given by: $\rho(0) = 0.1784\text{kg/m}^3,\ T(0) = 10000\text{K}$. Non-equilibrium conditions in the gas is seen by the development of anisotropy, where the translational temperature of the gas associated with each coordinate direction $T_{e_\alpha} = \langle \frac{m}{k_b N}\left[\sum_i^N ({v'_{\alpha,i}}^2)\right]\rangle,\ \alpha = 1,2,3$, separates. The temperature in the $\mathbf{e}_1$ direction $T_{\mathbf{e}_1}$ is widely different from the other two directions and decreases as the simulation evolves. The OMD evolution of the total temperature is shown by the black line which agrees with the RE prediction exceedingly well. On the other hand NS theory predicts a highly contrasting behavior where the temperature of the system increases with time. RE theory predicted temperature is computed by incorporating RE constitutive relation in the ODE for temperature derived from 2.28. Similarly, Fig. 3.16 shows various temperature evolutions for a 1d compression case where κ is non-positive and is given by $\kappa = -2.3041\text{x}10^8\text{s}^{-1}$. The initial equilibrium state of the system is: $\rho(0) = 0.01784\text{kg/m}^3,\ T(0) = 300\text{K}$. In contrast to the previous case, the temperature of the system increases with $T_{\mathbf{e}_1}$ being far higher than $T_{\mathbf{e}_2} = T_{\mathbf{e}_3}$. As shown, the Rivlin-Ericksen theory is able to capture the behavior of gas better than NS. Note that since κ is negative, this unsteady compressible flow has a singularity at $t = \tilde{t} = \frac{1}{\kappa}$.Therefore, the simulation is stopped before t reaches $\tilde{t}$. From these simulations it can be inferred that a multi temperature theory might not be required for the continuum description of translational non-equilibrium, given the correct non-linear terms. Interestingly, these effects are automatically incorporated in the underlying RE constitutive model with one temperature.

In Fig. 3.17(a) and 3.17(b) one-dimensional velocity distribution function $g(w_1)$ is

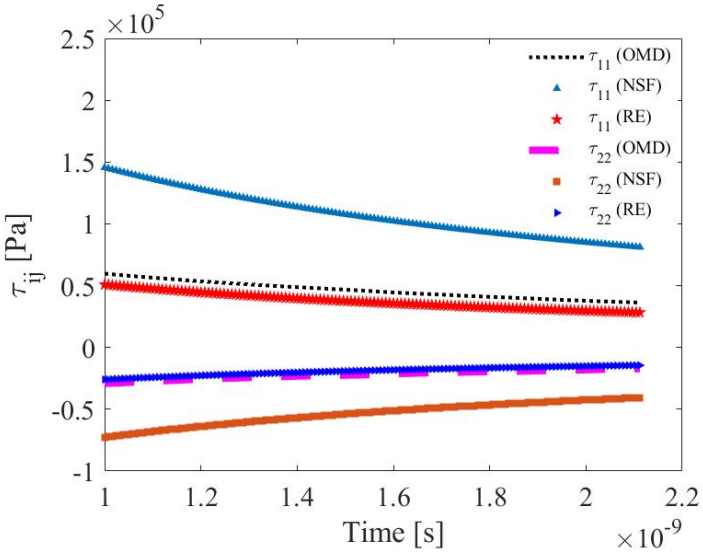

Figure 3.14: Comparison between OMD, NSF and Rivlin-Ericksen theory for argon gas under 1d extension.

examined for 1d compression and expansion respectively. This is obtained by averaging over all the thermal velocities in $\mathbf{e}_2$ and $\mathbf{e}_3$ directions. To compute $g(w_1)$ from OMD, fundamental domain is divided into equally spaced bins in $\mathbf{e}_1$ direction and population of atoms having certain thermal velocity is analyzed. For both the computations, the gas is started at equilibrium whose distribution matches with the Maxwellian velocity distribution at $t = 0$. As the gas evolves under compression, temperature increases and distribution gradually flattens and attains non-boltzmann character. It is apparent that high velocity tails are significantly overpopulated as compared to local Maxwellian evaluated at that instant. Similarly under expansion, distribution gradually shifts from Maxwellian at $t = 0$. Under expansion, temperature decreases with time and distribution becomes narrower. Contrary to the previous system, low velocity bins population are significantly high as compared to local equilibrium distribution.

It is concluded that RE theory has the potential to provide a rather complete description of universal flows in situations far-from equilibrium. It makes a significant

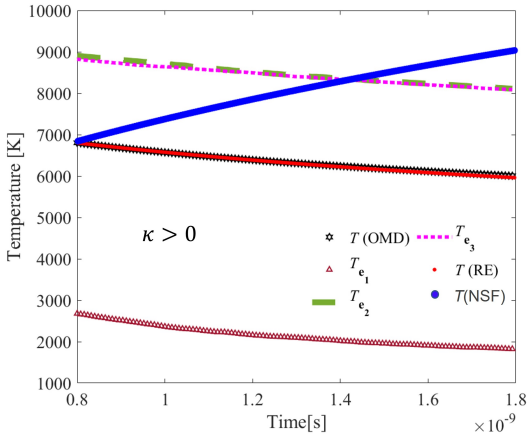

Figure 3.15: Different temperature evolution comparison between OMD, RE and NSF solution for 1d expansion

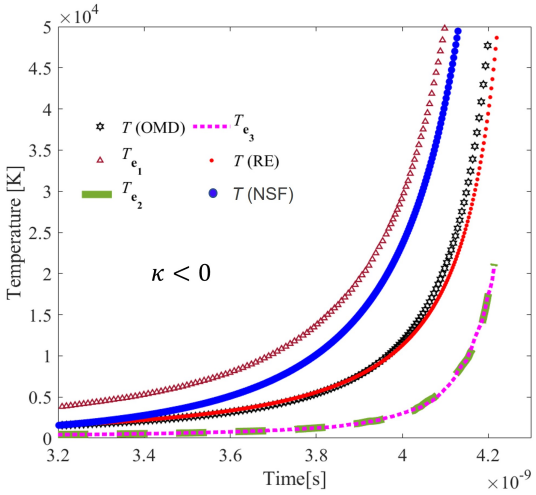

Figure 3.16: Different temperature evolution comparison between OMD, RE and NSF solution for 1d compression

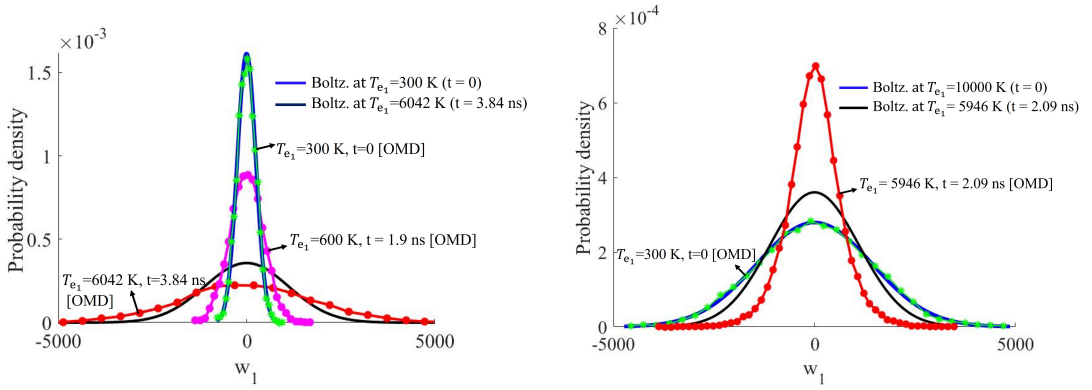

Figure 3.17: Velocity distribution function $g(\mathrm{w}_1)$ evolution for 1d (a) compression and (b) expansion. Blue and black lines depict Maxwellians evaluated at local flow conditions.

improvement on Newtonian transport model. The final form is given by

$$\boldsymbol{\tau} = \mu^* \mu_{\mathrm{NSF}} [\mathbf{A}_1 - \frac{\mathrm{tr}(\mathbf{A}_1)}{3}\mathbf{I}] + \frac{\alpha_1^* \mu_{\mathrm{NSF}^2}}{p}[(\mathbf{A}_2 - \frac{\mathrm{tr}(\mathbf{A}_2)}{3}\mathbf{I}) - 2(\mathbf{A}_1^2 - \frac{\mathrm{tr}(\mathbf{A}_1^2)}{3}\mathbf{I})] \quad (3.32)$$

where μ^* and α_1^* are given by (3.29). This generalizes the one proposed for uniform simple shear. The coefficients are generalized to take into account multi-axial gradients and compressibility effects.

There exists a class of mono-atomic flows for which the prediction of kinetic theory is in exact agreement with Navier-Stokes and Euler equations. This is pure dilatation of fluid with null bulk viscosity and sufficiently high density (still within dilute gas regime) to have a valid continuum description. The $\mathbf{A}$ tensor for the flow is given by $k\mathbf{e}_1 \otimes \mathbf{e}_1 + k\mathbf{e}_2 \otimes \mathbf{e}_2 + k\mathbf{e}_3 \otimes \mathbf{e}_3$. It is a dissipationless flow and thus indistinguishable from the corresponding flow of an inviscid fluid [107]. The model proposed in this work agrees with these results, i.e., s^* vanishes for these flows and $\boldsymbol{\sigma} = p\mathbf{I}, \tau = 0, \ \forall k$.

It is interesting to note that there exist a non-classical relationship between the two coefficients μ and α_1 as shown in Fig. 3.18. They closely obey a power law form given

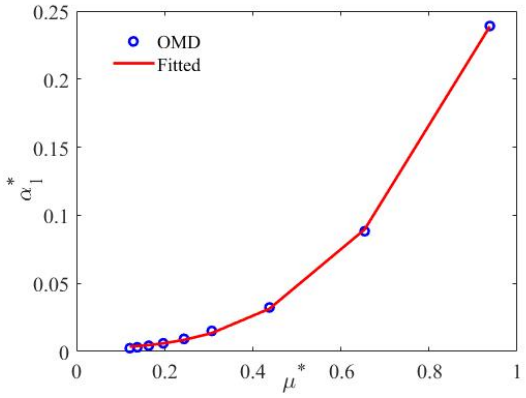

Figure 3.18: Non classical constitutive relationship between coefficients of Rivlin-Ericksen model of complexity two for dilute gas universal flows

Table 3.1: Fitted parameters of RE constitutive law

Constants	Values
c1	0.5
c2	1.5
c3	0.4766
c4	0.4599
c5	1.7714
c6	-0.8920
c7	3
c8	-2
c9	1.6076
c10	1.6139

by

$$\alpha_1^* = 0.282\mu^{*2.771}. \tag{3.33}$$

This can be interpreted as the existence of an unexpected scaling relationship between shear and normal stresses in the flow. The idea of having a non-classical stress constraint was also suggested by Myong et al [118] for simple shear using DSMC computations. Next, the thermodynamics and stability aspects of RE model is discussed.

3.5 Thermodynamics and Stability of Rivlin-Ericksen Fluid of Complexity 2

A well known special example of Rivlin-Ericksen fluids are fluids of second grade which satisfy the following constitutive model

$$\mathbf{M} = \frac{1}{3}\mathrm{tr}(\mathbf{M})\mathbf{I} + \alpha_0\mathbf{I} + \mu(T)\mathbf{A}_1 + \alpha_1(T)\mathbf{A}_2 + \alpha_2(T)\mathbf{A}_1^2$$

$$\begin{aligned}\tilde{\mathbf{M}} = \mathbf{M} - \frac{1}{3}(\mathrm{tr}(\mathbf{M})\mathbf{I}) = -(\boldsymbol{\sigma} - p\mathbf{I}) \\ = \boldsymbol{\tau} = \alpha_0\mathbf{I} + \mu(T)\mathbf{A}_1 + \alpha_1(T)\mathbf{A}_2 + \alpha_2(T)\mathbf{A}_1^2\end{aligned} \tag{3.34}$$

where coefficients μ, α_1, α_2 are constants which may depend on temperature. Note that Cauchy stress tensor $\mathbf{M}$ is negative of the stress tensor $\boldsymbol{\sigma}$ defined in this work.

When using this model as a general constitutive relation, it is known to cause unphysical response when the coefficients are not compatible with thermodynamics[119, 120]. It is shown that instability and unboundedness are unavoidable when this inconsistency occurs[121, 122]. The RE type second grade model in the literature has typically been questioned due to the discrepancy between thermodynamics and experimental measurements of the coefficients. Dunn and Fosdick studied stability and thermodynamics for second grade fluid and showed the following conditions on coefficients to be true [123].

$$\mu(T) \geq 0, \quad \alpha_1(T) \geq 0, \quad \alpha_1(T) + \alpha_2(T) = 0 \tag{3.35}$$

A large body of rheological measurements on polymeric fluids suggest otherwise. For example, consider a simple shear flow ($\mathbf{A} = \kappa\mathbf{e}_1 \otimes \mathbf{e}_2$). For Rivlin-Ericksen fluid of second grade, one can define first normal stress difference as

$$N_1 = -(\sigma_1 - \sigma_2) = (\tau_1 - \tau_2) = -2\alpha_1\kappa^2$$

Experimenters find $N_1 > 0$ which is inconsistent with the restriction imposed by thermodynamics. This lead to rejection of the idea of second grade model to be exact in its

own right. On the other hand, the molecular simulation results on dilute monoatomic gas obtained in this work seems to be consistent with this analysis as well as its extension by Dunn for new class of complexity 2 incompressible fluids considered in this work [123]. For these fluids the viscous stress tensor is given by

$$\boldsymbol{\tau} = \alpha_0 \mathbf{I} + \mu(T, \mathbf{A}_1)\mathbf{A}_1 + \alpha_1(T, \mathbf{A}_1)\mathbf{A}_1^2 + \alpha_2(T, \mathbf{A}_1)\mathbf{A}_2 \tag{3.36}$$

where the coefficients are arbitrary isotropic functions of temperature as well as $\mathbf{A}_1$. This family of models is wide enough to include "generalized-Newtonian fluids" ($\alpha_1 = 0, \alpha_2 = 0, \mu = \mu(|\mathbf{A}_1^2|, T)$) and "second grade fluids". It was shown that for second law of thermodynamics to hold and for the Helmholtz free energy to have minimum in equilibrium, the following conditions are necessary and sufficient:

$$\alpha_1(T, \mathbf{A}_1) = \alpha_1(T, |\mathbf{A}_1|) \tag{3.37}$$

$$\int_0^z \alpha_1(T, \zeta) d\zeta \geq 0 \quad z \in [0, \infty) \quad \text{for } z \in [0, \epsilon), \epsilon > 0 \tag{3.38}$$

$$\alpha_1(T, \mathbf{A}_1) + \alpha_2(T, \mathbf{A}_1) \to 0 \quad \text{for path } \mathbf{A}_1 = \mathbf{A}_1(\tau), |\mathbf{A}_1(\tau)| \to \infty \quad \text{as } \tau \to \infty \tag{3.39}$$

The coefficients calibrated in this work are functions of s^* and P, which in turn are functions of $|\mathbf{A}_1|$; thus it obeys Eq. (3.37).
The condition given by Eq. (3.38) is satisfied since the coefficient α_1 computed is positive everywhere in the domain. And the last condition given by (3.39) is applicable since

$$\alpha_1(T, \mathbf{A}_1) + \alpha_2(T, \mathbf{A}_1) = -\alpha_1(T, \mathbf{A}_1) = -\frac{p}{\mu_{\text{NSF}}^2}\frac{1}{2}(c_3 + c_4(s^*)^{c_5} + c_9(-|P|)^{c_{10}})^{c_6} \to 0 \quad \text{as} |\mathbf{A}_1(\tau)| \to \infty, \text{ for } c_6 < 0 \tag{3.40}$$

Thus the final rheological model proposed and calibrated in this work, in addition

to being properly invariant, also satisfies necessary restrictions coming from second law of thermodynamics for any incompressible fluid. This analysis needs to be extended to compressible flows to complete the argument. This investigation is beyond the scope of this work.

3.6 Connection with Burnett Equations

The Burnett equations are derived from Chapman-Enskog expansion where the Maxwellian distribution $\hat{f}_0$ is expanded for small values of ζ to obtain a VDF of the system.

$$\hat{f} = \hat{f}_0(1 + \zeta\phi_1 + \zeta^2\phi_2 + ...) \tag{3.41}$$

where ζ determines the degree of departure from the distribution. It can be written in physically meaningful manner [24],

$$\zeta = (\frac{\text{mean-collision-time}}{\text{characteristic flow time}}) = (\frac{\text{mean free path}}{\text{characteristic length}})$$

where the relation between mean free path and collision frequency is used. ζ is equivalent to breakdown parameter s^* defined in this work. Note that the focus was to only deal with homogeneous flows ($\nabla T = \nabla\rho = 0$) in this work so OMD captures departure from equilibrium in only temporal frame.

Substitution of the expansion of VDF for $\hat{f}$ into the non-dimensionalized Boltzmann equation yields a general constitutive relation for the stress tensor of the form

$$\boldsymbol{\tau}_{ij} = \boldsymbol{\tau}^0_{ij} + \boldsymbol{\tau}^1_{ij} + \boldsymbol{\tau}^2_{ij} + ... + o(\zeta^n).$$

The zeroth and first-order approximation yields the Euler and Navier-stokes equations.

Retaining terms up to second order provides the Burnett equation given by [30]

$$\begin{aligned}\boldsymbol{\tau} = \boldsymbol{\tau}^1 + \boldsymbol{\tau}^2 = -2\mu_{\mathrm{NSF}}\overline{\nabla \mathbf{v}} + \omega_1 \frac{\mu^2}{p}\nabla\cdot\mathbf{v}\overline{\nabla \mathbf{v}} \\ +\omega_2 \frac{\mu^2}{p}\left(\frac{D}{Dt}\overline{\nabla \mathbf{v}} - 2\overline{\nabla \mathbf{v}\overline{\nabla \mathbf{v}}}\right) + \omega_3 \frac{\mu^2}{\rho T}\overline{\nabla\nabla T} + \omega_4 \frac{\mu^2}{\rho p T}\overline{\nabla p \nabla T} \\ +\omega_5 \frac{\mu^2}{\rho T^2}\overline{\nabla T \nabla T} + \omega_6 \frac{\mu^2}{p}\overline{\overline{\nabla \mathbf{v}}\ \overline{\nabla \mathbf{v}}}\end{aligned} \tag{3.42}$$

where $\boldsymbol{\tau}^1$ and $\boldsymbol{\tau}^2$ show Navier-Stokes and Burnett contributions respectively. Time derivatives in Eq. (3.42) are eliminated using the conservation relation in the conventional Burnett equations, but here original form is used to establish its connection with RE theory. The ω_i are constant coefficients which depend on the interaction force field model. These are derived for some simple intermolecular force fields such as for Maxwellian gas [30]. For incompressible OMD flow (3.42) reduces to

$$\begin{aligned}\boldsymbol{\tau} = -\mu_{\mathrm{NSF}}\mathbf{A}_1 + \omega_2 \frac{\mu^2}{2p}\mathbf{A}_2 + (\omega_6 \frac{\mu^2}{2p})\mathbf{A}_1^2 + \omega_2 \frac{\mu^2}{p}(\nabla \mathbf{v}^{\mathrm{T}}\mathbf{A}_1 - \mathbf{A}_1\nabla \mathbf{v}) \\ +\omega_2 \frac{2\mu^2}{3p}(\mathrm{tr}(\nabla \mathbf{v}^{\mathrm{T}}\frac{\mathbf{A}_1}{2})\mathbf{I}) - \omega_6 \frac{\mu^2}{3\mathrm{p}}(\mathrm{tr}(\mathbf{A}_1^2)\mathbf{I})\end{aligned} \tag{3.43}$$

where $\mathbf{A}_i$ are Rivlin-Ericksen tensors. For OMD compressible flows, (3.42) reduces to a similar form but includes more terms in the summation which depends on the non-zero divergence of velocity gradient ($\nabla\cdot\mathbf{v}$).

Writing the Burnett equation in this form show its connection with Rivlin-Ericksen constitutive model. It is shown here that Burnett equations also contain terms which are of the form $\mathbf{A}_1$, $\mathbf{A}_2$ and $\mathbf{A}_1^2$ in accordance with RE equation but these are not frame-indifferent [31]. Additionally, the coefficients are constant, as opposed to our constitutive framework where they depend on the strength of flow field gradients captured by breakdown parameter s^* and P. Similar to Burnett equation, there underlies a non-equilibrium velocity distribution function beneath RE equations. Evidently, one needs to resort to a non-perturbative approach to find its full form.

3.7 Summary and Conclusions

This chapter introduced a nonlinear, non-classical constitutive relation for highly nonequilibrium flows of gases based on the use of the Rivlin-Ericksen (RE) tensors. It is shown that the resulting RE theory gives results that agree well with the Navier-Stokes-Fourier (NSF) theory in lower speed regimes but also performs well in diverse high speed flows where the NSF theory fails, in some cases severely. The constitutive relation is fully frame-indifferent, so the macroscopic flows corresponding to the OMD simulations are exact solutions for the proposed model. The success of the model indicates that it is not higher gradients that become important in the high rate regime, but rather higher rates of change of the of the strain rate tensor. While somewhat more complicated to implement than the Navier-Stokes relation, the proposed model is expected to be compatible with existing methods of Computational Fluid Dynamics (CFD) and may extend those methods to higher rate regimes, while preserving their ability to handle large spatial scales.

The chapter also established the link between RE type constitutive relation of continuum mechanics with kinetic theory for a gas of Maxwellian molecules in simple shear. The relation emerges as a special asymptotic of Maxwell moment equations where in the stress tensor attains steady state value well before the conserved variables $(\rho, T, \mathbf{v})$. Diagnostic parameters s^* and P that are sufficient to assess the applicability of NSF equations in a variety of flows is also introduced. The identification of these parameters opens the way to a hybrid RE/NSF method.

The method is applicable to highly nonequilibrium situations where the velocity distribution function departs significantly from a Maxwellian distribution. The success of the method indicates that the paradigm of constitutive relations as closure conditions for the continuum balance laws is a valid approach in this regime. Though the modeling and calibration is limited to Lennard-Jones argon gas, the framework adopted is quite general. It is believed that the fitted parameters will have a strong dependence on the particular force field but the (nondimensionalized) functional forms may be generic across various monatomic gases.

The next chapter extends the molecular investigation to high temperature, chemically reacting diatomic flows.

Chapter 4

Chemically Reacting Nitrogen Gas

4.1 Introduction

Internal energy of gas molecules comprises of translational, rotational, vibrational and electronic modes and all the modes are active at high temperatures. For a system at thermodynamic equilibrium, the total energy is partitioned equally among all these modes. On the other hand in strong shocks during hypersonic flight, flow transit time and shock stand-off distances are small enough that thermodynamic equilibrium is not reached in the gas due to finite relaxation times. Thus, there is significant lagging of internal energy modes in comparison with translational mode due to which the state of the gas cannot be characterized by a single temperature. This thermal non-equilibrium is in both ways coupled with chemical kinetics because of the microscopic favoring of certain internal energy levels when dissociating or recombining. This suggest the complexity of out-of-equilibrium thermo-chemical environment surrounding a vehicle during atmospheric entry where reaction and energy exchange rates do not keep pace with rapid flow changes [124]. Analysis based on particle methods can provide detailed insights of all these coupled processes from the molecular perspective. The motivation of this chapter is to understand the non-equilibrium physics behind internal energy excitation, dissociation and recombination under conditions relevant to hypersonic flows in the nitrogen gas using molecular dynamics.

In CFD, thermal nonequilibrium is often approximated by treating the vibrational energy separately from the rotational and translational components. This forms the basis of traditional two-temperature representation of the gas energy state. Additionally, one must also deal with special continuity equation for each individual chemical species. This requires physical inputs such as reaction rates, vibrational relaxation rates, and vibrational energy change due to dissociation and recombination. The most widely used model for chemical kinetics at hypersonic conditions is due to Chul Park[125]. The model uses vibrational relaxation times from Millikan and White[126]. Park's coefficient of dissociation is based on shock-tube experiments [127, 128] which is assumed to be an Arrhenius function of an 'effective' temperature $T_{av} = (T\ Tv)^{1/2}$ to account for the fact that vibrationally excited molecules are more likely to dissociate[129, 125]. For the vibrational energy change due to chemical reaction, Park recommended several models of preferential chemistry. However, these models were ill-suited for CFD implementation, and so non-preferential dissociation and recombination, where the average vibrational energy of dissociating/recombining molecules is set to the average vibrational energy of the molecules is typically used instead. In this chapter, the behaviour of this widely used model is assessed by making comparison with MD simulations data.

A non-equilibrium gas state may result when the flow particles pass through a strong shock wave (dissociation non-equilibrium) or undergo a rapid expansion (recombination non-equilibrium). Both the phenomena would occur at Shuttle entry conditions [22]. This chapter also illustrates the capability of OMD to study the rapid compression and expansion kinetics of dissociation-recombination nitrogen mixture. The method makes the use of deterministic molecular dynamics for the study of gas dynamics more affordable under these far-from-equilibrium conditions. This is achieved by considerable simplification where the coupled PDEs associated with the system of reacting flow are reduced to ODEs in macroscopic variables. In other words, OMD reactor is homoenergetic where spatial inhomogeneity is removed from an unsteady system.

There is continued development of high-fidelity PESs for high-temperature chemistry using quantum mechanical electronic structure calculations [60, 61]. The application of

these calculations has been limited to a four-atom system since its usage for a larger system composed of a multitude of atoms and molecules becomes prohibitively expensive. Though restricted, it is appropriate for DMS [130, 131, 132, 133] and quasi-classical trajectory (QCT)[134, 61] computations where the focus is on studying atom-diatom and diatom-diatom interactions. This development has made available the ab initio rate parameters for elementary collisional processes which have also enabled the development of state-to-state (STS) modeling[135, 136, 137]. Four-atom-based potential hypersurface in its current form is not suitable for molecular dynamics computation since in MD there is no control over the number of atoms interacting at once. In this chapter, use of two different PESs have been made for MD analysis. First, the combination of two-body Morse and Ling-Rigby potentials is used[138]. Morse potential defines the intramolecular interaction and Ling-Rigby defines inter-molecular interactions between N_2 molecules. The combination handles dissociation for both $N_2 + N_2$ and $N_2 + N$ collisions by hopping from Morse to Ling Rigby force field. However, it is not suitable for treating bond formation in the current setting due to energy discontinuity encountered during reversed hopping from Ling-Rigby to Morse. Later in the study, reactive ReaxFF potential energy surface [139] is used to overcome the above limitation. Reactive force field allows for a smooth transition from non-bonded to bonded system with no discontinuities in energy or forces during reaction thereby making the consideration of both dissociation as well as recombination in the Nitrogen gas mixture possible. The advantage of this PES is that it is fitted to an advanced quantum chemistry derived (4N) dataset generated using MS-CASPT2 calculations which is designed to treat breakage of bonds. [60].

This chapter is broadly divided into three sections. Section 4.2 presents reduced CFD equations corresponding to OMD system of non-equilibrium reacting flows. Section 4.3 focuses on molecular investigation using Morse and Ling-Rigby PESs and Section 4.4 focuses on the investigation using ReaxFF PES.

4.2 Reduced Fluid Dynamics for OMD

The two temperature (2T) characterization of system of vibrationally excited and chemically reacting gas assumes that the translational mode of energy is in equilibrium with rotational energy mode and vibrational mode is in equilibrium with electronic mode. This gives rise to two separate definitions of temperature: T and Tv which stands for translational-rotational and vibrational temperature respectively [125]. Additionally, mass conservation equations for every species with source terms containing reaction rates that govern the creation and removal of species are defined. In this study, the aim is to investigate relaxation and reactive processes in a system of Nitrogen gas. The corresponding reaction include

$$\mathrm{N_2 + M \rightleftharpoons 2\,N + M} \tag{4.1}$$

where M is the collision partner. The study takes into account both forward (dissociation) and backward (recombination) reactions where the conservation equations of fluid dynamics for two species N_2 and N take the form [140, 21]

$$\begin{aligned}
\frac{\partial \rho_{\mathrm{N_2}}}{\partial t} + \nabla\cdot(\rho_{\mathrm{N_2}}\mathbf{v}) &= -\nabla\cdot(\rho_{\mathrm{N_2}}\mathbf{u}_{\mathrm{N_2}}) + w_{\mathrm{N_2}}, \quad \frac{\partial \rho_{\mathrm{N}}}{\partial t} + \nabla\cdot(\rho_{\mathrm{N}}\mathbf{v}) = -\nabla\cdot(\rho_{\mathrm{N}}\mathbf{u}_{\mathrm{N}}) + w_{\mathrm{N}} \\
\frac{\partial \rho\mathbf{v}}{\partial t} + \nabla\cdot(\rho\mathbf{v}\otimes\mathbf{v} + p\mathbf{I}) &= \nabla\cdot\boldsymbol{\tau} \\
\frac{\partial e}{\partial t} + \nabla\cdot((e+p)\mathbf{v}) &= \nabla\cdot(\boldsymbol{\tau}\mathbf{v}) - \nabla\cdot(\mathbf{q}_t + \mathbf{q}_r + \mathbf{q}_v) - \nabla\cdot(\rho_{\mathrm{N_2}} h_{\mathrm{N_2}}\mathbf{u}_{\mathrm{N_2}} + \rho_{\mathrm{N}} h_{\mathrm{N}}\mathbf{u}_{\mathrm{N}}) \\
\frac{\partial e_v}{\partial t} + \nabla\cdot(e_v\mathbf{u}) &= -\nabla\cdot\mathbf{q}_{\mathbf{v}} - \nabla\cdot(\rho_{\mathrm{N_2}} e_{\mathrm{N_2}}\mathbf{u}_{\mathrm{N_2}} + \rho_{\mathrm{N}} e_{\mathrm{N}}\mathbf{u}_{\mathrm{N}}) + w_v
\end{aligned} \tag{4.2}$$

where $e = (\rho_{\mathrm{N_2}} C_{v_{\mathrm{N_2}}}\mathrm{T} + \rho_{\mathrm{N}}\mathrm{C_{v_N}}\mathrm{T} + \mathrm{e_{v_{N_2}}}\rho_{\mathrm{N_2}} + \mathrm{h^o_{N_2}}\rho_{\mathrm{N_2}} + \mathrm{h^o_N}\rho_{\mathrm{N}})$ and $e_v = e_{v_{\mathrm{N_2}}}\rho_{\mathrm{N_2}}$ are total energy and vibrational energy per unit volume respectively, $\rho = (\rho_{\mathrm{N_2}} + \rho_{\mathrm{N}})$ is the total density, p is the trace of pressure tensor $\boldsymbol{\sigma}$ ($p = \frac{\mathrm{tr}(\boldsymbol{\sigma})}{3}\mathbf{I}$), $\boldsymbol{\tau}$ is the viscous stress tensor ($\boldsymbol{\tau} = -(\boldsymbol{\sigma} - p\mathbf{I})$), $\mathbf{q}_t, \mathbf{q}_r, \mathbf{q}_v$ are translational, rotational and vibrational heat flux vectors, $\mathrm{h^o_s}$ is the total enthalpy per unit mass of species s, $\mathbf{u}_s$ is the species diffusion velocity, w_s is the rate of production of species s due to chemical reactions and w_v is the vibrational energy source term.

These conservation equations are greatly simplified for OMD flows, $\mathbf{v} = \mathbf{A}(\mathbf{I} + t\mathbf{A})^{-1}\mathbf{x}$ where due to absence of any spatial dependencies, PDEs of continuum mechanics reduces to a system of ODEs and heat flux vanishes[16]. The momentum conservation equation is identically satisfied for all accepted constitutive relations–newtonian or non-newtonian as shown in section 1.3. The other two reduced balance equations for nitrogen gas in an OMD reactor is given by

$$\begin{aligned} \frac{\mathrm{d}\rho_{\mathrm{N}_2}}{\mathrm{d}t} + \rho_{\mathrm{N}_2}\,\mathrm{tr}\big(\mathbf{A}(\mathbf{I}+t\mathbf{A})^{-1}\big) &= w_{\mathrm{N}_2}, \\ \frac{\mathrm{d}\rho_{\mathrm{N}}}{\mathrm{d}t} + \rho_{\mathrm{N}}\,\mathrm{tr}\big(\mathbf{A}(\mathbf{I}+t\mathbf{A})^{-1}\big) &= w_{\mathrm{N}}, \quad w_{\mathrm{N}_2} = -2w_{\mathrm{N}} \end{aligned} \tag{4.3}$$

$$\begin{aligned} \frac{\mathrm{d}e}{\mathrm{d}t} + (e+p)\,\mathrm{tr}\big(\mathbf{A}(\mathbf{I}+t\mathbf{A})^{-1}\big) &= (\mathbf{A}(\mathbf{I}+t\mathbf{A})^{-1})\cdot\boldsymbol{\tau}, \\ \frac{\mathrm{d}e_v}{\mathrm{d}t} + e_v\,\mathrm{tr}\big(\mathbf{A}(\mathbf{I}+t\mathbf{A})^{-1}\big) &= w_v \end{aligned} \tag{4.4}$$

The evolution of total density of the mixture which comes by summing species mass conservation equations in (4.3) can be solved explicitly as a function of time. This is given by

$$\rho_t = \rho_0 \exp\left(-\int_0^t \mathrm{tr}\big(\mathbf{A}(\mathbf{I}+s\mathbf{A})^{-1}\big)\mathrm{d}s \right) \tag{4.5}$$

.

4.3 Morse and Ling-Rigby PES

In this section, Morse potential is used to describe inter-atomic forces between two nitrogen atoms of a molecule in OMD computations. This is given by

$$V(r) = D_e[1 - e^{-f(y)(r-r_e)}]^2 - D_e \tag{4.6}$$

where $D_e = 228.7$ kcal/mol is the equilibrium bond dissociation energy, variable y is defined by

$$y = \frac{r^4 - r_e^4}{r^4 + r_e^4},$$

where r is the internuclear distance, and $r_e = 1.208$Å is the equilibrium bond length of N_2.
$f(y) = \sum_{i=0}^{6} a_i y^i$, and $a_0 = 2.70963254293\text{Å}^{-1}$, $a_1 = 0.132620177271\text{Å}^{-1}$, $a_2 = 0.296757048793\text{Å}^{-1}$, $a_3 = 0.197112432229\text{Å}^{-1}$, $a_4 = -0.502002309588\text{Å}^{-1}$, $a_5 = 0.380734244606\text{Å}^{-1}$, $a_6 = 0.121001628750\text{Å}^{-1}$.

The parameters chosen for 2 body Morse potential are consistent with the ones used in designing the ab-initio PES [60]. The site-site model of the Ling Rigby potential is used to evaluate inter molecular interactions between atoms of different molecules [138].

$$V(r_{ij}) = D_e \exp\big(\alpha r_{ij} - \beta r_{ij}^2\big) - f_d(r_{ij}) \frac{C_6}{r_{ij}^6} \tag{4.7}$$

where r_{ij} is the distance between atoms, $D_e = 14151.94$ kcal/mol, $\alpha = 2.2412\text{Å}^{-1}, \beta = 0.3214\text{Å}^{-2}$, and $C_6 = 336.46$ kcal/mol Å and $f_d(r_{ij})$ is a damping function defined by

$$f_d(r_{ij}) = \exp\left(\frac{-1}{4}(\frac{\delta}{r_{ij}})^2\right) - 1,$$

where $\delta = 4.14$Å. This potential surface has been used earlier and has been validated to reproduce correct transport properties of nitrogen [141]. It was also shown to be reproducing correct behavior of rotational and vibrational relaxation in a system of non-dissociative molecular nitrogen by Valentini et al [142]. In this work, dissociation of molecules is achieved in the simulations by hopping from Morse to Ling Rigby potential surface when distance between atoms in a molecule exceeds a critical length of 8Å and atoms in the molecule move in opposite directions. This length is chosen by running a number of computations to make sure that further increase in the critical length does not affect the dissociation evolution by an appreciable amount. It also ensures that jumping from one PES to another PES does not result in the discontinuity of energy. It is not suitable for treating recombination in the current setting and hence recombination is not

considered in this section. Electronic internal energy and ionization are also neglected in this work.

4.3.1 Comparison of MD with DMS under adiabatic conditions

The OMD and DMS methods are used to study thermochemical relaxation in a zero-dimensional adiabatic reactor. The ab initio potential energy surface for ground state nitrogen developed by Paukku et al. [60] is used for DMS calculations. This describes the interaction between 4 nitrogen atoms in an isolated system. The DMS method has been previously used to study adiabatic relaxation by Torres and Schwartzentruber [130].

In OMD, simple adiabatic reactor is achieved by choosing $\mathbf{A}$ to be zero which reduces it to traditional periodic MD. Two sets of initial conditions are studied. In the first case the gas is initialized at a translational temperature several thousand Kelvin higher than the rotational and vibrational ones. The translational temperature is initialized by sampling the center-of-mass velocity of the simulated molecules from a Maxwell-Boltzmann distribution. The initial rovibrational populations conform to a Maxwell-Boltzmann distribution at selected internal temperature. In the first case the translational temperature of the system is initialized to 30000K, which is different from rotational and vibrational temperature, initialized at 3000K. In the second case all the temperatures are set equal to 30000K. For both simulations, the initial density was set to $\rho = 1.25\text{kg/m}^3$. 5000 simulated molecules are used in OMD simulations.

In OMD simulations, phase-space trajectories of the system (positions and velocities of all simulated molecules) are stored after every few time steps for post-processing and visualization. These canonical coordinates are then further used to determine internal energy states of molecules. The vibrational prioritized framework of Jaffe [143] is used to split internal energy into rotational and vibrational modes. As the system evolves, the molecules become rovibrationally excited and further dissociate to form N atoms. The evolution of temperature and mole fraction of N_2 molecules in the system coming from OMD and DMS are compared in Figs. 4.1 and 4.2 (DMS computations are performed by Dr. Erik Torres at University of Minnesota). To extract internal temperature from simulations, the definitions given by Panesi et al. [135] is used where the total internal energy of system extracted from the simulation is equated to an equivalent average

energy based on the Maxwell-Boltzmann distribution for the rovibrational energy levels. Similar definitions are used for extracting rotational and vibrational temperature from simulations. In the first case compared in Fig. 4.1, rotational and vibrational energies of molecules increase due to translation-rotation and translation-vibration energy transfer during the simulation. Note that nitrogen dissociation is not significant in the early stage and most of the dissociation happens later, when all energy modes reach thermal equilibrium, Tr = Tv = Tt. On the other hand dissociation is rapid in the second case (Fig. 4.2) where the internal mode of the gas is fully excited at the initial stage. As the system evolves, translation and internal energy from both rotational and vibrational modes is rapidly removed due to dissociation with relaxation rates significantly coupled to each other.

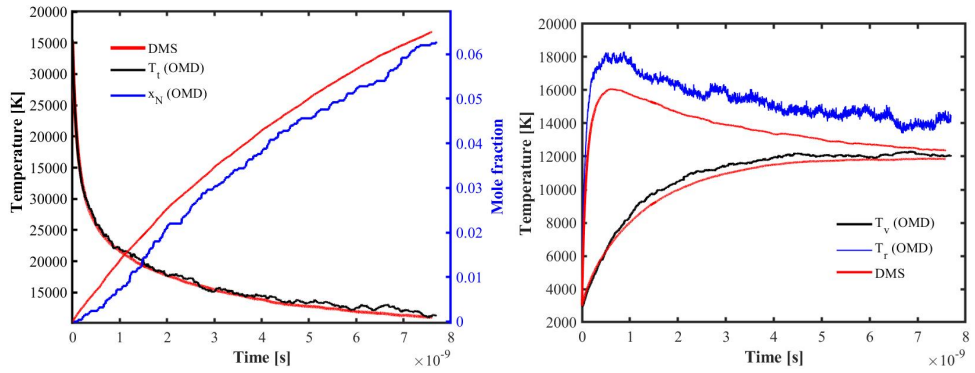

(a) Tt and mole fraction x_N (b) Tr and Tv of N_2

Figure 4.1: Comparison of evolution of different temperatures and composition obtained by OMD and DMS. The solid red lines represent DMS time history. Initial state: Tt = 30000K, Tr = 3000K, Tv = 3000K

The aim of this comparison is to treat the DMS computations as benchmark solutions and to investigate the ability of Morse and Ling Rigby potentials to capture the non-equilibrium phenomena for $N_2 - N_2$ adequately. Some loss of accuracy is expected due to neglecting many body effects when treating the system using the two-body potential surface.

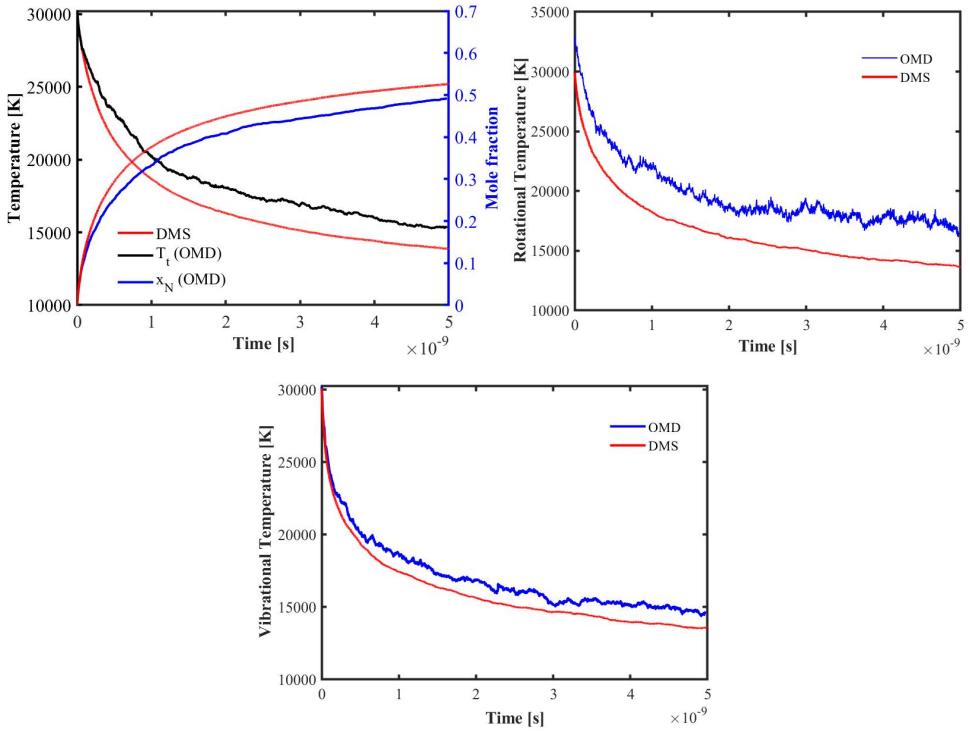

Figure 4.2: Comparison of evolution of different temperatures and composition obtained by OMD and DMS. The solid red lines represent DMS time history. Initial state: Tt = 30000K, Tr = 30000K, Tv = 30000K

4.3.2 Compression and relaxation of nitrogen gas

In this section, a system where the gas encounters a sudden compression followed by relaxation is investigated. It more closely mimics the non-equilibrium condition of gas in the shock front and immediately behind in a temporal frame. To achieve this $\mathbf{A}$ is chosen to be $\kappa\mathbf{e_1}\otimes\mathbf{e_1}+\kappa\mathbf{e_2}\otimes\mathbf{e_2}+\kappa\mathbf{e_3}\otimes\mathbf{e_3}, \kappa < \mathbf{0}$ corresponding to uniform compression. Then, beyond a pre-defined cut-off time, $\mathbf{A}$ is set to $\mathbf{0}$ in the relaxation stage. Under compression, the conservation of total energy and density of the mixture (4.4) and (4.5) for the non equilibrium inviscid flow considered reduces to

$$\frac{\mathrm{d}e}{\mathrm{d}t} = -(e+p)\,\mathrm{tr}(\mathbf{A}(\mathbf{I}+t\mathbf{A})^{-1}) = -(e+p)\frac{3}{(\kappa t+1)}$$

$$\rho_t = \frac{\rho_0}{(\kappa t + 1)^3} \tag{4.8}$$

where $-(e+p)\,\mathrm{tr}(\mathbf{A}(\mathbf{I}+t\mathbf{A})^{-1})$ acts as a source term which increases the total energy of the system in the compression regime. The initial density is set to 1.25×10^{-4} kg/m^3. Density increases in the compression stage and later remains constant in the relaxation stage. Very close agreement between the analytical density (4.8) and the one extracted from OMD simulation shown in Fig. 4.3(a) validates the setup of the computation. Figure 4.3(b) shows the translational, rotational, and vibrational temperature evolution of the gas under compression ($\kappa = -2.6 \times 10^8 \mathrm{s}^{-1}$) and relaxation cycle.

High speed compression does irreversible work on the system which causes a sudden increase in the translational energy followed by an increase in rotational energy. The vibrational energy mode remains nearly frozen during the compression stage. During relaxation, the translational temperature decreases. This happens due to onset of the chemical reaction and excitation of the internal energy modes. The rotational temperature peaks and then begins to decrease, followed by equilibration. The vibrational temperature on the other hand increases and equilibrates to a final ro-vibrational temperature. Dissociation of nitrogen does not begin until the molecules are sufficiently excited. Major dissociation starts in the relaxation stage. It is clearly visible from the simulations that under the conditions chosen, the rotational and vibrational modes become coupled in a complicated manner, and relaxation rates of rotational and vibrational temperature are comparable in magnitude. This signals the unsuitability of defining widely used single translational-rotational temperature to study non-equilibrium hypersonic flows at high enthalpy. Figure 4.4 shows the speed distribution of N_2 and N at different times during the simulation, which correspond to different translational and internal temperatures of the gas. These two times could be related to the distance from the shock in a spatial frame. Right before the relaxation, when the gas is in highly compressed state (Tt = 47390K), the instantaneous distribution of N_2 follows Maxwell-Boltzmann distribution closely within statistical uncertainty. This shows the rapid relaxation of the translational mode to the equilibrium speed distribution defined at corresponding instantaneous translation temperature. This also holds true for N_2 species at later times in the relaxation stage. Figure 4.4(b) shows the instantaneous speed distribution of N atoms at the time instant when Tt = 22742K, Tr = 20653K, Tv = 12765K. It shows

that even nitrogen atoms which are being generated by dissociation follow a Maxwellian distribution in far-from-equilibrium regime. It should be noted that across an actual shock wave the velocity distribution will depart significantly from Maxwellian, at least for a short duration. The current OMD simulations do not capture this effect. However, this is expected, given the particular choice of the **A**-matrix to describe isotropic compression.

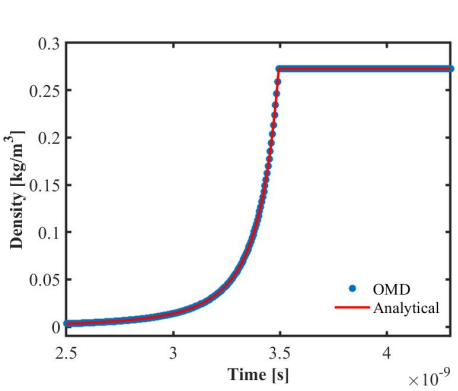

(a) Evolution of density

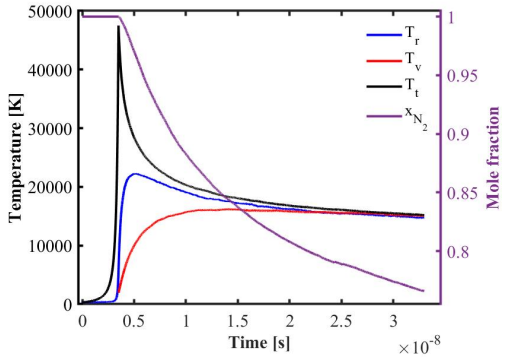

(b) Evolution of temperatures and mole fraction

Figure 4.3: Time history of density, system translation temperature, rotational and vibrational temperature of N_2 molecule and mole fraction of molecular nitrogen

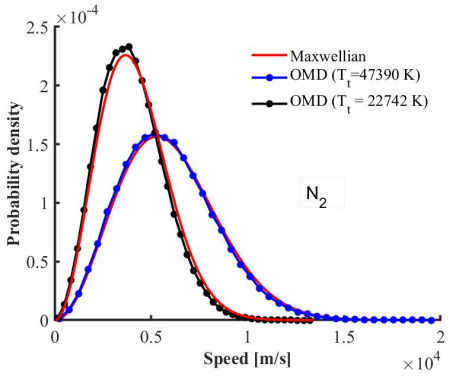

(a) $\mathbf{N_2}$

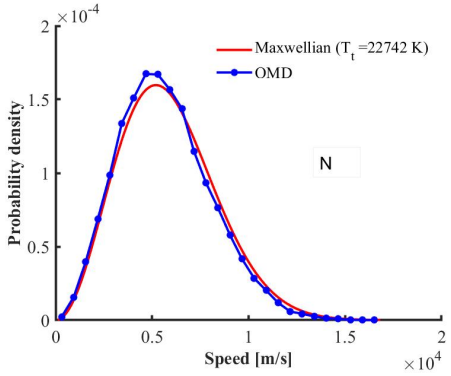

(b) **N**

Figure 4.4: Speed distribution of N_2 molecules and N atoms at different time instants within the simulation evolution. The solid red lines represent Maxwellian distributions at instantaneous Tt

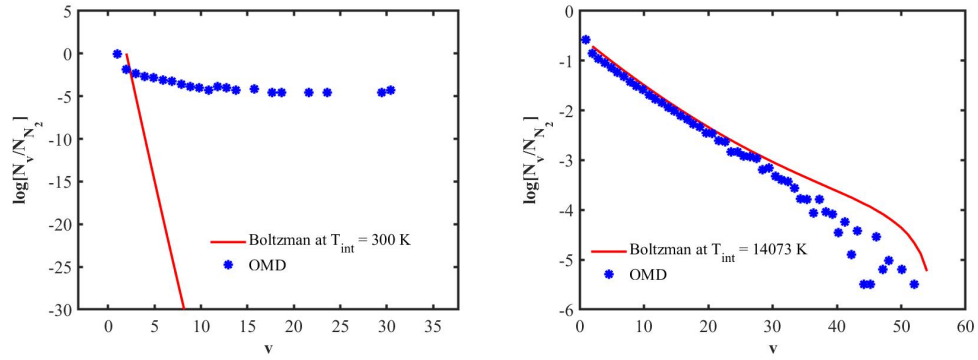

(a) Compression (b) Relaxation

Figure 4.5: Vibrational distribution functions for molecules right after compression (Tt = 47512K, Tr = 5579K, Tv = 300K) and during QSS (Tt ≈ Tr ≈ Tv ≈ T_{int} = 14073K). The solid red lines represent Boltzmann distributions.

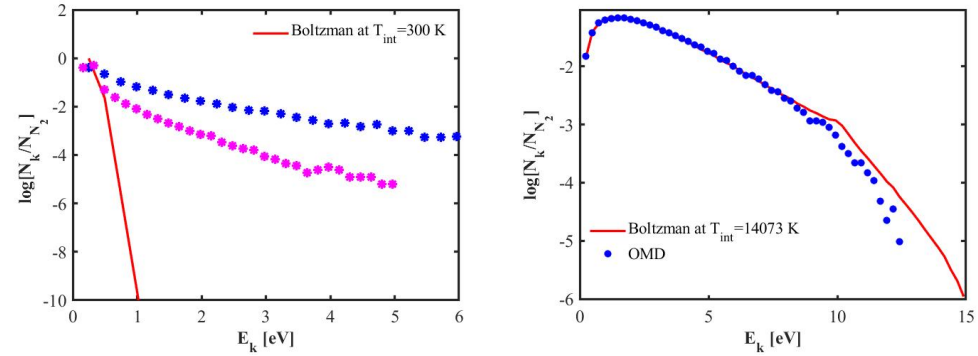

(a) Compression (b) Relaxation

Figure 4.6: Ro-vibrational energy distribution functions for molecules right after compression (Tt = 47512K, Tr = 5579K, Tv = 300K) and during QSS (Tt ≈ Tr ≈ Tv ≈ T_{int} = 14073K). The solid red lines represent Boltzmann distributions.

To gain more insight on the internal energy distribution of the gas, instantaneous population fractions of each vibrational, internal energy and rotational state are computed in Fig. 4.5, 4.6 and 4.7 respectively. To get better statistics, an ensemble average of 200 instances of separate simulations are done in phase space. This corresponds to 160000 simulated molecules. Figure 4.5(a) compares the instantaneous vibrational quantum number distribution of the gas just before the relaxation with the equilibrium (Boltzmann) distribution of the initial state of the gas at a temperature

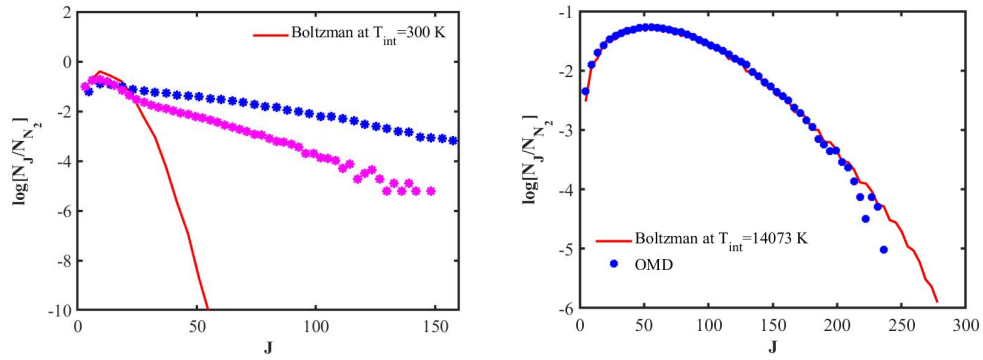

(a) Compression (b) Relaxation

Figure 4.7: Rotational distribution functions for molecules right after compression (Tt = 47512K, Tr = 5579K, Tv = 300K) and during QSS (Tt ≈ Tr ≈ Tv ≈ T_{int} = 14073K). The solid red lines represent Boltzmann distributions.

Tt = Tr = Tv = 300K. It clearly shows the non Boltzmann-like behavior where higher vibrational levels ($v > 5$) deviate a lot and are significantly overpopulated as compared to the equilibrium distribution. As the relaxation process continues and the gas dissociates, the non-equilibrium behavior of the gas reaches a Quasi-Steady State (QSS) where the population distribution becomes time invariant due to balance between inelastic and dissociative collisional process. In this region, high-energy tails ($v > 30$) are depleted relative to the corresponding Boltzmann distribution at Tt ≈ Tr ≈ Tv ≈ T_{int} = 14073K (Fig. 4.5(b)). The evolution of N_2 concentration (in Fig. 4.3(b)) shows that a significant portion (nearly 25%) of molecular dissociation happens before the gas reaches QSS. Thus, the early stage of the relaxation process is important when modeling dissociation under highly non-equilibrium conditions, since the vibrational energy of molecules directly relates to the probability of dissociation. Overpopulation of vibrational state distributions has been observed downstream of the shock in previous studies using DMS and full State-to-State (StS) approach [89, 144]. Also, numerous works have reported the generation and significance of an underpopulated QSS distribution [145, 136]. These are shown to reduce dissociation rate constants by a significant factor as compared to dissociation rates computed using equilibrium distributions [131].

4.4 ReaxFF Reactive PES

In this section, reactive ReaxFF PES is used to define the interaction between nitrogen atoms. ReaxFF is a bond-order based potential that accounts for the contribution from various energies which for binary collisions are given by [146]:

$$E_{ReaxFF} = E_{bond} + E_{over} + E_{under} + E_{val} + E_{pen} + E_{tors} + E_{conj} + E_{vdWaals} + E_{coulomb}$$

where terms on right hand side represents contribution from bond energy E_{bond}, over/undercoordination E_{over}, E_{under}, valence angle energy E_{val}, torsion energy E_{tors}, conjugation effects E_{conj}, Van-der-Waals interactions $E_{vdWaals}$ and Coulombic interactions $E_{coulomb}$ between every atom pairs. Each term is a function of bond-length dependent bond order of the pair of atoms which allows for a smooth transition from non-bonded to bonded system with no discontinuities in energy or forces during reaction. The terms have specific functional forms and respective fitting parameters associated. The reader is referred to [147, 139] for complete details on the fittings and forms for nitrogen system. Fig (4.8) presents the curve fit to a ReaxFF two-body potential. The dataset is constructed by computing ReaxFF energy of an isolated system of 2 interacting nitrogen atoms by sequentially varying the distance (r) between them. The aim of this least squares fitting is to compute quantized ro-vibrational energy levels based on ReaxFF potential using WKB approximation [61, 148, 149]. From this N_2 diatomic potential, total of 9194 rovibrational levels are found of which 7025 are bound and 2169 are quasi-bound states. Bound states have internal energy lower than dissociation energy $D^0 = 9.7746$ eV and quasi-bound states have internal energy higher than D^0. This spans a range of 288 and 54 rotational and vibrational states respectively. These quantized levels are used to find thermodynamic properties and equilibrium constant associated with the PES. It is also used later to construct equilibrium Boltzmann distribution of ro-vibrational energy states at a given temperature for comparison with instantaneous population distribution of an evolving gas under non-equilibrium conditions.

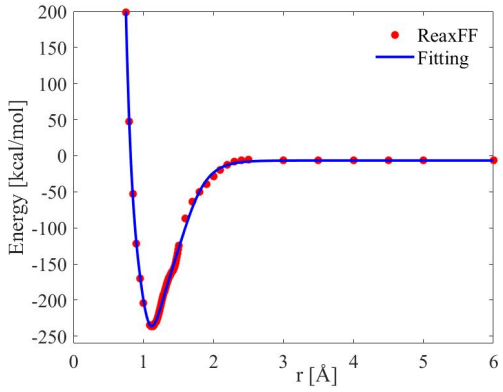

(a)

Figure 4.8: Curve fitting of 2-body ReaxFF potential

4.4.1 Comparison of MD with DMS under dissociation dominated adiabatic conditions

In this section, zero-dimensional MD adiabatic computation is performed under high-temperature conditions and compared with DMS [130]. This is equivalent to putting $\mathbf{A} = \mathbf{0}$ under the framework of OMD which corresponds to the NVE (constant energy) statistical ensemble. The DMS computation performed here is based on the same ab-initio data-set which is used for ReaxFF parameterization. The aim of the comparison is to consider DMS as a benchmark solution under this high-temperature dissociation-dominated regime and assess the performance of ReaxFF-based MD in analyzing non-equilibrium reacting flow. In this case, the system is initialized with pure molecular nitrogen with initial translational Tt, rotational Tr and vibrational temperature Tv set to 30000K.

In this case, all the system temperatures are initially high therefore the degree of dissociation is higher. Fig. 4.9(a) shows the time evolution of different temperatures and mass fraction of atomic nitrogen. As the system evolves, mass fraction of atomic nitrogen increases due to immediate dissociation. This process takes up energy from all the modes which result in the decrease of translational, rotational and vibrational temperatures until the system reaches macroscopic equilibrium. In this high-temperature case, both internal energy modes relax together and this relaxation overlaps reactive

processes which lead to a strong coupling between the two. Fig. 4.11(a) examines the corresponding rate of dissociation and recombination reactions. As expected, it shows the immediate majority of dissociations at an initial stage. As the system evolves, and temperature goes down, the rate of dissociation decreases and the rate of recombination increases. This is followed by a slow decrease in the rate of both the reactive processes together until it levels off and reaches a steady state. In conclusion, a very close comparison between MD and DMS in Fig. 4.9(b) and 4.10 verifies the suitability of ReaxFF potential in studying Nitrogen gas chemistry under non-equilibrium conditions. Note that the comparison between MD and DMS is performed only for the first few nanoseconds. This is owing to the reasoning that as temperature goes down with the increase in time, the contribution of recombination which is not modeled in DMS increases. This can lead to serious discrepancies in the long-time behavior between the two models.
Next, the analysis is proceeded by investigating population distribution functions (PDFs) at various time instants during dissociation to gain more microscopic insight into the gas dynamics. Fig. 4.11(b) shows the internal energy PDFs where the vertical dashed line corresponds to the dissociation energy of N_2 for the PES. The part towards the right with respect to this line corresponds to quasi-bound states and part towards the left corresponds to bound states. From the population distributions, it can be seen that the system initiates from the imposed equilibrium distribution at T = 30000K (solid brown line) and soon at $t = 0.5$ns (blue circles) becomes quickly depleted of higher rotational, vibrational and internal energy levels due to majority of heavy preferential dissociation. This depletion with respect to Boltzmann population at local internal temperature T_{int} in earlier stages can significantly lower the subsequent rate of dissociation as compared to gas in local equilibrium as reported in the earlier study [132, 130]. As time progresses the distribution starts converging to Boltzmann as shown by time-averaged red circles in 4.11(b) and 4.12. The same feature is also evident from the evolution of time-averaged dissociation probability density functions (pdfs) in Fig 4.13. The dissociation probability density from a given internal energy($p^D(\epsilon_{\text{int}}(j,v))$) / rotational($p^D(j)$) / vibrational state($p^D(v)$) is defined as the logarithm of ratio of number of molecules dissociating from that internal energy/rotational/vibrational level to the total number of molecules which dissociated in that time interval. This dissociation can be due to a collision with

either another molecule or an atom. The probability is time-averaged over a time window to reduce statistical noise. The dissociation pdfs based on internal energy levels at all times have a strong peak near the dissociation limit D^o as shown in Fig 4.13. Besides this, a significant number of dissociations also happen from bound states. The weightage of these low-lying energy states is greater than high-lying states initially as shown by blue circles at $t = 0.5\text{ns} \pm \Delta\text{t}_1$. This is due to the increased availability of collision energy from translation (Tt $\approx$ 18902K) which is enough to knock out atoms from molecular nitrogen bonded to a low-energy state. This probability decreases as the system evolves due to decrease in the translational temperature which unlevels the pdf and increases the contribution of the quasi-bound states lying on the right side as shown by red circles at $t = 2.5\text{ns} \pm \Delta\text{t}_2$. Note that time interval $\Delta\text{t}_1 = 1\text{ns}$ is chosen to be smaller than $\Delta\text{t}_2 = 3\text{ns}$ due to steep gradients observed at initial stage. The similar characteristics of non-equilibrium dissociation pdfs are also reported in the earlier DMS study [130]. The other plots in Fig 4.13 show the pre-collision rotational and vibrational energy distributions of dissociated reactants at two time instants where the binning is based on rotational and vibrational quantum levels respectively. It is apparent from the plots that molecules have strong biasing where the tendency of molecules dissociating from higher vibrational levels and intermediate rotational levels is significantly high. A similar assertion regarding vibrational favoring has been made in [132, 150]. Note that the probability suddenly drops as v is increased beyond 48. This is due to the scarcity of the molecules at high-levels of the vibrational manifold and hence the possibility of dissociating from those levels goes down. As time evolves, the weightage shifts to the left and right of dissociation pdfs based on vibrational and rotational quantum numbers respectively. This is due to continued dissociation with time which led to low population of molecules at higher vibrational and intermediate rotational levels in the underlying pool of undissociated molecules. Fig 4.14 also shows the post-collision exchange probability density (red circles). The pre-collision molecules also display similar distribution. In contrast to dissociation, exchange pdf roughly follows the instant population distribution of molecules in the gas. This suggests that the exchange reaction has no biasing towards any specific rovibrational state.

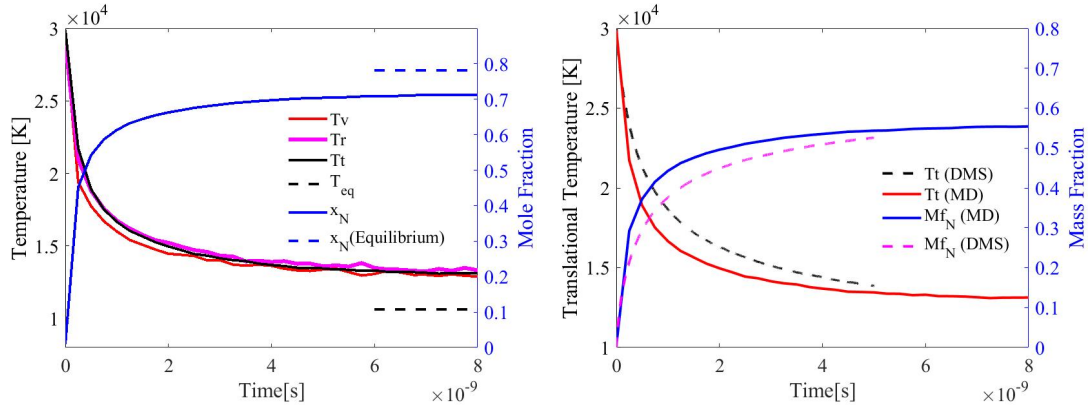

(a) (b)

Figure 4.9: (a)Evolution of different temperatures and composition obtained by MD in dissociation dominated regime. Initial state: Tt = Tr = Tv = 30000K. Comparison of translational temperature and mass fraction with DMS (dashed lines).

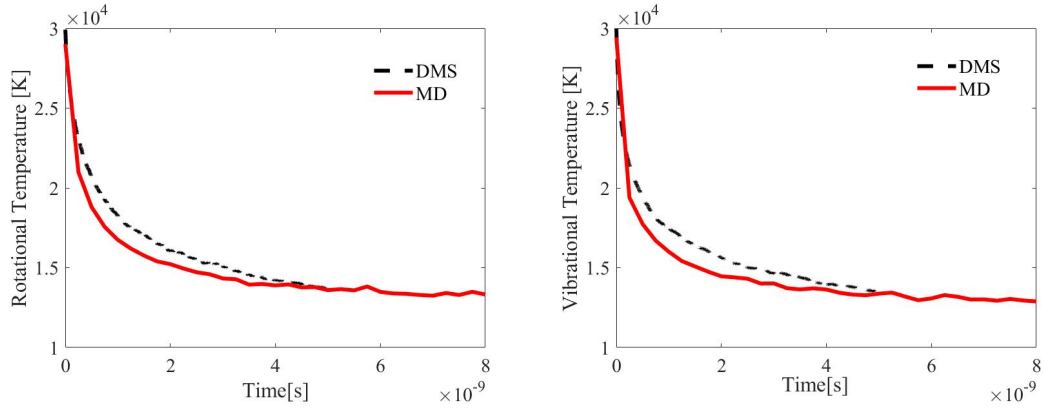

(a) (b)

Figure 4.10: Comparison of evolution of (a) rotational and (b) vibrational temperature with DMS (dashed lines).

4.4.2 Comparison of MD with CFD under recombination dominated adiabatic conditions

In this section, the focus is on the recombination-dominated regime. This means that at an initial state, the mole fraction of Nitrogen molecules is lower than the equilibrium

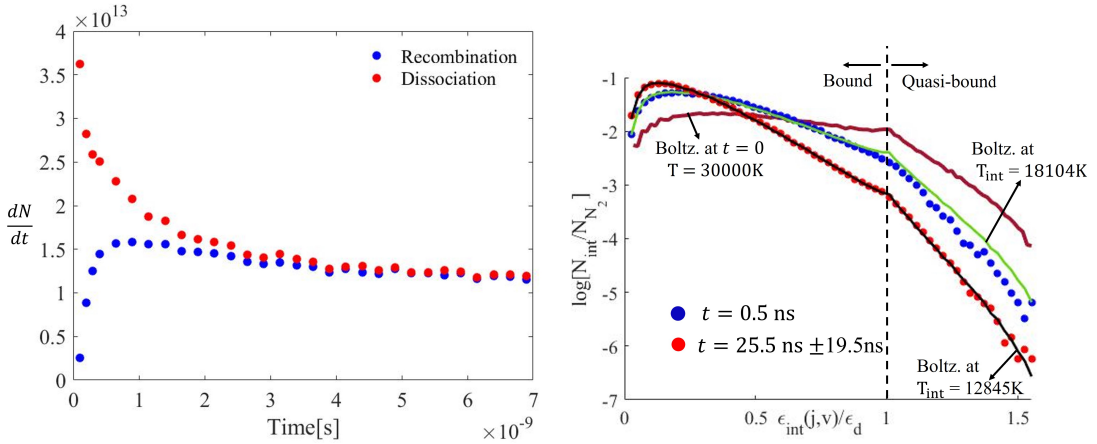

Figure 4.11: Time evolution of (a) number of dissociations and recombinations per unit time (b) rovibrational energy populations (blue and red circles). Brown line depicts theoretical Boltzmann distribution at $t = 0$. Green and black lines: Boltzmann distribution at local internal temperature T_{int}. Initial state: Tt = Tr = Tv = 30000K.

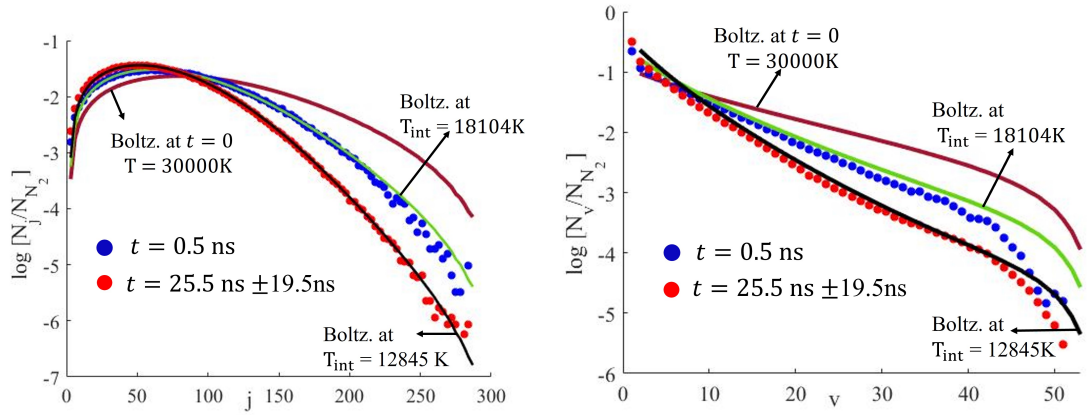

Figure 4.12: Time evolution of (a) rotational and (b) vibrational population distribution functions (blue and red circles). Brown line depicts theoretical Boltzmann distribution at $t = 0$. Green and black lines: Boltzmann distribution at local internal temperature T_{int}. Initial state: Tt = Tr = Tv = 30000K.

composition at that temperature. This will lead to the majority of net recombination processes as seen in Fig. 4.15(b) which shows an increase in the concentration of nitrogen

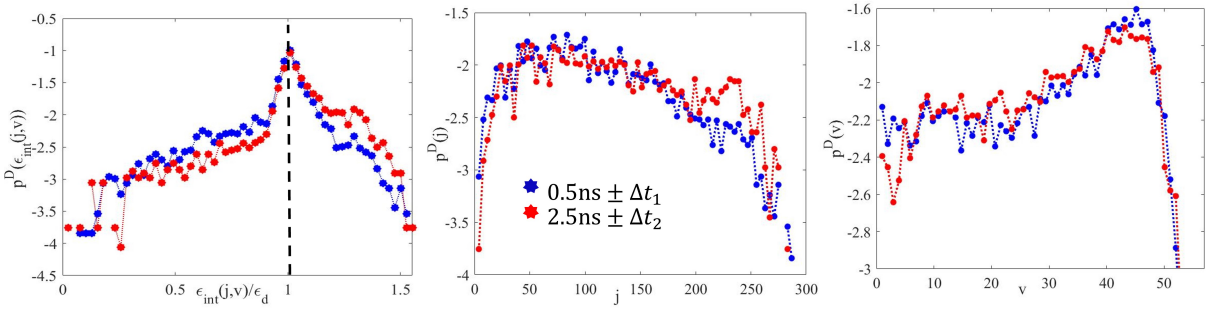

Figure 4.13: Time-averaged evolution of dissociation probability density. Blue and red circles depict density at different times t_1 and t_2 where $t_2 > t_1(\mathrm{Tt}_2 < \mathrm{Tt}_1)$ respectively.

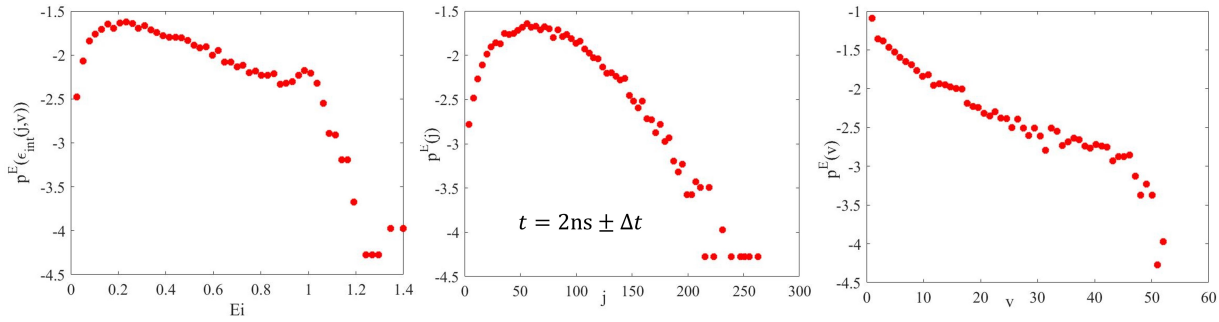

Figure 4.14: Time-averaged evolution of exchange probability density.

molecules with time. This net recombination process releases thermal energy into the gas which increases the translational, rotational and vibrational temperature of the system. It indicates that as the system evolves and nitrogen molecules appear, vibrational temperature increases at a higher rate than translational and rotational and overshoots the two temperatures. This is in contradiction with the behavior observed while using (2T) CFD. CFD modeling is based on a system of equations given in (4.3) and (4.4) where the standard Park's model for reaction rate coefficients, Landau-Teller model [151] for vibration exchange with relaxation times obtained from the Millikan-White correlation [126], harmonic oscillator model to represent the vibrational excitation of diatomic species and non-preferential model of vibrational energy change due to chemistry is employed. A more complete description of these models, is given by Nompelis [140]. CFD predicts qualitatively an opposite trend as shown in Fig. 4.15(a) where

translational-rotational temperature T increases at a faster rate than vibrational and is higher during initial evolution. To some extent, relaxation of rotational mode is slightly faster than vibrational but overall ro-vibrational relaxation is more rapid in MD than what CFD predicts. Note that **A** is identically zero for the adiabatic system investigated in this section.

Figure 4.15(b) shows a comparison between composition histories obtained from MD and CFD. MD predicts a change of curvature of the mole fraction profile at the initial stage during evolution. It follows the "s-shape" curve where the initial production of nitrogen molecules is slower in contrast to the behavior observed in CFD which predicts a fast steady production until it gradually levels off. State-to-state study by Colonna et al. [152] also reported a similar qualitative 's-shape' trend of their atomic nitrogen mole fraction profile in recombination dominated regime. This s-shape feature is also evident in Fig. 4.16(a) which shows the rate of reactive processes under these conditions. It shows that both recombinations, as well as dissociations, follow a similar trend with recombination being a little higher than dissociation in the early stages. This difference goes down as the system evolves and reaches equilibrium. The overall rate evolution can be divided into 3 stages where in the first stage, system see a slow rise in reactive processes. This is followed by a constant linear increase of recombinations and dissociations in the second stage. In the final stage, the rate goes down and the system reaches a steady state.

The population distributions extracted at different time instants during the evolution is also presented. Internal energy population distribution time evolution in Fig. 4.16(b) starts from the equilibrium distribution (brown solid line) at $t = 0$ (T = 2000K) which quickly becomes non-Boltzmann (blue solid points) and shows the cusp near dissociation limit of N_2 molecule. This happens due to a higher probability of recombining into a state whose energy is close to dissociation energy. Fig. 4.17(a) and (b) show the rotational and vibrational population distributions where rovibrational energies are binned based on rotational and vibrational numbers respectively. Rotational number-based distribution possesses significant non-Boltzmann character during early stages where overpopulation of high and low rotational levels and a dip in between as compared to local equilibrium Boltzmann at T_{int} is seen. A long plateau is also seen in the vibrational energy distribution which happens due to the majority of preferential

recombination. As time evolves the distribution starts converging to Boltzmann.

A similar characteristic of recombining non-equilibrium gas is also evident in the evolution of recombination probability density shown in Fig. 4.18. It shows the probability that atoms will recombine to a particular internal energy state at two time instants $t_1 = 3.75\text{ns} + \Delta\text{t}$ (blue circles) and $t_2 = 11.25\text{ns} + \Delta\text{t}$ (red circles). These instants correspond to different states where translational temperature at t_2 is higher than t_1 ($\text{Tt}_2 > \text{Tt}_1$). It shows that likelihood of a molecule recombining into a state close to the dissociation limit is high and as time progresses and translation temperature increases, density flattens increasing the contribution of quasi bound and bound states lying away from D^0. Fig. 4.18 also shows the corresponding density with respect to rotational and vibrational quantum numbers. At $t = t_1$, the majority of recombined molecules have high vibrational and intermediate rotational numbers. As Tt increases, more molecules starts appearing at low v. Corresponding to this, the rotational recombination probability function shifts towards the right and flattens. This is all consistent with the instantaneous snapshot of PDFs analyzed earlier. A similar trend is also reported in previous works based on QCT and theoretical analysis based on the principle of microscopic reversibility [51, 134].

For completeness, Fig. 4.19 shows the dissociation probability density at the same time instants as that of recombination pdfs. During the first time interval, the distribution exhibits similar behavior where the majority of pre-dissociation reactants are narrowed near $\epsilon_{\text{int}}(\text{j}, \text{v}) = \epsilon_{\text{d}}$ curve but the contribution of bound states is exceedingly small and the drop is sharp away from D^0 due to the low translational temperature in contrast to the case of dissociation dominated regime, investigated in the previous section. As time evolves and gas reaches closer to attaining an equilibrium state the dissociating pdf (red solid circles in Fig. 4.19) starts resembling recombination pdf (red solid circles in Fig. 4.18) as expected.

Fig. 4.20 shows the evolution of different components of energy as time progresses. Total energy of the system is a summation of these different components which include thermal energy of particles $[\rho e]^{\text{tra}}$, ro-vibrational energy of molecular nitrogen $[\rho e]^{\text{rovib}}_{\text{N}_2}$, and formation energy of atomic nitrogen $[\rho e]^{\text{form}}_{\text{N}}$.

$$[\rho e]_{\text{Total}} = [\rho e]^{\text{tra}} + [\rho e]^{\text{rovib}}_{\text{N}_2} + [\rho e]^{\text{form}}_{\text{N}} = \frac{3}{2}(\frac{\rho_{\text{N2}}}{M_{\text{N}_2}} + \frac{\rho_{\text{N}}}{M_{\text{N}}})\text{RTt} + [\rho \text{e}]^{\text{rovib}}_{\text{N2}} + \rho_{\text{N}}\text{h}^0_{\text{N}}$$

where $h^0_{N_2} = 0$, R is universal gas constant and M_s is mass per unit mole of species s. Since bulk velocity $\mathbf{v}$ is set to zero initially and it remains conserved, the contribution of kinetic energy has been ignored. As the gas evolves over time, translational temperature and mole fraction of molecular nitrogen increase. This results in an increase in thermal and ro-vibrational energy and a decrease in the formation energy of atomic nitrogen. The total energy of the system remains conserved as expected. This conservation of energy can be used to find the final equilibrium state of the gas as described in [133]. This state is characterized by a single equilibrium temperature where Tt=Tr=Tv and populations of internal energy levels satisfy Maxwell-Boltzmann statistics based on ReaxFF. The equilibrium constant is obtained utilizing the conventional approach of using partition functions derived from energy levels. The equilibrium temperature and mole fraction of molecular nitrogen corresponding to the system investigated here are shown in the green solid line in Fig. 4.15(a) and (b). The steady-state which ReaxFF predicts is higher in temperature and in mole fraction in comparison with theoretical equilibrium state. The source of this difference is suspected to be the incomplete representation of the MD reactor by the underlying ab-initio dataset of Paukku et al.[60] which is based on 4N atoms in isolation. Occasionally, MD can encounter instances where more than 4 N atoms interact which is not included in the training data set of ReaxFF parameterization and hence can create little inconsistency. Additionally, there can be some source of error in the 2-body ReaxFF fitting.

In conclusion, the stark discrepancy observed in this section between continuum and molecular predictions is an additive effect of the various shortcomings of the correlated models used in the CFD modeling. The system is majorly comprised of atomic nitrogen at $t = 0$. This will lead to the majority of molecule-atom $N_2 + N$ collisions at an initial instant. It is known from previous studies that internal energy relaxation is much faster for $N_2 + N$ as compared to the $N_2 + N_2$ system and is poorly captured by experimentally determined Millikan-White correlation [126]. Furthermore, the widely used non-preferential assumption that reactive processes like dissociation/recombination leads to removal /addition of average vibrational energy of the molecules in the ensemble multiplied by the rate of production of the molecules w_{N_2}, incorporated in the vibrational energy source term w_v [140] is highly inappropriate. This is supported by the

evolution of microscopic recombination and dissociation probability densities investigated in this and previous sections which showed that a major chunk of energy during reactive processes is contributed by a population close to the dissociation energy limit. This suggests that the vibrational energy of dissociating and recombining molecule is higher than the average vibrational energy of molecules in the reactor. Therefore, MD predicts preferential vibrational energy change due to chemistry which leads to high instantaneous Tv as compared to CFD in Fig. 4.15a. It is known that Park's model significantly overpredicts dissociation rates [129, 125]. Since recombination rate in CFD is obtained using the principle of detailed balance. This leads to higher resulting recombination rates which is manifested by the fast production of N_2 molecules in the early stages as shown in Fig. 4.15(b). Moreover, although recombination rates are obtained starting from a situation of thermodynamic equilibrium T = Tv, underlying dissociation rates are based on non-equilibrium conditions which creates irregularity[153]. These inconsistencies present in the physical models motivate the better modeling of relaxation, chemistry and internal energy production (source term) under far-from-equilibrium conditions. Few such efforts have been made in [51, 52, 154, 155, 156, 53].

Note that there is a significant difference between the macroscopic steady equilibrium state attained by CFD and MD. This is expected because Park model of the equilibrium constant used in the CFD modeling is different compared to the equilibrium constant which corresponds to the ReaxFF potential. Park model also includes the contribution from electronic degrees of freedoms which is absent in the computations based on the ground energy state PES performed in this work.

4.4.3 Comparison of MD with DSMC under recombination dominated adiabatic conditions

In this section, we make comparison of MD with the other modeling approach of DSMC which is shown in Fig. 4.21 (DSMC computation is performed by Michael Kroells at University of Minnesota). The simulation starts out with pure atomic nitrogen ($x_N = 1$) at translational temperature of 500K and mass density of 1.25 kg/m^3. The initial conditions are chosen such that it induces significant recombination. As simulation evolves, mass fraction of molecular nitrogen and translational temperature increases.

Both the profiles show similar "s-shape" trend where there is initial lagging before nitrogen molecule starts forming steadily until it levels off. Corresponding to this, rotational and vibrational temperature starts out with high values followed by rapid relaxation to a final trans-rovibrational temperature. The predictions of MD have severe disagreements with DSMC on multiple fronts. It is observed that relaxation of internal energy modes happen over much smaller time scales in MD as compared to DSMC. Under the conditions chosen, the coupling between the rotational and vibrational modes is more prominent in MD than what DSMC predicts. There exist separation in the time scale of relaxation of both the internal energy modes and hence rotational and vibrational modes are fairly decoupled in DSMC. Similar to recombination-dominated CFD predictions in the previous section, DSMC shows fast production of N_2 molecules and does not capture the correct trend of translational temperature and mole fraction profiles. The equilibrium steady state composition and temperature of both the models have significant discrepancy. This is expected because both the analysis corresponds to different equilibrium constants. Next, Fig. 4.22 shows the temperature and mole fraction evolution of systems, initialized at different densities. It is observed that with increase in density, the final equilibrium temperature increases and mole fraction decreases. The system with lowest density of 0.5kg/m^3, takes the longest time to approach the thermo-chemical equilbrium state as expected.

4.4.4 Compression and relaxation of nitrogen gas in an OMD reactor

In this section, non-equilibrium evolution of relatively cold gas under sudden uniform compression followed by relaxation is studied. This is achieved by setting $\mathbf{A}$ to $\kappa\mathbf{e}_1 \otimes \mathbf{e}_1 + \kappa\mathbf{e}_2 \otimes \mathbf{e}_2 + \kappa\mathbf{e}_3 \otimes \mathbf{e}_3$, $\kappa = -5\text{x}10^8\text{s}^{-1}$ and to $\mathbf{0}$ for compression and relaxation respectively. The system mimics the behavior of gas in the shock front and immediately behind in the temporal frame where the transient behavior of the system can be mapped to several locations across the shock wave. The initial temperature and mole fraction corresponds to an equilibrium system of cold nitrogen gas at 300 K with initial total mass density of $\rho(0) = 1.25\text{x}10^{-3}\text{kg/m}^3$. The initial population follows a Maxwell-Boltzmann distribution at this temperature. Fig. 4.23(a) plots the evolution of translation, internal temperatures and mole fraction of nitrogen atoms. Note that a little higher Tv than 300K at $t = 0$ is an artifact of the classical approach for vibrational

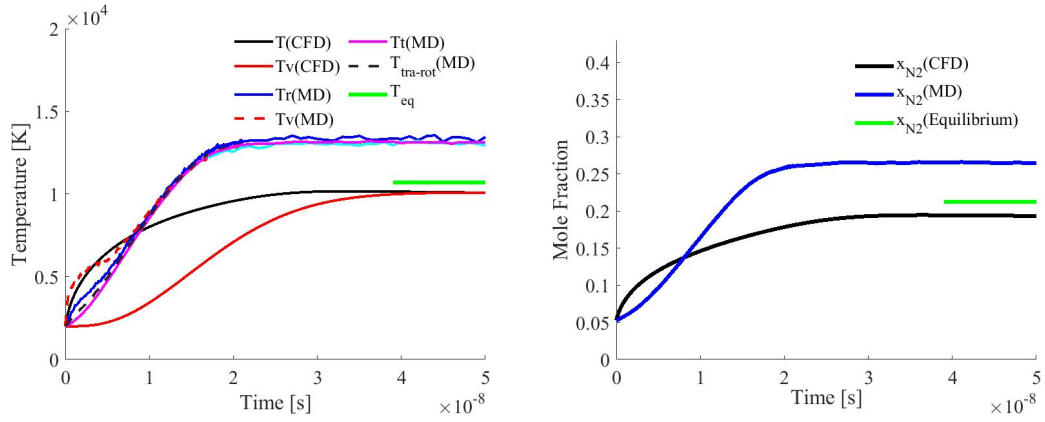

Figure 4.15: (a) Adiabatic recombination dominated relaxation. Initial state: Tt = Tr = Tv = 2000K. Translational, rotational, vibrational and trans-rotational temperature computed from MD are depicted by solid pink, solid blue, dashed red and dashed black lines respectively. Comparison with Park model: Red and black solid lines depict vibrational and ro-translational temperature respectively. (b) Corresponding evolution of mole fraction of molecular nitrogen computed from MD (solid blue line) and CFD (solid black line).

energy determination which is significant at lower temperatures.

During the compression phase, gas excites and translational temperature increases rapidly, whereas the excitation of internal energy mode is slower. This results in thermal non-equilibrium between various energy modes of the gas which indicates that the two-temperature definition which is used in CFD modeling is not adequate to characterize the state of the gas under these conditions. This is clearly evident in Fig. 4.23(b) which shows zoomed-in view of compression. It is observed that dissociation of the gas doesn't initiate until the vibrational mode is sufficiently excited which majorly happens in the relaxation regime.

During relaxation, internal energy modes excite and gas immediately starts dissociating which removes translation energy from the system. The equilibration of rotational energy with translational is observed to be more rapid than the vibrational energy. Rotational temperature increases and equilibrates with translational temperature at about 11150K followed by equilibration with vibrational temperature at about

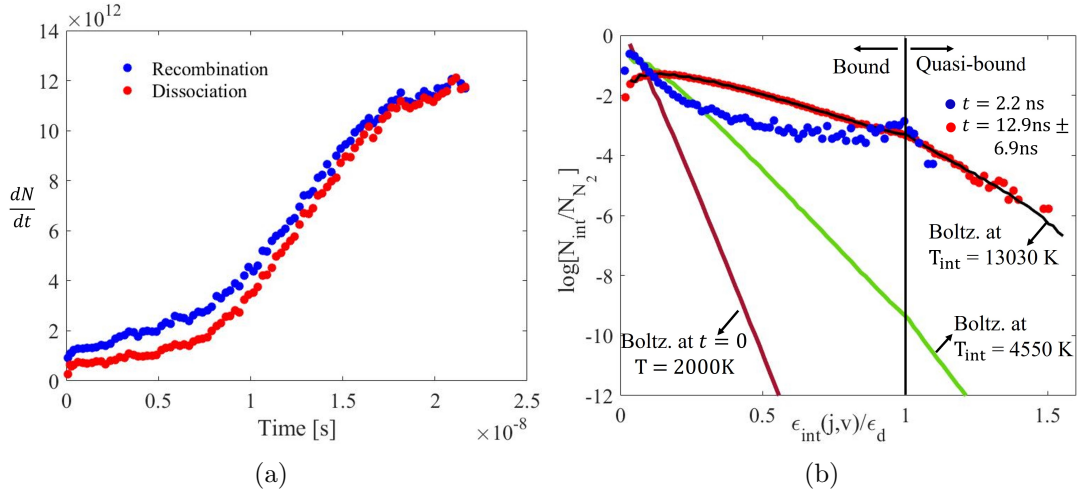

Figure 4.16: Time evolution of (a) number of dissociations and recombinations per unit time (b) ro-vibrational energy PDFs (blue and red circles). Brown line depicts theoretical Boltzmann distribution at $t = 0$. Green and black lines: Boltzmann distribution at local internal temperature T_{int}.

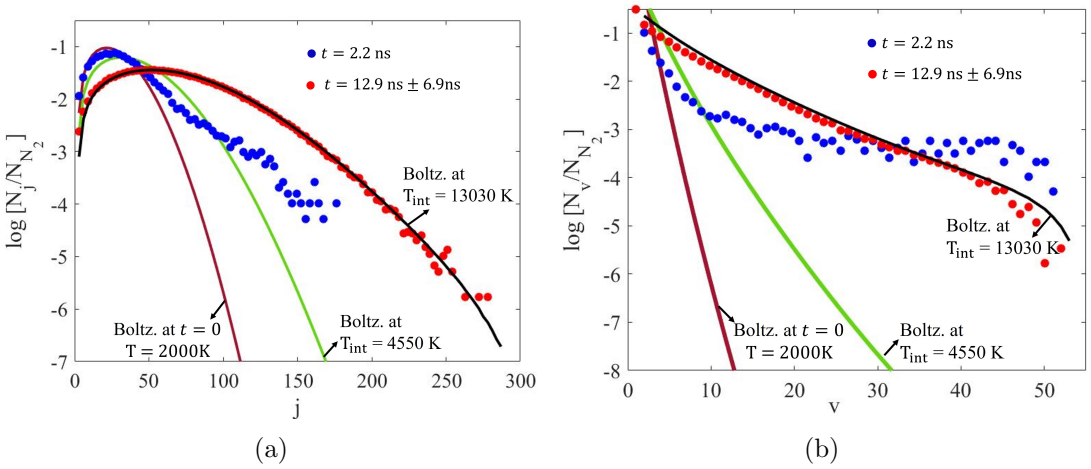

Figure 4.17: Time evolution of (a) rotational and (b) vibrational population distribution functions (blue and red circles). Brown line depicts theoretical Boltzmann distribution at $t = 0$. Green and black lines: Boltzmann distribution at local internal temperature T_{int}.

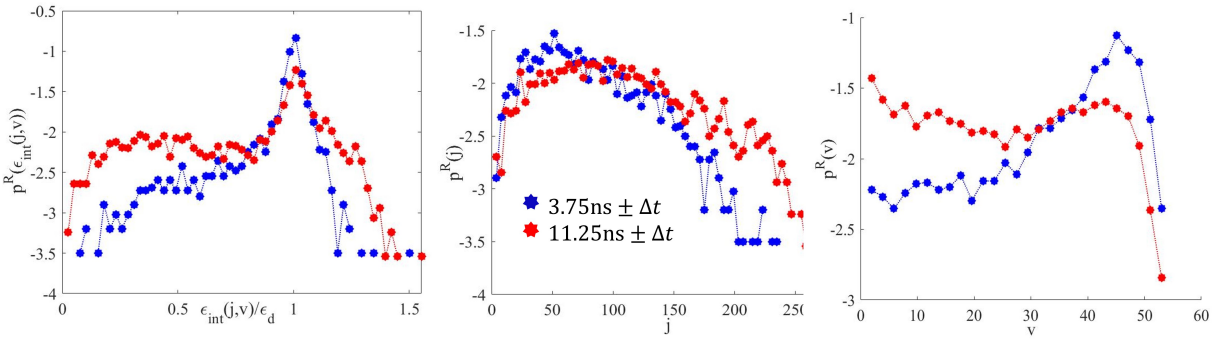

Figure 4.18: Time evolution of recombination probability density. Blue and red circles depict density at different times t_1 and t_2, where $t_2 > t_1 (\mathrm{Tt}_2 > \mathrm{Tt}_1)$ respectively.

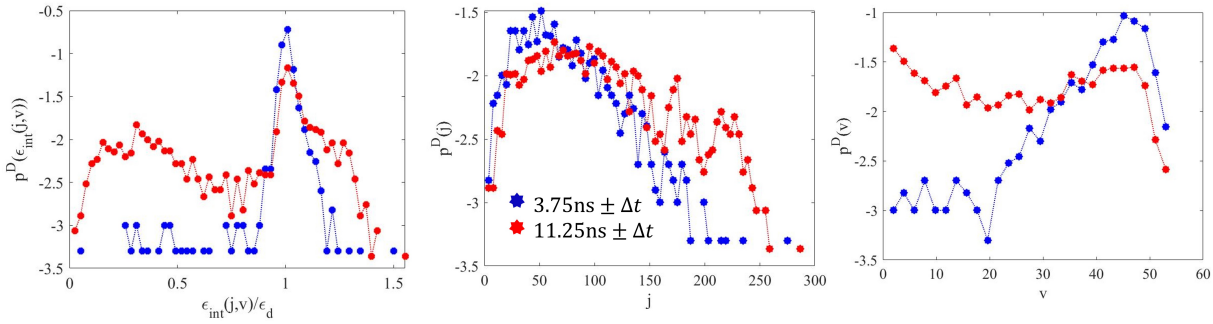

Figure 4.19: Time evolution of dissociation probability density. Blue and red circles depict density at different times t_1 and t_2, where $t_2 > t_1 (\mathrm{Tt}_2 > \mathrm{Tt}_1)$ respectively.

$\mathrm{Tt} \approx \mathrm{Tr} \approx \mathrm{Tv} \approx 9765\mathrm{K}$. Only about 3 percent of dissociation happens in this rovibrational excitation period whereas the majority of reactive collisions occur in a regime where all the energy modes are in thermal equilibrium with each other and is cooling gradually. Thus, the internal energy relaxation and reactive zones are separated. Careful choice of the **A** tensor and time duration of the compression regime can qualitatively provide different non-equilibrium behavior of a gas under different strengths (enthalpy) of the shocks. Fig. 4.23(b) shows the evolution of the inverse of total density $\rho = \rho_{\mathrm{N}_2} + \rho_{\mathrm{N}}$ of the system in the compression regime which decreases abruptly, over a short period of time. This is given by eq(4.5) which simplifies to $\rho_t = \frac{\rho_0}{(\kappa t+1)^3}$ for uniform dilatation.

Further insight may be gained by examining population distribution evolution based

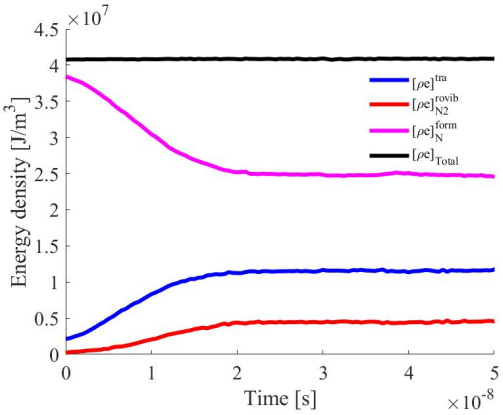

Figure 4.20: Time history of different components of energy for a system under recombination-dominated-regime.

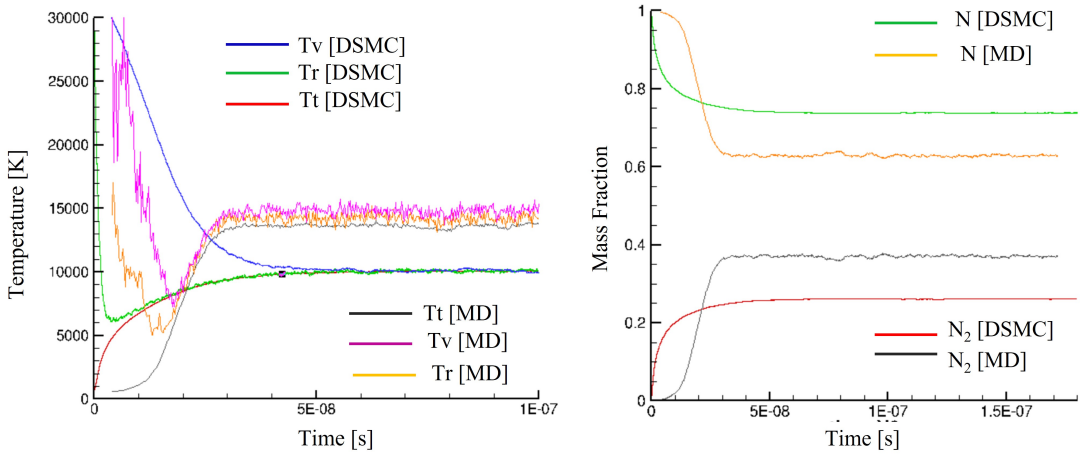

(a) (b)

Figure 4.21: Comparison of the evolution of (a) different temperatures and (b) mass fractions obtained by MD with with DSMC. Initial state: $\rho = 1.25\text{kg/m}^3, \text{Tt} = 500\text{ K}, \text{mf}_\text{N} = 1$

on internal energy, and rotational and vibrational quantum numbers during compression phase as shown in Fig. 4.24. In the early stages of the compression, due to very high translational temperature, non-Boltzmann-like behavior is observed where higher internal energy, rotational and vibrational states get substantially populated rapidly as

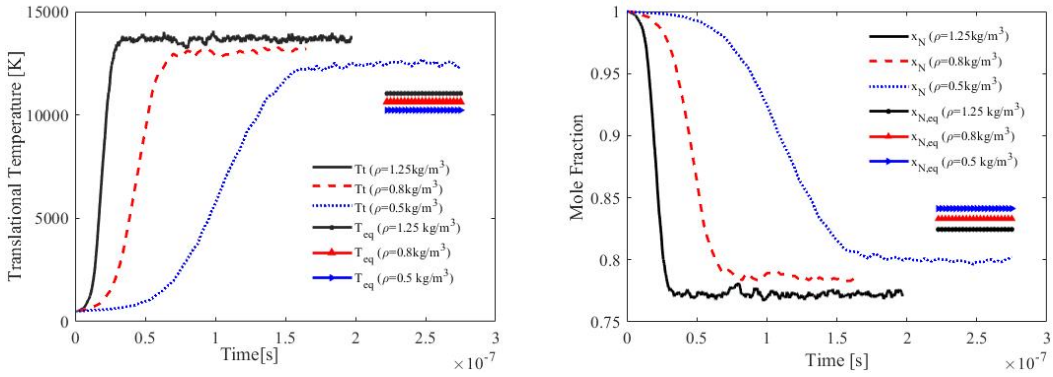

(a) (b)

Figure 4.22: Comparison of the evolution of (a) temperature and (b) mole fraction between different adiabatic reactors, initiated at different densities. Initial states: (1) $\rho = 1.25\text{kg/m}^3, \text{Tt} = 500\text{K}, \text{x}_\text{N} = 1$, (2) $\rho = 0.8\text{kg/m}^3, \text{Tt} = 500\text{K}, \text{x}_\text{N} = 1$, (3) $\rho = 0.5\text{kg/m}^3, \text{Tt} = 500\text{K}, \text{x}_\text{N} = 1$

gas evolves. The higher-lying levels become more populated the further gas excites in compression regime. These features are in line with what has been observed in previous DMS and state-resolved master equation studies of shock wave [89]. The disruption of rotational number-binned PDF in Fig. 4.24(b) relative to the equilibrium distribution at $t = 0$ starts from levels with lower quantum numbers as gas evolves under compression thus eventually reaching a distribution that is far-from-Boltzmann. Fig. 4.25(a) shows vibrational number based PDF at the end of compression cycle. It is evident from the plot that in the current situation, local Boltzmann-like vibrational-binned distribution at characteristic vibrational temperature Tv or internal temperature T_int can not not be defined to characterize non-equilibrium physics. OMD computed distribution (in blue solid circles) shows significant departure from Boltzmann statistics. The time history of PDF in the relaxation regime is omitted here due to its similarity with the behavior of a gas under adiabatic conditions in dissociation-dominated regime investigated in section 4.4.1. Fig. 4.25(b) finally shows the speed distribution of N_2 molecules at an instant where the gas is in a highly compressed state. It shows the rapid relaxation of the translational mode of the gas where speed distribution quickly becomes locally Maxwellian defined at an average translational temperature of the mixture. The distribution can

strongly deviate when one makes different choice of flow guided by tensor **A** as shown in section 3.4.3.

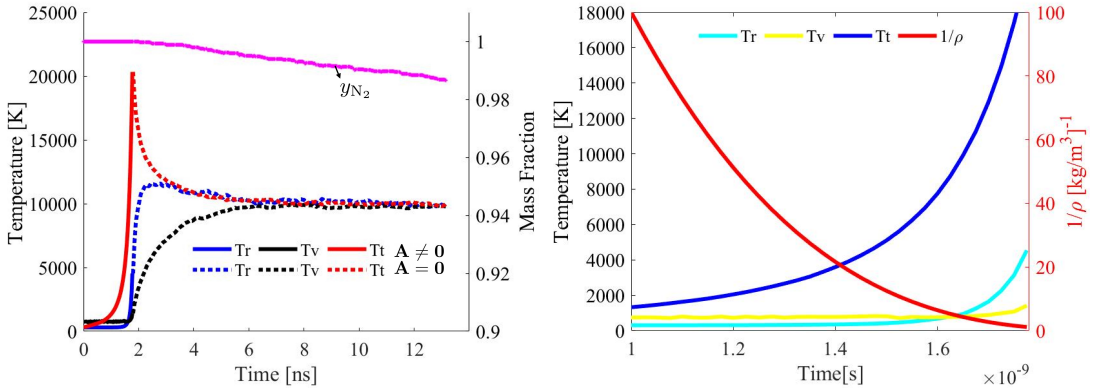

(a) (b)

Figure 4.23: (a) Time history of mass fraction of molecular nitrogen, system translation temperature, rotational and vibrational temperature during compression $\mathbf{A} \neq \mathbf{0}$ and relaxation regime $\mathbf{A} = \mathbf{0}$ (b) Zoomed in view of compression evolution.

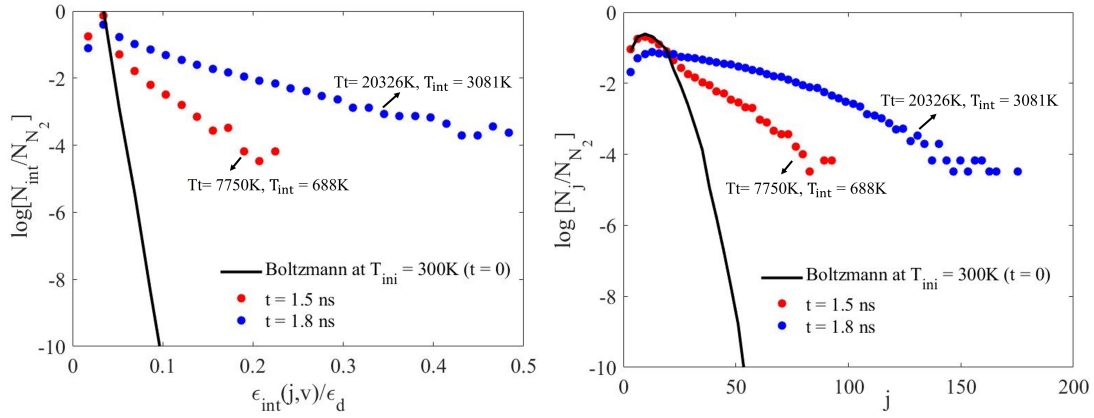

(a) (b)

Figure 4.24: Evolution of (a) rovibrational energy and (b) rotational number binned populations (blue and red circles) during compression. Black line depicts theoretical Boltzmann distribution at $t = 0$.

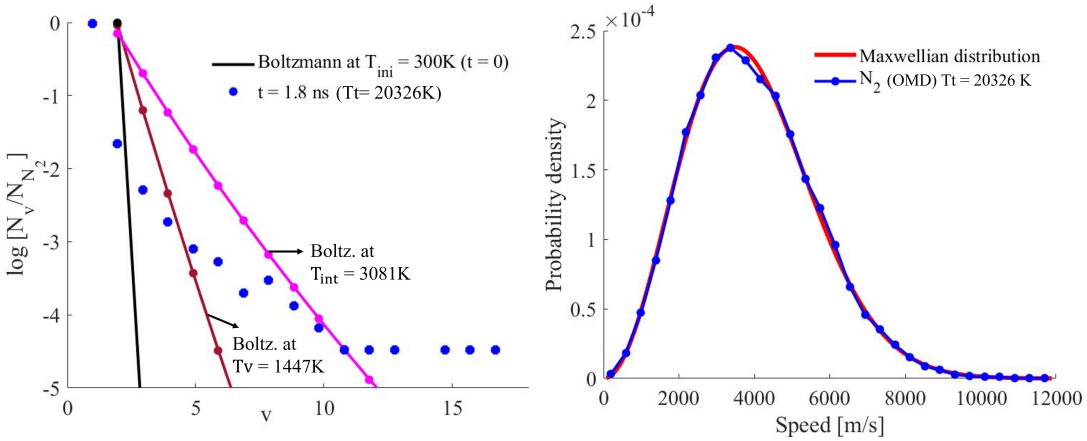

(a) (b)

Figure 4.25: Vibrational population distribution function (blue circles) for molecules at the end of compression. Black line depicts theoretical Boltzmann distribution at $t = 0$. Brown and pink solid lines: Boltzmann distribution at local vibrational Tv and internal temperature T_{int} respectively. (b) Speed distribution of N2 molecules at the end of compression regime. The solid red lines represent Maxwellian distributions at instantaneous Tt.

4.4.5 Expansion and relaxation of nitrogen gas in an OMD reactor

Expansion and relaxation are achieved by choosing the same form of **A** as done in the previous case. The only difference is that κ is positive ($\kappa = 1\text{x}10^9\text{s}^{-1}$) here which results in the enlargement of the fundamental domain of simulated atoms with time. This setting replicates the behavior of gas in nozzle expansion in the time domain. The analysis is initiated with the partially dissociated gas at thermal equilibrium at 10000 K with $\rho^0 = 10\text{kg/m}^3$ and 50 percent diatomic nitrogen (by mass fraction). Higher initial density (still in dilute gas regime) is chosen to capture the noticeable impact of recombination reactions on the behavior of expanding gas within the time scale of MD. The result of temperature and mass fraction evolution during the expansion and relaxation regime is plotted in Fig. 4.26(a). Contrary to the previous case, sudden expansion leads to rapid cooling which decreases the translational temperature followed by rotational and vibrational. During expansion, large drop in gas density and temperature,

increases internal energy relaxation time which results in freezing of rotational and vibrational temperature. This leads to situation where Tt < Tr < Tv at the end of the expansion cycle as shown in Fig. 4.26(b). During this time, atomic nitrogen recombines and the mass fraction of molecular nitrogen increases followed by its freezing. This is reminiscent of the behavior observed downstream of the throat of nozzle. In the relaxation regime, the translational mode excites and internal energy modes relax. The rotational temperature equilibrates with translational temperature first at about $\approx$ 4703K followed by vibrational at about $\approx$ 5010K. The dynamics of gas in the relaxation regime is slower due to a smaller mass density which resulted from expansion ($\rho_t = \frac{\rho_0}{(\kappa t+1)^3}$). This is evident from slow recombination and rate of change of temperature as compared to dynamics in the first nanosecond of expansion.

Next, PDF evolution is shown in the Fig. 4.27(a), (b) and 4.28(a). At $t = 0$ gas initiates with the Boltzmann distribution at given equilibrium temperature of 10000K. As time evolves, internal energy distributions show a strong cusp near the dissociation limit due to the strong favorability of the formation of recombined states there. Vibrational distributions in Fig. 4.28(a) start relaxing from tails and show characteristic "L shape" driven by majority of recombinations, vibration- to-vibration energy exchange (V-V) and vibration-to-translation (V-T) relaxation. The plateau part in the distributions becomes longer as time evolves and the population of low-lying levels remain almost constant. Local Boltzmann distributions at T_{int} shown by solid black and green line are located significantly lower for high-lying vibrational levels and are little higher for low-lying levels. The departure from Boltzmann statistics for low-lying levels is less extreme in comparison to gas under compression, investigated in the previous section. Overall, one can see the qualitative similarity of the OMD computed vibrational distribution reported here with state-to-state modeling and experimental studies undertaken to study nozzle expansion and nonequilibrium vibrational kinetics in the literature. [137, 144, 157]. These strong non-equilibrium distributions can directly influence the corresponding energy flux and reaction rates as investigated in [137, 152, 158].

Low-lying internal energy states in Fig. 4.27(a) are in thermal equilibrium at an internal temperature where they follow Boltzmann distribution (solid black and green lines) plotted at local internal temperature(T_{int}). High-lying states are overpopulated and the distribution deviates from Boltzmann-like shape. This disruption starts from lower

levels as the gas evolves and expands. Corresponding to this, population of low and high-lying rotational states are higher as compared to Boltzmann at T_{int}.

As the relaxation process continues and the gas slowly recombines, we see that non-equilibrium behavior of the gas reaches a Quasi-Steady State (QSS) where the population distribution becomes time invariant due to balance between inelastic and recombinative collisional process. In this region, high internal energy, rotational and vibrational tails are overpopulated relative to the corresponding Boltzmann distribution at Tt $\approx$ Tr $\approx$ Tv $\approx$ 5280K as shown in Fig. 4.29. Fig. 4.28(b) shows the speed distribution of N_2 and N at the end of the expansion regime. This state corresponds to thermal and chemical non-equilibrium where translational and internal temperatures of the gas are different. Right before the relaxation, when the gas is in a highly expanded state, the instantaneous distribution of N_2 and N follows the Maxwell-Boltzmann distribution closely within statistical uncertainty. This shows that the translational mode rapidly relaxes to the local equilibrium speed distribution defined at the corresponding instantaneous translation temperature.

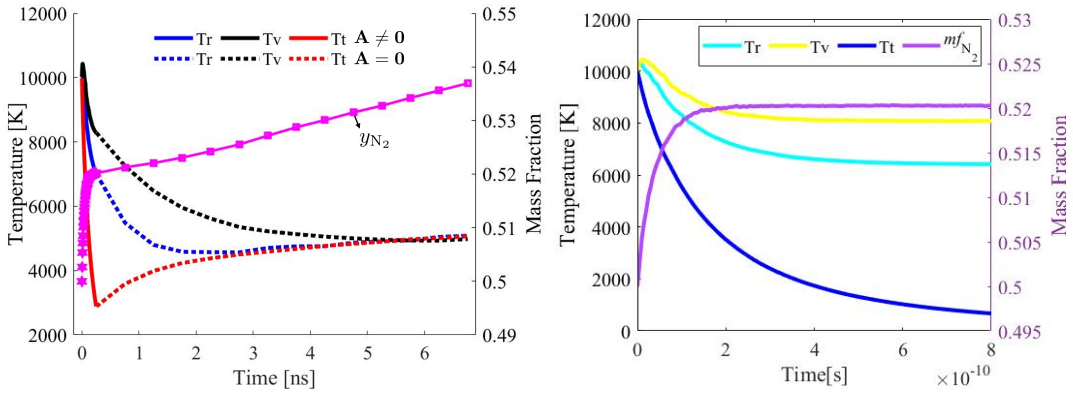

Figure 4.26: (a) Time history of mass fraction of molecular nitrogen, system translation temperature, rotational and vibrational temperature during expansion $\mathbf{A} \neq 0$ and relaxation regime $\mathbf{A} = 0$. (b) Zoomed in view of expansion evolution.

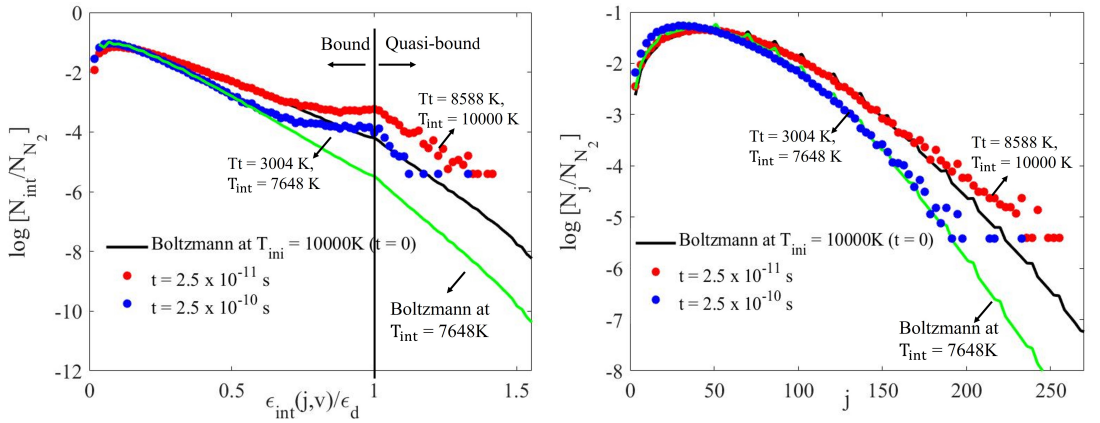

Figure 4.27: Evolution of (a) rovibrational energy and (b) rotational number binned populations (blue and red circles) during expansion. Black (equilibrium distribution at $t = 0$) and green lines: theoretical Boltzmann distribution at local internal temperature $\mathrm{T_{int}}$.

4.4.6 Comparison of OMD with reduced fluid dynamics

Next, comparison of the OMD predicted composition and temperature time history of gas under uniform compression $\kappa < 0$ and expansion $\kappa > 0$ investigated in previous sections is made with reduced CFD model. The set of ODE's given in (4.3) and (4.4) for the chosen value of $\mathbf{A}$ tensor for this system simplifies to

$$\frac{\mathrm{d}\rho_{\mathrm{N}_2}}{\mathrm{d}t} + \rho_{\mathrm{N}_2}\frac{3\kappa}{\kappa t+1} = w_{\mathrm{N}_2},\ \frac{\mathrm{d}\rho_{\mathrm{N}}}{\mathrm{d}t} + \rho_{\mathrm{N}}\frac{\kappa}{\kappa t+1} = w_{\mathrm{N}}$$
$$\frac{\mathrm{d}e}{\mathrm{d}t} + ((e+\tilde{p})\frac{3\kappa}{\kappa t+1}) = 0,\ \frac{\mathrm{d}e_v}{\mathrm{d}t} + e_v\frac{3\kappa}{\kappa t+1} = w_v \tag{4.9}$$

where velocity field has been substituted with $\mathbf{v} = \frac{3}{\kappa t+1}\mathbf{A}\mathbf{x}$, $\mathbf{A} = \kappa\mathbf{e}_1 \otimes \mathbf{e}_1 + \kappa\mathbf{e}_2 \otimes \mathbf{e}_2 + \kappa\mathbf{e}_3 \otimes \mathbf{e}_3$. The chosen flow is a case of pure dilatation where the traceless symmetric part of the velocity gradient tensor $\mathbf{E} = (\frac{1}{2}(\nabla\mathbf{v} + \nabla\mathbf{v}^{\mathrm{T}}) - \frac{1}{3}(\nabla\cdot\mathbf{v})\mathbf{I})$ and hence Newtonian viscous stress tensor τ are identically zero for fluids whose bulk viscosity vanishes. It is known from previous studies that under strong gradients Navier-Stokes-Fourier equation breaks down [48]. Choosing this special family of pure uniform dilatation in the framework of OMD allows us to remove the extra complexity of the presence of

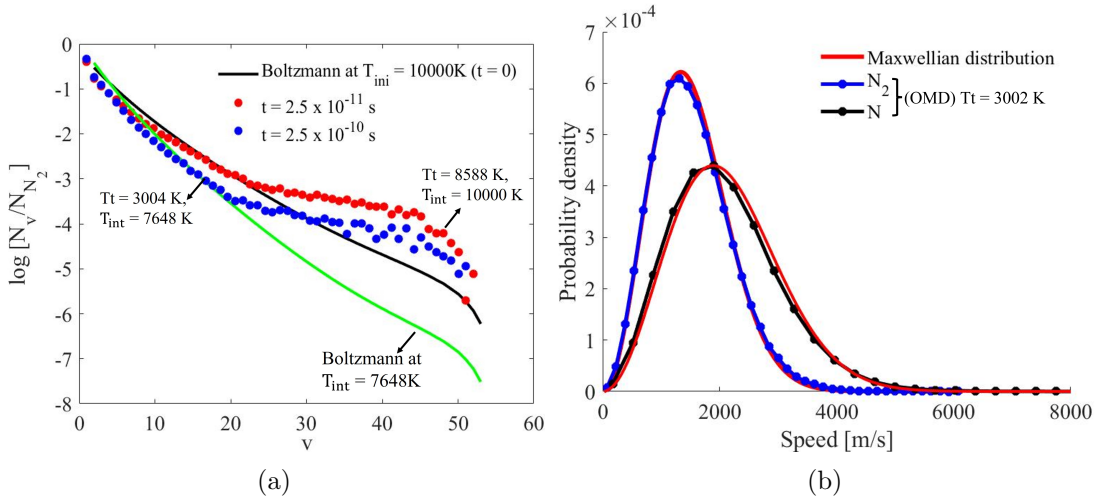

Figure 4.28: (a) Evolution of vibrational population distribution functions (blue and red circles) for molecules during expansion. Black (equilibrium distribution at $t = 0$) and green lines: theoretical Boltzmann distribution at local internal temperature T_{int}. (b) Speed distribution of N_2 molecules (dashed-circle blue line) and N (dashed-circle black line) atoms at the end of expansion. The solid red lines represent Maxwellian distributions at instantaneous Tt.

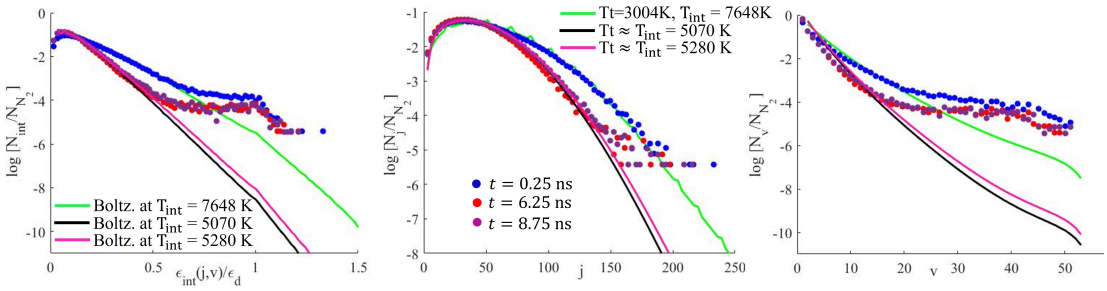

Figure 4.29: (a) Evolution of internal energy, rotational and vibrational population distribution functions (solid circles) for molecules during relaxation. Green (equilibrium distribution at the extreme extent of expansion), black and and magenta lines: theoretical Boltzmann distribution at local internal temperature T_{int}.

non-Newtonian momentum and non-Fourier energy transport contributed from **E** and temperature gradients in the system.

Note that it is assumed that Stokes' hypothesis holds true when deriving eq(4.9) for

the system of Nitrogen gas. This assumption being valid for dilute mono-atomic gas as predicted by kinetic theory and experiments [159] does not hold true for diatomic systems with large dilatations which results in an added effect of bulk viscosity in the total energy conservation equation[160]. Under those conditions, p is given by $p = \frac{1}{3}\text{tr}(\sigma)\mathbf{I}$ which is not necessarily equal to thermodynamic pressure $\tilde{p}$ defined by perfect gas law with respect to translational-rotational temperature. Additionally under strong gradients (large κ) considered in this work, system has large departure from equilibrium due to which p can have non-linear effects and may not be simply equal to $(\tilde{p}+(\lambda+\frac{2}{3}\mu)\nabla\cdot\mathbf{v})$. It is shown in [55] that bulk viscosity is not a physical property of the gas but an approximation designed to simulate the effect of thermal relaxation when the state of gas is described by governing equations in terms of a single temperature. This is based on the assumption of fast relaxation of rotational mode in comparison to flow time scale. Under highly non-equilibrium regime, this assumption breaks down and separate rotational energy conservation equation is required to characterize the gas state.

Fig. 4.30 shows the comparison between OMD and continuum fluid dynamics defined by the set of equations in (4.9). Both the comparisons show the shortcomings of continuum modeling with state-of-the-art energy exchange, reaction rates and transport models in the field. In both the case of pure compression and expansion investigated, there is strong thermal non-equilibrium where Tt $\neq$ Tr $\neq$ Tv and hence two-temperature 2T based CFD modeling is inappropriate. If adopted, then CFD predicts a delayed response in compression in Fig. 4.28(a) where OMD shows an early increase in translational and vibrational temperature than what CFD predicts. The gas in the time span of the compression regime does not dissociate significantly therefore composition history is not shown in the figure. Fig. 4.28(b) shows the expansion regime where a stronger failure is seen even in the general trends. The decrease in vibrational temperature is very rapid in CFD which is in complete contrast to what OMD indicates.

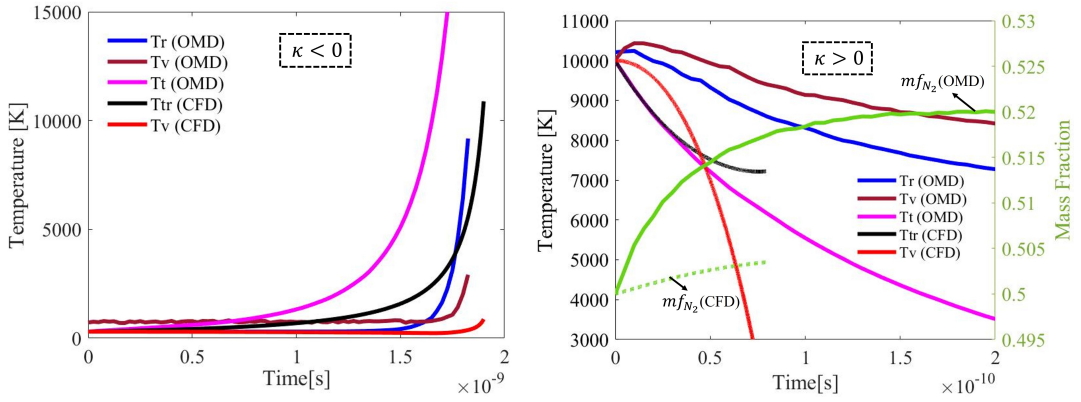

(a) (b)

Figure 4.30: Comparison between OMD and CFD for a system under uniform (a) compression and (b) expansion.

4.5 Summary and Conclusions

This chapter reports the simulation of important concurrent processes of dissociation, recombination, and exchange as they happen in the nitrogen gas system evolving under non-equilibrium conditions using pure MD, based on ab-initio (electronic structure calculations) dataset derived reactive force field. Comparison of MD with CFD reveals strong limitations of Park two-temperature reaction rate models and Millikan-White correlation in the far-from-equilibrium thermo-chemical regime. There is an inherent assumption that vibrational populations obey Boltzmann distribution embedded in these formulations which is not the case as seen by the evolution of PDFs investigated in this work. The distribution reveals significant non-Boltzmann features of distribution during relaxation of gas in an adiabatic and OMD reactor under recombination and dissociation-dominated regimes.

Analysis of recombination and dissociation probability densities suggest microscopic selectivity of these processes where preferential favoring of certain rovibrational states is observed. On the other hand, the exchange process shows no biasedness and hence its post-collision ro-vibrational probability density looks like the instantaneous population distribution of molecular nitrogen in the mixture.

Net dissociation probability density in the non-equilibrium gas is an aggregate effect of the instantaneous population distribution of molecules and selectivity of dissociation. It is observed that nitrogen gas tends to dissociate from states whose energy is close to dissociation energy of N_2 molecule (D^0) and which have high vibrational numbers. As temperature increases, the system gains enough translational energy to overcome the large barrier corresponding to the dissociation of bound states, and hence its weightage in dissociation pdf increases. Similarly, atoms have a tendency to recombine to the states close to the dissociation limit with high vibrational and intermediate rotational levels. As temperature increases density function flattens and the probability of recombining into states far from D^0 increases. On vibrational and rotational recombination pdfs, this corresponds to an increase in the contribution of low vibrational and high rotational numbers thus making the whole rotational and vibrational manifold attain uniform characterstics.

Very few works in the past have used a pure deterministic method of molecular dynamics to study the physics of dilute gases in non-equilibrium regime. OMD provides an optimal choice to conduct these studies. The chapter introduced its application for the modeling of thermo-chemical nonequilibrium in gases at an atomistic level. The illustration of the method in this chapter has only focused on one special choice of $\mathbf{A}$ tensor (uniform dilatation). The family of motion given by $\mathbf{v} = \mathbf{A}(\mathbf{I} + t\mathbf{A})^{-1}\mathbf{x}$ is quite broad whose scope includes many other examples of steady and unsteady compressible and incompressible flows.

From the analysis of underlying PDFs, in compression and expansion regime relevant to shock layer and nozzle expansion respectively, significant non-Boltzmann non-equilibrium features produced by the combination of selectivity of the chemistry and separation in the time scale of relaxation of different internal energy modes is seen. It is shown that OMD analysis can produce all the relevant features and can provide the necessary details needed for higher-scale modeling. The method qualitatively reproduces the formation of "L-shape" vibrational distribution with an overpopulation of high-lying vibrational states created by the recombination and energy exchange processes under

expansion.

The next chapter investigates the application of OMD in material science. Particularly the focus is on the dynamics of dislocations which are micro carriers of plasticity in crystalline materials.

Chapter 5

Cross-slip Under High-rate Deformation

5.1 Introduction

Dislocations are crystal linear defects that carry plastic flow at microscopic scale. Its existence was proposed by Orowan, Polany, and Taylor in 1934 [161, 162] to explain the discrepancy between the theoretical shear stress and the experimental yield stress. Electron microscopy later confirmed the theory of dislocation-based plasticity in the late 1940's and 1950. Dislocations are characterized by the line direction ξ and the Burgers vector $\mathbf{b}$. Dislocation line is the line separating sheared and not yet sheared parts of the crystal and burger vector characterizes the direction and magnitude of the relative shear displacement.

The relative orientation between ξ and $\mathbf{b}$ distinguishes two principal types of dislocations: Edge and Screw and also places the constraints on their glide plane. Edge dislocations with $\xi \cdot \mathbf{b} = 0$ glides on the unique lattice plane, spanned by these two vectors. On the other hand, screw dislocations with $\xi || \mathbf{b}$, can move on any lattice plane that contains $\mathbf{b}$. The process by which dislocations change between planes is referred to as cross-slip[163, 164].

Screw dislocations could change glide planes easily if they maintained their perfect

structure (whose Burgers vector is a translation vector of the lattice). However, in FCC metals, in general they do not and therefore FCC cross-slip is a thermally activated process which requires the overcoming of an energy barrier. This is due to splitting of perfect dislocations into pairs of Shockley partials which reduces the elastic strain energy according to Frank criterion. Partials connects a perfect crystal lattice at one side and an intrinsic stacking fault (i.e. two atomic planes with Hexagonal Close-Packed (HCP) coordination), at the other side. As the Shockley partials always have a mixed character, they can hardly cross-slip readily and requires some transformation and change in core structure first. There are several types of cross-slip mechanism, each having its own activation energy. There is great effort in the literature to understand various factors that influences the activation energy such as presence of jog and intersection with forest dislocation and free surfaces [66]. All of these factors can either aid or hinder the cross-slipping. In spite of numerous atomistic and continuum analysis, complete understanding is not attained yet. This work focuses on the idealized case of homogeneous/bulk cross-slip with no contribution from any other crystalline defect.

The two most plausible homogeneous cross-slip models for FCC crystals are the Fleischer (FL) and Friedel-Escaig (FE) mechanisms and its variants. The FL model was developed by Fleischer (1959)[165]. The FE model was developed by Escaig (1968) [166] based on J. Friedel's ideas (Friedel 1964) [167]. The domination of any particular mechanism is dependent on many factors. This chapter aims at investigating cross-slip at an atomic scale using OMD where various mechanism of cross-slip is seen operational under different macroscopic motions which corresponds to different choices of $\mathbf{A}$ in the far-from-equilbrium regime. The material of study in this work is FCC nickel due to the existence of its stress-dependent energy barrier of homogeneous cross-slip via FE and FL mechanisms, proposed by Kuykendall et al. (2020) [168]. In addition to understanding the mechanism by which cross-slip occurs, it is also important to understand the critical stress at which cross-slip happens. This understanding can also be important for higher-scale modeling like DD. In order to investigate that, the activation barrier developed in [168] is used as an input to assess the behaviour of equilibrium transition state theory in predicting the critical stress of cross-slip via FL mechanism under high-rate loading. This chapter is broadly divided into two sections. Section 5.2 presents atomic

investigation of the dynamics of screw dislocations. Section 5.3 illustrates the modeling of sliding surfaces using the same framework of OMD.

5.2 Screw Dislocations

5.2.1 Initialization

In this case screw dislocations are introduced into the initial conditions for the simulated atoms of Ni, which are otherwise in a relaxed FCC structure. The interatomic interaction is described by an embedded-atom method (EAM) potential developed by Rao et al [169] based on the Voter and Chen format [170]. Table 5.2.1 lists the lattice parameter, cohesive energy, elastic constants and stacking fault energy for the potential. The correct prediction of the stacking fault energy (SFE) which is defined as the energy cost per unit area for changing the local stacking of the fcc {111} planes from ABCABC to ABC|BCA is especially important for dislocation related mechanisms. This force field gives good agreement between experiment and theory for the SFE [171, 172].

To construct the initial atomic configuration, Atomsk package is used [173]. The atoms are assigned random initial velocities extracted from a Maxwell-Boltzmann distribution at a given temperature T. Two perfect screw dislocations with opposite Burgers vectors $\pm\mathbf{b}$ are introduced into the domain along the $\mathbf{e}_2$ axis to maintain a net Burgers vector of zero, so as to be consistent with the approximate periodicity of the surrounding lattice. These are located on parallel $(\bar{1}11)$ planes as shown in Fig. 5.1. Note that the dislocations generated by Atomsk are not relaxed. They correspond to the displacement fields predicted by anisotropic elasticity theory for a given set of material properties. To equilibrate them, the system under $\mathbf{A} = \mathbf{0}$ before applying any motion to the domain is simulated. This is equivalent to periodic MD at macroscopic equilibrium.

Fig. 5.1 shows the initial state of two screw dislocations. Cyan colored atoms shown there are in FCC coordination. Starting with a rectangular atomic cell, defined by vectors $\mathbf{e}_1, \mathbf{e}_2$ and $\mathbf{e}_3$ at $[1\bar{1}2]$, $[\bar{1}11]$ and $[110]$, respectively, a dipole of infinite straight parallel perfect screw dislocations, $\mathbf{b} = \frac{a}{2}[110]$ (shown as the blue dislocation lines in Fig 5.1(a)) is first generated. The orientations of the domain are chosen such that the

axes correspond to the glide plane $(\bar{1}11)$ and glide direction $[1\bar{1}2]$. Equilibration under the NVE ensemble then leads to splitting of the perfect dislocation into the cores of the two Shockley partials identified by Burgers vectors $\mathbf{b}_1$, $\mathbf{b}_2$ and with an intervening stacking fault in accordance with the energetic argument provided by Frank's rule, Figs. 5.1(b,c). The screw dislocations can have different equilibrium core structures which can lead to splitting of screw dipoles on either glide $(\bar{1}11)$ or cross-slip (111) planes creating 4 possible combinations. The first case is chosen where both partials reside on glide plane as our starting point. This equilibrated configuration is then further used to perform non-equilibrium OMD simulations.

The use of OMD results in an infinite array of dislocation dipoles which gives rise to image forces. The sizes of the fundamental domains is systematically varied to examine the effect of these forces: the simulation cell was increased in the in-plane directions $\mathbf{e}_1$ and $\mathbf{e}_2$ keeping the dislocation line length constant. Table 5.2.1 lists domain sizes for the different cases considered. These have a high aspect ratio of the fundamental domain, which is known to mitigate the effects of image and dipole interaction forces [174]. From prior work [175] the contribution of these forces was found to be insignificant if the externally applied stress σ_{ext} is greater than $\sigma_c = \frac{\mu b L}{8\pi^2 r_0^2}$. For the smallest domain considered, $\sigma_c = 7.9$MPa which is three orders of magnitude smaller than the dominant peak external stress applied to the domain.

Dislocations are identified in atomistic simulations performed here using the Dislocation Extraction Algorithm (DXA) implemented in the OVITO package [176]. The DXA algorithm constructs Burgers circuits to find the existing dislocations. The correct search space is identified using Common Neighbor analysis which locates atoms that form a perfect (but elastically strained) crystal lattice. The width of the stacking faults is found to constantly fluctuate, governed by a balance between elastic and thermal forces. This known phenomenon is termed dislocation breathing in [175].

The OMD simulations focused on simple shear of bulk crystalline materials is conducted here by adapting the classical molecular dynamics simulator LAMMPS. "Fix deform" with style "erate" is used to apply "constant engineering strain rate" to the

material. It is accommodated with keyword "remap" for positions and velocities. This is to enable use of the relationship (2.9) and (2.12) to find the trajectory of a nonsimulated atom that enters the fundamental domain as its corresponding simulated atom exits. The box motion is updated at every time step and the velocity Verlet algorithm is used to integrate the Newton's equations of motion with a time step of 1 fs.

Property	Value
a_0(nm)	0.3526
c_{11}(N/m^2)	2.44 x 10^{11}
c_{22}(N/m^2)	1.49 x 10^{11}
c_{44}(N/m^2)	1.19 x 10^{11}
E_c(eV)	-4.43
γ(J/m^2)	0.119

Table 5.1: Lattice parameter, elastic constants, cohesive energy and stacking fault energy given by the Ni EAM "vnih" potential

Domain	Dimension ($a_1\mathring{A}$ x $a_2\mathring{A}$ x $a_3\mathring{A}$)	N
(1)	(77.6 x 304.8 x 19.9)	43200
(2)	(142.27 x 353.61 x 19.9)	91872
(3)	(107.8 x 353.6 x 79.6)	278400
(4)	(142.27 x 353.6 x 82.13)	378972
(5)	(142.27 x 353.61 x 149.335)	689040

Table 5.2: Different choices of the size of fundamental domain and number of simulated atoms N

5.2.2 Effect of external loading on cross slip mechanism

The simple shearing motion along various directions is used to explore the effect of different components of stress on the detailed dislocation reactions during dynamic evolution. Different mechanisms of cross-slip is investigated by varying the stress state in the material. The external loading is characterized using two definitions of stress: Escaig and Schmid stress. Stress that acts on the edge component of a Shockley partial dislocation and controls its width is referred to as Escaig stress and the one which interacts with screw component is referred to as the Schmid stress. These same definitions hold for both glide and cross-slip planes [69, 168]. These stresses are given in terms of stress components in $\mathbf{e}_1, \mathbf{e}_2, \mathbf{e}_3$ coordinate system as follows:

$$\sigma_{\mathrm{s}}^{\mathrm{g}} = \sigma_{23}, \quad \sigma_{\mathrm{s}}^{\mathrm{cs}} = \sin\theta\sigma_{13} - \cos\theta\sigma_{23}$$

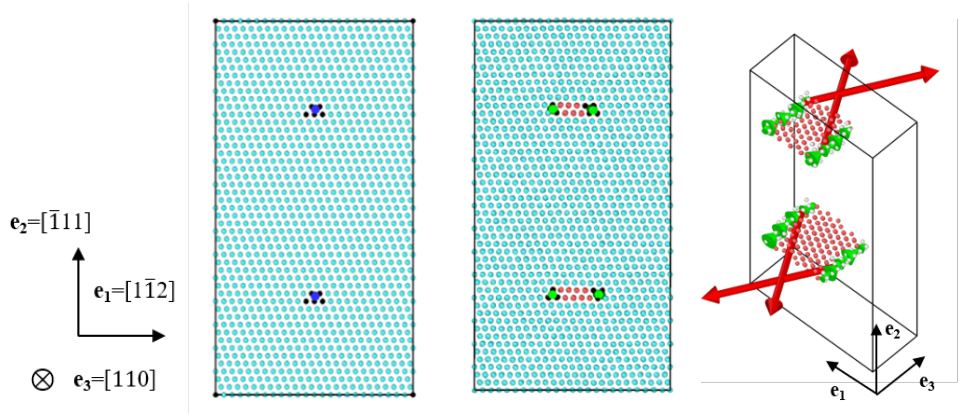

Figure 5.1: (a) Initialization of the atomistic domain (a) Two perfect screw dislocation (depicted by blue lines) are introduced on $(\bar{1}11)$ planes. Cyan colored atoms are in FCC coordination. (b) Dissociation of perfect dislocations into Shockley partial dislocations (depicted by green lines) with an intervening stacking fault. Red atoms are in HCP coordination. (c) Red vectors depict Burgers vectors of the dissociated partials.

$$\sigma_{\mathrm{e}}^{\mathrm{g}} = \sigma_{12}, \quad \sigma_{\mathrm{e}}^{\mathrm{cs}} = \cos 2\theta(\sigma_{12}) + \frac{\sin 2\theta}{2}(\sigma_{11} - \sigma_{22}) \tag{5.1}$$

where, θ is the angle between primary and cross-slip plane, subscripts e and s refer to Escaig and Schmid, and superscripts g and cs refer to glide and cross-slip plane, respectively.

The correct atomistic definition of stress under non-equilibrium conditions is an actively studied subject. Different definitions used in the literature have been unified by Admal et al., [177]. They find that the Hardy stress tensor has many favorable features under non-equilibrium conditions, assuming that the system is in local thermodynamic equilibrium [178, 179]. Also the Hardy stress is equivalent to the virial stress when a constant weighting function over the entire fundamental domain is used for the averaging. This definition is used below to compute a pointwise uniform instantaneous stress which is composed of kinetic and virial contributions. These pointwise values are then averaged over an ensemble of OMD trajectories (random momentum at given

temperature T is assigned to each atom using a fresh random number seed) to compute macroscopic stress.

Three elementary cases are considered in this work. The first is where the pure Escaig stress on the glide and cross-slip plane is the main non zero component and is positive. In the second case the Escaig stress is negative, and in the third case Schmid stress on the cross-slip plane is the main non zero component. An appropriate assignment of $\mathbf{A}$ yields these stresses. Note that minor hydrostatic stresses ($\sigma_{11} = \sigma_{22} = \sigma_{33}$) are present in the material after equilibration under NVE ensemble at finite temperatures due to thermal expansion but their influence on the cross-slip phenomenon is negligible.

Friedel-Escaig (FE) Mechanism

$\mathbf{A}$ chosen to be $K_1\mathbf{e}_1 \otimes \mathbf{e}_2$ results in the generation of stress σ_g^e. This also induces Escaig stress on CS plane σ_{cs}^e as seen from (5.1). The stacking fault width (SFW) is guided by the interaction between Shockley partials, stacking fault energy, internal stress from the images, and the dominant stress σ_{12}. The condition $K_1 < 0$, results in negative $\sigma_{\mathrm{e}}^{\mathrm{g}}$ which promotes decrease in the width of the stacking fault ribbon on the glide plane which, in turn, favors cross-slip. This results in constriction of each partial which leads to the formation of a perfect screw dislocation followed by a further dissociation of that perfect dislocation into partials on the cross slip plane. The latter is oriented at an angle of $\theta = 70.53°$ with respect to the primary slip plane.

The effect of the dislocation line length on cross-slip is investigated. Shorter dislocation segment of $8|\mathbf{b}|$ (dimension of fundamental domain) along $\mathbf{e}_3$, follows FE mechanism uniformly. This means that the constriction of partials happens along the entire dislocation line leading to a perfect screw dislocation, which then cross-slips uniformly without bowing. On the other hand, for the longer dislocation segments $32|\mathbf{b}|$ and $60|\mathbf{b}|$, the partials recombine over a short segment of the full dislocation line and protrude partially into the cross-slip plane, forming constriction joints (joints which separate partials from perfect dislocation). The two constrictions move apart along the dislocation line to complete the cross-slip process. Fig. 5.2 illustrates the mechanism and shows the corresponding transition state for a longer dislocation. The dynamic variant of the Friedel–Escaig [180] mechanism, which incorporates dislocation breathing all along its

length is observed.

Next $K_1 > 0$ is chosen for the same choice of $\mathbf{A}$. In this case the Escaig stress on the glide plane is positive which enlarges the intrinsic stacking fault area between the two partial dislocations on the primary slip plane. Under continued loading, the SFW increases until it starts interacting with a neighboring partial on the same $(\bar{1}11)$ glide plane. This leads to constriction of the leading partial with the trailing partial of the image forming a perfect dislocation. The perfect dislocation then causes slip, immediately followed by re-dissociation into partials on the adjacent $(\bar{1}11)$ glide plane, climbing upwards by one atomic layer. This double slip phenomenon continues as the deformation progresses. The mechanical twin boundary gradually propagates towards the end of a domain under the shear strain produced during the loading. This results in twin boundary motion mediated by the creation, motion and annihilation of steps. Fig. 5.3 shows the temporal sequence of snapshots illustrating the mechanism for a small dislocation line length. In this case the imposition of periodic boundary conditions, in addition to the particular loading orientation used for high rate motion, also have an important effect on the pathway chosen and avoidance of stress buildup by cross-slip.

Fleischer Mechanism

In this case the same initial conditions is taken but $\mathbf{A} = K_2\, \mathbf{e}_1 \otimes \mathbf{e}_3$ with $K_2 > 0$ or $K_2 < 0$, which generates the stress σ_s^{cs}. Contrary to the previous cases, the stacking fault width doesn't vary much due to absence of an Escaig stress. After some time, one partial dissociates into a stair-rod dislocation – a pure edge dislocation whose Burgers vector doesn't lie on the primary or cross-slip plane – and a Shockley partial which bows out into cross-slip plane. This is followed by the reaction of remaining partial in the primary plane with the stair-rod, forming a glissile trailing partial on the CS plane. As in cases above, only part of the dislocation bows out into CS plane for the longer flexible dislocations, whereas the shorter dislocations dissociate uniformly along their entire line length. The core structure of the activated dislocation undergoing cross slip contains a three-dimensional stacking fault structure and resembles that of Lomer Cottrell junction. The mechanism is shown in Fig. 5.4 (cf.,[165]).

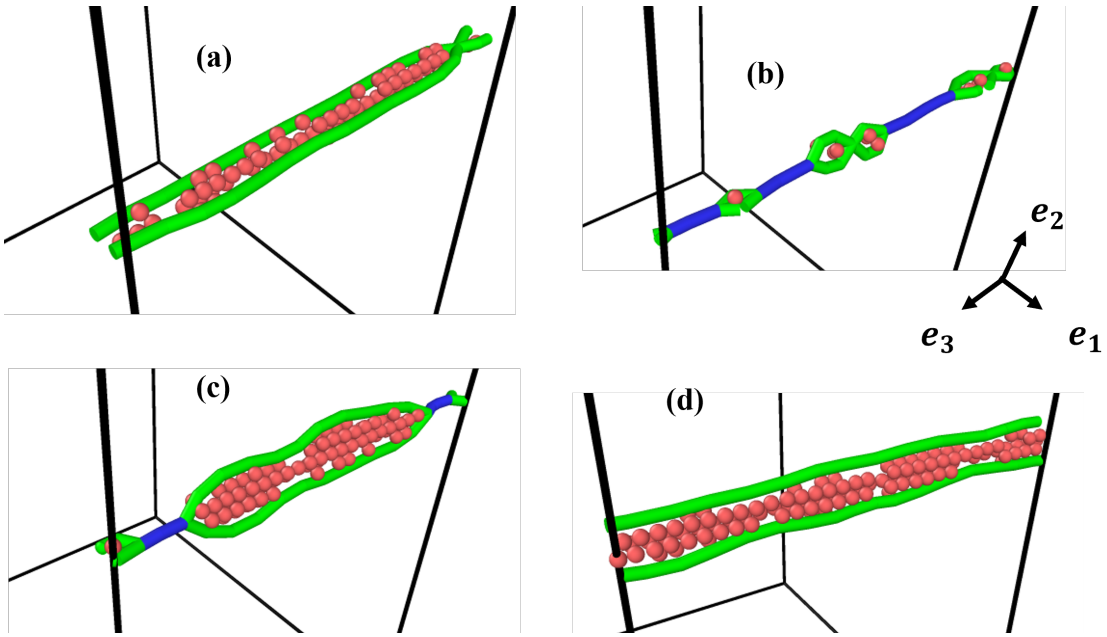

Figure 5.2: Atomistic snapshots illustrating motion of dislocation lines during the Friedel-Escaig mechanism of cross-slip for flexible dislocations. FCC atoms are omitted. Green lines depict partials and blue line depicts perfect screw dislocation.

Simulations under mixed loading conditions are also conducted. This is achieved by sampling phase space where both K_1 and K_2 are non zero ($\mathbf{A} = K_1\ \mathbf{e}_1 \otimes \mathbf{e}_2 + K_2\ \mathbf{e}_2 \otimes \mathbf{e}_3$). It was observed that under mixed loading in the high-strain rate regime ($K_1, K_2 \approx 10^7$), combination of FE and FL mechanism may occur where part of the dislocation cross slips by one mechanism and is completed by the other. The mechanism is illustrated in Fig. 5.5 where cross-slip initiates by constriction of partials into finite length screw and is later assisted by formation of stair rod dislocation at the intersection of primary and cross-slip plane. In some cases of mixed loading, initiation happened by the FL mechanism and in some, mixture of perfect and stair rod dislocation appears at an initial stage.

In summary, four observed dynamical pathways in these highly non-equilibrium situations are reported. In the range of conditions studied, cross-slip occurs via the acute variant (i.e., the angle between the glide direction in the cross-slip and the primary plane is acute) which is known to have lower activation energy. The FE mechanism operates

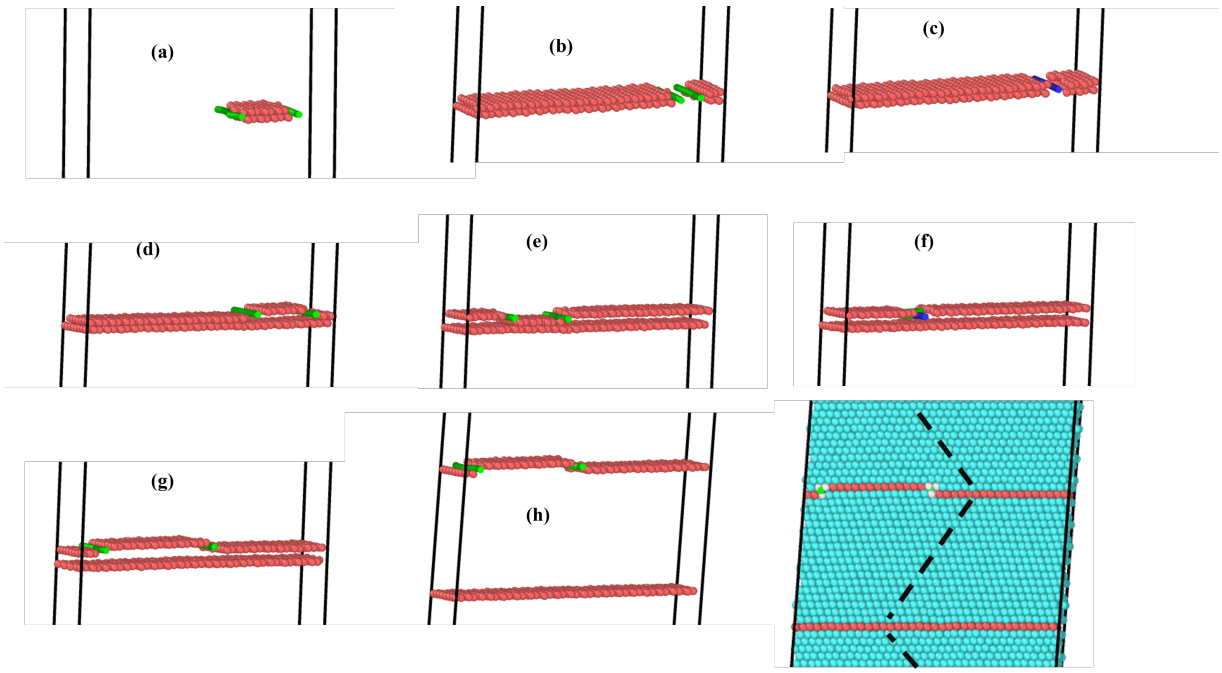

Figure 5.3: Atomistic snapshots illustrating formation of thickening mechanical twin and the motion of dislocation lines during the multiple cross-slip of shorter dislocation segments. Cyan colored atoms are in FCC coordination.

when $\sigma_{\mathrm{e}}^{\mathrm{g}}$ is the only non-zero dominant stress component and its direction is such that it reduces the separation between two partials on the glide plane. Hence the sign of $\sigma_{\mathrm{e}}^{\mathrm{g}}$ is relevant. On the other hand, the Fleischer mechanism operates in the regime where $\sigma_{\mathrm{s}}^{\mathrm{cs}}$ is non-zero and is independent of the direction of stress (i.e., the sign of K_2). This is consistent with earlier work where the dependence of the energy barrier for cross-slip on $\sigma_{\mathrm{s}}^{\mathrm{cs}}$ is predicted to be quadratic [168]. Moreover, the mechanism observed for a given shear loading remains independent of the strain rate K_1, K_2 varying within four orders of magnitude (from $10^4\mathrm{s}^{-1}$ to $10^8\mathrm{s}^{-1}$), investigated in this work. (Simulations with lower strain rates are computationally demanding especially with the bigger fundamental domains of simulated atoms.) The effect of dislocation line length on cross-slip is also explored. The preferred pathway is seen to remain invariant with respect to the length of the dislocation ranging from $8|\mathbf{b}|$ to $60|\mathbf{b}|$. This is in contrast to the finding reported in the literature where only the Fleischer mechanism was observed for shorter

dislocation segments under constant stress at low temperature [181]. A similar conclusion was made using NEB calculations in Al at zero temperature [182]. However, it is found that the dislocation length has a strong effect on the critical stress for cross-slip for a particular mechanism. This will be further investigated in the next section.

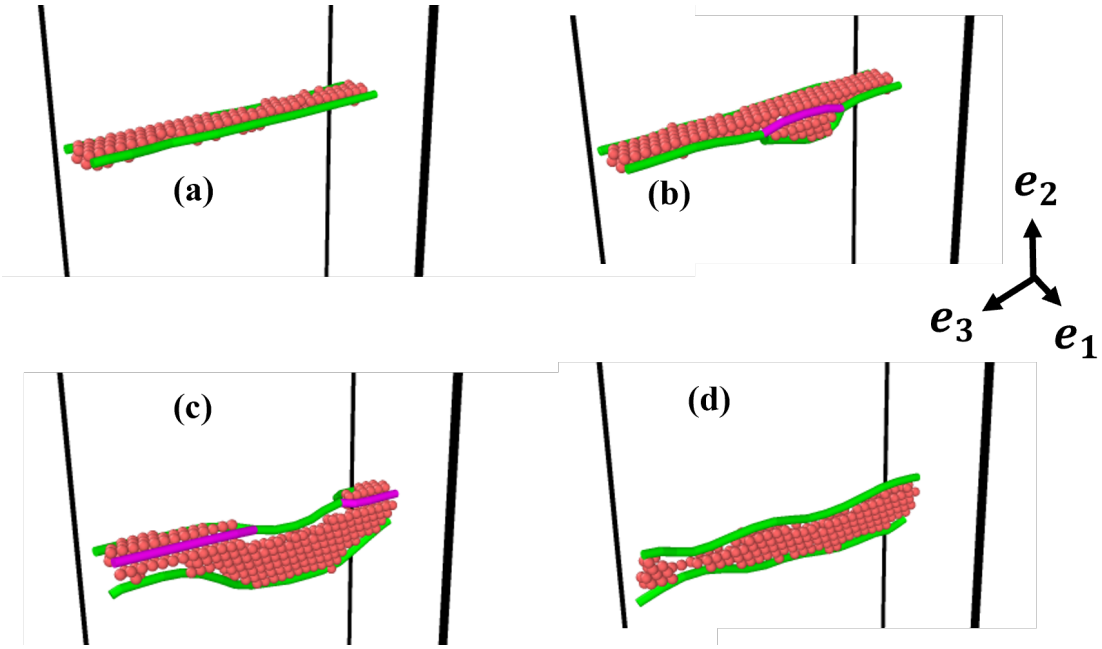

Figure 5.4: Atomistic snapshots illustrating motion of dislocation lines during the Fleischer mechanism of cross-slip for flexible dislocations.

5.2.3 Effect of strain rate and temperature on the critical stress for cross-slip

In this subsection the focus is on the Fleischer mechanism where the effect of strain rate and temperature is investigated in the large strain-rate regime. Fig. 5.6 shows the typical stress-strain response of the material at different strain rates that vary from $1x10^5$ to $1x10^8 s^{-1}$. The stress–strain curve abruptly decreases after linearly increasing to a local maximum at the first transition from elastic to plastic deformation. When the dislocation cross-slips, unloading waves are released immediately, modifying the local state. This in turn results in the fall of the global stress. The shear modulus is obtained

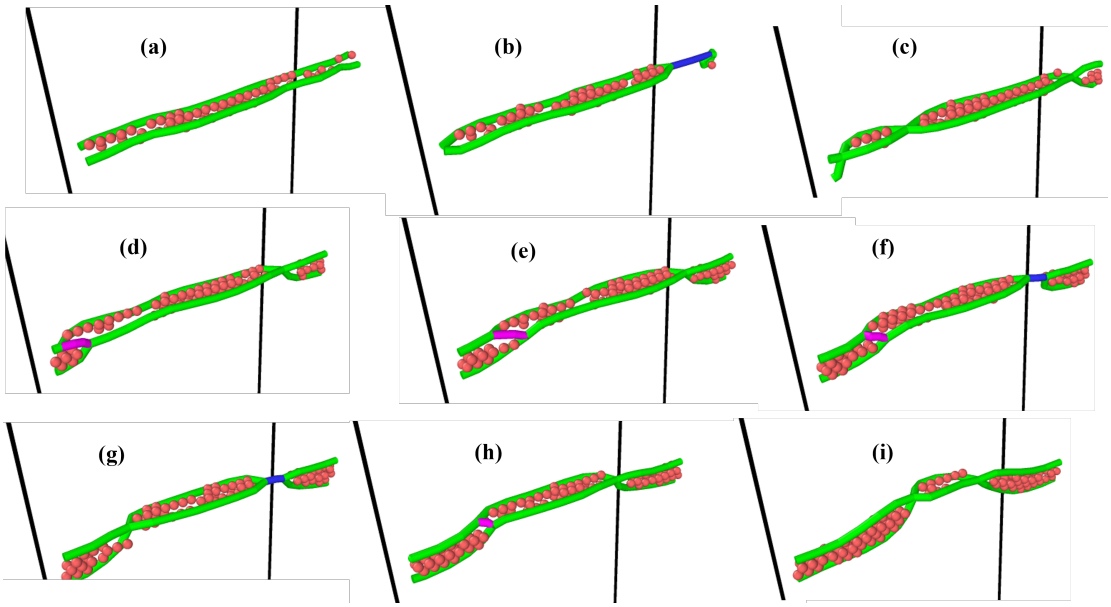

Figure 5.5: Atomistic snapshots illustrating motion of dislocation lines during the Fleischer mechanism of cross-slip for flexible dislocations.

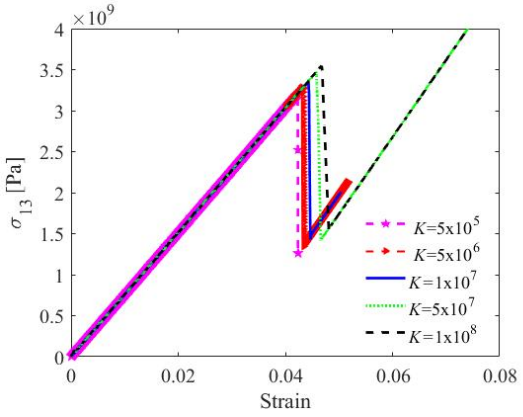

Figure 5.6: Stress-strain response under different strain rates for the system undergoing cross-slipping by Fleischer mechanism.

by linear fitting of the stress–strain curve when the strain is < 0.03 in the elastic region. It is given by $G = 75$MPa which is in agreement with the effective isotropic shear modulus predicted by theory [183, 184, 185] Inspection of the stress-strain curve reveals

that strain rates in this range during shear loading have little effect on the elastic phase of the stress–strain relationship and a modest effect on the plastic phase. An increase in the strain-rate increases the local peak stress. This peak shear stress coincides with the stress at which the material begins to undergo cross-slip. These simulations serve as clear evidence of the dependence of plastic yield on the rate of deformation.

The interesting question is whether the transition state theory (TST) is valid under these conditions of high rate deformation. This is tried to answer here for dislocation cross-slip by making a direct comparison of predictions of OMD with TST. A few studies in the literature have used the TST approach in the context of dislocation-defect interaction [186], mobility of an edge dislocation [187] and dislocation nucleation [188]. Originally, TST was developed for chemical reactions or diffusion of atoms [189, 190]. Vineyard [191] later generalized this theory for multibody systems. A general multiscale method based on TST was formulated by Voter et al. [192]. TST determines the rate at which system at equilibrium jumps between two metastable basins by crossing the saddle region [192]. Generally, one could question whether the system of dislocations in far-from-equilibrium regime stays in a basin for a sufficiently long time so as to reach a macroscopic equilibrium described by the formulas of equilibrium statistical mechanics, but we press ahead and evaluate it anyway. This transition rate at a given temperature T and effective stress σ is then expressed as [193]

$$\nu = \tilde{\nu} \exp\left\{ \frac{-G_c(\sigma, T)}{k_B T} \right\}, \tag{5.2}$$

where $\tilde{\nu}$ is a frequency prefactor, G_c is the activation Gibbs free energy for cross-slip and k_B is Boltzmann constant. The activation enthalpy H_c and activation entropy S_c are assumed to be insensitive to temperature under the range considered and G_c is defined by

$$G_c(\sigma, T) = H_c(\sigma) - T S_c(\sigma).$$

The cross-slip rate can be rewritten as

$$\nu = \tilde{\nu} \exp\left\{ \frac{S_c(\sigma)}{k_B} \right\} \exp\left\{ \frac{-H_c(\sigma, T)}{k_B T} \right\}. \tag{5.3}$$

Hence, the contribution of activation entropy is contained in the overall multiplicative

factor $\exp\left\{\frac{S_c(\sigma)}{k_B}\right\}$. Harmonic transition state theory (HTST) simplifies the rate equation by assuming vibrations to be simple harmonic near the basin and saddle point. This leads to

$$\nu_{\mathrm{HTST}} = \nu_1 \Pi_{i=2}^{N} \frac{\nu_i}{\nu_i'} \exp\left\{\frac{-H_c(\sigma,T)}{k_B T}\right\} \tag{5.4}$$

where ν_1 is the fundamental frequency, ν_i and ν_i' are eigenfrequencies of the i^{th} mode of the original and transition state respectively. Under the framework of HTST, the entropic factor $\exp\left\{\frac{S_c(\sigma)}{k_B}\right\}$ is given by $\Pi_{i=2}^{N} \frac{\nu_i}{\nu_i'}$ if $\tilde{\nu}$ is considered to be ν_1. The activation entropy is typically approximated using an empirical thermodynamic compensation law, or the Meyer–Neldel (M-N) rule which accounts for anharmonic effects such as temperature dependence of shear modulus, thermal expansion, and surface energies [193, 194]. It is based on empirical observation that activation entropy is proportional to activation enthalpy and is given by

$$S_c(\sigma) = \frac{H_c(\sigma)}{T_m} \tag{5.5}$$

where T_m is the melting temperature. The M-N rule is used which reduces the cross-slip rate to

$$\nu = \tilde{\nu} \exp\left\{\frac{-H_c(\sigma)(1-\frac{T}{T_m})}{k_B T}\right\}, \tag{5.6}$$

where G_c is taken to be $G_c(\sigma,T) = (1 - T/T_m)H_c$ in (5.2) under a first approximation of the effect of temperature on the activation free energy. Manzanares et al., [69] has shown the applicability of the M-N rule for aluminium within NPT dynamics of cross-slip via the Friedel-Escaig mechanism in a temperature range of 400-600 K.

The average critical stress for cross-slip is derived using the survival probability in an initial elastic bulk solid [188], and is given by

$$\frac{df(t)}{dt} = -\nu f(t),$$

where ν is given by (5.6). The loading applied can be considered a constant engineering shear strain rate K applied to the solid; thus in the linear elastic deformation regime before cross-slip, the state of stress becomes time-dependent and is given by $\sigma = GKt$, as in Fig. 5.6, where K is the shear rate. Following [187], this can be used to make

change of variables which yields

$$\frac{df(\sigma)}{d\sigma} = -\frac{\nu}{GK} f(\sigma), \quad f(\sigma) = \frac{\exp\{-\int_0^\sigma (\nu(\sigma')/GK) d\sigma'\}}{C}, \tag{5.7}$$

where $p(\sigma) = -\frac{df(\sigma)}{d\sigma} = \frac{1}{C}\frac{\nu(\sigma)}{GK}\exp\{-\int_0^\sigma (\nu(\sigma')/GK) d\sigma'\}$ is the first escape probability distribution and C is normalization factor given by

$$\int_0^{\sigma_c} p(\sigma) d\sigma = 1 \implies \quad C = \int_0^{\sigma_c} \frac{\nu(\sigma)}{GK} \exp\Big\{-\int_0^\sigma (\nu(\sigma')/GK) d\sigma'\Big\} d\sigma. \tag{5.8}$$

Here, cross-slip is being treated as a probabilistic event. Thus the critical stress obtained follows a distribution associated to repeated computational tests. The expected critical stress is achieved by taking first moment of the escape probability distribution:

$$\sigma_{(\text{avg})} = \int_0^{\sigma_c} \sigma p(\sigma) d\sigma = \frac{\int_0^{\sigma_c} \sigma\nu(\sigma) \exp\{-\int_0^\sigma (\nu(\sigma')/GK) d\sigma'\} d\sigma}{\int_0^{\sigma_c} \nu(\sigma) \exp\{-\int_0^\sigma (\nu(\sigma')/GK) d\sigma'\} d\sigma}. \tag{5.9}$$

Equation (5.9) predicts the TST guided temperature and shear rate dependence of the critical slip stress at a given activation enthalpy H_c. Note that since the material undergoes a linear elastic deformation before cross-slip, the constant stress and constant strain ensembles are equivalent here; either preferred choice of independent variable could be used to find $\sigma_{(\text{avg})}$.

Several studies in the literature have estimated the contribution of the stress to the energy barrier associated with different mechanisms of cross-slip [69, 168]. The energy barrier proposed by Kuykendall et al. [168] is used, based on a modified string method for homogeneous cross-slip by Fleischer mechanism as a function of Escaig and Schmid stress acting on glide and cross-slip plane. This is given by

$$H_c(\tilde{\sigma}) = A[1 - (\frac{\tilde{\sigma}}{\sigma_c})^p]^q, \qquad \tilde{\sigma} = C_{\text{e}}^{\text{g}}\sigma_{\text{e}}^{\text{g}} + C_{\text{e}}^{\text{c}}\sigma_{\text{e}}^{\text{cs}} + (D_s^{\text{c}}\sigma_{\text{s}}^{\text{cs}})^2 \tag{5.10}$$

In this comparison, the focus is on the effect of Schmid stress on cross-slip plane $\sigma_{\text{s}}^{\text{cs}}$ on

the average critical flow stress σ^*_{13}. Thus, the activation barrier is reparameterized as

$$\sigma^{\rm g}_{\rm e} = \sigma^{\rm cs}_{\rm e} = 0, \qquad \sigma^{\rm cs}_{\rm s} = \frac{2\sqrt{2}}{3}\sigma_{13} \;\Rightarrow\; H_c(\sigma_{13}) = A[1 - (\frac{\sigma_{13}}{\sigma'_c})^{p'}]^{q'} \tag{5.11}$$

where $A = 2.2352$ eV, $\sigma'_c = 3.3478$GPa, $p' = 1.4576$ and $q' = 1.4428$, This is substituted into (5.9) to obtain the TST-based average theoretical critical stress σ^*_{13}.

In Fig. 5.7(a) the variation of critical stress vs. strain rate for shorter dislocation segments at a constant temperature of 320 K and, in Fig. 5.7(b), vs. temperature at a constant strain rate of $10^7 {\rm s}^{-1}$ is compared. Fig. 5.8 illustrates a similar variation of flow stress for longer dislocations. Different choices of domain reproduce effectively the similar critical stress within statistical uncertainty. The critical stress does not show a large variation in the range investigated. This is consistent with the nature of the energy barrier which is found to be less sensitive to $\sigma^{\rm cs}_{\rm s}$ as compared to other stress components [168].

The predictions of OMD are in reasonable agreement with those of TST for the constant value of $\tilde{\nu}$ taken to be 6.7x10^{12} and 1x10^9 s^{-1} for shorter and longer segments respectively. These estimates are less than the Debye frequency, as expected. As dislocations become longer, the critical stress for cross-slip increases at all temperatures and strain rates. It is concluded that the frequency prefactor is approximately inversely proportional to the length of the dislocation. This is consistent with the analysis by Friedel [167] and Sobie [195] who predicted using a line tension model that the fundamental frequency of dislocations exhibits inverse dependence on the length. Thus, relatively short dislocation segments are activated for cross-slip more quickly than longer segments. Moreover, for a constant strain rate and temperature the temperature and strain-rate sensitivity of the critical stress decreases with an increase in the length of the dislocation.

At a given temperature, it is seen that the deviations from the thermal activation stress begin appearing at strain rates which exceed a certain critical strain rate K^*. Evidently, this happens when the strain rate is so high that cross-slip is no longer thermally activated in that regime and it is purely stress driven. Therefore, the stress is being

ramped up in the system until the athermal limit is reached. K^* is seen to be higher for shorter segments as compared to longer ones and is also a function of temperature of the system. For a given system, decreasing the temperature lowers this critical strain rate, allowing sufficient time for the dislocations to overcome the barrier via thermal assistance, and this time is inversely proportional to the temperature. However, the same system at higher temperatures for the same strain rate can be thermally activated. Similarly, it is seen that for a given shear rate, as the temperature decreases, there is an overshoot of the critical stress which correlates well with the suppression of thermal activation. This discrepancy is present in systems with different dislocation sizes, but it is more noticeable and it kicks in earlier, at a higher temperature, for the longer ones as compared to shorter segments. On the other hand, for all temperatures higher than T^*, the agreement is surprisingly good. Thus, a system can be divided into two regimes: 1) thermally activated and 2) athermal/stress driven, based on critical strain rate K^* at a given temperature T. Similarly for a sufficiently small shear rate K, a similar transition happens at a critical temperature T^*. T^* shifts towards a higher value as K increases.

These results can be useful for the calibration of mesoscopic dislocation dynamics (DD) methods at high strain rates. DD methods employ physics-based rules for the motion of dislocations. An activated theory-based probability model has been used to incorporate cross-slip in DD simulations, but different studies have adopted different choices of the effective activation energy barrier [73, 74, 75]. The study conducted here provides confidence on the usage of an Escaig/Schmidt stress dependent energy barrier for the modeling of cross-slip of screw dislocation segments under high rate deformation. It is an important finding that the frequency prefactors $\tilde{\nu}$ obtained in this study for both longer and shorter segments are smaller than the ones typically reported for the similar system under equilibrium at some constant stress σ and temperature T [69, 168]. This suggests that higher strain rates lead to suppression of cross-slip. This can significantly affect the macroscopic response of system and can result in widely different behavior as compared to system under quasi-static loading. Thus, this work promotes the inclusion of appropriate strain-rate dependence of frequency prefactors for mesoscale modeling. The investigation also allows to understand the transition from homogeneous cross-slip,

seen for short dislocation segments, to inhomogeneous slip for larger dislocation lengths.

Uncertainty present in these results can be due to neglect of local stress experienced by a dislocation. A dissociated screw dipole could introduce both Schmid and Escaig stresses on the glide and cross-slip planes of the image partial in addition to the external applied stress. This would induce a difference between the global stress computed here and the local stress state of the dislocation. This effect has been suppressed here owing to the sufficiently big size of the fundamental domain. On the other hand, even the definition of the essentially macroscopic quantity 'stress' is unclear in these situations. It may be that some kind of purely atomistic replacement for stress that accounts for fluctuations is needed in TST.

The frequency prefactor obtained for the shorter segments might be an under estimate. This is owing to the fact that the activation barrier used here for both our studies of shorter and flexible dislocations was originally derived for longer segments. In some prior studies, e.g. [196], the barrier is found to rise proportionally to the dislocation length for short dislocation segments and it saturates at constant value for sufficient long dislocations.

5.3 Unlubricated Sliding

Friction is one of the most common phenomenon encountered in everyday life, and yet is one of the least understood physical phenomena. In this section, it is briefly shown that how OMD can be used to conduct sliding simulations which can help to investigate non-equilibrium processes occurring at the atomistic scale. The purpose of this section is to show an unexpected capability of our method, and also to see the formation of dislocations in a frictional sliding simulation. A comprehensive study of the physics of frictional sliding based on OMD will be presented elsewhere.

The technical details on the design of OMD computational method for frictional sliding is, apart from initial conditions, almost the same as used above (For detailed information on the implementation, see Chapter 2). In these simulations, it is more informative to adopt Lagrangian approach and follow the motion of simulated atoms

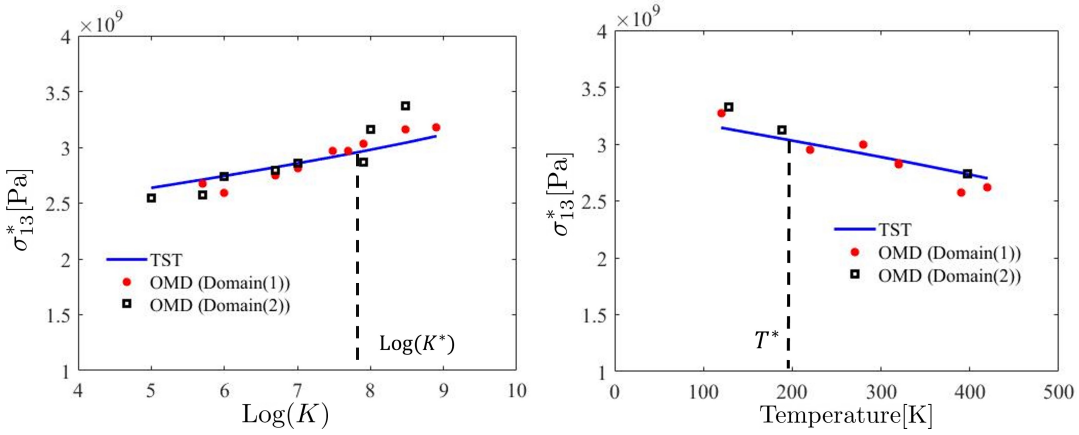

Figure 5.7: Critical stress of cross-slip as a function of (a) logarithm of strain rate and (b) temperature for short dislocation segments undergoing cross-slipping by Fleischer mechanism.

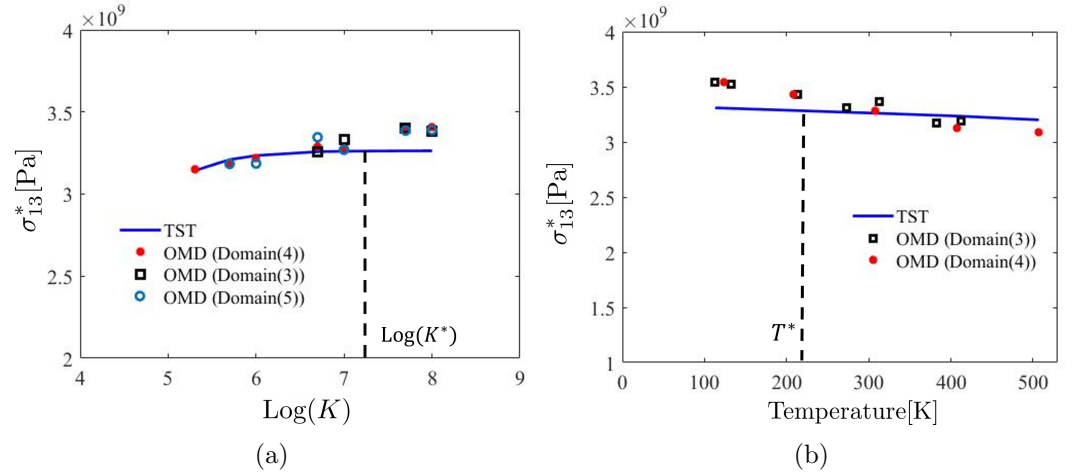

Figure 5.8: Critical stress of cross-slip as a function of (a) logarithm of strain rate and (b) temperature for long and flexible dislocation segments undergoing cross-slipping by Fleischer mechanism.

which are defined at $t = 0$. To achieve that, remapping and redefinition of simulated atoms are not required, and therefore they are free to leave or enter the fundamental domain. This requires a slight modification in the approach for the neighbor search

adopted earlier in section 2.3. In the cell list method [3] the fundamental domain is divided into cells; all atoms are assigned to the cells according to their positions. In the present case one can have simulated atoms outside the fundamental domain (Fig. 5.8(b)); each of those exterior simulated atoms is assigned a cell based on the position of its corresponding non simulated atom that lies inside the fundamental domain. That cell identifier is then used to find the atoms in the neighboring 27 cells which can interact with that atom. After this, the same procedure is followed which was used earlier to find the nearest image. The distance between simulated atoms $1, k$ and $1, m$ at time t can be written as:

$$\mathbf{r}_{k,m} = \mathbf{y}_{1,k} - \mathbf{y}_{1,m} = \{\lambda_1(\mathbf{I} + t\mathbf{A})\mathbf{e}_1 + \lambda_2(\mathbf{I} + t\mathbf{A})\mathbf{e}_2 + \lambda_3(\mathbf{I} + t\mathbf{A})\mathbf{e}_3\} \tag{5.12}$$

$\mathbf{r}_{k,m}$ is the shortest distance if and only if $|\lambda_i| \leq 0.5$. If $|\lambda_i| > 0.5$ then either simulated atom $1, k$ or simulated atom $1, m$ lies outside the domain. Atom $1, k$ then interacts with an image of the simulated atom $1, m$, and the distance between them is given by $\mathbf{r}_{k,m} - \lfloor(\lambda_i)\rfloor(\mathbf{I} + t\mathbf{A})\mathbf{e}_i$ where $\mathbf{r}_{k,m}$ is known from the calculation above and $\lfloor x \rfloor$ is the closest integer greater than or equal to x. This is repeated for each simulated atom whether it lies outside or inside the domain. Based on these computed inter-atomic distances, the force is calculated and then the trajectory is evolved.

The setup for the MD simulations of sliding is illustrated in Figure 5.9. The system consist of two slabs. Both upper and lower slab are made of Argon atoms which interacts via Lennard-Jones (LJ) potential. The two body interaction between atoms i and j is given by

$$\phi(r_{ij}) = 4\epsilon_{\mathrm{LJ}}[(\frac{\sigma_{\mathrm{LJ}}}{r_{ij}})^{12} - (\frac{\sigma_{\mathrm{LJ}}}{r_{ij}})^{6}] \tag{5.13}$$

where $\sigma_{\mathrm{LJ}} = 3.4$ x 10^{-10}m and $\epsilon_{\mathrm{LJ}} = 1.65$ x 10^{-21}J. Basic physical properties can be expressed in LJ units: $\sigma_{\mathrm{LJ}}, \epsilon_{\mathrm{LJ}}, \frac{\epsilon_{\mathrm{LJ}}}{kb}, \frac{\epsilon_{\mathrm{LJ}}}{\sigma^3_{\mathrm{LJ}}}, \sqrt{\frac{m\sigma^2_{\mathrm{LJ}}}{\epsilon_{\mathrm{LJ}}}}$ for length, energy, temperature, pressure and time respectively. FCC crystal is the ground state of this potential with a lattice constant of $a = 1.556\sigma_{\mathrm{LJ}}$. The computational domain containing $N = 10000$ simulated atoms is used. The two slabs are specified by adding random noise to the positions of atoms at mid plane along $\mathbf{e}_2$. It is emphasized that the only essential difference between these simulations and the ones above involving dislocations (or those involving hypersonic flows of fluids [48]) is a change of initial conditions.

Besides the random noise at the interface, the system is otherwise initialized using random velocities sampled from Maxwell-Boltzmann distribution at initial temperature T_0 and further equilibrated to a steady state by running it under an NVE ensemble achieved by using OMD with $\mathbf{A} = 0$. The equilibrated system is illustrated in Fig. 5.8(a) where red and blue colored atoms simply highlight the slabs above and below the initially perturbed layer and aid in showing where the atoms go (The coloring is Lagrangian.) Next, the OMD simulation is performed under simple shearing by choosing $\mathbf{A} = K_1\mathbf{e}_1 \otimes \mathbf{e}_2$ in the basis $\mathbf{e}_1 = [100], \mathbf{e}_2 = [010]$ and $\mathbf{e}_3 = [001]$, where $\mathbf{e}_1, \mathbf{e}_2$ defines the sliding plane.

The perturbed layer quickly evolves to an well-defined interface along which the two blocks slide as a frictional system, Fig. 9(b). Note that the portion of these slabs which is composed of non-simulated atoms is omitted from the visualization; only simulated atoms are shown. (The full set of atoms satisfying the equations of molecular dynamics fills all of space.) To represent frictional sliding, it is found that the size of the fundamental domain needs to be big enough such that interaction between elastic shear waves, which originate from the interface, and their images under the translation group is negligible. This interaction is estimated from the propagation time based on the macroscopic shear wave velocity and the size of the fundamental domain. The value of the K_1 is chosen such that the duration of the simulation is well within the propagation time to avoid shear wave reverberations.

Fig. 5.9(c) gives insight into the deformation process; atoms in FCC coordination are omitted in Fig. 5.9(c). At first, perfect, stair rod and mixed dislocations nucleate under the midplane. The dislocations are identified using the same DXA algorithm within Ovito that was used earlier. As sliding evolves, the Shockley partials cross slips, majorly dominant by Fleischer mechanism (in the system investigated) followed by the propagation of stacking faults in the lower slab on the preferred close packed slip plane. The temperature of the system increases with time since there are no thermostats applied and the external work is being done on the system. The instantaneous temperature

at time t is computed by:

$$T(t) = \frac{m}{3k_bN}\left[\sum_i (v'^{\,2}_{1,i} + v'^{\,2}_{2,i} + v'^{\,2}_{3,i})\right] \tag{5.14}$$

where, $v'_{j,i}$ denotes the thermal velocity (difference between particle velocity and mean velocity) of particle i in direction $\mathbf{e}_j$, and k_b is the boltzmann constant.

In Fig. 5.10(b) the temperature profile across the material for the relative speed between slabs of 100 m/s is plotted. The profile is computed by partitioning the fundamental domain into bins in the $\mathbf{e}_2$ direction. The temperature in each bin is then computed by local averaging of the variance of kinetic energy of the atoms present in the bin. The temperature at the interface is highest and decreases monotonically. The temperature at the interface reaches approximately 48K which gives rise to onset of melting and mechanical mixing at the interface.

Fig. 5.10(a) shows the evolution of sliding stress τ_{12}, computed using the Virial stress given by

$$\sigma(t) = -\frac{1}{V}\left(\sum_{i=1}^{N} m_i(\mathbf{v}_i - \bar{\mathbf{v}}) \otimes (\mathbf{v}_i - \bar{\mathbf{v}}) + \sum_{j\neq i}^{N}\sum_{i=1}^{N} \mathbf{r}_{ij} \otimes \mathbf{F}_{ij}\right), \tag{5.15}$$

where N is the number of simulated atoms, $\bar{\mathbf{v}}$ is the mean velocity, $\mathbf{r}_{ij}$ is the interatomic distance, $\mathbf{F}_{ij}$ is the interatomic force between atom i and j and $\tau = \sigma - \frac{1}{3}\mathrm{tr}(\sigma)\mathbf{I}$. This stress increases elastically until the initiation of sliding, at which time the stress drops rapidly. The tangential stress can have a strong dependence on the velocity as described by Rigney et al. [197]. It is also seen that the sliding stress follows an oscillating behavior reminiscent of widely observed microscopic stick-slip behavior as the two slabs move past each other. During the 'stick' phase, both the slabs are stuck to each other. This is followed by sudden slip. Similar behavior is observed in the slab's velocity field as well. When the relative velocity between the blocks is small then materials can cold weld together. Conversely, if it is very high then sliding can occur at the junction between simulated and non-simulated atoms away from the interface,

indicating a more general disintegration at these extremely high rates. These results indicate that, with an appropriate choice of **A** and initial conditions within the OMD framework, one is able to conduct high speed sliding studies at the molecular scale. Modeling in this manner avoids the need of widely adopted strategy of introducing additional reservoirs for applying boundary conditions [198] which is more realistic and also simplifies the simulation.

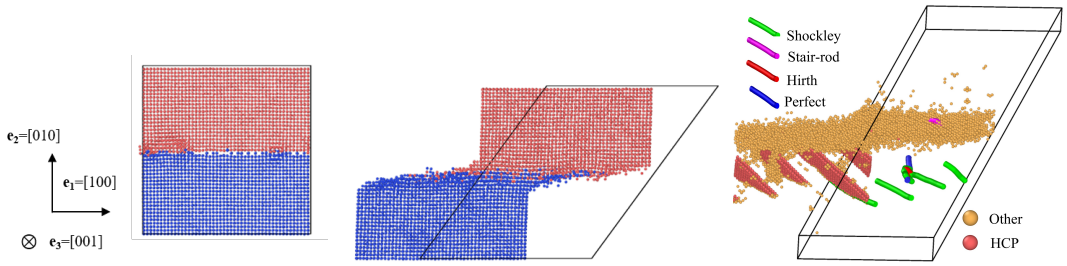

Figure 5.9: Atomic configuration associated with the system at an (a) initial state and (b) during sliding. Red and blue colored atoms constitute two LJ slabs of simulated atoms. (c) Nucleation and motion of dislocations in the lower slab during sliding.

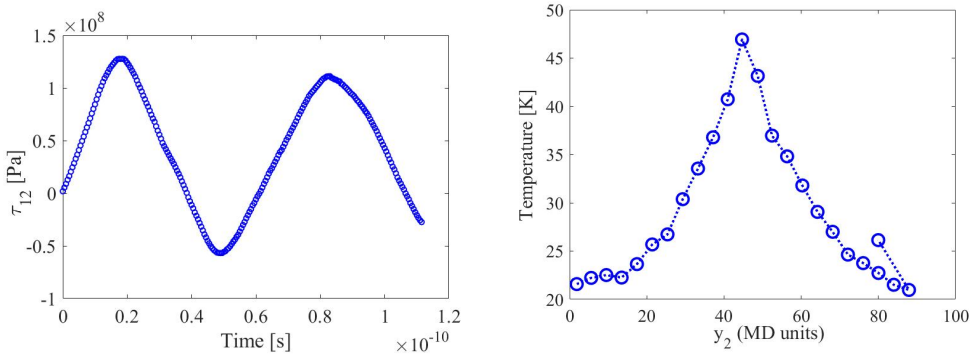

Figure 5.10: (a) Evolution of sliding stress (b) Temperature profile across $\mathbf{e}_2$ direction. Dimension of the domain: 15.8 nm x 31.7 nm x 5.29 nm

5.4 Summary and Conclusions

This chapter focused on the modeling of cross-slip in a bulk crystal under high-rate loading. A detailed description of the onset of cross-slip by Friedel-Escaig or Fleischer or mixed mechanisms under different macroscopic motions, and also the appearance of twinning and step motion is given. No nucleation criteria were used. Surprisingly, it was found that the response of the material under far-from-equilibrium conditions is consistent with an equilibrium theory of activation within a constant stress ensemble, under appropriate evaluations. The critical stress for cross-slip depends on the thermodynamic properties of activation, such as activation free energy, enthalpy and entropy. The use of a stress-dependent activation energy in conjunction with the Meyer-Neldel rule for the entropic contribution captures the correct probabilistic behavior of the system across a wide range of shear rate and temperature. The study also verified the dependence of the activation energy on an effective stress composed of Escaig and Schmid components. These findings can easily be incorporated in dislocation dynamics simulations to improve probabilistic models of bulk cross-slip.

Finally, initial results of frictional sliding at high rates is presented. Wave interactions with images could be avoided in these simulations without compromising the method. Dislocations formed initially at the interface and, under various conditions, stick-slip, a temperature rise at the interface and, at extremely high rates, a type of fragmentation is observed.

The next chapter concludes this thesis and provides potential future directions.

Chapter 6

Conclusion and Future Work

The thesis developed an effective atomistic implementation of the flows of form $\mathbf{v} = \mathbf{A}(\mathbf{I} + t\mathbf{A})^{-1}\mathbf{x}$ by exploiting the fundamental invariances (invariance under orthogonal transformations, translations and permutations) of the underlying potential energy surface of MD. This special family of homogeneous motion allows the reduction of the governing PDE's in macroscopic variables of continuum mechanics (CM) into the system of ODE's. The macroscopic motion for any 3×3 matrix $\mathbf{A}$, together with a suitable temperature $T(t)$ satisfying an explicit ordinary differential equation, are exact solutions of the balances of mass, momentum, and energy together with general constitutive relations. The atomistic simulations produce exactly this macroscopic motion and a time-dependent temperature. It also separates the continuum differential equations of fluid motion from the boundary conditions which would be required to complete a well-posed problem. Thus, the method of OMD provides a potential candidate for the development of constitutive relations for higher scale theories from first principles.

This synergy between atomistic and continuum theories is used in this thesis to develop a higher-order non-linear constitutive model using OMD as the method of computational viscometry. The model is based on the theory proposed by Rivlin and Ericksen (RE) in 1926. The RE theory based constitutive model developed in this work generalizes Navier-Stokes (NS) theory for OMD flows in the regime of strong gradients and is shown to have better agreement with atomistic predictions than NS. This regime

corresponds to continuum-transition flows which are important for many practical engineering problems, such as the simulation of microscale flows and hypersonic flow around space vehicles in low earth orbit. The thesis also makes necessary connections of the proposed RE model with other extended hydrodynamics approaches such as Burnett equations and the moment method applied for Maxwellian molecules.

As part of future work, it will be important to investigate the classification and the strategies for the numerical solution of PDE's obtained when RE constitutive relations are used to close conservation equations of fluid dynamics. While it is expected to be somewhat more complicated to implement than the Navier-Stokes equations, the proposed model is expected to be compatible with existing methods of Computational Fluid Dynamics (CFD) and may extend those methods to higher rate regimes, while preserving their ability to handle large spatial scales.

The proposed RE model is shown to be consistent with the second law of thermodynamics for incompressible flows. The consistency of compressible RE flows is yet to be investigated. It is important to note that OMD only captures non-linear momentum transport since the heat flux is identically zero. The future aim is to explore further if the proposed RE constitutive relation for the stress tensor is also suitable for other flows where energy transport is as significant as momentum transport, which may lead to coupling. This can be achieved by making a direct comparison of RE model predictions for flows with all the effects operational either with experiments or with other modeling approaches for dilute gas such as Direct Simulation Monte Carlo (DSMC). If the energy-momentum transport coupling is suspected then the current calibration of the proposed RE model needs to be augmented to capture that effect. To achieve that, one could follow the same recipe as adopted in this work and introduce the general dependence on temperature gradient and its higher orders in addition to velocity gradients. This in conjunction with the principle of material objectivity, underlying symmetry, and necessary restrictions from the second law of thermodynamics can provide general dependence of the stress functional on the kinematic quantities and temperature gradient. On the other hand, while it cannot be ruled out *a priori*, a dependence of the stress on, say, the temperature gradient is quite unusual, and there are no known accepted

constitutive relations for any material having this dependence.

In addition to the constitutive relation for momentum transport, one also needs better continuum-transition regime models for energy and mass transport as closures which is beyond the scope of the current work. For rarefied gas flows, non-slip boundary conditions are unrealistic for continuum transition flows as there are not enough collisions near the wall to equilibrate the flow field. For this reason, slip boundary conditions should be described at the wall. Chapter 2 illustrates the use of OMD for modeling wall-bounded flows. It is seen that the most well-known type of velocity slip kind of boundary condition which is the Maxwell first-order slip condition is inappropriate in the transition regime. The velocity slip predicted by OMD is shown to be better captured by logarithm variation in Knudsen number in contrast to the Maxwell slip model. This encourages its further validation for a wide range of flow systems.

The extension of the proposed momentum transport model for diatomic gas will require consideration on bulk viscosity (to account for the deviation of average normal stress from pressure) which is non-zero for diatomic flows in non-equilibrium. In fact, the definition of bulk viscosity as a physical property of the gas itself is questionable under such conditions. The complexity associated with the modeling of diatomic and polyatomic gases under high enthalpy is further increased due to the presence of active internal energy modes and chemical reactions. Since OMD works for any force field including those generated by adiabatic quantum mechanics, and also works for mixture, molecular gases, liquids, or solids, the method is equally capable of simulating hypersonic chemistry. The primary potential of OMD (similar to MD) is that it is not limited to binary collisions. Thus, it provides a suitable machinery to study recombination and condensation which require models in many statistical based methods developed for the regime of dilute gas. OMD was used in the work to analyze non-equilibrium reacting flows using the force field of ReaxFF, calibrated using electronic structure calculations. The method extends the capability of MD to systems beyond adiabatic and isothermal reactors for analyzing the non-equilibrium physics of gases.

The simulations performed in this thesis of chemically reacting nitrogen flows are

the first ever reported pure exhaustive MD simulations. At first the validity of ReaxFF was accessed by making comparisons with another modeling approach of Direct Molecular Simulation (DMS) in the dissociation dominated regime which showed a good quantitative agreement. Later, the comparison with CFD reveals strong limitations of the standard Park's thermochemical kinetics and Newtonian transport models in the far-from-equilibrium regime across various fronts. The insights obtained on the microscopic dynamics can provide important feedback on kinetic and continuum model development. Thus, OMD is shown to provide new pathways for developing first-principle based higher-scale models for molecular flows similar to what is achieved for monoatomic flows in this work. The immediate path forward is to use this method to validate the accuracy of the vast literature on thermo-chemistry models proposed in the aerothermodynamics community.

Taken together, a surprising aspect of this OMD implementation is that essentially the same numerical method, with the same atomic forces, can be used to study diverse behavior such as slip, cross-slip, twinning, and step motion, and frictional sliding, simply by changing the initial conditions. This investigation is performed in Chapter 5. The key finding is that the macroscopic motion (i.e., loading conditions) and initial conditions greatly affect the atomic scale deformation mechanisms—such as the formation, motion, multiplication, annihilation, and abrupt changes of the slip plane and Burgers vector of dislocations (without any nucleation criteria or artificial perturbations). Furthermore, small changes in the macroscopic loading conditions generate a rich variety of atomic deformation pathways. For example, in certain macroscopic motions, the growth of a stacking fault into a mechanical twin is observed, which subsequently thickens by a process of step motion. In other macroscopic motions, one can see the initiation and subsequent development of cross-slip by the Friedel–Escaig or Fleischer mechanisms or the combination of two. The findings on the effect of external strain rate and temperature on the critical stress for homogeneous cross-slip by the Fleischer mechanism quantitatively agree with the transition state theory which has a stress-dependent activation barrier. The analysis suggests that higher strain rates lead to suppression of cross-slip. This is owing to the fact that the frequency prefactors $\tilde{\nu}$ obtained in this

study are smaller than the ones typically reported for a similar system under equilibrium (phase space probability density is time-invariant) at some constant effective stress σ and temperature T. This is in agreement with the understanding that large strain rates result in inertia dominated conditions due to which thermal fluctuations become less efficient, i.e., the critical stress of cross-slip corresponds to an effective temperature which is smaller than actual one. Overall, It is surprising that there is some level of agreement between a modified version of TST and the simulations. There is no persuasive evidence of atoms entering a well, equilibrating, and then passing out of a well through a low barrier in the simulations. A similar analysis can be extended to other mechanisms.

The thesis also provided the framework to study the dynamics of phase change and frictional sliding. Overall, the thesis suggests the method of OMD to future investigators to analyze problems which requires atomistic investigation in highly non-equilibrium settings.

References

[1] B. J. Alder and T. E. Wainwright, "Molecular dynamics by electronic computers," Transport processes in statistical mechanics, pp. 97–131, 1958.

[2] B. J. Alder and T. E. Wainwright, "Studies in molecular dynamics. i. general method," The Journal of Chemical Physics, vol. 31, no. 2, pp. 459–466, 1959.

[3] M. P. Allen and D. J. Tildesley, Computer simulation of liquids. Oxford university press, 2017.

[4] E. Cances, M. Defranceschi, W. Kutzelnigg, C. Le Bris, and Y. Maday, "Computational quantum chemistry: a primer," Handbook of numerical analysis, vol. 10, pp. 3–270, 2003.

[5] B. F. Curchod, U. Rothlisberger, and I. Tavernelli, "Trajectory-based nonadiabatic dynamics with time-dependent density functional theory," ChemPhysChem, vol. 14, no. 7, pp. 1314–1340, 2013.

[6] O. Penrose, "Foundations of statistical mechanics," Reports on Progress in Physics, vol. 42, no. 12, p. 1937, 1979.

[7] O. Penrose, Foundations of statistical mechanics: a deductive treatment. Courier Corporation, 2005.

[8] E. B. Tadmor and R. E. Miller, Modeling materials: continuum, atomistic and multiscale techniques. Cambridge University Press, 2011.

[9] E. H. Kennard et al., Kinetic theory of gases, vol. 483. McGraw-hill New York, 1938.

[10] J. W. Gibbs, Elementary principles in statistical mechanics: developed with especial reference to the rational foundations of thermodynamics. C. Scribner's sons, 1902.

[11] D. J Evans and G. P Morriss, Statistical mechanics of nonequilbrium liquids. ANU Press, 2007.

[12] B. D. Todd and P. J. Daivis, Nonequilibrium molecular dynamics: theory, algorithms and applications. Cambridge University Press, 2017.

[13] W.-T. Ashurst and W. Hoover, "Dense-fluid shear viscosity via nonequilibrium molecular dynamics," Physical Review A, vol. 11, no. 2, p. 658, 1975.

[14] A. Lees and S. Edwards, "The computer study of transport processes under extreme conditions," Journal of Physics C: Solid State Physics, vol. 5, no. 15, p. 1921, 1972.

[15] T. Dumitrică and R. D. James, "Objective molecular dynamics," Journal of the Mechanics and Physics of Solids, vol. 55, no. 10, pp. 2206–2236, 2007.

[16] K. Dayal and R. D. James, "Nonequilibrium molecular dynamics for bulk materials and nanostructures," Journal of the Mechanics and Physics of Solids, vol. 58, no. 2, pp. 145–163, 2010.

[17] R. D. James, "Objective structures," Journal of the Mechanics and Physics of Solids, vol. 54, no. 11, pp. 2354–2390, 2006.

[18] K. Dayal and R. D. James, "Design of viscometers corresponding to a universal molecular simulation method," Journal of Fluid Mechanics, vol. 691, pp. 461–486, 2012.

[19] W. G. Hoover, D. J. Evans, R. B. Hickman, A. J. Ladd, W. T. Ashurst, and B. Moran, "Lennard-jones triple-point bulk and shear viscosities. green-kubo theory, hamiltonian mechanics, and nonequilibrium molecular dynamics," Physical Review A, vol. 22, no. 4, p. 1690, 1980.

[20] B. Todd and P. J. Daivis, "Homogeneous non-equilibrium molecular dynamics simulations of viscous flow: techniques and applications," Molecular Simulation, vol. 33, no. 3, pp. 189–229, 2007.

[21] G. V. Candler, "Rate effects in hypersonic flows," Annual Review of Fluid Mechanics, vol. 51, pp. 379–402, 2019.

[22] J. J. Bertin, Hypersonic aerothermodynamics. AIAA, 1994.

[23] G. A. Bird, "Molecular gas dynamics and the direct simulation of gas flows," Molecular gas dynamics and the direct simulation of gas flows, 1994.

[24] I. D. Boyd and T. E. Schwartzentruber, Nonequilibrium gas dynamics and molecular simulation, vol. 42. Cambridge University Press, 2017.

[25] H. Struchtrup, "Macroscopic transport equations for rarefied gas flows," in Macroscopic transport equations for rarefied gas flows, pp. 145–160, Springer, 2005.

[26] S. Chapman, "Vi. on the law of distribution of molecular velocities, and on the theory of viscosity and thermal conduction, in a non-uniform simple monatomic gas," Philosophical Transactions of the Royal Society of London. Series A, Containing Papers of a Mathematical or Physical Character, vol. 216, no. 538-548, pp. 279–348, 1916.

[27] S. Chapman, "V. on the kinetic theory of a gas. part ii.—a composite monatomic gas: Diffusion, viscosity, and thermal conduction," Philosophical Transactions of the Royal Society of London. Series A, Containing Papers of a Mathematical or Physical Character, vol. 217, no. 549-560, pp. 115–197, 1918.

[28] C. Cercignani, Theory and application of the Boltzmann equation. Elsevier Science & Technology, 1975.

[29] S. Chapman and T. G. Cowling, The mathematical theory of non-uniform gases: an account of the kinetic theory of viscosity, thermal conduction and diffusion in gases. Cambridge university press, 1990.

[30] K. Comeaux, D. Chapman, Ma, and R. Cormack, "An analysis of the burnett equations based on the second law of thermodynamics," in 33rd Aerospace sciences meeting and exhibit, p. 415, 1995.

[31] I. Müller, "On the frame dependence of stress and heat flux," Archive for rational mechanics and analysis, vol. 45, no. 4, pp. 241–250, 1972.

[32] X. Zhong, R. W. MacCormack, and D. R. Chapman, "Stabilization of the burnett equations and application to hypersonicflows," AIAA journal, vol. 31, no. 6, pp. 1036–1043, 1993.

[33] R. Balakrishnan, R. K. Agarwal, and K.-Y. Yun, "Bgk-burnett equations for flows in the continuum-transition regime," Journal of thermophysics and heat transfer, vol. 13, no. 4, pp. 397–410, 1999.

[34] H. Grad, "Asymptotic theory of the boltzmann equation," The physics of Fluids, vol. 6, no. 2, pp. 147–181, 1963.

[35] W. Weiss, Zur Hierarchie der Erweiterten Thermodynamik. PhD thesis, Technische Universität Berlin, 1990.

[36] I. Müller, "Extended thermodynamics: a theory of symmetric hyperbolic field equations," Entropy, vol. 10, no. 4, pp. 477–492, 2008.

[37] H. Grad, "On the kinetic theory of rarefied gases," Communications on pure and applied mathematics, vol. 2, no. 4, pp. 331–407, 1949.

[38] H. Grad, "Principles of the kinetic theory of gases," in Thermodynamik der Gase/Thermodynamics of Gases, pp. 205–294, Springer, 1958.

[39] I. Müller and T. Ruggeri, Rational extended thermodynamics, vol. 37. Springer Science & Business Media, 2013.

[40] C. D. Levermore, "Moment closure hierarchies for kinetic theories," Journal of statistical Physics, vol. 83, no. 5, pp. 1021–1065, 1996.

[41] B. C. Eu, "Kinetic theory and irreversible thermodynamics," NASA STI/Recon Technical Report A, vol. 93, p. 24498, 1992.

[42] R. Myong, "Thermodynamically consistent hydrodynamic computational models for high-knudsen-number gas flows," Physics of Fluids, vol. 11, no. 9, pp. 2788–2802, 1999.

[43] N. Singh and A. Agrawal, "Onsager's-principle-consistent 13-moment transport equations," Physical Review E, vol. 93, no. 6, p. 063111, 2016.

[44] N. Singh, R. S. Jadhav, and A. Agrawal, "Derivation of stable burnett equations for rarefied gas flows," Physical Review E, vol. 96, no. 1, p. 013106, 2017.

[45] H. Struchtrup and M. Torrilhon, "Regularization of grad's 13 moment equations: Derivation and linear analysis," Physics of Fluids, vol. 15, no. 9, pp. 2668–2680, 2003.

[46] G. V. Candler and R. W. MacCormack, "Computation of weakly ionized hypersonic flows in thermochemical nonequilibrium," Journal of Thermophysics and heat transfer, vol. 5, no. 3, pp. 266–273, 1991.

[47] G. V. Candler and I. Nompelis, "Computational fluid dynamics for atmospheric entry," tech. rep., MINNESOTA UNIV MINNEAPOLIS DEPT OF AEROSPACE ENGINEERING AND MECHANICS, 2009.

[48] G. Pahlani, T. E. Schwartzentruber, and R. James, "Investigation of the breakdown of navier-stokes equation using objective molecular dynamics," in AIAA SCITECH 2022 Forum, p. 1012, 2022.

[49] V. Garzó and A. Santos, Kinetic theory of gases in shear flows: nonlinear transport, vol. 131. Springer Science & Business Media, 2003.

[50] M. D. Kroells, C. Amato, E. Torres, T. E. Schwartzentruber, and G. V. Candler, "Detailed comparison of diffusive transport phenomena between cfd and dsmc," in AIAA Scitech 2020 Forum, p. 1229, 2020.

[51] N. Singh and T. Schwartzentruber, "Consistent kinetic-continuum recombination model for high temperature reacting flows," arXiv preprint arXiv:2009.05882, 2020.

[52] N. Singh and T. Schwartzentruber, "Consistent kinetic-continuum dissociation model. ii. continuum formulation and verification," The Journal of chemical physics, vol. 152, no. 22, p. 224303, 2020.

[53] R. S. Chaudhry, N. Singh, M. S. Grover, T. E. Schwartzentruber, and G. V. Candler, "Implementation of a nitrogen chemical kinetics model based on ab-initio data for hypersonic cfd," in 2018 Joint Thermophysics and Heat Transfer Conference, p. 3439, 2018.

[54] D. Frenkel and B. Smit, Understanding molecular simulation: from algorithms to applications, vol. 1. Elsevier, 2001.

[55] K. Xu and E. Josyula, "Continuum formulation for non-equilibrium shock structure calculation," Communications in computational physics, vol. 1, no. 3, pp. 425–448, 2006.

[56] J. G. Kim and I. D. Boyd, "State-resolved master equation analysis of thermochemical nonequilibrium of nitrogen," Chemical Physics, vol. 415, pp. 237–246, 2013.

[57] T. E. Schwartzentruber, M. S. Grover, and P. Valentini, "Direct molecular simulation of nonequilibrium dilute gases," Journal of Thermophysics and Heat Transfer, vol. 32, no. 4, pp. 892–903, 2018.

[58] P. Valentini, P. Norman, C. Zhang, and T. E. Schwartzentruber, "Rovibrational coupling in molecular nitrogen at high temperature: An atomic-level study," Physics of Fluids, vol. 26, no. 5, p. 056103, 2014.

[59] K. Koura, "4 carlo direct simulation of rotational relaxation of diatomic molecules using classical trajectory calculations: Nitrogen shock wave," Physics of Fluids, vol. 9, no. 11, pp. 3543–3549, 1997.

[60] Y. Paukku, K. R. Yang, Z. Varga, and D. G. Truhlar, "Global ab initio ground-state potential energy surface of n4," The Journal of chemical physics, vol. 139, no. 4, p. 044309, 2013.

[61] R. Jaffe, D. Schwenke, and G. Chaban, "Vibration-rotation excitation and dissociation in n2-n2 collisions from accurate theoretical calculations," in 10th AIAA/ASME Joint Thermophysics and Heat Transfer Conference, p. 4517, 2010.

[62] E. B. Tadmor, R. Phillips, and M. Ortiz, "Mixed atomistic and continuum models of deformation in solids," Langmuir, vol. 12, no. 19, pp. 4529–4534, 1996.

[63] S. Conti, P. Hauret, and M. Ortiz, "Concurrent multiscale computing of deformation microstructure by relaxation and local enrichment with application to single-crystal plasticity," Multiscale Modeling & Simulation, vol. 6, no. 1, pp. 135–157, 2007.

[64] D. Hull and D. J. Bacon, Introduction to dislocations. Butterworth-Heinemann, 2001.

[65] R. B. Sills, W. P. Kuykendall, A. Aghaei, and W. Cai, "Fundamentals of dislocation dynamics simulations," in Multiscale materials modeling for nanomechanics, pp. 53–87, Springer, 2016.

[66] L. Kubin, Dislocations, mesoscale simulations and plastic flow, vol. 5. Oxford University Press, 2013.

[67] W. Püschl, "Models for dislocation cross-slip in close-packed crystal structures: a critical review," Progress in materials science, vol. 47, no. 4, pp. 415–461, 2002.

[68] R. Madec, B. Devincre, and L. Kubin, "Simulation of dislocation patterns in multislip," Scripta materialia, vol. 47, no. 10, pp. 689–695, 2002.

[69] G. Esteban-Manzanares, R. Santos-Güemes, I. Papadimitriou, E. Martínez, and J. LLorca, "Influence of the stress state on the cross-slip free energy barrier in al: an atomistic investigation," Acta Materialia, vol. 184, pp. 109–119, 2020.

[70] E. Oren, E. Yahel, and G. Makov, "Kinetics of dislocation cross-slip: A molecular dynamics study," Computational Materials Science, vol. 138, pp. 246–254, 2017.

[71] M. Parrinello and A. Rahman, "Polymorphic transitions in single crystals: A new molecular dynamics method," Journal of Applied physics, vol. 52, no. 12, pp. 7182–7190, 1981.

[72] R. E. Miller, E. B. Tadmor, J. S. Gibson, N. Bernstein, and F. Pavia, "Molecular dynamics at constant cauchy stress," The Journal of chemical physics, vol. 144, no. 18, p. 184107, 2016.

[73] L. P. Kubin, G. Canova, M. Condat, B. Devincre, V. Pontikis, and Y. Bréchet, "Dislocation microstructures and plastic flow: a 3d simulation," in Solid state phenomena, vol. 23, pp. 455–472, Trans Tech Publ, 1992.

[74] A. M. Hussein, S. I. Rao, M. D. Uchic, D. M. Dimiduk, and J. A. El-Awady, "Microstructurally based cross-slip mechanisms and their effects on dislocation microstructure evolution in fcc crystals," Acta Materialia, vol. 85, pp. 180–190, 2015.

[75] M. Longsworth and M. Fivel, "Investigating the cross-slip rate in face-centered cubic metals using an atomistic-based cross-slip model in dislocation dynamics simulations," Journal of the Mechanics and Physics of Solids, vol. 153, p. 104449, 2021.

[76] K. Dayal, R. Elliott, and R. D. James, "Objective formulas," preprint, 2015.

[77] L. Verlet, "Computer" experiments" on classical fluids. i. thermodynamical properties of lennard-jones molecules," Physical review, vol. 159, no. 1, p. 98, 1967.

[78] W. C. Swope, H. C. Andersen, P. H. Berens, and K. R. Wilson, "A computer simulation method for the calculation of equilibrium constants for the formation of physical clusters of molecules: Application to small water clusters," The Journal of chemical physics, vol. 76, no. 1, pp. 637–649, 1982.

[79] M. Dobson, I. Fox, and A. Saracino, "Cell list algorithms for nonequilibrium molecular dynamics," Journal of Computational Physics, vol. 315, pp. 211–220, 2016.

[80] S. D. Galbraith, Mathematics of public key cryptography. Cambridge University Press, 2012.

[81] A. K. Lenstra, H. W. Lenstra, and L. Lovász, "Factoring polynomials with rational coefficients," Mathematische annalen, vol. 261, no. ARTICLE, pp. 515–534, 1982.

[82] X. Deng, "An introduction to lenstra-lenstra-lovasz lattice basis reduction algorithm," 2016.

[83] A. Baranyai and P. T. Cummings, "Steady state simulation of planar elongation flow by nonequilibrium molecular dynamics," The Journal of chemical physics, vol. 110, no. 1, pp. 42–45, 1999.

[84] A. Kraynik and D. Reinelt, "Extensional motions of spatially periodic lattices," International journal of multiphase flow, vol. 18, no. 6, pp. 1045–1059, 1992.

[85] T. A. Hunt, S. Bernardi, and B. Todd, "A new algorithm for extended nonequilibrium molecular dynamics simulations of mixed flow," The Journal of chemical physics, vol. 133, no. 15, p. 154116, 2010.

[86] A. Stukowski, "Visualization and analysis of atomistic simulation data with ovito–the open visualization tool," Modelling and simulation in materials science and engineering, vol. 18, no. 1, p. 015012, 2009.

[87] B. D. Coleman, H. Markovitz, and W. Noll, Viscometric flows of non-Newtonian fluids: theory and experiment, vol. 5. Springer Science & Business Media, 2012.

[88] S. U. Kim and C. W. Monroe, "High-accuracy calculations of sixteen collision integrals for lennard-jones (12–6) gases and their interpolation to parameterize neon, argon, and krypton," Journal of Computational Physics, vol. 273, pp. 358–373, 2014.

[89] E. Torres and T. E. Schwartzentruber, "Direct molecular simulation of oxygen dissociation across normal shocks," Theoretical and Computational Fluid Dynamics, vol. 36, no. 1, pp. 41–80, 2022.

[90] T. Kraska, "Molecular-dynamics simulation of argon nucleation from supersaturated vapor in the nve ensemble," The Journal of chemical physics, vol. 124, no. 5, p. 054507, 2006.

[91] J. Diemand, R. Angélil, K. K. Tanaka, and H. Tanaka, "Large scale molecular dynamics simulations of homogeneous nucleation," The Journal of chemical physics, vol. 139, no. 7, p. 074309, 2013.

[92] W. T. Ashurst and B. L. Holian, "Droplet formation by rapid expansion of a liquid," Physical Review E, vol. 59, no. 6, p. 6742, 1999.

[93] B. Todd and P. J. Daivis, "A new algorithm for unrestricted duration nonequilibrium molecular dynamics simulations of planar elongational flow," Computer physics communications, vol. 117, no. 3, pp. 191–199, 1999.

[94] P. Spijker, A. J. Markvoort, S. V. Nedea, and P. A. Hilbers, "Computation of accommodation coefficients and the use of velocity correlation profiles in molecular dynamics simulations," Physical Review E, vol. 81, no. 1, p. 011203, 2010.

[95] C. Cercignani et al., Mathematical methods in kinetic theory, vol. 1. Springer, 1969.

[96] J. C. Maxwell, The Scientific Letters and Papers of James Clerk Maxwell: Volume 1, 1846-1862, vol. 1. CUP Archive, 1990.

[97] D. Bhattacharya and G. Lie, "Nonequilibrium gas flow in the transition regime: a molecular-dynamics study," Physical Review A, vol. 43, no. 2, p. 761, 1991.

[98] N. Dongari, Y. Zhang, and J. M. Reese, "The importance of mean free path in determining gas micro flow behaviour," in International Conference on Nanochannels, Microchannels, and Minichannels, vol. 54501, pp. 481–490, 2010.

[99] D. L. Morris, L. Hannon, and A. L. Garcia, "Slip length in a dilute gas," Physical review A, vol. 46, no. 8, p. 5279, 1992.

[100] J. M. Reese and Y. Zhang, "Simulating fluid flows in micro and nano devices: the challenge of non-equilibrium behaviour," Journal of Computational and Theoretical Nanoscience, vol. 6, no. 10, pp. 2061–2074, 2009.

[101] M. Reiner, "A mathematical theory of dilatancy," American Journal of Mathematics, vol. 67, no. 3, pp. 350–362, 1945.

[102] R. S. Rivlin and J. L. Ericksen, Stress-Deformation Relations for Isotropic Materials, pp. 911–1013. New York, NY: Springer New York, 1997.

[103] R. Rivlin, "Forty years of non-linear continuum mechanics," in Collected Papers of RS Rivlin, pp. 2783–2811, Springer, 1997.

[104] W. Noll, "A mathematical theory of the mechanical behavior of continuous media," Archive for rational Mechanics and Analysis, vol. 2, no. 1, pp. 197–226, 1958.

[105] I. D. Boyd, G. Chen, and G. V. Candler, "Predicting failure of the continuum fluid equations in transitional hypersonic flows," Physics of fluids, vol. 7, no. 1, pp. 210–219, 1995.

[106] I. D. Boyd, "Predicting breakdown of the continuum equations under rarefied flow conditions," in AIP Conference Proceedings, vol. 663, pp. 899–906, American Institute of Physics, 2003.

[107] C. Truesdell and R. G. Muncaster, Fundamentals of Maxwel's Kinetic Theory of a Simple Monatomic Gas: Treated as a Branch of Rational Mechanics. Academic Press, 1980.

[108] J. Ou and J. Chen, "Nonlinear transport of rarefied couette flows from low speed to high speed," Physics of Fluids, vol. 32, no. 11, p. 112021, 2020.

[109] R. D. James, A. Nota, and J. J. Velázquez, "Self-similar profiles for homoenergetic solutions of the boltzmann equation: particle velocity distribution and entropy," Archive for Rational Mechanics and Analysis, vol. 231, no. 2, pp. 787–843, 2019.

[110] R. D. James, A. Nota, and J. J. Velázquez, "Long-time asymptotics for homoenergetic solutions of the boltzmann equation: collision-dominated case," Journal of Nonlinear Science, vol. 29, no. 5, pp. 1943–1973, 2019.

[111] R. D. James, A. Nota, and J. J. Velázquez, "Long time asymptotics for homoenergetic solutions of the boltzmann equation. hyperbolic-dominated case," Nonlinearity, vol. 33, no. 8, p. 3781, 2020.

[112] A. E. Green and R. S. Rivlin, "The mechanics of non-linear materials with memory," Archive for rational mechanics and analysis, vol. 1, no. 1, pp. 1–21, 1957.

[113] R. Rivlin, "Solution of some problems in the exact theory of visco-elasticity," Journal of Rational Mechanics and Analysis, vol. 5, no. 1, pp. 179–188, 1956.

[114] C. Bird and R. Huilgol, "Stress tensor in a non-viscometric flow such that the rivlin–ericksen tensors of order three and higher are zero," Journal of non-newtonian fluid mechanics, vol. 85, no. 1, pp. 1–10, 1999.

[115] B. C. Eu, "A modified moment method and irreversible thermodynamics," The Journal of Chemical Physics, vol. 73, no. 6, pp. 2958–2969, 1980.

[116] B. C. Eu, Nonequilibrium statistical mechanics: ensemble method, vol. 93. Springer Science & Business Media, 2013.

[117] G. Bird, "Breakdown of translational and rotational equilibrium in gaseous expansions," Aiaa Journal, vol. 8, no. 11, pp. 1998–2003, 1970.

[118] R. Myong and J. Park, "Confirmation of non-classical laws in nonequilibrium gases and application of conservation laws to verification of dsmc," in AIP Conference Proceedings, vol. 1501, pp. 621–628, American Institute of Physics, 2012.

[119] J. E. Dunn, "On the free energy and stability of nonlinear fluids," Journal of Rheology, vol. 26, no. 1, pp. 43–68, 1982.

[120] R. Fosdick and K. Rajagopal, "Anomalous features in the model of "second order fluids"," Archive for Rational Mechanics and Analysis, vol. 70, no. 2, pp. 145–152, 1979.

[121] B. D. Coleman, R. J. Duffin, and V. J. Mizel, "Instability, uniqueness, and nonexistence theorems for the equation ut= uxx- uxtx on a strip," Archive for Rational Mechanics and Analysis, vol. 19, no. 2, pp. 100–116, 1965.

[122] B. D. Coleman and V. J. Mizel, "Breakdown of laminar shearing flows for second-order fluids in channels of critical width," ZAMM-Journal of Applied Mathematics and Mechanics/Zeitschrift für Angewandte Mathematik und Mechanik, vol. 46, no. 7, pp. 445–448, 1966.

[123] J. E. Dunn and R. L. Fosdick, "Thermodynamics, stability, and boundedness of fluids of complexity 2 and fluids of second grade," Archive for Rational mechanics and Analysis, vol. 56, no. 3, pp. 191–252, 1974.

[124] J. D. Anderson, Hypersonic and high temperature gas dynamics. Aiaa, 2000.

[125] C. Park, "Nonequilibrium hypersonic aerothermodynamics," 1989.

[126] R. C. Millikan and D. R. White, "Systematics of vibrational relaxation," The Journal of chemical physics, vol. 39, no. 12, pp. 3209–3213, 1963.

[127] J. Appleton, M. Steinberg, and D. Liquornik, "Shock-tube study of nitrogen dissociation using vacuum-ultraviolet light absorption," The Journal of Chemical Physics, vol. 48, no. 2, pp. 599–608, 1968.

[128] S. Byron, "Shock-tube measurement of the rate of dissociation of nitrogen," The Journal of Chemical Physics, vol. 44, no. 4, pp. 1378–1388, 1966.

[129] C. Park, "Two-temperature interpretation of dissociation rate data for n2 and o2," in 26th Aerospace Sciences Meeting, p. 458, 1988.

[130] E. Torres and T. E. Schwartzentruber, "Direct molecular simulation of nitrogen dissociation under adiabatic postshock conditions," Journal of Thermophysics and Heat transfer, vol. 34, no. 4, pp. 801–815, 2020.

[131] P. Valentini, T. E. Schwartzentruber, J. D. Bender, and G. V. Candler, "Dynamics of nitrogen dissociation from direct molecular simulation," Physical Review Fluids, vol. 1, no. 4, p. 043402, 2016.

[132] P. Valentini, T. E. Schwartzentruber, J. D. Bender, I. Nompelis, and G. V. Candler, "Direct molecular simulation of nitrogen dissociation based on an ab initio potential energy surface," Physics of Fluids, vol. 27, no. 8, p. 086102, 2015.

[133] E. Torres and T. E. Schwartzentruber, "Direct molecular simulation of dissociating nitrogen in an adiabatic reactor," in AIAA Scitech 2019 Forum, p. 1049, 2019.

[134] C. Kondur and K. A. Stephani, "Molecular recombination dynamics of nitrogen from quasi-classical trajectory simulations of the n3 system," in AIAA SCITECH 2022 Forum, p. 1906, 2022.

[135] M. Panesi, R. L. Jaffe, D. W. Schwenke, and T. E. Magin, "Rovibrational internal energy transfer and dissociation of n 2 (1 σ g+)- n (4 s u) system in hypersonic flows," The Journal of chemical physics, vol. 138, no. 4, p. 044312, 2013.

[136] M. Panesi, A. Munafò, T. Magin, and R. Jaffe, "Nonequilibrium shock-heated nitrogen flows using a rovibrational state-to-state method," Physical Review E, vol. 90, no. 1, p. 013009, 2014.

[137] M. Capitelli, G. Colonna, and F. Esposito, "On the coupling of vibrational relaxation with the dissociation- recombination kinetics: From dynamics to aerospace applications," The Journal of Physical Chemistry A, vol. 108, no. 41, pp. 8930–8934, 2004.

[138] M. S. Ling and M. Rigby, "Towards an intermolecular potential for nitrogen," Molecular Physics, vol. 51, no. 4, pp. 855–882, 1984.

[139] N. Parsons, D. A. Levin, A. C. van Duin, and T. Zhu, "Modeling of molecular nitrogen collisions and dissociation processes for direct simulation monte carlo," The Journal of chemical physics, vol. 141, no. 23, p. 234307, 2014.

[140] I. Nompelis, Computational study of hypersonic double-cone experiments for code validation. University of Minnesota, 2004.

[141] C. Nyeland and G. D. Billing, "Transport coefficients of diatomic gases: internal-state analysis for rotational and vibrational degrees of freedom," The Journal of Physical Chemistry, vol. 92, no. 7, pp. 1752–1755, 1988.

[142] P. Norman, P. Valentini, and T. Schwartzentruber, "Gpu-accelerated classical trajectory calculation direct simulation monte carlo applied to shock waves," Journal of Computational Physics, vol. 247, pp. 153–167, 2013.

[143] R. Jaffe, "The calculation of high-temperature equilibrium and nonequilibrium specific heat data for n2, o2 and no," in 22nd Thermophysics Conference, p. 1633, 1987.

[144] G. Colonna, I. Armenise, D. Bruno, and M. Capitelli, "Reduction of state-to-state kinetics to macroscopic models in hypersonic flows," Journal of thermophysics and heat transfer, vol. 20, no. 3, pp. 477–486, 2006.

[145] I. Kadochnikov and I. Arsentiev, "Kinetics of nonequilibrium processes in air plasma formed behind shock waves: state-to-state consideration," Journal of Physics D: Applied Physics, vol. 51, no. 37, p. 374001, 2018.

[146] A. C. Van Duin, S. Dasgupta, F. Lorant, and W. A. Goddard, "Reaxff: a reactive force field for hydrocarbons," The Journal of Physical Chemistry A, vol. 105, no. 41, pp. 9396–9409, 2001.

[147] N. S. Parsons, T. Zhu, D. A. Levin, and A. C. Van Duin, "Development of dsmc chemistry models for nitrogen collisions using accurate theoretical calculations," in 52nd Aerospace Sciences Meeting, p. 1213, 2014.

[148] D. W. Schwenke, "Calculations of rate constants for the three-body recombination of h2 in the presence of h2," The Journal of chemical physics, vol. 89, no. 4, pp. 2076–2091, 1988.

[149] J. D. Bender, P. Valentini, I. Nompelis, Y. Paukku, Z. Varga, D. G. Truhlar, T. Schwartzentruber, and G. V. Candler, "An improved potential energy surface and multi-temperature quasiclassical trajectory calculations of n2+ n2 dissociation reactions," The Journal of chemical physics, vol. 143, no. 5, p. 054304, 2015.

[150] M. S. Grover, P. Valentini, E. Josyula, and R. S. Chaudhry, "Vibrational state-to-state and multiquantum effects for n2+ n2 interactions at high temperatures for aerothermodynamic applications," in AIAA Scitech 2020 Forum, p. 1227, 2020.

[151] L. Landau and E. Teller, "Zur theorie der schalldispersion," Phys. Z. Sowjetunion, vol. 10, no. 1, pp. 34–43, 1936.

[152] G. Colonna, L. D. Pietanza, and M. Capitelli, "Recombination-assisted nitrogen dissociation rates under nonequilibrium conditions," Journal of Thermophysics and Heat Transfer, vol. 22, no. 3, pp. 399–406, 2008.

[153] E. Marineau and H. Hornung, "High-enthalpy nonequilibrium nozzle flow of air: experiments and computations," in 39th AIAA Fluid Dynamics Conference, p. 4216, 2009.

[154] P. V. Marrone and C. E. Treanor, "Chemical relaxation with preferential dissociation from excited vibrational levels," The Physics of Fluids, vol. 6, no. 9, pp. 1215–1221, 1963.

[155] D. Bose and G. V. Candler, "Simulation of hypersonic flows using a detailed nitric oxide formation model," Physics of Fluids, vol. 9, no. 4, pp. 1171–1181, 1997.

[156] H. Luo, A. A. Alexeenko, and S. O. Macheret, "Assessment of classical impulsive models of dissociation in thermochemical nonequilibrium," Journal of Thermophysics and Heat Transfer, vol. 32, no. 4, pp. 861–868, 2018.

[157] E. Plönjes, P. Palm, W. Lee, M. D. Chidley, I. V. Adamovich, W. R. Lempert, and J. W. Rich, "Vibrational energy storage in high pressure mixtures of diatomic molecules," Chemical Physics, vol. 260, no. 3, pp. 353–366, 2000.

[158] E. Kustova, E. Nagnibeda, T. Y. Alexandrova, and A. Chikhaoui, "On the non-equilibrium kinetics and heat transfer in nozzle flows," Chemical physics, vol. 276, no. 2, pp. 139–154, 2002.

[159] W. Vincenti and C. Kruger, "Introduction to physical gas dynamics 1967," New Yor: Wiley.

[160] R. E. Graves and B. M. Argrow, "Bulk viscosity: past to present," Journal of Thermophysics and Heat Transfer, vol. 13, no. 3, pp. 337–342, 1999.

[161] J. Hirth, "A brief history of dislocation theory," Metallurgical Transactions A, vol. 16, no. 12, pp. 2085–2090, 1985.

[162] G. I. Taylor, "The mechanism of plastic deformation of crystals. part i.—theoretical," Proceedings of the Royal Society of London. Series A, Containing Papers of a Mathematical and Physical Character, vol. 145, no. 855, pp. 362–387, 1934.

[163] D. Hull and D. J. Bacon, Introduction to dislocations, vol. 37. Elsevier, 2011.

[164] W. Cai and W. D. Nix, Imperfections in crystalline solids. Cambridge University Press, 2016.

[165] R. Fleischer, "Cross slip of extended dislocations," Acta Metallurgica, vol. 7, no. 2, pp. 134–135, 1959.

[166] B. Escaig, "Sur le glissement dévié des dislocations dans la structure cubique à faces centrées," Journal de Physique, vol. 29, no. 2-3, pp. 225–239, 1968.

[167] J. Friedel, Dislocations: international series of monographs on solid state physics, vol. 3. Elsevier, 2013.

[168] W. P. Kuykendall, Y. Wang, and W. Cai, "Stress effects on the energy barrier and mechanisms of cross-slip in fcc nickel," Journal of the Mechanics and Physics of Solids, vol. 144, p. 104105, 2020.

[169] S. Rao, T. Parthasarathy, and C. Woodward, "Atomistic simulation of cross-slip processes in model fcc structures," Philosophical Magazine A, vol. 79, no. 5, pp. 1167–1192, 1999.

[170] A. F. Voter and S. P. Chen, "Accurate interatomic potentials for ni, al and ni3al," MRS Online Proceedings Library (OPL), vol. 82, 1986.

[171] D. J. Siegel, "Generalized stacking fault energies, ductilities, and twinnabilities of ni and selected ni alloys," Applied Physics Letters, vol. 87, no. 12, p. 121901, 2005.

[172] N. Bernstein and E. Tadmor, "Tight-binding calculations of stacking energies and twinnability in fcc metals," Physical Review B, vol. 69, no. 9, p. 094116, 2004.

[173] P. Hirel, "Atomsk: A tool for manipulating and converting atomic data files," Computer Physics Communications, vol. 197, pp. 212–219, 2015.

[174] E. Oren, E. Yahel, and G. Makov, "Dislocation kinematics: a molecular dynamics study in cu," Modelling and Simulation in Materials Science and Engineering, vol. 25, no. 2, p. 025002, 2016.

[175] D. Mordehai, Y. Ashkenazy, I. Kelson, and G. Makov, "Dynamic properties of screw dislocations in cu: a molecular dynamics study," Physical Review B, vol. 67, no. 2, p. 024112, 2003.

[176] A. Stukowski and K. Albe, "Extracting dislocations and non-dislocation crystal defects from atomistic simulation data," Modelling and Simulation in Materials Science and Engineering, vol. 18, no. 8, p. 085001, 2010.

[177] N. C. Admal and E. B. Tadmor, "A unified interpretation of stress in molecular systems," Journal of elasticity, vol. 100, no. 1, pp. 63–143, 2010.

[178] R. J. Hardy, "Formulas for determining local properties in molecular-dynamics simulations: Shock waves," The Journal of Chemical Physics, vol. 76, no. 1, pp. 622–628, 1982.

[179] R. J. Hardy, S. Root, and D. R. Swanson, "Continuum properties from molecular simulations," in AIP Conference Proceedings, vol. 620, pp. 363–366, American Institute of Physics, 2002.

[180] J. Bonneville and B. Escaig, "Cross-slipping process and the stress-orientation dependence in pure copper," Acta Metallurgica, vol. 27, no. 9, pp. 1477–1486, 1979.

[181] S. Xu, L. Xiong, Y. Chen, and D. L. McDowell, "Shear stress-and line length-dependent screw dislocation cross-slip in fcc ni," Acta Materialia, vol. 122, pp. 412–419, 2017.

[182] C. Jin, Y. Xiang, and G. Lu, "Dislocation cross-slip mechanisms in aluminum," Philosophical Magazine, vol. 91, no. 32, pp. 4109–4125, 2011.

[183] K. Kang, J. Yin, and W. Cai, "Stress dependence of cross slip energy barrier for face-centered cubic nickel," Journal of the Mechanics and Physics of Solids, vol. 62, pp. 181–193, 2014.

[184] R. Scattergood and D. Bacon, "The orowan mechanism in anisotropic crystals," Philosophical Magazine, vol. 31, no. 1, pp. 179–198, 1975.

[185] R. Scattergood and D. Bacon, "The strengthening effect of voids," Acta Metallurgica, vol. 30, no. 8, pp. 1665–1677, 1982.

[186] Y. Fan, Y. N. Osetskiy, S. Yip, and B. Yildiz, "Mapping strain rate dependence of dislocation-defect interactions by atomistic simulations," Proceedings of the National Academy of Sciences, vol. 110, no. 44, pp. 17756–17761, 2013.

[187] Y. Fan, Y. N. Osetsky, S. Yip, and B. Yildiz, "Onset mechanism of strain-rate-induced flow stress upturn," Physical review letters, vol. 109, no. 13, p. 135503, 2012.

[188] T. Zhu, J. Li, A. Samanta, A. Leach, and K. Gall, "Temperature and strain-rate dependence of surface dislocation nucleation," Physical Review Letters, vol. 100, no. 2, p. 025502, 2008.

[189] R. Marcelin, "Physicochemical kinetics," Ann. Phys, vol. 3, pp. 120–184, 1915.

[190] H. Eyring, "The activated complex in chemical reactions," The Journal of Chemical Physics, vol. 3, no. 2, pp. 107–115, 1935.

[191] G. H. Vineyard, "Frequency factors and isotope effects in solid state rate processes," Journal of Physics and Chemistry of Solids, vol. 3, no. 1-2, pp. 121–127, 1957.

[192] A. F. Voter, F. Montalenti, and T. C. Germann, "Extending the time scale in atomistic simulation of materials," Annual review of materials research, vol. 32, no. 1, pp. 321–346, 2002.

[193] S. Ryu, K. Kang, and W. Cai, "Predicting the dislocation nucleation rate as a function of temperature and stress," Journal of Materials Research, vol. 26, no. 18, pp. 2335–2354, 2011.

[194] W. Meyer and H. Neldel, "Relation between the energy constant and the quantity constant in the conductivity–temperature formula of oxide semiconductors," Z. tech. Phys, vol. 18, no. 12, pp. 588–593, 1937.

[195] C. Sobie, L. Capolungo, D. L. McDowell, and E. Martinez, "Modal analysis of dislocation vibration and reaction attempt frequency," Acta Materialia, vol. 134, pp. 203–210, 2017.

[196] T. Rasmussen, Vegge, T. Leffers, O. Pedersen, and K. W. Jacobsen, "Simulation of structure and annihilation of screw dislocation dipoles," Philosophical Magazine A, vol. 80, no. 5, pp. 1273–1290, 2000.

[197] D. Rigney and J. Hammerberg, "Unlubricated sliding behavior of metals," Mrs Bulletin, vol. 23, no. 6, pp. 32–36, 1998.

[198] N. Epiphaniou, "Modelling of dynamic friction across solid material interfaces using molecular dynamics techniques," 2010.

Appendix A

Rivlin-Ericksen Constitutive Model

A.1 Connection of RE model with Burnett equations

The viscous stress tensor to Burnett order for OMD flows is given by

$$\boldsymbol{\tau} = \boldsymbol{\tau}^1 + \boldsymbol{\tau}^2 = -2\mu_{\mathrm{NSF}}\overline{\nabla \mathbf{v}} + \omega_1 \frac{\mu^2}{p}\nabla\cdot\mathbf{v}\overline{\nabla \mathbf{v}}$$
$$+\omega_2 \frac{\mu^2}{p}\left(\frac{D}{Dt}\overline{\nabla \mathbf{v}} - 2\overline{\nabla \mathbf{v}\cdot\overline{\nabla \mathbf{v}}}\right) + \omega_6 \frac{\mu^2}{p}\overline{\overline{\nabla \mathbf{v}}\cdot\overline{\nabla \mathbf{v}}} \tag{A.1}$$

where single bar over velocity gradient denotes $\overline{\nabla \mathbf{v}} = \frac{1}{2}(\nabla \mathbf{v} + (\nabla \mathbf{v})^{\mathrm{T}}) - \frac{1}{3}\nabla\cdot\mathbf{v}\mathbf{I}$. Simplifying terms involved in the summation (A.1) for incompressible flows ($\nabla\cdot\mathbf{v} = 0$) gives:

$$\overline{\nabla \mathbf{v}} = \frac{1}{2}(\nabla \mathbf{v} + (\nabla \mathbf{v})^{\mathrm{T}}) = \frac{\mathbf{A}_1}{2} \tag{A.2}$$

$$\nabla \mathbf{v}\cdot\overline{\nabla \mathbf{v}} = \nabla \mathbf{v}\cdot\frac{\mathbf{A}_1}{2} = \nabla \mathbf{v}^{\mathrm{T}}\frac{\mathbf{A}_1^{\mathrm{T}}}{2}$$

$$\overline{\nabla\mathbf{v}\cdot\overline{\nabla\mathbf{v}}} = \frac{1}{2}(\nabla\mathbf{v}^{\mathrm{T}}\frac{\mathbf{A}_1^{\mathrm{T}}}{2} + (\nabla\mathbf{v}^{\mathrm{T}}\frac{\mathbf{A}_1^{\mathrm{T}}}{2})^{\mathrm{T}}) - \frac{1}{3}\mathrm{tr}(\nabla\mathbf{v}^{\mathrm{T}}\frac{\mathbf{A}_1^{\mathrm{T}}}{2})\mathbf{I}$$

$$\frac{D}{Dt}\overline{\nabla\mathbf{v}} = \frac{1}{2}\frac{D\mathbf{A}_1}{Dt}$$

$$(\frac{D}{Dt}\overline{\nabla\mathbf{v}} - 2\overline{\nabla\mathbf{v}\cdot\overline{\nabla\mathbf{v}}}) = \frac{1}{2}\left[\frac{D\mathbf{A}_1}{Dt} - (\nabla\mathbf{v}^{\mathrm{T}}\mathbf{A}_1^{\mathrm{T}} + (\nabla\mathbf{v}^{\mathrm{T}}\mathbf{A}_1^{\mathrm{T}})^{\mathrm{T}})\right] + \frac{2}{3}\mathrm{tr}(\nabla\mathbf{v}^{\mathrm{T}}\frac{\mathbf{A}_1^{\mathrm{T}}}{2})\mathbf{I} \tag{A.3}$$

Substituting the definition of $\mathbf{A}_2 = \frac{D\mathbf{A}_1}{Dt} + (\nabla\mathbf{v})^{\mathrm{T}}\mathbf{A}_1 + \mathbf{A}_1(\nabla\mathbf{v})$ in (A.3) gives:

$$\frac{D}{Dt}\overline{\nabla\mathbf{v}} - 2\overline{\nabla\mathbf{v}\overline{\nabla\mathbf{v}}} = \frac{1}{2}\left[\mathbf{A}_2 - 2(\nabla\mathbf{v})^{\mathrm{T}}\mathbf{A}_1 - 2\mathbf{A}_1(\nabla\mathbf{v})\right] + \frac{2}{3}\mathrm{tr}(\nabla\mathbf{v}^{\mathrm{T}}\frac{\mathbf{A}_1}{2})\mathbf{I} \tag{A.4}$$

$$\overline{\overline{\nabla\mathbf{v}}\cdot\overline{\nabla\mathbf{v}}} = \frac{1}{4}(\mathbf{A}_1^2 + \mathbf{A}_1^{2^{\mathrm{T}}}) - \frac{1}{3}\mathrm{tr}(\mathbf{A}_1^2) = \frac{\mathbf{A}_1^2}{2} - \frac{1}{3}\mathrm{tr}(\mathbf{A}_1^2)\mathbf{I} \tag{A.5}$$

Use of (A.2), (A.4) and (A.5) reduces (A.1) for incompressible flows to

$$\boldsymbol{\tau} = \boldsymbol{\tau}^1 + \boldsymbol{\tau}^2 = -\mu_{\mathrm{NSF}}\mathbf{A}_1 + \omega_2\frac{\mu^2}{2p}\left[\mathbf{A}_2 - 2\nabla\mathbf{v}^{\mathrm{T}}\mathbf{A}_1 - 2\mathbf{A}_1\nabla\mathbf{v} + \frac{4}{3}\mathrm{tr}(\nabla\mathbf{v}^{\mathrm{T}}\frac{\mathbf{A}_1}{2})\mathbf{I}\right] + \omega_6\frac{\mu^2}{\mathrm{p}}\left[\frac{\mathbf{A}_1^2}{2} - \frac{1}{3}\mathrm{tr}(\mathbf{A}_1^2)\mathbf{I}\right] \tag{A.6}$$

$$\boldsymbol{\tau} = -\mu_{\mathrm{NSF}}\mathbf{A}_1 + \omega_2\frac{\mu^2}{2p}\mathbf{A}_2 + (\omega_6\frac{\mu^2}{2p})\mathbf{A}_1^2 + \omega_2\frac{\mu^2}{p}(\nabla\mathbf{v}^{\mathrm{T}}\mathbf{A}_1 - \mathbf{A}_1\nabla\mathbf{v}) + \omega_2\frac{2\mu^2}{3p}(\mathrm{tr}(\nabla\mathbf{v}^{\mathrm{T}}\frac{\mathbf{A}_1}{2})\mathbf{I}) - \omega_6\frac{\mu^2}{3\mathrm{p}}(\mathrm{tr}(\mathbf{A}_1^2)\mathbf{I}) \tag{A.7}$$

A.2 RE model fitted coefficients

s^*	P	μ^*	α_1^*
1.49	-0.688	0.938	0.239
3.15	-1.46	0.654	0.083
6.59	-3.05	0.438	0.0323
10.2	-4.74	0.307	0.0151
14	-6.48	0.244	0.00925
17.8	-8.26	0.197	0.00601
21.8	-10.1	0.164	0.00423
25.8	-11.9	0.138	0.00308
29.9	-13.9	0.121	0.00242

Table A.1: OMD computed coefficients for compressible planar shear flow

s^*	μ^*	α_1^*
0.557	0.852	0.744
1.11	0.622	0.486
2.23	0.359	0.234
3.34	0.244	0.134
4.46	0.18	0.0864
5.57	0.142	0.0608
8.36	0.08952	0.0306
11.1	0.0642	0.0183
13.9	0.0490	0.0122
16.7	0.0391	0.00875
19.5	0.0317	0.0382
22.3	0.0262	0.00514

Table A.2: OMD computed coefficients for incompressible simple shear flow ($P = 0$)

A.3 Critical cross-slip stress

Strain rate (K)	Theoretical [GPa]	σ^*_{13} (Domain(1)) [GPa]	σ^*_{13} (Domain(2)) [GPa]
$1e5$	2.63	-	2.544
$5e5$	2.71	2.67	2.57
$1e6$	2.74	2.59	2.73
$5e6$	2.82	2.75	2.79
$1e7$	2.85	2.81	2.86
$3e7$	2.91	2.97	-
$5e7$	2.94	2.97	-
$8e7$	2.96	3.03	2.86
$1e8$	2.98	-	3.156
$3e8$	3.04	3.16	3.36
$8e8$	3.10	3.18	-

Table A.3: Critical stresses of cross slip for different strain rates K at temperature $T = 320$K for small dislocation segment

Temperature [K]	Theoretical [GPa]	σ^*_{13} (Domain(1)) [GPa]	σ^*_{13} (Domain(2)) [GPa]
120	3.14	3.27	-
128	3.13	-	3.322
180	3.06	2.72	-
188	3.05	-	3.122
220	3.00	2.95	-
280	2.91	3	-
320	2.86	2.82	-
390	2.75	2.57	-
397	2.74	-	2.73
420	2.69	2.08	-

Table A.4: Critical stresses of cross slip for different temperatures at the strain rate of $K = 10^7 \mathrm{s}^{-1}$ for small dislocation segment

Strain rate (K)	Theoretical [GPa]	σ^*_{13} (Domain(4)) [GPa]	σ^*_{13} (Domain(3)) [GPa]	σ^*_{13} (Domain(5)) [GPa]
$5e4$	3.05	3.14	-	-
$2e5$	3.14	3.15	-	-
$5e5$	3.21	3.19	-	3.184
$1e6$	3.23	3.22	-	3.185
$5e6$	3.25	3.29	3.26	3.24
$1e7$	3.26	3.28	3.33	3.27
$5e7$	3.26	3.40	3.40	3.387
$1e8$	3.26	3.41	3.38	3.388

Table A.5: Critical stresses of cross slip for different strain rates K at temperature $T = 320$K for large/flexible dislocation segment

Temperature [K]	Theoretical [GPa]	σ^*_{13} (Domain(3)) [GPa]	σ^*_{13} (Domain(4)) [GPa]
113	3.09	3.54	-
124	3.30	-	3.53
133	3.30	3.52	-
208	3.28	-	3.42
213	3.28	3.43	-
273	3.27	3.31	-
308	3.26	-	3.28
313	3.26	3.37	-
383	3.24	3.17	-
408	3.23	-	3.121
413	3.23	3.19	-
507	3.21	-	3.08

Table A.6: Critical stresses of cross slip for different temperatures at the strain rate of $K = 10^7 \mathrm{s}^{-1}$ for large/flexible dislocation segment